NREL
NATIONAL RENEWABLE ENERGY LABORATORY

Wind Turbine Gearbox Condition Monitoring Round Robin Study – Vibration Analysis

S. Sheng, Editor
National Renewable Energy Laboratory

NREL is a national laboratory of the U.S. Department of Energy, Office of Energy Efficiency & Renewable Energy, operated by the Alliance for Sustainable Energy, LLC.

Technical Report
NREL/TP-5000-54530
July 2012

Contract No. DE-AC36-08GO28308

NREL
NATIONAL RENEWABLE ENERGY LABORATORY

Wind Turbine Gearbox Condition Monitoring Round Robin Study – Vibration Analysis

S. Sheng, Editor
National Renewable Energy Laboratory

Prepared under Task No. WE11.0305

NREL is a national laboratory of the U.S. Department of Energy, Office of Energy Efficiency & Renewable Energy, operated by the Alliance for Sustainable Energy, LLC.

National Renewable Energy Laboratory
15013 Denver West Parkway
Golden, Colorado 80401
303-275-3000 • www.nrel.gov

Technical Report
NREL/TP-5000-54530
July 2012

Contract No. DE-AC36-08GO28308

NOTICE

This report was prepared as an account of work sponsored by an agency of the United States government. Neither the United States government nor any agency thereof, nor any of their employees, makes any warranty, express or implied, or assumes any legal liability or responsibility for the accuracy, completeness, or usefulness of any information, apparatus, product, or process disclosed, or represents that its use would not infringe privately owned rights. Reference herein to any specific commercial product, process, or service by trade name, trademark, manufacturer, or otherwise does not necessarily constitute or imply its endorsement, recommendation, or favoring by the United States government or any agency thereof. The views and opinions of authors expressed herein do not necessarily state or reflect those of the United States government or any agency thereof.

Available electronically at http://www.osti.gov/bridge

Available for a processing fee to U.S. Department of Energy
and its contractors, in paper, from:

U.S. Department of Energy
Office of Scientific and Technical Information
P.O. Box 62
Oak Ridge, TN 37831-0062
phone: 865.576.8401
fax: 865.576.5728
email: mailto:reports@adonis.osti.gov

Available for sale to the public, in paper, from:

U.S. Department of Commerce
National Technical Information Service
5285 Port Royal Road
Springfield, VA 22161
phone: 800.553.6847
fax: 703.605.6900
email: orders@ntis.fedworld.gov
online ordering: http://www.ntis.gov/help/ordermethods.aspx

Cover Photos: (left to right) PIX 16416, PIX 17423, PIX 16560, PIX 17613, PIX 17436, PIX 17721

Printed on paper containing at least 50% wastepaper, including 10% post consumer waste.

Acknowledgements

The National Renewable Energy Laboratory's (NREL) contributions to this report were funded by the Wind and Water Power Program, Office of Energy Efficiency and Renewable Energy of the U.S. Department of Energy, under contract No. DE-AC02-05CH11231. The authors are solely responsible for any omission or errors contained herein. NREL wishes to acknowledge and thank the Office of Energy Efficiency and Renewable Energy and its staff who have supported this work from its inception. Specifically, NREL would like to thank Mark Higgins and Michael Derby for their support and guidance.

NREL deeply appreciates the voluntarily support from all sixteen partners of the Wind Turbine Gearbox Condition Monitoring Round Robin project. One project partner estimates that the value of the voluntary support from all partners would be worth $2 to $3 million.

Nomenclature

Acronym	Definition
A/D	analog to digital
AM	amplitude modulation
BPFI	ball-passing frequency inner race
BPFO	ball-passing frequency outer race
BSF	ball-spinning frequency
CF	crest factor
CI	condition indicator
CM	condition monitoring
COE	cost of energy
CRB	cylindrical roller bearing
DAS	data acquisition system
DOD	Department of Defense
DOE	Department Of Energy
DSTO	Defence Science and Technology Organisation (Australia)
DTF	Dynamometer Test Facility
EO	energy operator
fcCRB	full complement cylindrical roller bearing
FFT	Fast Fourier Transform
FTF	fundamental train frequency
FM	frequency modulation
GE	General Electric
GL	Germanischer Lloyd
GRC	Gearbox Reliability Collaborative
GMF	gear meshing frequency
HS	High speed
HSGM	high-speed gear meshing stage
HSIS	high-speed intermediate shaft
HSS	high-speed shaft
ISGM	intermediate speed gear meshing stage
IMS	intermediate-speed shaft
IMS	Intelligent Maintenance Systems
INT	intermediate
JTFA	joint time frequency analysis

Acronym	Definition
LS	low speed
LSIS	low-speed intermediate shaft
LSS	low-speed shaft
MS	main shaft
NASA	National Aeronautics and Space Administration
NREL	National Renewable Energy Laboratory
NWTC	National Wind Technology Center
O&M	operation and maintenance
PGSF	spin frequency of the planetary gear
PLC	planet carrier
PLTGM	planetary gear meshing stage
RMS	root mean square
RPM	revolutions per minute
SER	sideband energy ratio
SF	severity factor
SH	shaft
SK	spectral kurtosis
SO	shaft order
TRB	tapered roller bearing
TSA	time synchronous averaging

Executive Summary

Utility-scale wind turbines have historically experienced premature component failures, which subsequently increase the cost of energy. The majority of these failures are caused by faults in the drivetrain, led by the main gearbox. To understand the possible causes for gearbox failures and recommend practices for improvement, the National Wind Technology Center (NWTC), at the National Renewable Energy Laboratory (NREL), started a project called the Gearbox Reliability Collaborative (GRC). Condition Monitoring (CM) is one research area under the GRC. It is a method to assess a system's health, which enables proactive maintenance planning, reduces downtime and operations and maintenance costs, and, to some extent, increases safety.

To understand the dynamic responses of wind turbine gearboxes under different loading conditions, the GRC tested two identical gearboxes. One was tested on the NWTC's 2.5 MW dynamometer and the other was first tested in the dynamometer, and then field tested in a turbine in a nearby wind plant. In the field, the test gearbox experienced two oil loss events that resulted in damage to its internal bearings and gears. Since the damage was not catastrophic, the test gearbox was removed from the field and retested in the NWTC's dynamometer before it was disassembled. During the dynamometer retest, various condition monitoring systems, e.g., vibration and oil debris, collected data along with testing condition information. The vibration-based condition monitoring system and the test condition data enabled NREL to launch a Wind Turbine Gearbox Condition Monitoring Round Robin project, as described in this report. The main objective of this project is to evaluate different vibration analysis algorithms used in wind turbine CM and determine whether typical practices are effective. With the involvement of both academic researchers and industrial partners, the Round Robin provides cutting edge research results to industry stakeholders.

Under this project, the collected vibration and testing condition data, along with the test gearbox configuration information, were shared with partners who signed memoranda of understanding documents with NREL. The partners were given a time window of two months to analyze the shared data using whichever algorithms they had or could develop. Partners did not have prior knowledge of the extent or location of the damage in the test gearbox. After their diagnostic results were submitted to NREL, the actual damage information on the test gearbox was disclosed to them so they could further fine tune their results. The project had sixteen partners, including seven universities and nine from the private sector. The main body of this report discusses detailed analysis algorithms and diagnostic results from eight of the sixteen partners.

Below is a brief synopsis for this report:

- In Chapter 1, the background and objectives of this Round Robin project are presented, along with the summary of blind study stage diagnostics results from all sixteen project partners.
- In Chapter 2, the test gearbox, dynamometer test facility, one customized vibration data acquisition system, test conditions, and actual damage found on the test gearbox through its disassembly are presented.

- In Chapter 3, to overcome the inaccuracy incurred by speed variations, a synchronous sampling technique is introduced. To accommodate high gear ratios in wind turbine gearboxes, a digital domain synchronous re-sampling technique is presented.
- In Chapter 4, an evaluation is conducted of analysis algorithms originally developed for Department of Defense applications, including the results of these algorithms when applied to the GRC wind turbine dataset. The algorithms consist of sensor validation, bearing fault detection/isolation, and gear fault detection/isolation modules. A joint time frequency analysis is also discussed.
- In Chapter 5, a validation is presented of analysis algorithms that are used in the aerospace community for the wind industry. The focus is on two methodologies: synchronous analysis of shaft/gear components and non-synchronous analysis of bearings.
- In Chapter 6, various vibration signal processing and feature extraction algorithms are evaluated. It details the evaluated methods including frequency domain, cepstrum, bearing envelope analysis, spectral kurtosis filtering, time synchronous averaging, and a planet separation method.
- In Chapter 7, sideband pattern analysis is performed on all gears for gear fault diagnosis. Data from torque measurements have also been analyzed to facilitate annulus gear diagnosis. For the bearing diagnosis, a multi-scale enveloping spectra technique is investigated.
- In Chapter 8, analysis of "jerk" data derived from vibration acceleration data of the test wind turbine gearbox are discussed. For component failure identification, the correlation coefficient analysis and clustering analysis are applied to identify the failure stage of the gearbox in the time domain.
- In Chapter 9, the algorithms for bearing diagnostics are presented. They consist of several different stages to separate and enhance the bearing signals, and then envelope analysis is applied. For parallel stage gear diagnostics, classic synchronously-averaged signatures are studied and comparisons are made of spectra and cepstra from the healthy and faulty conditions. For individual planet and sun gear diagnostics, the premium current method is investigated.
- In Chapter 10, a two stage fault detection framework, with analytical and graphical analysis for wind turbine gearbox CM, is proposed. The analytical diagnostics and graphical analysis are performed for fault detection and defect severity level evaluation of different damage modes based on sideband and kurtosis analyses.
- In Chapter 11, some recommended practices for data acquisition and data analysis are described for use in conducting vibration-based wind turbine drivetrain condition monitoring.

It is worth noting that the synopses detailed for Chapters 3-10 were based on the analysis algorithms of the project's partners. Detailed diagnostic results obtained by each partner are listed in this report.

The study has demonstrated that the wind industry can improve vibration analysis algorithms for drivetrain condition monitoring. Both the presented algorithms and the recommended practices can be considered by CM equipment suppliers in their future product releases for the benefit of the wind industry.

Table of Contents

List of Figures

List of Tables

1 Introduction

Wind energy is currently the fastest growing type of renewable energy resource in the world [1]. However, the industry still experiences premature component failures, which increase operation and maintenance (O&M) costs, and subsequently, the cost of energy (COE) for wind power. As turbines increase in size and are installed offshore, these failures will become even more costly. To make wind power more competitive, there is a need for the industry to improve turbine reliability and availability.

Given that the gearbox is the most costly drivetrain component to maintain throughout the expected 20-year design life of a wind turbine, the National Renewable Energy Laboratory (NREL) organized a consortium called the Gearbox Reliability Collaborative (GRC) to address the gearbox reliability and availability challenges. The GRC engages key representatives in the wind turbine gearbox supply chain, including turbine owners, operators, gearbox manufacturers, bearing manufacturers, lubricant companies, and wind turbine manufacturers. The GRC's goals are to conduct research that improves gearbox reliability and increases turbine availability. The GRC engages a multi-track approach, which includes modeling and analysis, dynamometer testing, field testing, condition monitoring (CM), and developing a gearbox failure database [2]. CM is a method to assess a system's health, which enables proactive maintenance planning, reduces downtime and operations and maintenance costs, and, to some extent, increases safety [3]. It will be the main focus of this report.

The GRC uses two identical test gearboxes: one was tested on NREL's 2.5 MW dynamometer; the other was first tested in the dynamometer, and then field tested in a turbine in a nearby wind plant. In the field, the test gearbox experienced two oil loss events that resulted in damage to its internal bearings and gears. Additional field tests of this gearbox were terminated to prevent further damage to the gearbox. From the CM point of view, however, it provided a unique opportunity to evaluate different monitoring techniques by retesting the gearbox in NREL's dynamometer under controlled testing conditions. The gearbox was removed from the field and retested in the NREL's 2.5 MW dynamometer before it was disassembled. During the dynamometer retest, various condition monitoring systems data were collected, e.g., vibration and oil debris, along with testing condition information. The vibration-based condition monitoring system and the test condition data enabled NREL to launch the Wind Turbine Gearbox Condition Monitoring Round Robin (Round Robin) project that involves the analysis of the collected vibration data by several independent research partners and then draws conclusions from the comparison of their analysis results.

The main objective of the CM Round Robin project was to evaluate different vibration analysis algorithms used in wind turbine CM and to determine whether typical practices are effective. Another project objective was to assess the capability of vibration-based CM and to establish a baseline from which future improvements can be measured. With the involvement of both academic researchers and industrial partners, the Round Robin provides cutting edge research results to industry stakeholders.

In the project, the collected vibration and testing condition data, along with the test gearbox configuration information, were shared with partners who signed memorandum of understanding

documents with NREL. The partners were given a time window of two months to analyze the shared data using whichever algorithms they had or could develop. Partners did not have prior knowledge of the actual damage within the test gearbox. After their diagnostics results were submitted to NREL, the actual damage information within the test gearbox was disclosed to them, so they could further fine tune their results. The project had sixteen partners, including seven universities and nine from the private sector. The main body of this report discusses detailed analysis algorithms and diagnostics results from eight of the sixteen partners. (For a list of partners, see Appendix A.)

The project is unique since the initial diagnostic results from the partners were obtained during a blind study. Also, the test gearbox did not begin with seeded faults, as have been investigated in many other studies. Based on the particulars of the actual damage found after the test gearbox was disassembled [4], all of the partners agreed that seven damage instances could be detected through vibration analysis. These damage instances were chosen as the reference for the partners' diagnostics performance evaluation. The evaluation criteria included successful identifications, false alarms, and missed detections. A comparison of the results, without the partners' names is illustrated in Figure 1.1. The chart depicts the highest ratio of successful identification as five of the seven damage instances. Most partners had more missed detections than false alarms. Thus, there is room for the industry to improve vibration-based diagnostic algorithms. Most of the Round Robin study partners agreed that this project was a valuable effort.

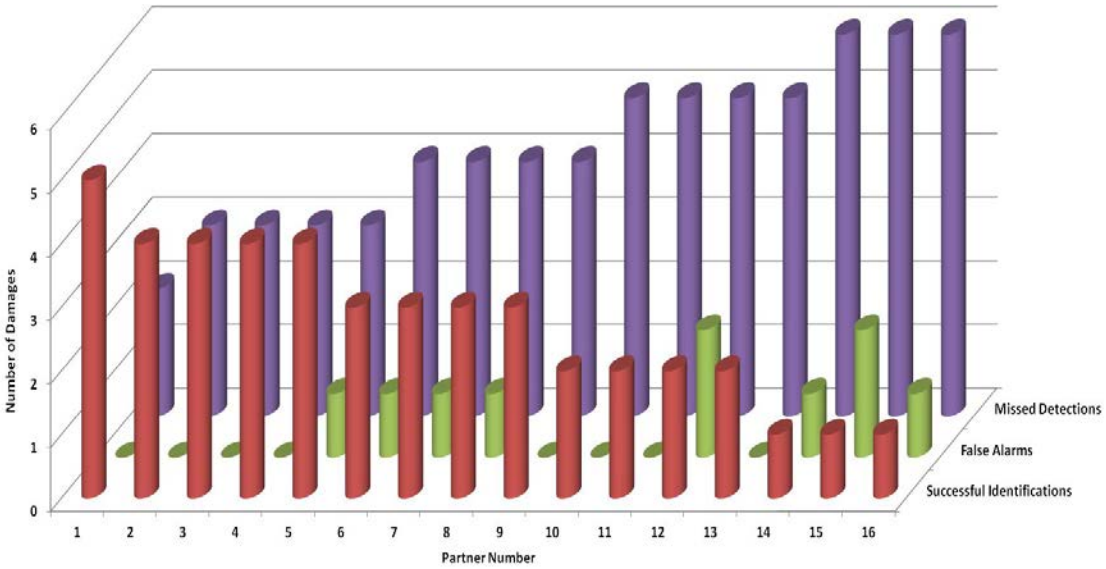

Figure 1.1. Blind study stage diagnostics results comparison

The next chapter of this report describes the test gearbox configuration, its customized data acquisition system, test conditions, and actual damage information obtained during the test gearbox disassembly. The main body of the report contains a detailed presentation of the analysis algorithms and diagnostic results from eight out of the sixteen research partners. Finally, the report concludes with some recommended practices for conducting vibration-based wind turbine drivetrain CM.

2 Tests and Actual Gearbox Damage

The test gearbox, dynamometer test facility, one customized vibration data acquisition system, test conditions, and actual damage found on the test gearbox through its disassembly are presented in this chapter.

2.1 Test Article

The GRC test turbine drivetrain (Figure 2.1) is designed for a stall-controlled, three-bladed, upwind turbine, with a rated power of 750kW. The turbine generator operates at 1800 rpm and 1200 rpm nominal, on two different sets of windings, depending on the wind conditions.

The gearbox under test was one of two units, which were originally taken from the field and redesigned, rebuilt and instrumented with more than 125 sensors. The gearbox first finished its run-in in the NREL dynamometer test facility and later was sent to a wind plant located near to NREL for field tests, where two oil loss events occurred while the turbine was being tested. The gearbox has an overall ratio of 1:81.491. It is composed of one low speed (LS) planetary stage and two parallel stages, as shown in the expanded view in Figure 2.2. Nomenclature for the internal elements is described in Figure 2.3, and the gear dimensions, teeth number, and helix angles are listed in Table 2.1.

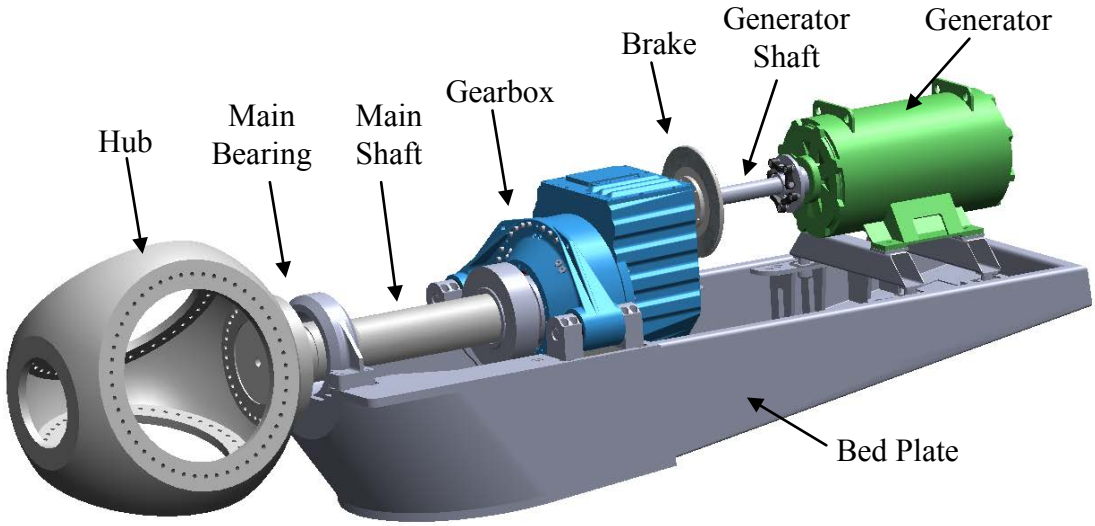

Figure 2.1. GRC test turbine

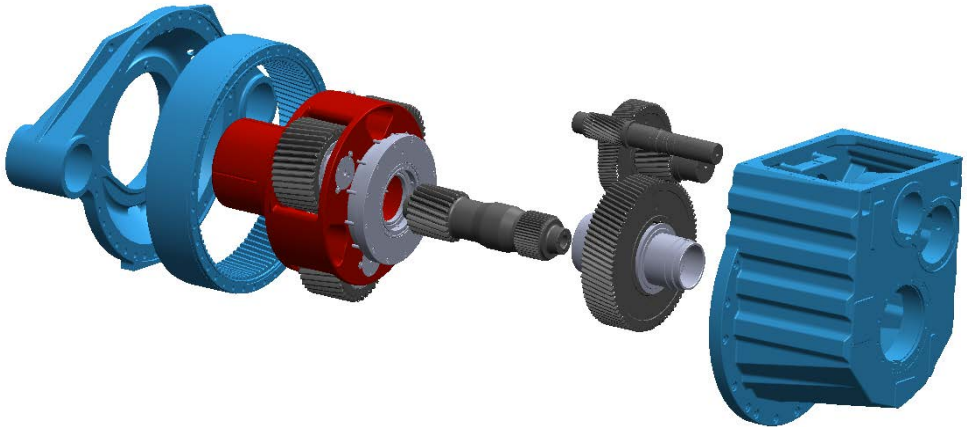

Figure 2.2. GRC gearbox internal components view

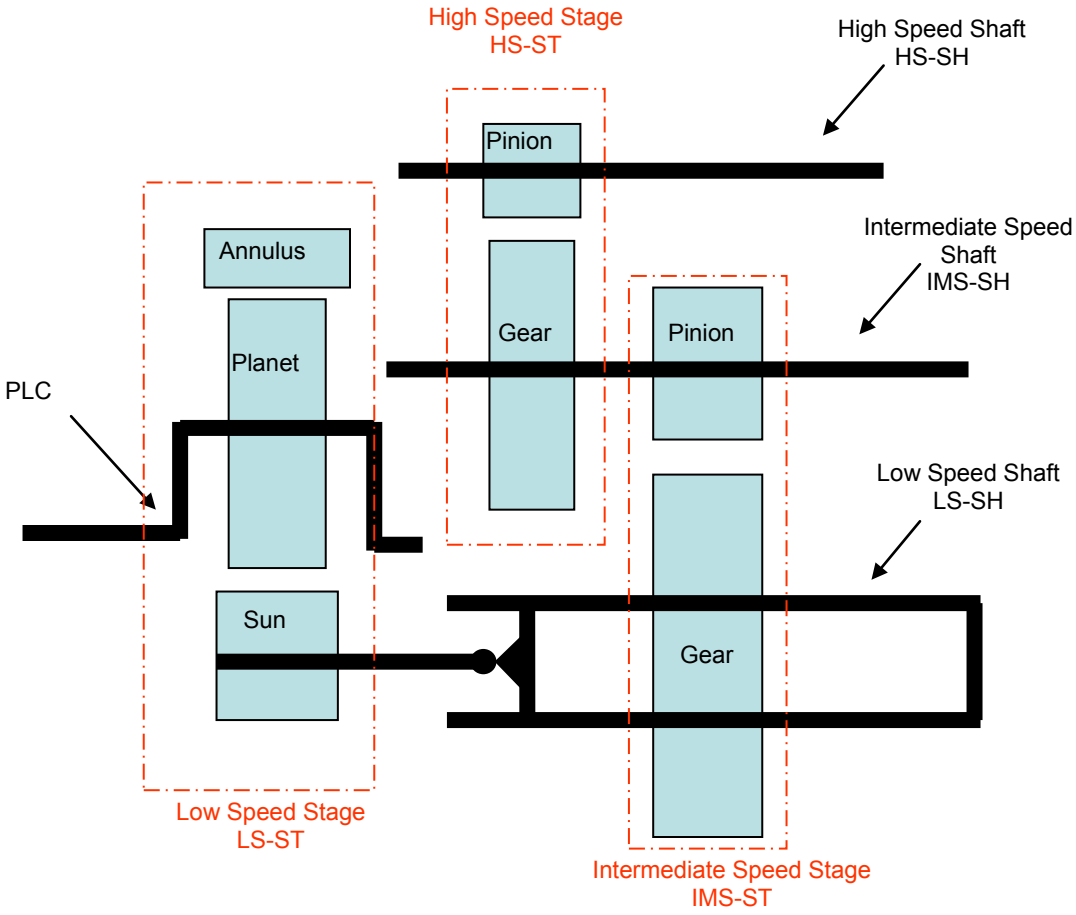

Figure 2.3. GRC gearbox internal nomenclature and abbreviations

Table 2.1. Gear element dimensions and detail

Gear Element	No. of Teeth	Mate teeth	Root diameter (mm)	Helix angle	Face width (mm)	Ratio
Ring gear	99	39	1047	7.5L	230	
Planet gear	39	99	372	7.5L	227.5	
Sun pinion	21	39	186	7.5R	220	5.71
Intermediate gear	82	23	678	14R	170	
Intermediate pinion	23	82	174	14L	186	3.57
HSS gear	88	22	440	14L	110	
HSS pinion	22	88	100	14R	120	4.0
					Overall:	81.49

Several bearing types are employed in the gearbox, according to the loading conditions and gearbox life requirements. The planet carrier is supported by two full-complement cylindrical roller bearings (fcCRB) and each planet gear is supported by two identical cylindrical roller bearings (CRB). Each parallel shaft in the gearbox is supported by a CRB on the upwind side of the assembly, and by two back-to-back mounted, tapered roller bearings (TRB) on the downwind side. Table 2.2 provides the location and bearing manufacturer part number of all bearings in the gearbox. Location and shaft designations are as noted in Figure 2.4. The letter following the abbreviation indicates the position of the bearing according to the component from upwind (A) to downwind (B, C). Lubrication oil is another important component in the test gearbox, although it is not shown in either Table 2.2 or Figure 2.4.

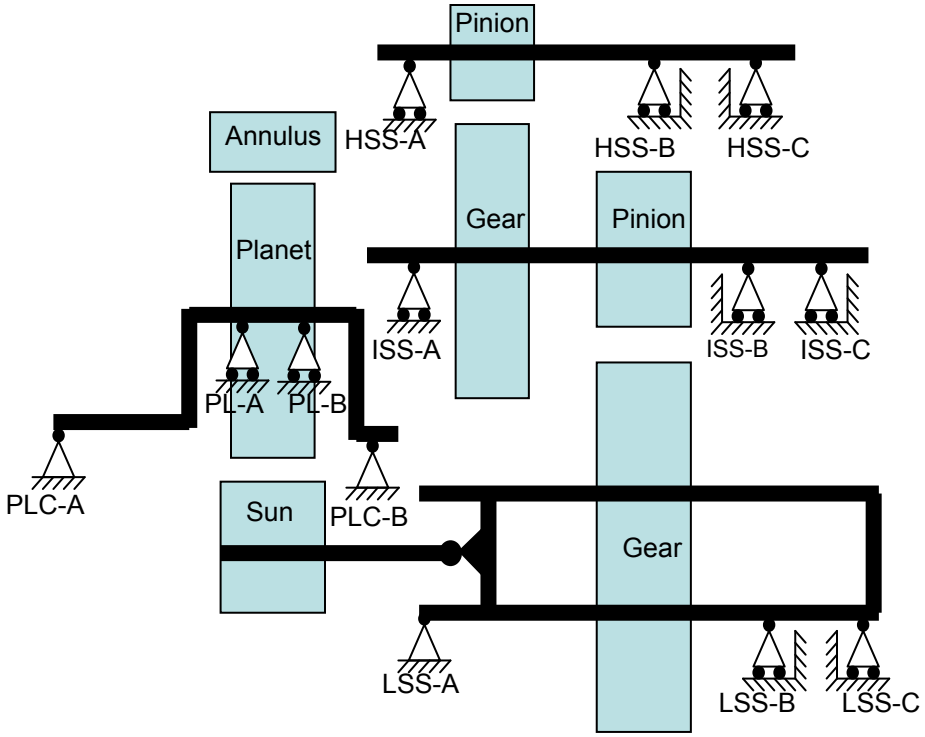

Figure 2.4. GRC gearbox layout and bearing nomenclature

Table 2.2. Bearing type, number, and location

Location	Location Designation	Type	Provider	Part Number
Planet carrier	PLC-A	fcCRB	INA	SL 18 1892 E
	PLC-B	fcCRB	INA	SL 18 1880 E
Planet	PL-A	CRB	FAG	NJ 2232 E.M1.C3
	PL-B	CRB	FAG	NJ 2232 E.M1.C3
Low Speed Shaft	LS-SH-A	fcCRB	INA	SL 18 1856E
	LS-SH-B	TRB	SKF	32948
	LS-SH-C	TRB	SKF	32948
Intermediate Speed Shaft	IMS-SH-A	CRB	FAG	NU 2220 E.M1.C3
	IMS-SH-B	TRB	SKF	32032 X
	IMS-SH-C	TRB	SKF	32032 X
High Speed Shaft	HS-SH-A	CRB	FAG	NU 2220 E.M1.C3
	HS-SH-B	TRB	SKF	32222 J2
	HS-SH-C	TRB	SKF	32222 J2

The operating gear mesh and bearing characteristic frequencies can be determined by the project partners, based on the data shown in Tables 2.1 and 2.2, along with catalogue information from bearing suppliers.

2.2 Dynamometer Test Facility

The retest of the damaged gearbox was conducted in the NREL 2.5 MW dynamometer test facility (DTF), which conducts performance and reliability tests on wind turbine drivetrain prototypes and commercial machines [5,6]. The facility is capable of providing static, highly accelerated life and model-in-the-loop tests. The prime movers of the dynamometer are a 2.5 MW induction motor, a three-stage epicyclical reducer, and a variable-frequency drive, with full regeneration capacity. The rated torque provided by the dynamometer to a test article can be up to 1.4 meganewton meters (MNm), with speeds varying from 0 rpm to 16.7 rpm. Non-torque loading actuators, rated up to 440 kilonewtons (kN) for radial load and 156kN for thrust load, also can be utilized in the dynamometer to apply thrust, bending, and shear loads similar to those typically generated by a wind turbine rotor. Figure 2.5 provides a diagram of the test facility. Figure 2.6 is a photo of the test implementation, with the test gearbox installed. The complete nacelle and drivetrain was installed in the NREL DTF and hard fixed to the floor, without the hub, rotor, yaw bearing, or yaw drives. The actual field controller was used to provide start-up and system safety response.

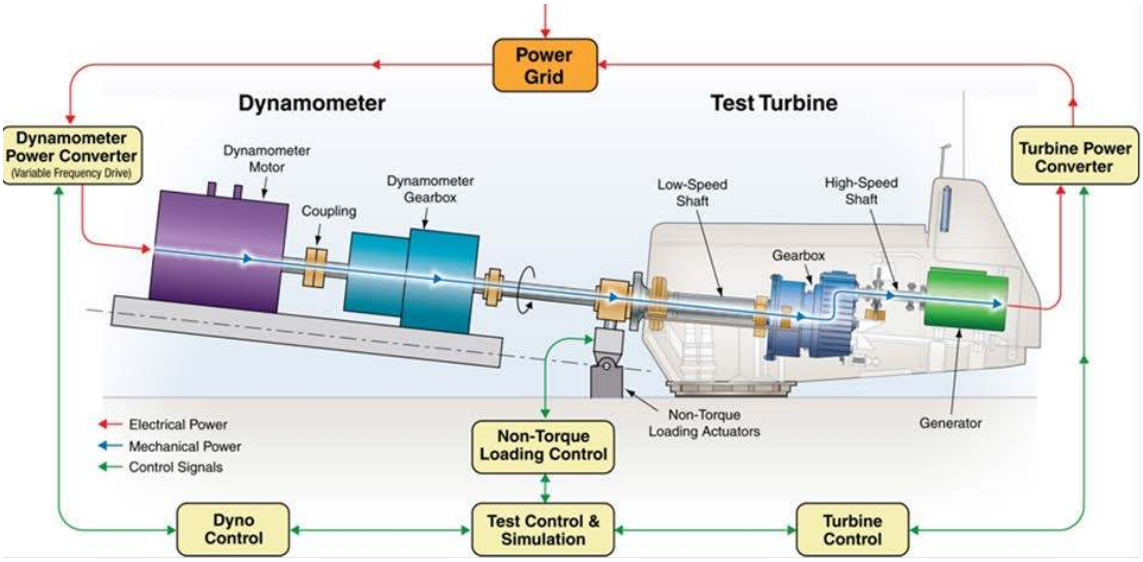

Figure 2.5. Diagram of NREL 2.5 MW dynamometer test facility

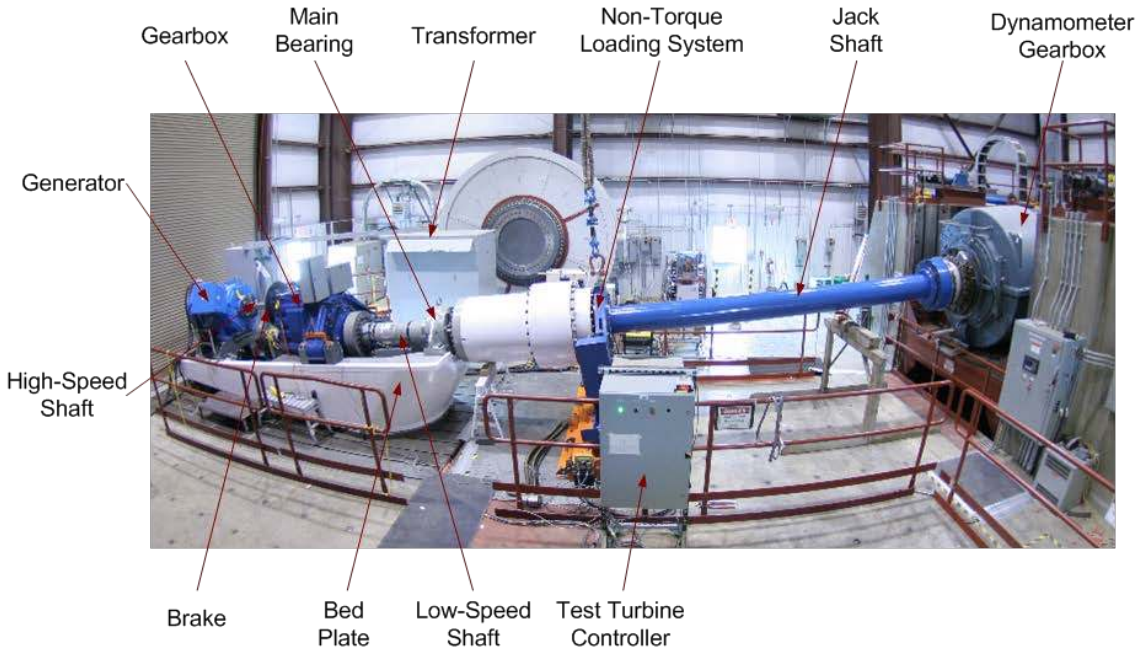

Figure 2.6. NREL dynamometer test stand with the test article installed. *NREL/PIX #16913.*

2.3 One Customized Vibration Data Acquisition System

During the dynamometer retest of the damaged gearbox, the data for this Round Robin project was collected by a vibration data acquisition system (DAS) customized by NREL. It is composed of twelve accelerometers. Low speed shaft torque and generator speed were recorded, in addition to the accelerometer data. The HSS speed measurement was obtained by an optical encoder. For

simplicity of implementation, data was collected at 40 kHz per channel using a National Instruments PXI -4472B high speed DAS.

The accelerometers mounting locations are illustrated in Figure 2.7, with sensor labels and descriptions given in Table 2.3. The mounting locations were chosen to reflect typical sensor placement practices seen in commercial wind turbine drivetrain vibration-based condition monitoring systems. The physical installation of these accelerometers is shown in Figure 2.8.

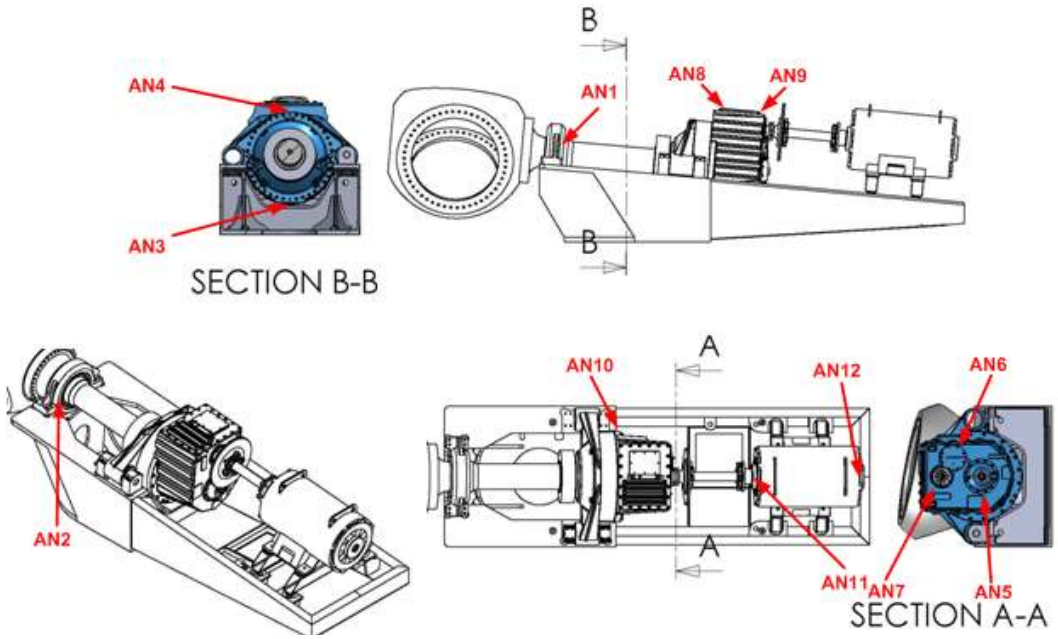

Figure 2.7. Vibration data acquisition system sensor locations

Table 2.3. Sensor notations and descriptions

Sensor Label	Description
AN1	Main bearing radial
AN2	Main bearing axial
AN3	Ring gear radial 6 o'clock
AN4	Ring gear radial 12 o'clock
AN5	LSS radial
AN6	ISS radial
AN7	HSS radial
AN8	HSS upwind bearing radial
AN9	HSS downwind bearing radial
AN10	Carrier downwind radial
AN11	Generator drive end radial
AN12	Generator non-drive end axial

a) AN1, AN2, AN3, and AN4 (From left to right, *NREL/PIX #19589, 19590, 19588, 19587)*

b) AN5, AN6, AN7, and AN8 (From left to right, *NREL/PIX #19591, 19592, 19594, 19593)*

c) AN9, AN10, AN11, and AN12 (From left to right, *NREL/PIX #19595, 19598, 19597, 19596)*

Figure 2.8. Physical sensor installation

2.4 Test Conditions

The vibration data was collected under the test conditions shown in Table 2.4. The highest test load applied was 50% of rated power to reduce the chances of a catastrophic gearbox failure. Under each test condition, ten minutes of data was collected and broken into 10 separate files, each containing one minute of test data. In total, thirty data files from three test conditions were shared with the project partners.

Table 2.4. Test conditions

Test Case	LSS Speed (rpm)	Nominal HSS Speed (rpm)	Electric Power (% of rated)	Duration (min)
CM_2a	14.72	1200	25%	10
CM_2b	22.09	1800	25%	10
CM_2c	22.09	1800	50%	10

2.5 Actual Gearbox Damage

After the dynamometer retest, the gearbox was sent to a rebuild shop, where it was disassembled and a detailed failure analysis [4] was conducted. A complete list of actual damage found through the failure analysis is given in Table 2.5. For example, the high speed stage gear damage in Figure 2.9 shows clear scuffing marks.

Table 2.5. Actual damage on the test gearbox

Damage #	Instances	Mode
1	HSS Gear Set	Scuffing
2	HSS Downwind Bearings	Overheating
3	ISS Gear Set	Fretting Corrosion
		Scuffing
		Polishing Wear
4	ISS Upwind Bearing	Assembly damage
		Plastic deformation
		Scuffing
		False brinelling
		Debris dents
		Contact Corrosion
5	ISS Downwind Bearings	Assembly damage
		Plastic deformation
		Dents
6	Annulus/Ring Gear, or Sun Pinion	Scuffing and polishing
		Fretting Corrosion
7	Planet Carrier Upwind Bearing	Fretting Corrosion
8	Sun Pinion Thrust Rings	Fretting Corrosion
		Adhesive Wear
9	Oil Transfer Ring for Planet Carrier	Polishing
10	LSS Seal Plate	Scuffing
11	LSS Downwind Bearings	Abrasion
12	HSS Shaft	Misalignment

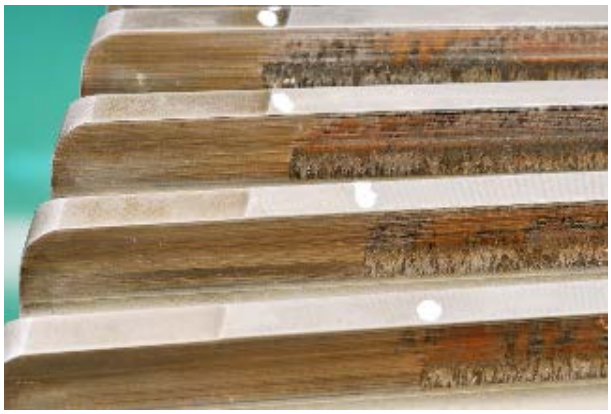

Figure 2.9. Test gearbox high speed stage gear damage. *NREL/PIX #19599.*

The root cause of the faults was assembly damage and oil starvation resulting from the two oil loss events in the field test. Among the 12 damaged items listed in Table 2.5, the consensus reached among the sixteen Round Robin partners was that the first seven should be detectable by vibration analysis. Damage 12 could potentially be detected by vibration analysis as well, but most partners considered it to be an operational condition and not damage. Therefore, the first seven damage instances were used as references for performance evaluations of the partner's diagnostic results, as discussed in the introduction chapter of this report. The task for the partners was to diagnose possible internal component damage of the test gearbox based on the shared vibration, rpm, and torque data. As the project progressed, each of the partners recognized that some baseline data collected from a healthy test gearbox would be beneficial. Therefore, vibration spectrum data collected by several accelerometers mounted on the test gearbox, when it was considered healthy, were later shared with the project partners. The following report sections were submitted by eight out of the sixteen partners who took part in the CM study.

3 Analysis Algorithms and Diagnostics Results from General Electric

Huageng Luo*, Charles Hatch, Matthew Kalb, Jesse Hanna, Adam Weiss
General Electric Energy
*Corresponding Author Email: luoh@ge.com

3.1 Fundamentals

Solutions provided by the General Electric (GE) Energy Team are mainly based on order analysis to accommodate the constant speed variations in a wind farm. For gear damage detection, the sideband distributions were used to estimate the gear meshing condition and a sideband energy ratio was used to qualitatively evaluate the gear damage. For early bearing damage detection, the acceleration enveloping detection technique was used.

In the wind farm, the wind speed is not predictable, thus many wind turbines are operated at variable speed. As a result, the gearbox operational speed is constantly changing. Due to this kind of speed variation, a direct application of the conventional Fast Fourier Transform (FFT) will not result in accurate gearbox condition features, especially those features extracted from high frequency response, such as acceleration enveloping analysis techniques [7,8]. On the other hand, to improve the energy extraction efficiency, the wind turbine rotor speed has to be geared up about two orders of magnitude before being used to drive the generator shaft. Because of the high gear ratio, a very high-count encoder is needed. For example, in a 1.5 MW wind turbine, the ratio between the high-speed gear meshing frequency and the rotor frequency can easily be greater than 1500.

To overcome these difficulties, the GE team utilized a series of signal processing techniques, such as synchronous sampling, synchronous analysis, digital domain encoder synthesizing, acceleration enveloping analysis, and sideband energy ratio (SER), in the data processing and damage feature extractions.

3.1.1 Synchronous Sampling

For rotating machinery, vibrations may occur at multiples and submultiples of the shaft speed. For example, if the shaft is rotating at 3600 rpm, which is 60 Hz, then the vibration response at multiples of this frequency, and sometimes fractions of this frequency, can be seen. These multiples are called orders (or harmonics in musical terms). The general relationship between the order (O), the shaft speed (RPM), and the frequency (f) in Hz is

$$f = \frac{O \times RPM}{60} \tag{1}$$

If the rotating speed is fixed, a regular FFT analysis can have the desired results. However, if the rotor speed changes within the time window of data acquisition, the variation of the rotor speed will cause the fundamental order and harmonics in the frequency domain to be smeared into multiple frequency bins. On the other hand, the frequency of interest may not always be right at a bin, depending on the resolution of the frequency analysis. The signal energy has to be split into neighboring bins, in such a case. That is why in rotor dynamics, order analysis is preferred over the frequency spectrum analysis. In the order domain, the values of the fundamental order

and the harmonics remain constant with respect to the shaft speed; the first order is always at the shaft speed and the second order is always twice the shaft speed, and so on.

To achieve order analysis in rotating machinery applications with variable running speeds, instead of sampling at equal increments of time, a different sampling technique has to be used. Sampling is conducted at equal increments of shaft rotation position, thus reducing the effect of the shaft speed variations. This is called synchronous sampling. The synchronous sampling technique is very useful for rotating machinery-related data processing, especially in instances of varying shaft speed.

Generally, there are two approaches to achieving synchronous sampling - analog and digital approaches. One of the analog approaches uses an Analog to Digital (A/D) sampling clock to achieve the synchronous sampling. The key to this approach is generating an appropriate sampling clock based on shaft rotation conditions. As shown in Figure 3.1, the sampling clock is derived from the shaft encoder by an analog ratio generator to meet the desired order analysis requirements (such as order resolution and maximum order). In cases where only lower order components are of interest, the encoder output can be used as a sampling clock directly.

In the digital approach, or synthesized synchronous sampling [9], both vibration and encoder signals are discretized simultaneously, preferably at high speed. Different signal processing techniques can be used to resample the data and convert time domain data into shaft cycle domain data, with the help of an encoder signal from the shaft (refer to Figure 3.2). In this approach, both the encoder and key phaser can be used as a shaft speed reference. Regardless, the availability of the shaft encoder/key phaser is crucial to both analog and digital synchronous sampling approaches.

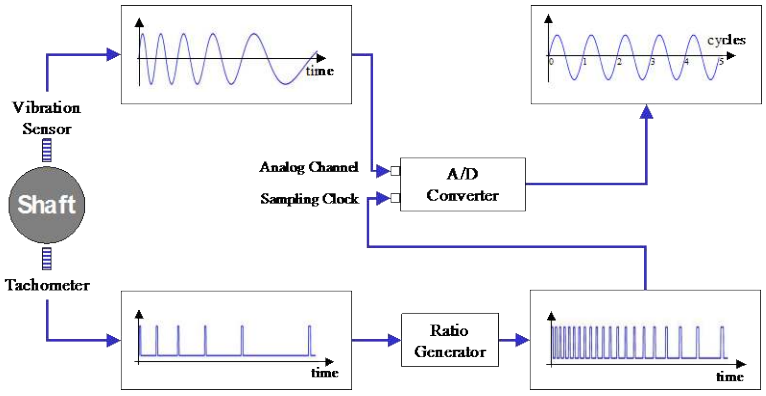

Figure 3.1. Synchronous sampling – analog approach

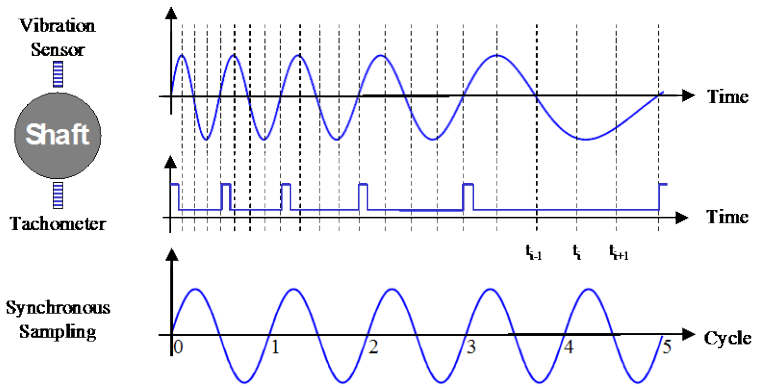

Figure 3.2. Synchronous sampling– digital approach

With the synchronously sampled data, a common way to enhance the signal components of interest is through time synchronous averaging [10]. With a shaft encoder/key phaser, the vibration signal detected contains three major components: the synchronous coherent signal component, the synchronous, non-coherent component, and random noise. Conventional time synchronous averaging can only enhance the synchronous coherent signal component. The synchronous, non-coherent component and the random noise will be averaged out with a sufficient number of averages.

Figure 3.3 (a) shows a simulation result with a combination of the shaft response, $a\sin(2\pi f_0 t)$; its second harmonic, $b\sin(4\pi f_0 t)$; a nonsynchronous coherent signal, $c\sin(2\pi \cdot 1.3 \cdot f_0 t)$; and a uniform random noise. After 250 times of synchronous averaging, the results are shown in Figure 3.3 (b); the random noise and the nonsynchronous coherent component have been successfully removed.

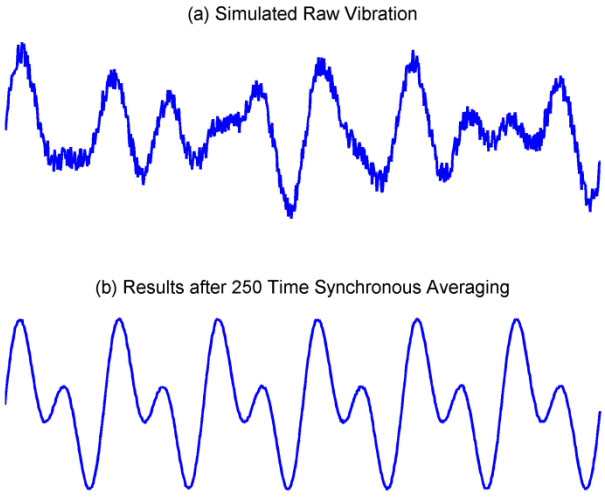

Figure 3.3. Time synchronous averaging

When applying the synchronous sampling technique to diagnose bearing/gear damage, there are two issues that need to be resolved. The first is that the bearing damage signatures are usually nonsynchronous to the shaft order. In complicated gear sets, such as in the planetary gear, not all gear meshing frequencies are integer multipliers of a shaft frequency. So, if the regular time domain synchronous averaging technique is applied to the vibration response, the bearing damage signatures will be averaged out. Thus, instead of averaging in the time domain, order domain averaging should be used in gearbox health feature extractions. The second problem is unique to a wind turbine gearbox. For example, in a typical 1.5 MW wind turbine, the order span between the main shaft and the third stage gear meshing (the high speed shaft gear meshing frequency) can be above 1500. Care must be taken on the order resolution and on the maximum order applied during the data acquisition.

3.1.2 Synthesized Synchronous Sampling

With the help of a tachometer, the equal time sampled data can be converted into equal shaft angular space data as shown in Figure 3.2.

In the event that the direct shaft tachometer signal is not available, traditional synchronized sampling becomes difficult, if not infeasible. For example, in this Round Robin project, only the speed profile is provided. If a synthesized tachometer signal can be generated from the speed signal, then the equal circumferential space sampling (synchronous sampling) can be carried out following well-established routines.

The following describes a procedure to synthesize a tachometer from the shaft speed profiles. In Figure 3.4, assume we have determined that the synthesized tachometer generated a pulse at time t_i. We need to find out the location of the next pulse timing t_{i+1}. The time elapsed, from t_i to t_{i+1}, i.e., $\Delta t_1 = t_{i+1} - t_i$, is the instantaneous shaft rotation period. On the other hand, if we have determined the t_{i+1}, since we know the shaft speed as a function of time, the average speed, n, between t_i and t_{i+1} can be calculated numerically. Therefore, the shaft instantaneous period can also be approximated by the averaged instantaneous shaft speed, i.e., $\Delta t_2 = 60/n$. In theory, by equalizing Δt_1 and Δt_2, we can determine t_{i+1}; thus, calculating the next pulse location. In practice, due to time resolution and speed accuracy, an approximation procedure is used instead of solving for an exact solution. The following steps further explain the procedure of the synthesized synchrophaser:

1. Assume a synchrophaser pulse at time zero.
2. Once the ith synchrophaser pulse is located, at t_i, assume the (i+1)th pulse be located at t_{i+1}.
3. Calculate the average shaft speed, *n* in RPM, which is a function of t_{i+1}, from t_i to t_{i+1}

$$n(t_{i+1}) = \frac{1}{t_{i+1} - t_i} \int_{t_i}^{t_{i+1}} ShaftSpeed(t)dt \tag{2}$$

4. Formulate the time elapsed from t_i to t_{i+1}

$$\Delta t_1 = t_{i+1} - t_i \tag{3}$$

and the time elapsed by one instantaneous rotation

$$\Delta t_2 = 60/n \tag{4}$$

5. Find t_{i+1} such that $\left|\Delta t_1 - \Delta t_2\right|$ is minimized.

The t_{i+1} then is the approximate location of the $(i+1)^{th}$ synchrophaser pulse. The tachometer can be generated from the synchrophaser, say, by equal spacing between the consecutive synchrophaser pulses.

With this method, one of the major error sources is the discretization resolution. The maximum error in the shaft period is $\frac{T}{2}$, where T the sampling period is. Fortunately, for bearing and gear dynamic response analysis, especially acceleration enveloping analysis, the frequency of interest is usually much higher than the shaft speed. In other words, the digitization rate is usually several orders of magnitude higher than the shaft speed. Thus, the synthesizing error from the digitization error is expected to be negligibly small.

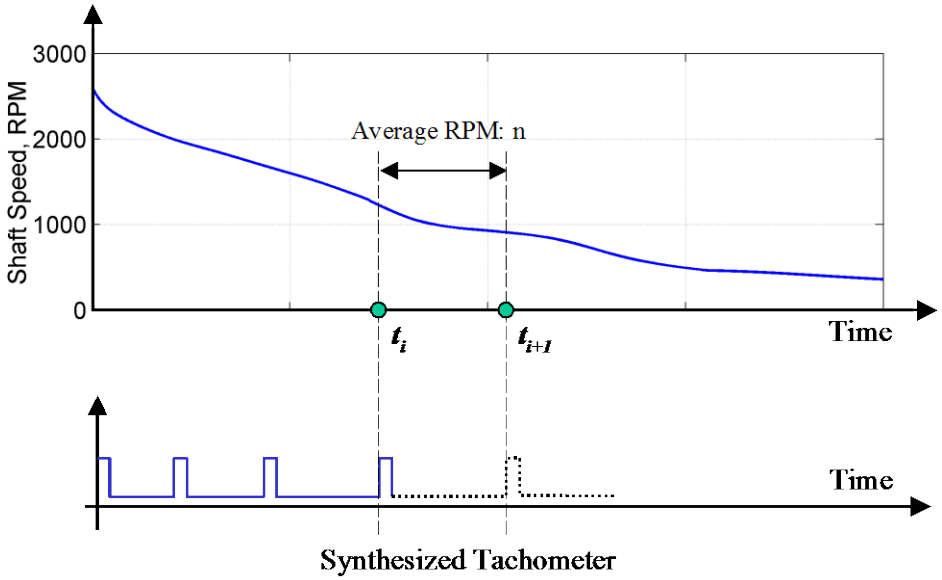

Figure 3.4. Synthesized tachometer generation from speed function

3.1.3 Sideband Energy Ratio

Sideband Energy Ratio (SER) [11] is calculated from high resolution spectrum data. Each spectrum is created from time-based waveform data generated by an accelerometer sensor and collected by the monitoring system. Several accelerometer sensors were mounted in strategic locations on the wind turbine gearbox to monitor each gear mesh. The waveforms from each sensor were synchronously sampled so that the sampling frequency tracks change in speed. This technique produces narrow spectral lines of speed-dependent frequencies, like gear mesh frequencies and associated sidebands, for variable speed machines; they are essential to

accurately calculate SER. Once the spectrum is generated the SER algorithm sums the amplitudes of the first six sideband peaks on each side of the center mesh frequency and divides by the amplitude of the center mesh frequency.

$$\text{SER} = \frac{\sum_{i=1}^{6} \text{Sideband Amplitude}_i}{\text{Center mesh frequency amplitude}} \quad (5)$$

SER is sensitive to the sideband amplitudes relative to the center mesh frequency. In a healthy gear mesh, any sidebands have small amplitude compared to the center mesh frequency, or they may be missing altogether resulting in a low SER. SER is typically less than one for a healthy gear mesh. As damage develops on a gear tooth that passes through the gear mesh, the sidebands increase in amplitude, as well as in number, and SER will go up. In GE Bently Nevada's wind turbine condition monitoring system, ADAPT.wind, SER is calculated for the fundamental mesh frequency and the first two harmonics of each gear mesh.

3.1.4 Acceleration Enveloping

The acceleration enveloping technique was originally called the high frequency resonance technique. It was discovered, almost accidentally, from an oscilloscope display [7] in the early 1970s, through a National Aeronautics and Space Administration (NASA) funded project [8]. The acceleration enveloping technique is based on the following assumptions. When a defect occurs in a bearing, repetitive impacts occur during rotation. These kinds of impacts are a broadband excitation. This broadband excitation stimulates the resonant response of the bearing's support system. However, the resonant response levels from the defect impacts, such as unbalance, are usually very low compared to the shaft excitation; though, the frequency contents of the resonant response are usually much higher. If the dynamic range of the vibration sensor and the consequent analyzer is low, the resonant response signals are down in the noise level. The key to detecting bearing faults is to capture the low amplitude response caused by bearing defect excitation, without including the high amplitude rotational vibration signals and system fundamental resonant frequency responses. To accomplish this, a band pass filter is used to isolate the signal. Once the high frequency damage response is captured, the signal goes through a rectification device and the envelope of the signal is detected from the rectified signal. Applying FFT to the envelope signal will reveal the frequency and amplitude, which is uniquely associated with the damaged bearing component.

In theory, any vibration sensor can achieve bearing/gear damage detection through the enveloping or demodulation processes, as long as the sensor has the frequency range required. Since the bearing/gear damage excited response is known to have high frequency content, the accelerometer has an advantage over velocity and displacement sensors.

In the early days, this enveloping detection process was performed using several analog devices. As shown in Figure 3.5, the conditioned vibration sensor signal is first passed through an analog filter to isolate the impulse response excited by the bearing damage. The filtered response is then passed through a rectifier to flip the negative half of the oscillation signal to the positive side. The rectified signal is fed into an envelope detector to identify the envelope of the signal. The envelope signal is then used to identify bearing damage signature through a signal analyzer. If necessary, a low-pass filter can be added before the analyzer.

The process shown in Figure 3.5 works well, if all the analog devices are appropriately designed for a particular application. However, a different application may require different parameter settings of the analog devices. For example, the bearing support system may have a different resonant structure; thus, it requires a different cut-off frequency design for the band-pass filter to isolate the damage impulse response. For different structural damping, the envelope detector needs a different time constant design to match the impulse response decay rate, so that the bearing damage-related high frequency and low amplitude vibration signals can be maximized. More importantly, the bearing damage detection is usually conducted in a harsh environment. An increased number of electronic components involved in the bearing defect detection process will usually decrease the overall system reliability.

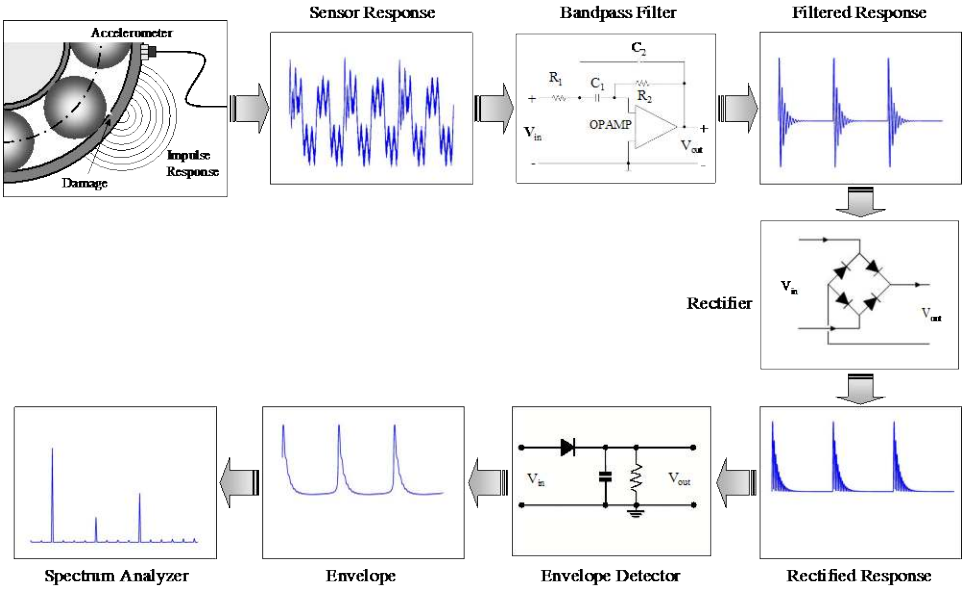

Figure 3.5. Analog devices-based approach

With the improvement of computer technology and the development of high dynamic range A/D converters, the acceleration enveloping-based bearing damage detection becomes much easier to implement. Many of the analog devices, as shown in Figure 3.5, can now be replaced by digital signal processing techniques, thus improving detection accuracy and system reliability. One possible digital signal processing-based realization of acceleration enveloping is shown in Figure 3.6. The conditioned acceleration signal is first digitized with high speed and high dynamic range A/D converter. The high speed and high dynamic range A/D is especially important because it ensures that the digitized vibration data contain low amplitude high frequency resonant responses excited by the bearing damage impulse. The digitized data are then passed through a digital band pass filter to isolate the resonant response excited by the bearing damage. Next, the enveloping detection algorithm is used to detect the envelope of the filtered data. In the digital domain, this process can be achieved by the Hilbert transform. The digital Hilbert transform is related to the FFT and can be easily achieved [12]. If accurate enveloping detection is required, a local maximum interpolation technique can provide better results [13]. The bearing damage detection is then accomplished by spectrum analysis on the enveloped data.

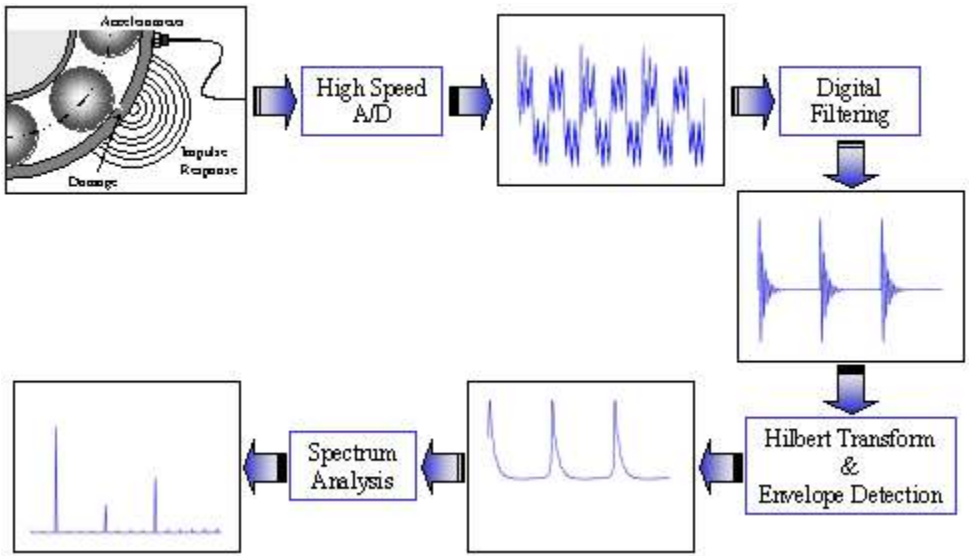

Figure 3.6. Digital processing-based approach

3.2 Round Robin Analysis Results

3.2.1 Bearing and Gear Damage Features

Based on the gear configuration data given by NREL, the gear damage features were calculated and listed in Table 3.1. Similarly, the bearing damage features were calculated and listed in Table 3.2. In both tables, MS stands for Main Shaft. The bearing notations used in Table 3.2 is the same as those used in the test gearbox failure analysis report [4] and illustrated in Figure 3.7. The numbers of gear mesh teeth count are also marked in Figure 3.7.

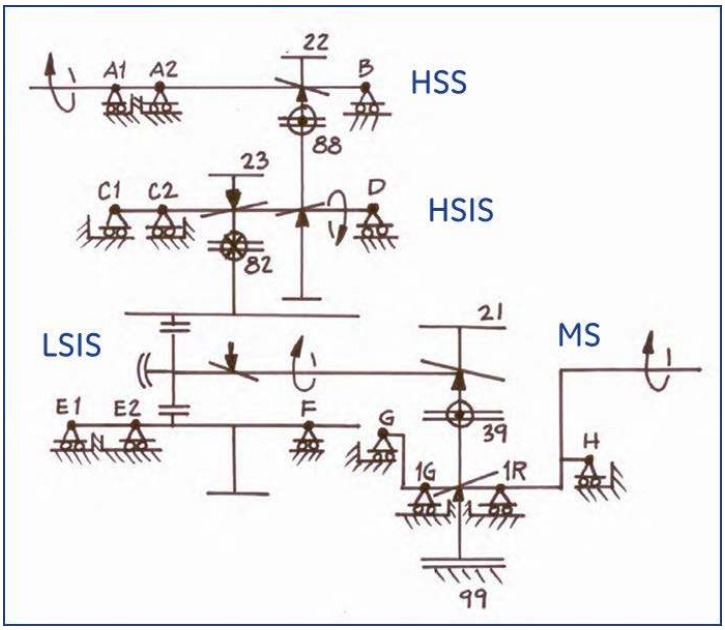

Figure 3.7. Gearbox power flow

Table 3.1. Gear damage features

Shaft frequencies	Relative freq		at 1800 rpm		at 1200 rpm	
	MS	**HSS**	[rpm]	[Hz]	[rpm]	[Hz]
Rotor/carrier	1.00	**0.012**	22.1	0.37	14.7	0.25
Planets (minus carrier rotation)	2.54	**0.031**	56.1	0.93	37.4	0.62
Planets	3.54	**0.043**	78.2	1.30	52.1	0.87
Sun shaft (minus carrier rotation)	4.71	**0.058**	104.1	1.74	69.4	1.16
Sun shaft	5.71	**0.070**	126.2	2.10	84.1	1.40
Intermediate shaft	20.37	**0.250**	450.0	7.50	300.0	5.00
Generator shaft	81.49	**1.000**	1800.0	30.00	1200.0	20.00
Gear mesh tooth passing freqs						
Gear mesh - Planet > Ring	99.00	**1.215**	3048.2	36.45	2032.1	33.87
Gear mesh - Sun > Planet	99.00	**1.215**	3048.2	36.45	2032.1	33.87
Gear mesh - Sun shaft > Intermediate	468.57	**5.750**	10350.0	172.50	6900.0	115.00
Gear mesh - Intermediate > HSS	1792.80	**22.000**	39600.0	660.00	26400.0	440.00
Single gear tooth fault freqs						
HSS gear set pinion (HSS)	81.49	**1.000**	1800.0	30.00	1200.0	20.00
HSS gear set wheel (intermediate shaft)	20.37	**0.250**	450.0	7.50	300.0	5.00
Intermediate gear set pinion (intermediate shaft)	20.37	**0.250**	450.0	7.50	300.0	5.00
Intermediate gear set wheel (sun shaft)	5.71	**0.070**	126.2	2.10	84.1	1.40
Sun gear	14.14	**0.174**	312.4	5.21	208.3	3.47
Planet gear	7.08	**0.087**	156.3	2.61	104.2	1.74
Ring gear	3.00	**0.037**	66.3	1.10	44.2	0.74

Table 3.2. Bearing damage features

Bearings	Relative Freq	
Main Bearing	MS	**HSS**
Main bearing (INP-A) - roller rotation freq	5.22	**0.064**
Main bearing (INP-A) - cage freq	0.45	**0.006**
Main bearing (INP-A) - roller defect freq (= 2 x roller rotation freq)	10.44	**0.128**
Main bearing (INP-A) - outer race defect freq	12.70	**0.156**
Main bearing (INP-A) - inner race defect freq	15.30	**0.188**

HSS A1 & A2	**Relative freq**	
HSS-A1 and A2 - roller rotation freq	253.99	**3.117**
HSS-A1 and A2 - cage freq	34.63	**0.425**
HSS-A1 and A2 - roller defect freq (= 2 x roller)	507.98	**6.234**
HSS-A1 and A2 - outer race defect freq	691.89	**8.490**
HSS-A1 and A2 - inner race defect freq	937.93	**11.510**

HSS B	**Relative freq**	
HSS-B - roller rotation freq	254.78	**3.127**
HSS-B - cage freq	47.10	**0.578**
HSS-B- roller defect freq (= 2 x roller)	509.56	**6.253**
HSS-B- outer race defect freq	584.60	**7.174**
HSS-B - inner race defect freq	800.74	**9.826**

ISS C1 &C2	**Relative freq**	
ISS-C1&C2 - roller rotation freq	106.14	**1.303**
ISS-C1&C2 - cage freq	9.25	**0.114**
ISS-C1&C2 - roller defect freq (= 2 x roller)	211.88	**2.600**
ISS-C1&C2 - outer race defect freq	287.25	**3.525**
ISS-C1&C2 - inner race defect freq	344.30	**4.225**

ISS D	**Relative freq**	
ISS-D - roller rotation freq	63.70	**0.782**
ISS-D - cage freq	11.78	**0.145**
ISS-D- roller defect freq (= 2 x roller)	127.39	**1.563**
ISS-D- outer race defect freq	146.15	**1.793**
ISS-D - inner race defect freq	200.19	**2.457**

Table 3.2. Bearing damage features (continued)

Bearings	Relative Freq	
LSS E1&E2	**Relative freq**	
LSS-E1&E2 - roller rotation freq	41.37	**0.508**
LSS-E1&E2 - cage freq	2.67	**0.033**
LSS-E1&E2 - roller defect freq (= 2 x roller)	82.86	**1.017**
LSS-E1&E2 - outer race defect freq	109.71	**1.346**
LSS-E1&E2 - inner race defect freq	124.57	**1.529**
Hollow Shaft F	**Relative freq**	
HS-F - roller rotation freq	47.20	**0.579**
HS-F - cage freq	3.03	**0.037**
HS-F - roller defect freq (= 2 x roller)	94.39	**1.158**
HS-F - outer race defect freq	139.61	**1.713**
HS-F - inner race defect freq	157.53	**1.933**
Carrier G	**Relative freq**	
Carrier-G - roller rotation freq	8.59	**0.105**
Carrier-G - cage freq	0.53	**0.006**
Carrier-G - roller defect freq (= 2 x roller)	17.17	**0.211**
Carrier-G - outer race defect freq	25.43	**0.312**
Carrier-G - inner race defect freq	28.57	**0.351**
Carrier H	**Relative freq**	
Carrier-H - roller rotation freq	8.11	**0.100**
Carrier-H - cage freq	0.53	**0.007**
Carrier-H - roller defect freq (= 2 x roller)	16.22	**0.199**
Carrier-H - outer race defect freq	23.93	**0.294**
Carrier-H - inner race defect freq	27.07	**0.332**
Planet 1G&1R	**Relative freq**	
Planet-1G&1R - roller rotation freq	8.28	**0.102**
Planet-1G&1R - cage freq	1.46	**0.018**
Planet-1G&1R - roller defect freq (= 2 x roller)	16.57	**0.203**
Planet-1G&1R - outer race defect freq	19.42	**0.238**
Planet-1G&1R - inner race defect freq	26.27	**0.322**

3.2.2 Tool Development

A MATLAB-based tool was developed for easy data processing operations. The tool incorporated regular FFT spectrum analysis, acceleration enveloping analysis, synthesized synchronous sampling, and order analysis.

3.2.3 Damaged Gearbox Data analysis

The main goal of the Round Robin project was to identify the gear and bearing damage associated with the gearbox. In our analysis, we categorized the gear damage according to the gearbox meshing stages: the high speed gear meshing stage (HSGM), the intermediate gear meshing stage (ISGM), and the planetary gear meshing stage (PLTGM). For bearings, we categorize the damage according to the shaft, which the bearing is associated with, i.e., the High Speed Shaft (HSS), the High Speed Intermediate Shaft (HSIS), the Low Speed Intermediate Shaft (LSIS), and the Low Speed Shaft (LSS) or the Main Shaft (MS).

3.2.3.1 HSGM

The sensor AN7 was used to evaluate the HSGM stage health condition. From the order spectrum, it can be clearly seen that the fundamental gear meshing order is heavily modulated by the HSS speed, as seen in Figure 3.8.The sideband energy ratio (SER) is over three, which indicates severe gear damage in the HSGM pinion. The sideband contents in the higher order harmonics of HSGM also indicate the pinion damage, as seen in Figure 3.9 and Figure 3.10. Post-test examination indicated that the HSP had severe scuffing [4].

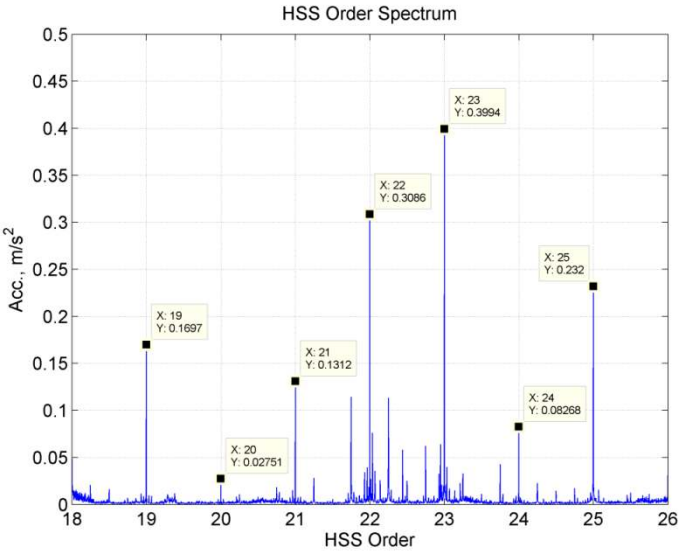

Figure 3.8. HSGM (22) modulated by HSS (1)

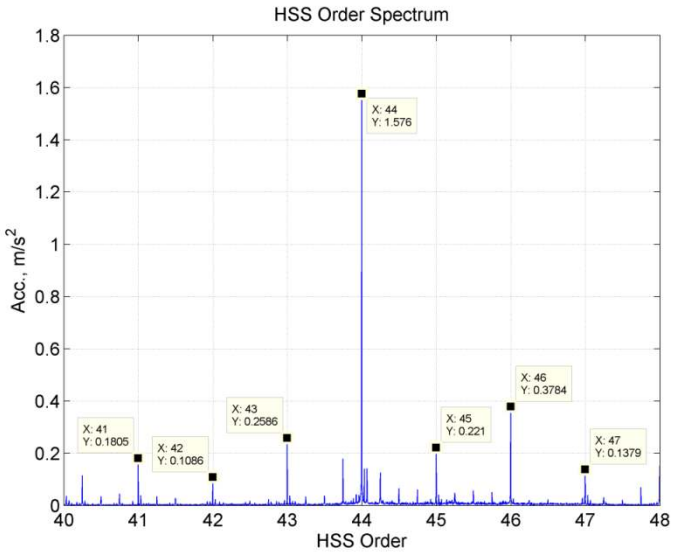

Figure 3.9. HSGM X2 (44) modulated by HSS (1)

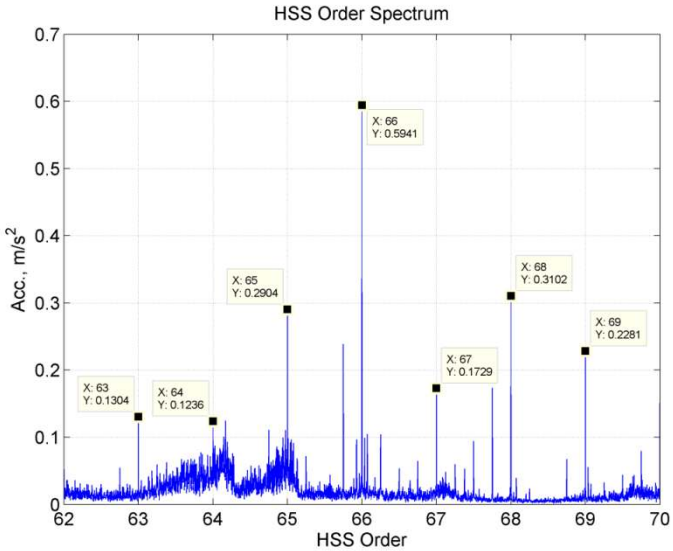

Figure 3.10. HSGM X3 (66) modulated by HSS (1)

Similar order analyses also indicated that the HSGM order was modulated by the HSIS shaft (Figure 3.11). This kind of modulation is visible in the HSGMX2 and HSGMX3 as well (refer to Figure 3.12 and Figure 3.13 respectively). Post-test examination indicated that the HSG also had severe scuffing [4].

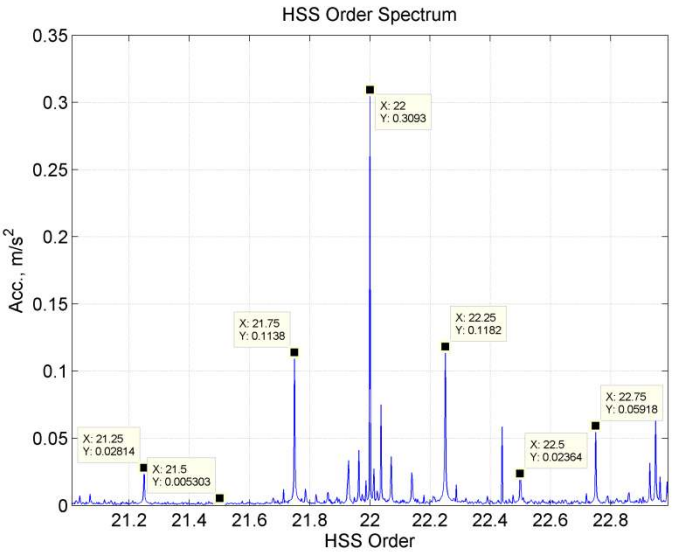

Figure 3.11. HSGM (22) modulated by HSIS (0.25)

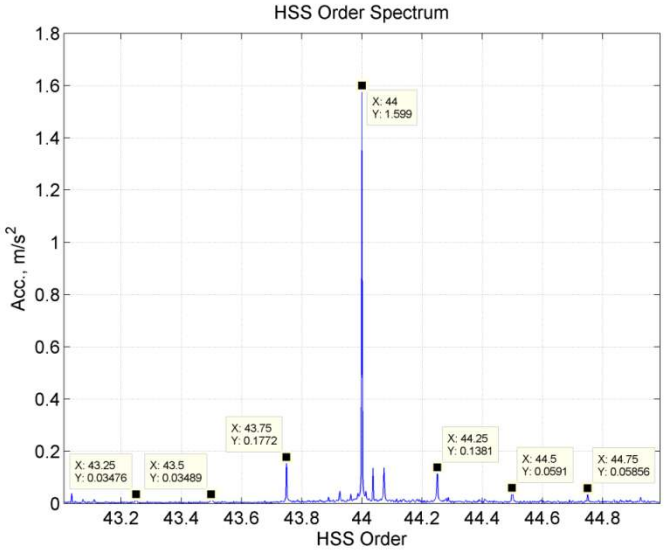

Figure 3.12. HSGM X2 (44) modulated by HSIS (0.25)

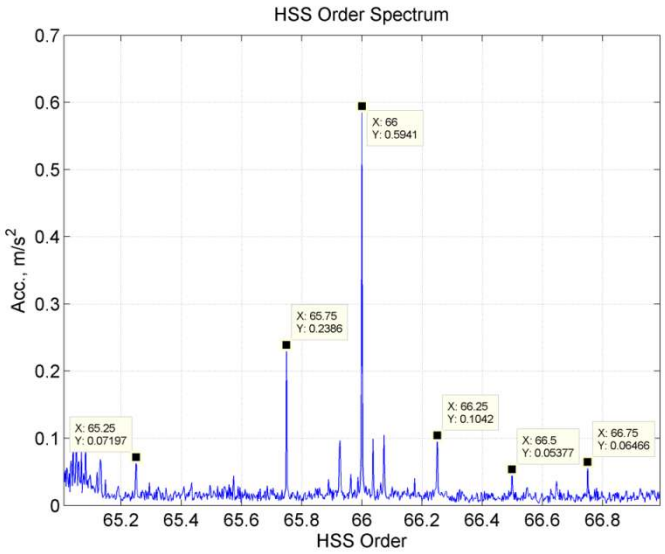

Figure 3.13. HSGM X2 (66) modulated by HSIS (0.25)

3.2.3.2 ISGM

Damage signatures related to the ISGM were not shown in the vibration analysis. As seen in Figure 3.14 though, the ISGM and higher order harmonics do exist. However, the shaft modulations are too small to draw any conclusion regarding the gear damage. The post-test examinations revealed fretting corrosion, polishing wear, and scuffing damage in the ISGM pinion; however, the damage was imprinted on all teeth because the gear-set had a hunting tooth gear ratio, which has potentially smoothed out the damages and reduced vibration responses incurred by the damage.

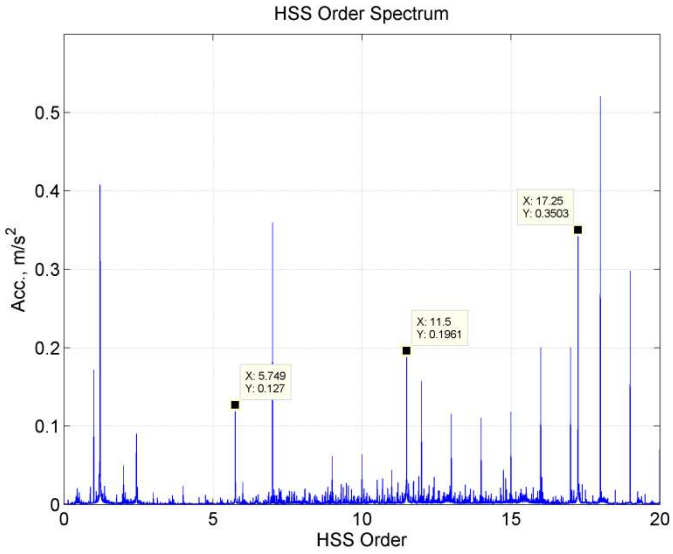

Figure 3.14. ISGM and higher order harmonics

3.2.3.3 PLTGM

For planetary gear stage damage detection, sensors AN3 and AN4 were used (refer to Table 2.3 for more information on sensors). The planetary gear set arrangement in this gearbox is a simultaneous mesh; thus, there was no cancellation/enhancement around the gear mesh frequency and harmonics, as seen in the sequential mesh design. Detailed order spectrum analysis indicated that the planetary gear mesh order and its harmonics are present Figure 3.15 for sensor AN4). Sidebands of planet passing are visible around the PLTGM and its harmonics. The modulation is significant at the third harmonic of the PLTGM (Figure 3.16). Similar information can be extracted from the sensor AN3 and the corresponding order spectra are shown in Figure 3.17 and Figure 3.18, respectively.

The acceleration enveloping analysis of the sensor AN3 (Figure 3.19) indicated that the damage is likely associated with the ring gear (0.037 Order), instead of planet gear (0.087 Order) or sun gear (0.174 Order). Post-test examination confirmed the ring gear scuffing and polishing damage [4].

The post-test also indicated severe fretting corrosion on the sun pinion. Though the sun/plant gear meshing is evident in the data analysis, as shown in Figure 3.15 and Figure 3.17, the LSIS shaft modulation (0.07 Order) is very small (Figure 3.20); thus, the sun pinion damage is inconclusive using current vibration-based analysis.

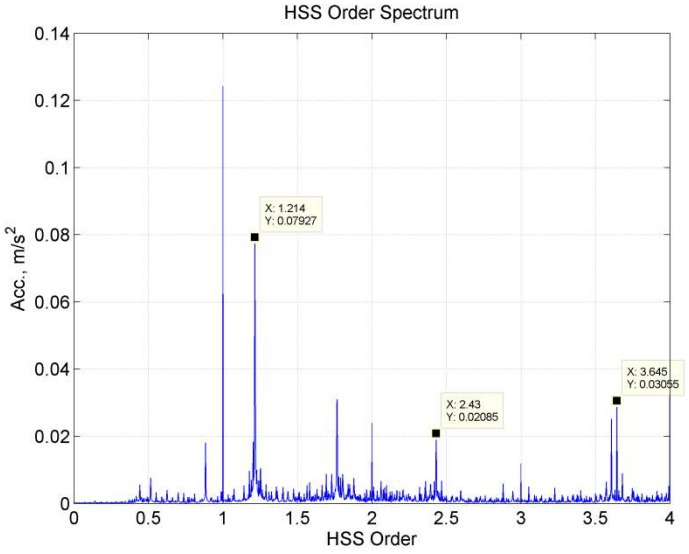

Figure 3.15. Planetary gear stage meshing order and harmonics from AN4

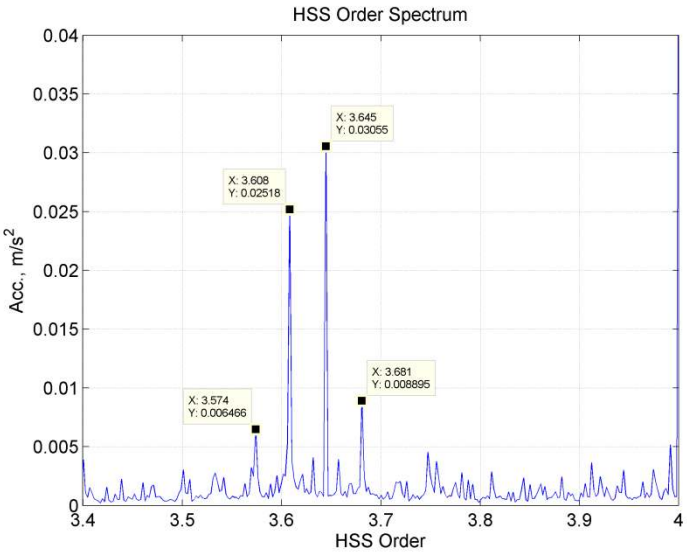

Figure 3.16. PLTGM X3 modulated by planet passing order (0.037)

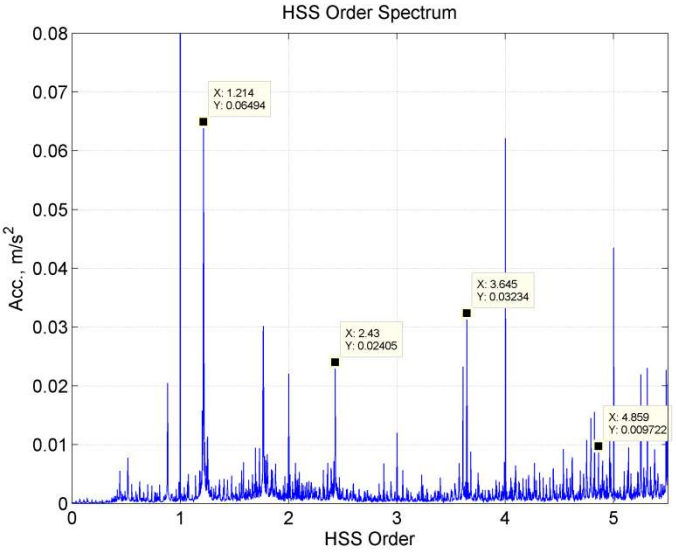

Figure 3.17. Planetary gear stage meshing order and harmonics from AN3

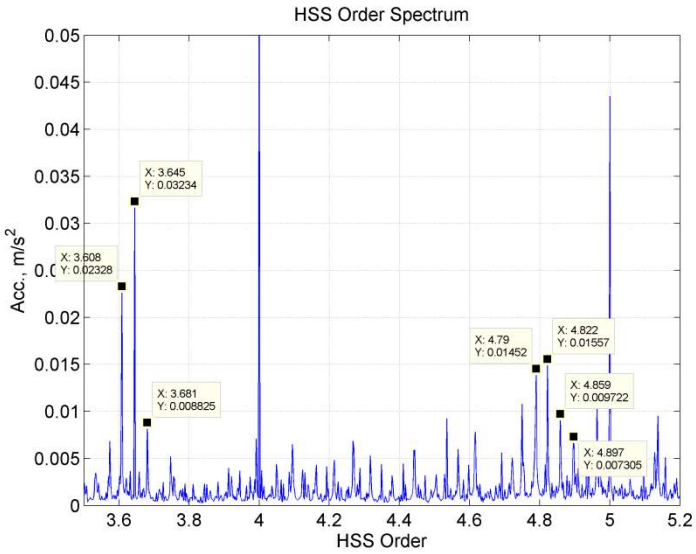

Figure 3.18. PLTGM X3 and X4 modulated by planet passing order (0.037)

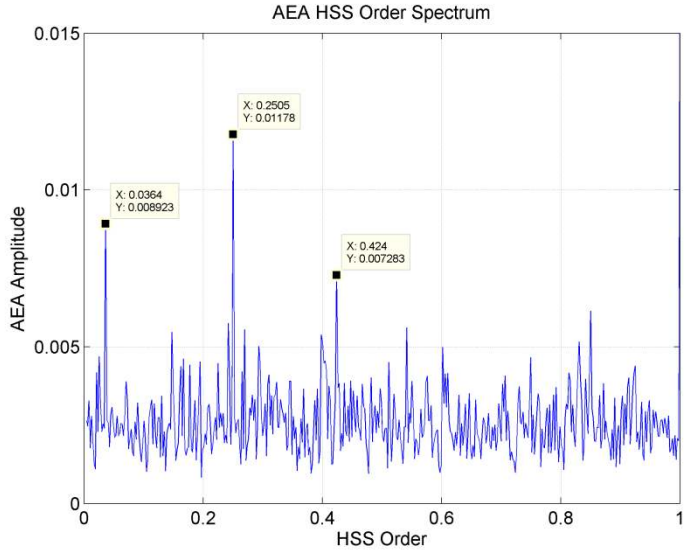

Figure 3.19. Sensor AN3 acceleration enveloping order spectrum

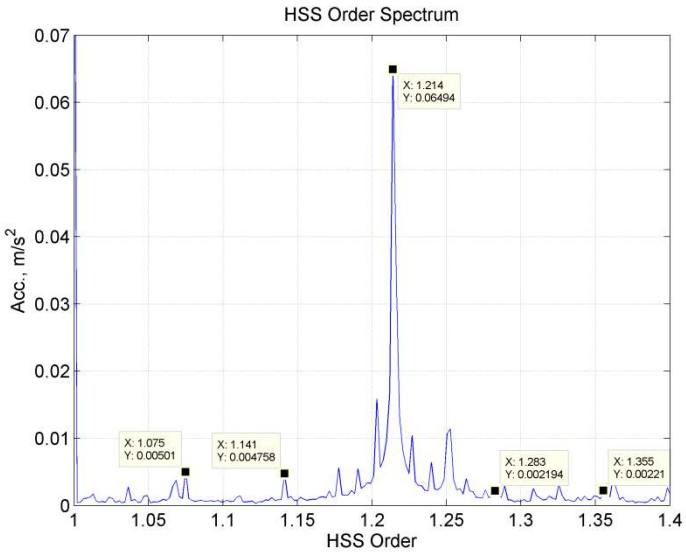

Figure 3.20. Modulation by LSIS in PLTGM is very small

3.2.3.4 HSS Bearings

An acceleration enveloping analysis (AEA) on the high speed shaft sensor, AN7, indicated possible damage initiation of the HSS downwind bearing inner race. As seen in Figure 3.21, there was a fundamental order of 11.48 and its harmonics (22.95 and 34.42) in the envelope order spectrum. These orders re modulated by the HSS shaft speed. By referring to Table 3.2, we can identify that the order 11.48 is very close to the 11.51, the HSS-A_1 and/or HSS-A_2 inner race defect frequency. These two bearings are identical; therefore, further differentiation is not feasible.

The post-test examination revealed that the HSS-A_1 bearing had mild overheating, which created straw-yellow temper colors near each end of the IR raceway [4]. However, it is not likely the overheating caused the BPFI response in the envelope spectrum. Acceleration enveloping analysis can be very sensitive to bearing mechanical damage. It is likely that the damage response was caused by the minor scratches on the race edge or the small indentations in the middle of the raceway.

An acceleration enveloping analysis on the high speed shaft sensor AN7 also indicated possible HSS-A_1 cage damage. In the envelope spectrum (Figure 3.22), there is a minor but clear tone at 0.4261 Order and its harmonics at 0.8522 and 1.278 Order. By referring to Table 3.2, we can see that this fundamental tone of 0.4261 Order is very close to HSS-A_1 cage damage tone of 0.425 Order. However, HSS-A_1 cage damage was not reported in the post-test inspection.

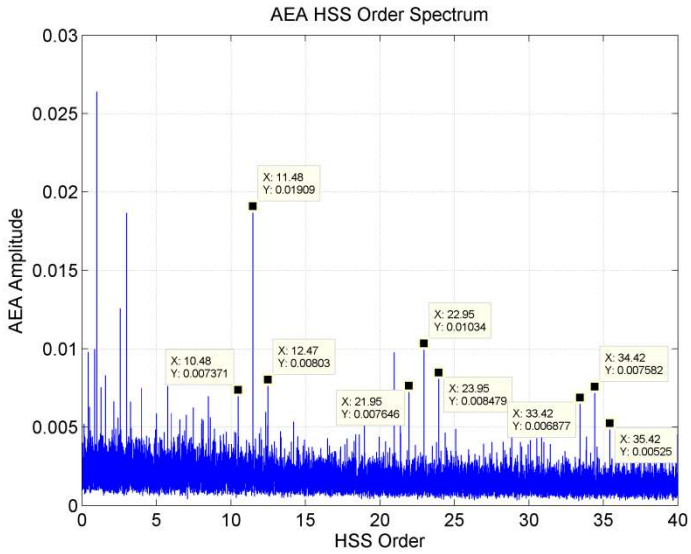

Figure 3.21. Envelope spectrum of AN7

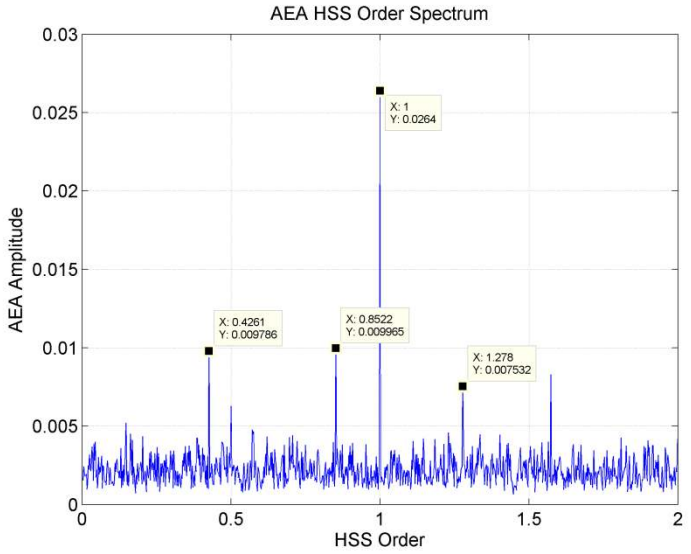

Figure 3.22. Zoomed envelope spectrum of AN7

3.2.3.5 HSIS Bearings

Initial data analysis did not reveal any damage signatures of the bearings on the HSIS shaft. However, the post-test examinations indicated moderate assembly damage and mild contact corrosions on the bearing D inner race [4].

By careful re-examination of the order spectrum Figure 3.23, we saw that there was a small peak at 2.43 Order, which is very close to bearing D BPFI 2.457 Order; however, it was also the second harmonic of the planet gear mesh between the ring gear and the planets. Therefore, it

was very difficult to draw a conclusion about the bearing D BPFI damage signature at the current stage.

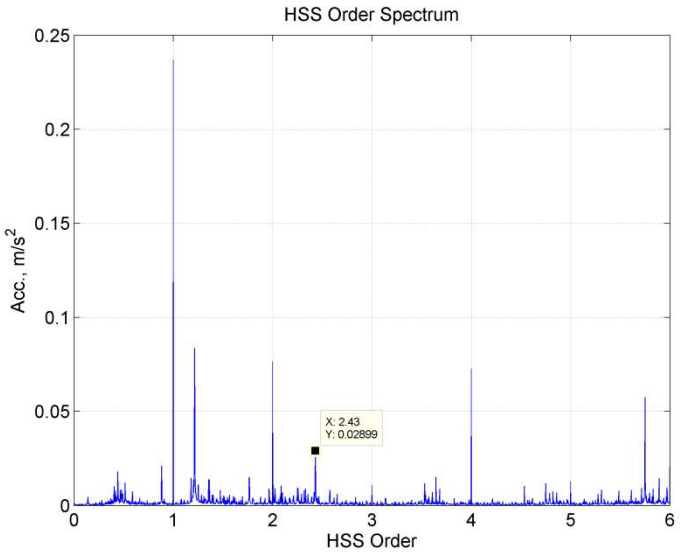

Figure 3.23. Possible bearing D BPFI

3.2.3.6 LSIS Bearings

No damage signatures were identified from post-test inspection or from data analysis.

3.2.3.7 Carrier/ Main Shaft Bearing

Post-test inspection found severe fretting corrosion on the bearing H outer race [4]. However, no damage signature was identified from data analysis, because, even though the corrosion was severe in this bearing, the outer race surface was still smooth. Thus, it does not incur any additional vibrations. In conclusion, this kind of bearing damage cannot be detected by a vibration-based condition monitoring system.

3.3 Discussions

This Round Robin project provided a platform for commercial wind turbine condition monitoring system suppliers, as well as, academic institutions to exercise different methodologies. The GE Bently Nevada team provided a unique set of solutions based on the techniques developed and implemented into its commercially available wind turbine drivetrain condition monitoring system, ADAPT.wind.

Compared to the condition monitoring systems for other rotating machinery, condition monitoring systems for wind turbines face a few unique challenges including constantly variable operating speeds and a high gear-up ratio from the rotor to the high-speed shaft. To overcome the inaccuracy incurred by speed variations, synchronous sampling is the preferred data acquisition technique. Subsequently, a synchronous analysis technique can be used to extract the bearing and gear damage signatures. To accommodate high gear ratios in wind turbine gearboxes, a digital domain synchronous re-sampling is very useful for signature extraction. The digital synchronous re-sampling utilizes a low count mechanically- or electrically- based

encoder, or a key phaser, and interpolates the data between the pulses, with linear or more sophisticated speed variation assumptions.

The data provided by NREL for the Round Robin analysis included accelerometer data and speed profile data. To carry out the digital synchronous sampling, without shaft encoder or key phaser data, the GE team developed and implemented a so-called synthesized synchronous sampling technique. Although the phase information cannot be recovered, the technique successfully carried out the synchronous analysis using the shaft speed profile.

The vibration sensing-based method is believed to be the cost effective approach for wind turbine condition monitoring. However, any gearbox anomalies that do not incur additional vibrations, such as overheating, minor fretting, and smoothed polishing will not be effectively detected by vibration sensors.

Generally speaking, vibration-based wind turbine condition monitoring systems can detect damage in the high speed side with higher confidence than that from the low speed side, especially planetary gear set-related component damage. This is because accelerometers are inherently more sensitive to high frequency vibrations. In addition, the mechanical transmissibility from planetary gear components is usually low. Damage detection and condition monitoring related to the gearbox low speed side is an area that needs more research attention in the future.

4 Combining Novel Approaches with Proven Algorithms for Robust Wind Turbine Gearbox Fault Detection

Jeremy Sheldon*, Matthew Watson, Genna Mott and Hyungdae Lee
Impact Technologies, A Sikorsky Innovations Company
*Corresponding Author Email: jeremy.sheldon@impact-tek.com

4.1 Introduction

Impact Technologies' analysis efforts focused on applying a number of novel vibration diagnostic algorithms to the GRC data set. They have been developed and matured by the team in Department of Defense (DOD) applications for more than 10 years. The algorithms and results are summarized herein. Generally, the methods employed by the team worked well, once the challenges and peculiarities of the data set were realized. In particular, the absence of raw, time-domain data from a healthy system (only FFT plots were provided) made it difficult to baseline the system for comparison purposes. Regardless, the results of the automated algorithms were corroborated with visual spectral analysis and are provided herein.

4.2 Algorithm Overview

Impact applied several component-specific analysis modules to the GRC data set. Each algorithm is briefly introduced below.

4.2.1 FirstCheck: Sensor Validation

Having accurate and validated data is critical to performing effective condition monitoring. Even the most durable sensors often become loose, disconnected, or damaged providing corrupted system information. Consequently, changes in the dynamics of a vibration signal that are characteristic of various sensor faults can be deceptively similar to those of mechanical failures, or vice versa, inevitably resulting in false alarms.

For example, Figure 4.1 shows the result of the authors' previous analysis of a gear pinion failure that occurred on the test stand of a high-speed (thousands of RPMs), high-power (tens of thousands of horsepower) military fighter aircraft drive train. As seen, several vibration features react simultaneously, indicating that a potential fault is present in the system. Information gathered solely from this sensor would confidently indicate a fault. However, upon further investigation of the raw sensor data (shown in the top plot of the figure), one can see that this reaction was caused by faulty (intermittent) data and, therefore, should not be trusted.

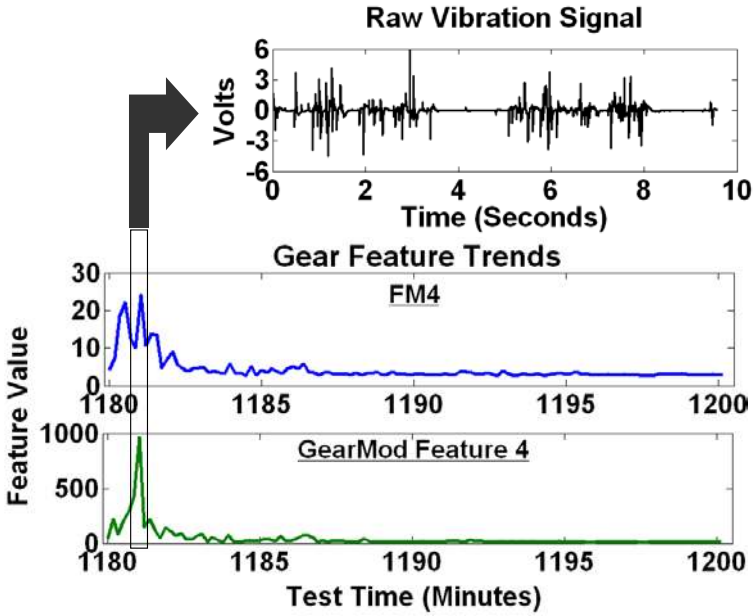

Figure 4.1. False alarm caused by faulty sensor

In addition, because many diagnostic feature algorithms are based on higher order statistics and energy measures; it is possible for a corrupt signal to generate feature values that are within an acceptable range despite the signal containing no periodic frequency content. Rigorous and automated analysis of the integrity of accelerometer data is, therefore, critical to providing accurate health assessments. To address this potential source of false alarms, the validity of the high frequency vibration sensors is first evaluated as an initial step in the analysis, using an approach termed FirstCheck. This module looks at a number of signal characteristics (including the range, bias, and other proprietary characteristics) to verify the integrity of the vibration signal before it is analyzed by the other algorithms.

4.2.2 ImpactEnergy: Bearing Fault Detection and Isolation

Bearing fault detection and isolation was performed using a set of algorithms termed ImpactEnergy. Although bearing characteristic frequencies are easily calculated, they are not always easily detected by conventional frequency domain techniques. Incipient bearing damage is most often characterized as short-burst impulses in the vibration signature. Vibration amplitudes at these frequencies, due to incipient faults (and sometimes more developed faults), are often indistinguishable from background noise or obscured by much higher amplitude vibration from other sources in a running machine, including rotors, blade passing, and gear meshes. Similarly, time domain energy features, such as root mean square (RMS) or kurtosis, are not significantly affected by such short burst of low intensity vibrations. Traditional time domain or frequency domain analyses, therefore, encounter problems in detecting early stages of bearing failure.

The ImpactEnergy module (Figure 4.2) integrates traditional spectral analysis techniques with high-frequency demodulation and advanced feature extraction algorithms, providing a more effective solution. The advantages of using the high frequency response to identify and track

bearing damage is well documented [14,15] and proven to be an effective method. Demodulation, or enveloping, allows the broadband energy caused by failure effects to be differentiated from the energy due to normal system noise. This approach provides the ability to detect defect impulse events much easier than traditional analysis techniques allow. A key consideration is selecting the band-pass filter that is centered on the expected carrier frequencies. Through proprietary knowledge and field-application experience, the authors have developed a process to identify key carrier frequencies.

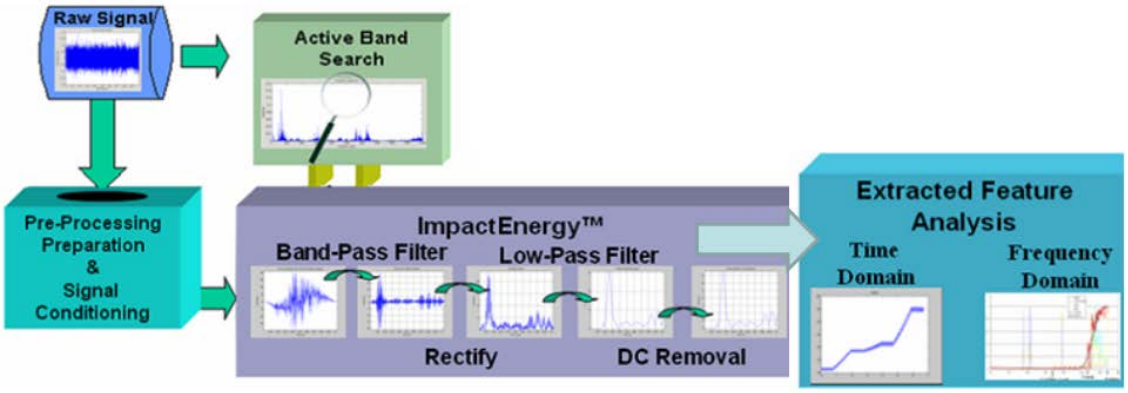

Figure 4.2. ImpactEnergy overview

For complete characterization of bearing health from incipient fault to failure, the ImpactEnergy module includes algorithms to extract an extensive set of time and frequency domain features from both the raw, unprocessed, and demodulated vibration signals. Some time domain features include traditional statistical measures, such as RMS, kurtosis, and Crest Factor. Frequency domain features include the power levels of specific bearing defect frequencies compared against known, health baseline thresholds, which can be very useful in diagnosing a fault [16].

4.2.3 GearMod and GearMod-Shaft: Gear and Shaft Fault Detection and Isolation

The GearMod module (Figure 4.3) is used to extract diagnostic features that are used for gear fault detection and isolation. This module contains a broad range of statistical methods based on the time synchronous averaged (TSA) signal and other processed signals. The time synchronous averaging technique is a useful technique to reduce the random noise level, as well as disturbances from events unrelated to the gear of interest, and it has been extensively used to pre-process gear vibration signals [17,18]. The fundamental principle of the TSA is that the vibration components related to a shaft rotation and the gears on that shaft repeat periodically with the shaft rotation. By dividing the vibration signal into contiguous segments, of exactly one shaft rotation, and averaging a sufficiently large number of segments, the vibration components that are synchronous to the shaft rotation, are reinforced. Non-synchronous vibrations are cancelled out because they are out of phase in consecutive rotations.

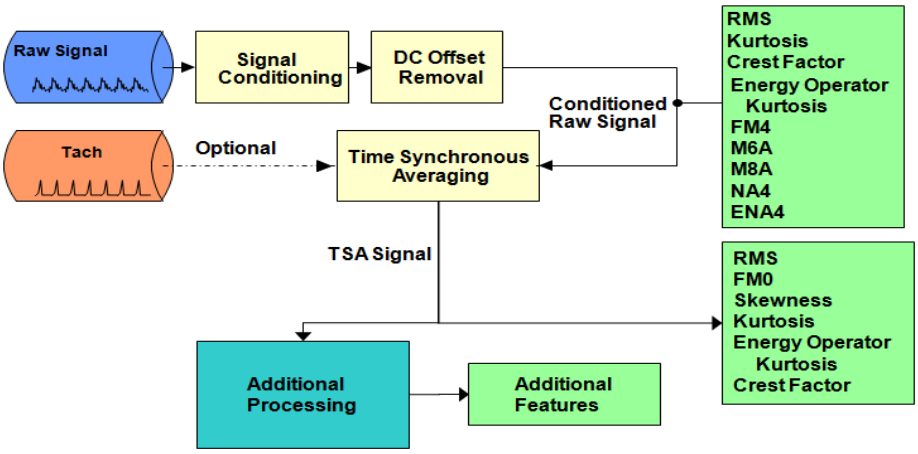

Figure 4.3. GearMod overview

GearMod calculates time-domain features, such as RMS, skewness, kurtosis, and Crest Factor, as well as features from the spectrum of the averaged signal, including FM0 (the peak-to-peak amplitude compared to summation of GMF & harmonic magnitudes), Sideband Index (the average spectral magnitude from sidebands on the 1st GMF), and Sideband Level Factor (the spectral magnitude of sidebands on the 1st GMF, normalized by TSA RMS). The equations for some of these features are included in Table 4.1 [19-21].

Table 4.1. Select gear diagnostic feature definitions

Feature Name	Equation	Symbols
FM0	$FM0 = \frac{PPA}{\sum_{i=1}^{n} A(f_i)}$	PPA = peak-to-peak amplitude A(fi) = GMF & harmonic amplitudes
Sideband Index	$SI = \frac{RMC^{sb}_{1,n_{do\min ant}-1}(s) + RMC^{sb}_{1,n_{do\min ant}+1}(s)}{2}$	$RMC^{sb}_{1,n_{do\min ant}-1}$ and $RMC^{sb}_{1,n_{do\min ant}+1}$ = 1st order sideband amplitudes about fundamental GMF
Sideband Level Factor	$SIL = \frac{RMC^{sb}_{1,n_{do\min ant}-1}(s) + RMC^{sb}_{1,n_{do\min ant}+1}(s)}{\sigma}$	σ = standard deviation

Additional features are also calculated using proprietary methods. In addition, GearMod contains built-in functionality to extract the TSA signal without a tachometer signal, making it appropriate for situations when an accurate or useable tachometer signal does not exist.

4.2.4 Joint Time Frequency Analysis (JTFA) Overview

Gearbox vibration diagnostics are often based on frequency domain analysis, which assumes the monitored signal is "stationary" during the analysis period. However, because operating conditions are often non-stationary and evolving, this assumption leads to spectral smearing and erroneous analysis that creates uncertainty in the health assessment.

Spectral smearing, in which energy from an evolving characteristic frequency (i.e., shaft frequency, bearing fault frequency, gear mesh frequency) is spread across multiple frequency bins, can reduce the efficacy of traditional frequency domain analysis, including Fourier transforms. Typically, this is avoided by defining steady-state operating conditions in which to perform the analysis. Although this may be acceptable for some systems, most wind turbines have constantly varying shaft speeds and loads. In addition, certain component faults and their progressions can also lead to non-stationary signals that could be missed by traditional techniques. As a result, the authors have developed a novel vibration diagnostics methodology that is applicable during non-steady operation through application of joint time-frequency analysis (JTFA)[22]. These methods use various techniques to transform the two dimensional time domain signal into a three dimensional, time-frequency domain signal to increase feature extraction accuracy. An example is shown in Figure 4.4. Various features are then extracted from the three dimensional signals for fault detection.

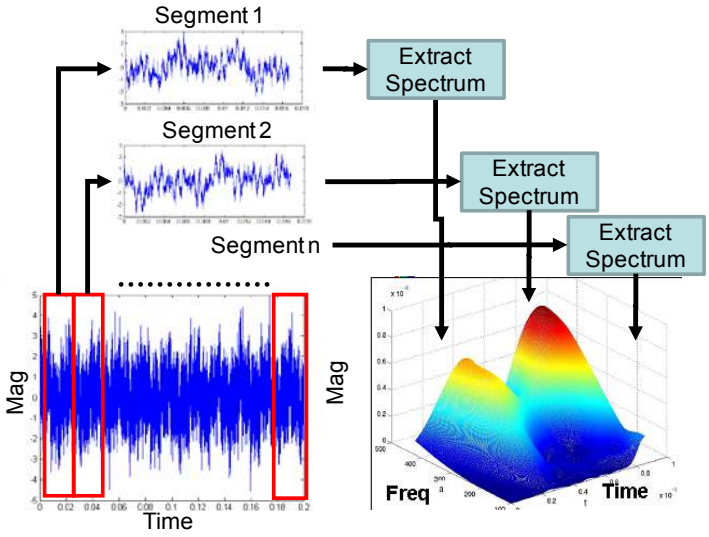

Figure 4.4. Example JTFA approach (short time Fourier transform)

4.3 Results Summary

The results of the analysis performed by Impact are briefly discussed in the following sections. Both the blind results, obtained without knowing details on actual gearbox condition, and the conclusions that were drawn after learning the actual damage, are discussed separately. It is worth noting that FirstCheck was applied to all vibration data and no sensor faults were detected.

4.3.1 "Blind" Results

The results obtained without knowing the actual gearbox faults are summarized in Table 4.2. The table includes the suspected damage, location, or component, severity, and the suspected damage mode, as identified by Impact's "blind" analysis. As shown, Impact correctly identified three of the seven damage instances and had one false alarm (planet gear fault was called out but not correct). Some specific evidence and results are shown in the following sections.

Table 4.2. Initial blind results summary

Damage #	Component / Location	Mode	Rationale	Severity
1	HSS Gear Set (HSS Gear and HSS Pinion)	Scuffing	High RMS and sidebands Trending of JTFA features during 2b & 2c	Severe
2	HSS Downwind Bearings (IR and Rollers)	Overheating		Mild
3	ISS Gear Set (ISS Gear and Pinion, all teeth, sun spline)	Fretting Corrosion, Scuffing, Polishing Wear		Severe
4	ISS Upwind Bearing (IR)	Assembly damage, Plastic Deformation, Scuffing, False Brinelling, Debris Dents, Contact Corrosion		Moderate
5	ISS Downwind Bearings (OR Spacer for both Bearings)	Assembly damage, Plastic Deformation, Dents	BPFO harmonics (2x) clear in conventional FFT from multiple sensors with +/- shaft harmonics	Severe
6	Annulus/Ring Gear, or Sun Pinion	Scuffing and polishing, Fretting Corrosion	High energy ratio/NB4/FM0 and low GMF harmonics	Moderate, Severe
7	Planet Carrier Upwind Bearing (Container and OR)	Fretting Corrosion	Detected low frequency (0.2 & 0.3 Hz) impact events	Severe

*Fault isolation between B/C bearings not possible since they are identical design at same location

Successfully Detected and correctly isolated
Missed Detection

4.3.1.1 High Speed Shaft Gears

Figures 4.5 and 4.6 show the results of Impact's GearMod analysis of data sets 2b and 2c for the high speed gear/pinion pair. As seen, the analysis showed typical gear fault indicators, especially on accelerometers AN6 and AN7. The distinct harmonics (1-4 and some higher) of the high speed gear mesh frequency (GMF) combined with the numerous sidebands around each GMF indicated teeth scuffing or other distributed wear (Figure 4.5). In addition, the high second order GMF, clearly visible in Figure 4.6, indicated potentially misaligned gears/shafts.

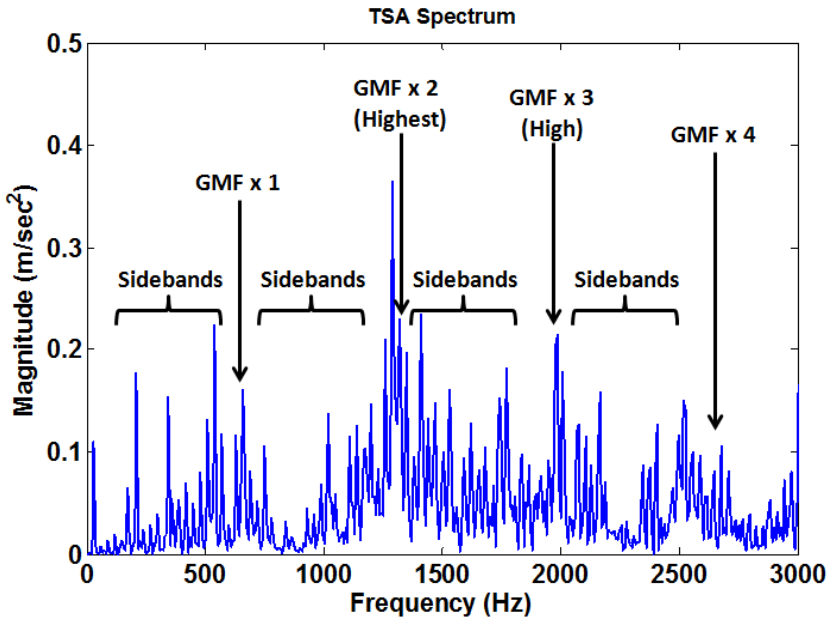

Distinct sidebands around GMF harmonics
and increased GMFx2 and GMFx3

Figure 4.5. High speed gear fault evidence, blind results (AN6)

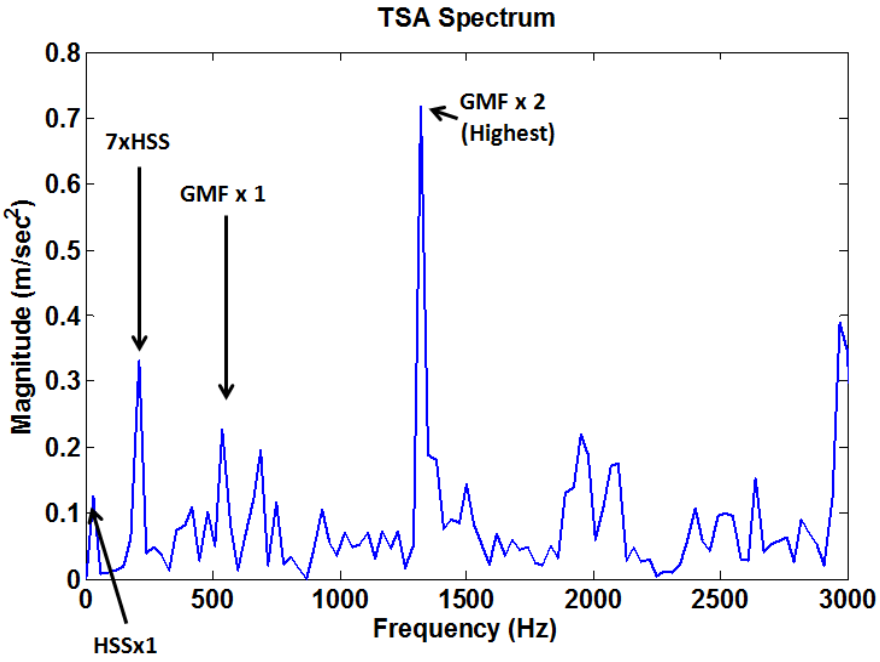

Dominant GMFx2

Figure 4.6. High speed gear fault evidence, blind results (AN7)

4.3.1.2 Intermediate Shaft Bearings

Impact's ImpactEnergy analysis of the bearings on the intermediate shaft is summarized by the spectral plots in Figure 4.7 and Figure 4.8. For the downwind bearings (IMS-SH B&C, which are indistinguishable since they are the same model bearing running at the same speed), the clear peaks in the conventional, non-demodulated spectrum (Figure 4.7) at the outer raceway fault frequency indicated substantial localize defects. Notice, too, the clear spectral peak at the IMS-SH-A inner raceway defect frequency, in both the faulted and baseline (supposed healthy) FFT. Because the bearing fault frequency was visible in the baseline FFT data that was provided, Impact was not confident in the evidence enough to call out the fault. As such, this fault was not called out in the blind analysis (see Section 4.3.2.1 for more details). .

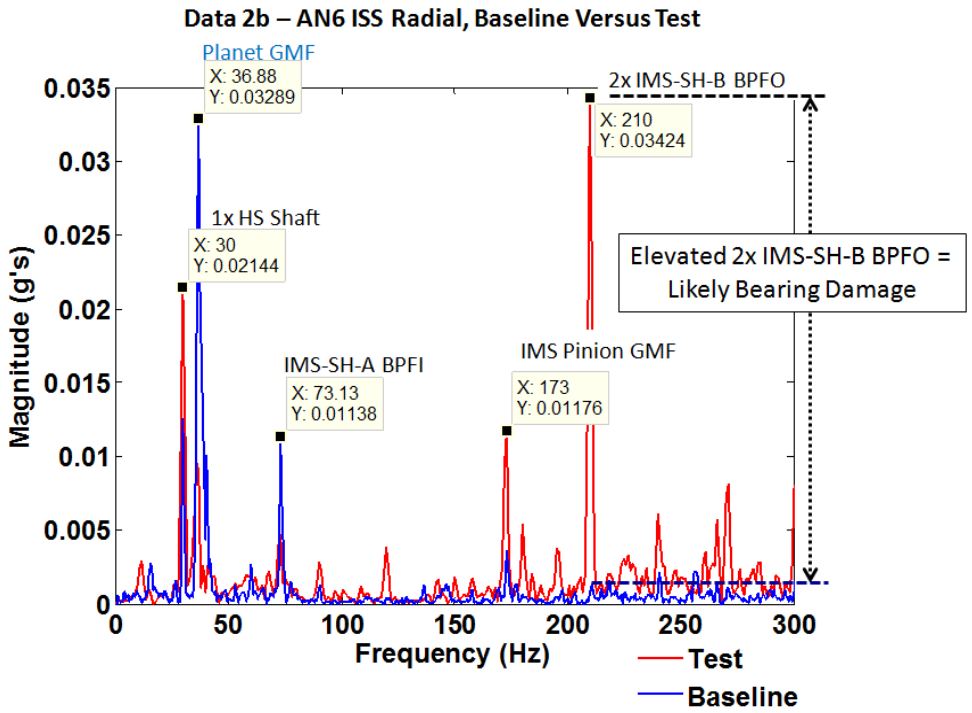

Figure 4.7. Intermediate speed downwind bearing fault evidence, blind results (AN6, Data 2b)

Damage in the IMS-SH B component was also evident by the elevated levels of multiple harmonics of the inner raceway fault frequency seen in the demodulated spectrum (Figure 4.8).

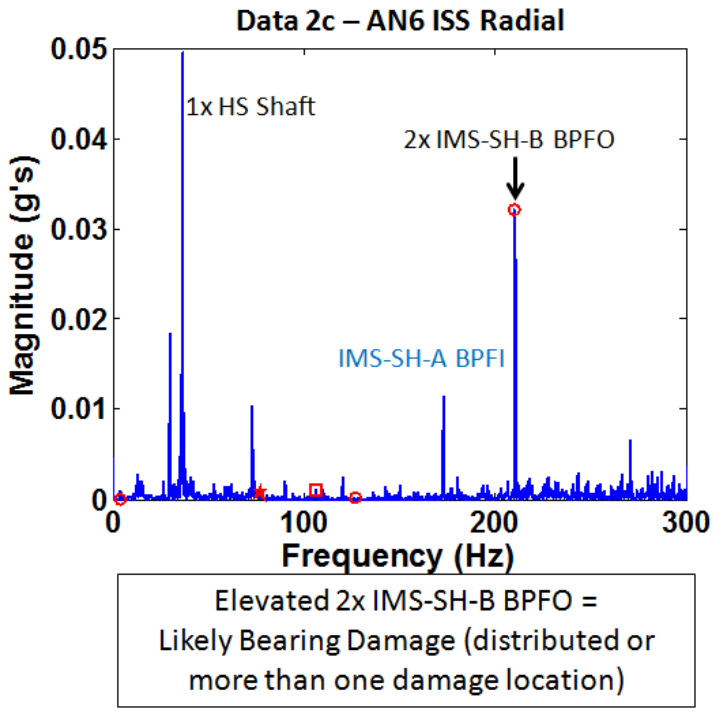

Figure 4.8. Intermediate speed downwind bearing fault evidence, blind results

4.3.1.3 Sun Pinion Gear

Focusing on the planetary gear analysis, Impact found evidence of heavy distributed or uniform wear on the Sun Pinion Gear, specifically using the AN3 Ring Gear Radial 180° accelerometer. In addition to the relatively low GMF harmonics and high sidebands, as shown in Figure 4.9, Impact's analysis showed higher than normal statistical features, including Energy Ratio (ER, ratio of spectral energies between Difference and Regular signals), NB4 (time averaged kurtosis of the envelope of the TSA signal band-pass filtered around dominant meshing frequency), FM0, and RMS.

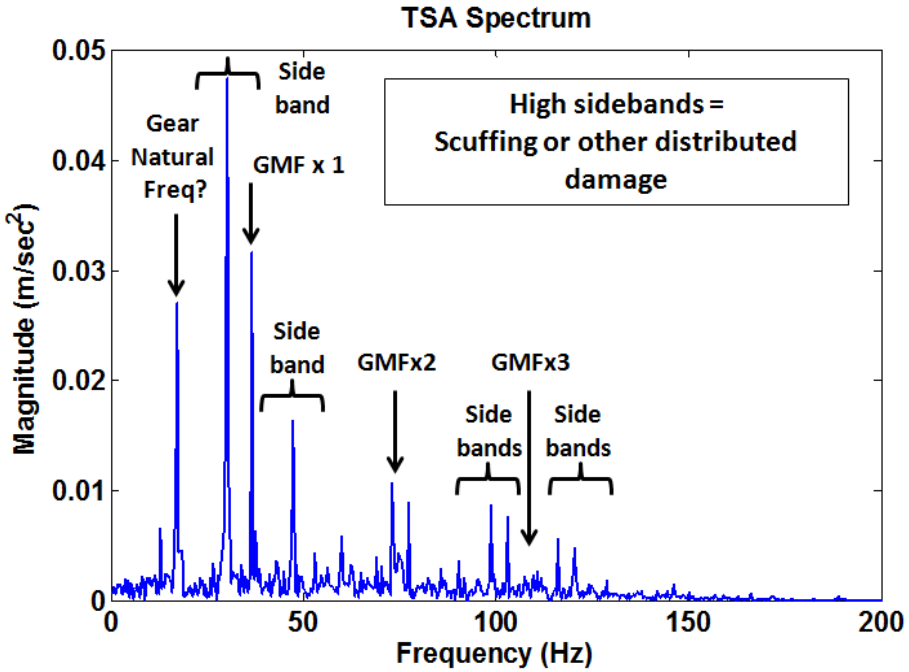

Figure 4.9. Sun pinion gear fault evidence, blind results

4.3.1.4 Intermediate and High Speed Gear JTFA Results

As mentioned above, Impact applied a set of JTFA algorithms to this data set. Since these algorithms are still under development, the results summarized in Figure 4.10 were enough to raise suspicion, but were not enough alone to call out a fault for the intermediate speed gear pairs (and were thus missed). However, when combined with the above gear analysis, Impact's JTFA results further confirmed distributed faults in the high speed gear pairs. Interestingly, several of the JTFA features exhibited upward trends, normally indicating fault progression, but there was no evidence of fault progression provided to Impact to confirm this behavior. Although the torque load increased from 2a to 2c in Figure 4.10, the change was a step change and torque levels were fairly steady during each segment. Therefore the upward trends of the features within each segment (most noticeably 2b and 2c) seem to indicate some other evolving/influencing phenomena.

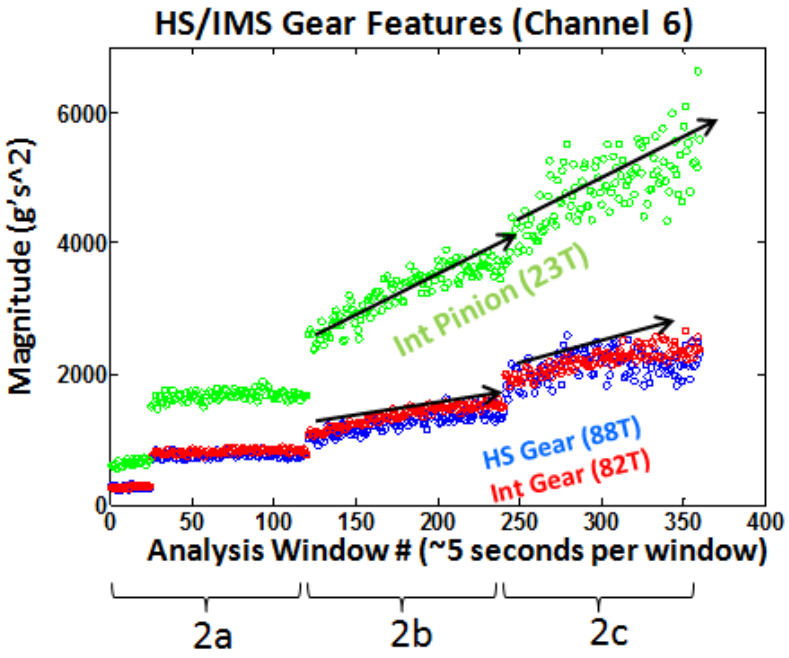

Figure 4.10. JTFA speed gear fault evidence, blind results

4.3.2 Revisited Results

After providing NREL with the above results from the blind analysis, the gearbox inspection results were provided to the Round Robin team. Knowing what to look for, Impact revisited the analysis to determine if any additional fault/damage signatures were present in the data. The results of the subsequent analysis are described below and in Table 4.3. As seen, most of the faults not called out in the blind analysis were detected in hindsight, resulting in the detection of six of the seven damage instances. Specifically the intermediate speed shaft upwind bearings and the high speed shaft downwind bearing damages were detected. These are described in more detail in the following sections. Note that Impact didn't reevaluate the planet carrier bearing fault since it was our opinion that this type of fault is not detectable with vibration analysis due to the fact that the damage appears on the outside bore of the outer raceway, not in the contact zone of the bearing.

Table 4.3. Post-inspection results summary

Damage #	Component / Location	Rationale/Notes
1	HSS Gear Set (HSS Gear and HSS Pinion)	High RMS and sidebands Trending of JTFA features during 2b & 2c
2	HSS Downwind Bearings (IR and Rollers)	Multiple BPFI harmonics (1x-4x) dominant in demodulated FFT (2a and 2c)
3	ISS Gear Set (ISS Gear and Pinion, all teeth, sun spline)	Trending of JTFA features during 2b & 2c
4	ISS Upwind Bearing (IR)	Little modulation clear, BPFI in conv. spectra
5	ISS Downwind Bearings (OR Spacer for both Bearings)	BPFO harmonics (2x) clear in conventional FFT from multiple sensors with +/- shaft harmonics
6	Annulus/Ring Gear, or Sun Pinion	High energy ratio/NB4/FM0 and low GMF harmonics
7	Planet Carrier Upwind Bearing (Container and OR)	Likely not diagnosable via vibration

Successfully Detected and correctly isolated
Not detectable by vibration

4.3.2.1 Intermediate Shaft Upwind Bearings

As briefly mentioned previously, Impact's analysis during the blind portion of this effort revealed a high inner race defect frequency magnitude for both the test data and the provided baseline data, as shown in Figure 4.11. Initially this decreased the confidence in diagnosing a fault in the IMS Upwind bearing (IMS-SH-A). However, the inspection report revealed that the damage was due to an assembly error and, therefore, it was also present during the baseline testing.

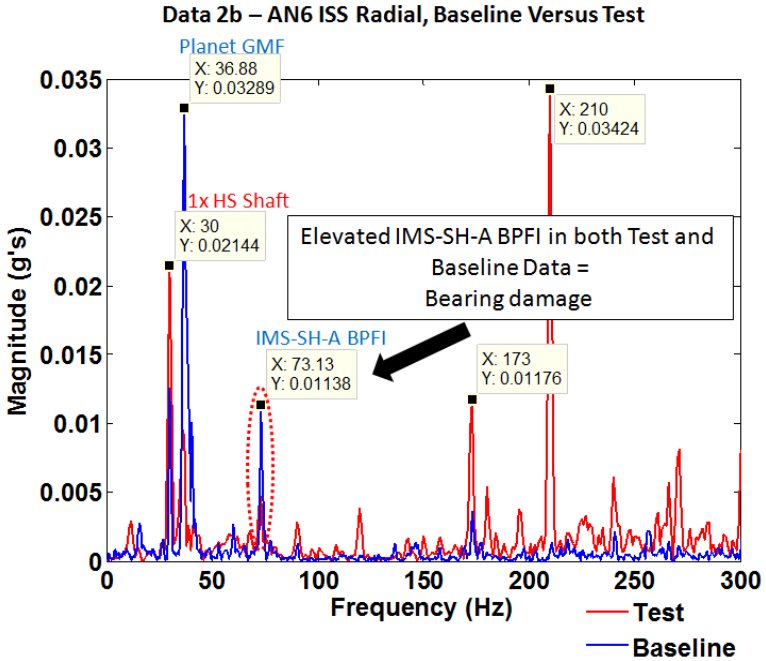

Figure 4.11. Intermediate speed upwind bearing damage evidence

With this information and the results exemplified by Figure 4.12, Impact could correctly identify the fault as a progressed or distributed inner raceway fault because there was little modulation and clear inner raceway frequency vibration.

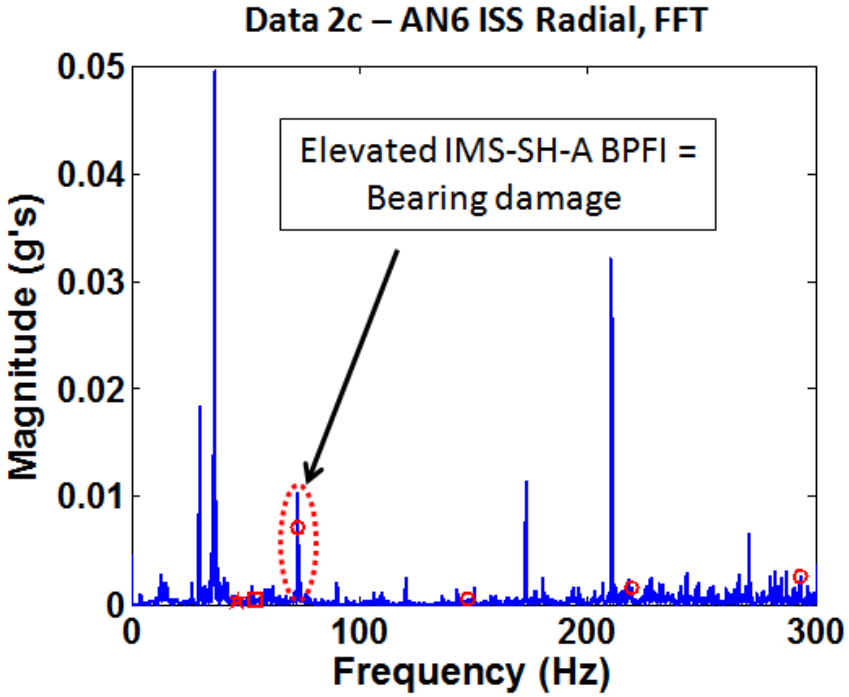

Figure 4.12. Intermediate speed upwind bearing fault evidence, post-inspection results

4.3.2.2 High Speed Shaft Downwind Bearings

During the blind portion of this effort, Impact did not diagnose the defect present on the high speed shaft downwind bearings (HSS-SH-B/C). Based on the information contained in the inspection report, a discrepancy in the bearing part numbers was found. The initially provided documentation listed the HSS-SH-B/C bearings as 32222J2 SKF, but the inspection report visually confirmed them as 32222A FAG. Although similar in size, these bearings have different fault frequencies.

Using the correct fault frequencies, Impact's analysis clearly showed small, early stage inner raceway defects, as evident by the multiple BPFI harmonics (1x-4x) that are dominant in the demodulated FFT (for data sets 2a and 2c). Example demodulated spectra and fault frequency peaks are shown in Figures 4.13 and 4.14. Although Impact did detect a defect in the bearing, the diagnosed fault signature seems unlikely to have been caused by only the cited overheating event. Instead, Impact believes the evidence points to some additional defect, which may have resulted from the overheating.

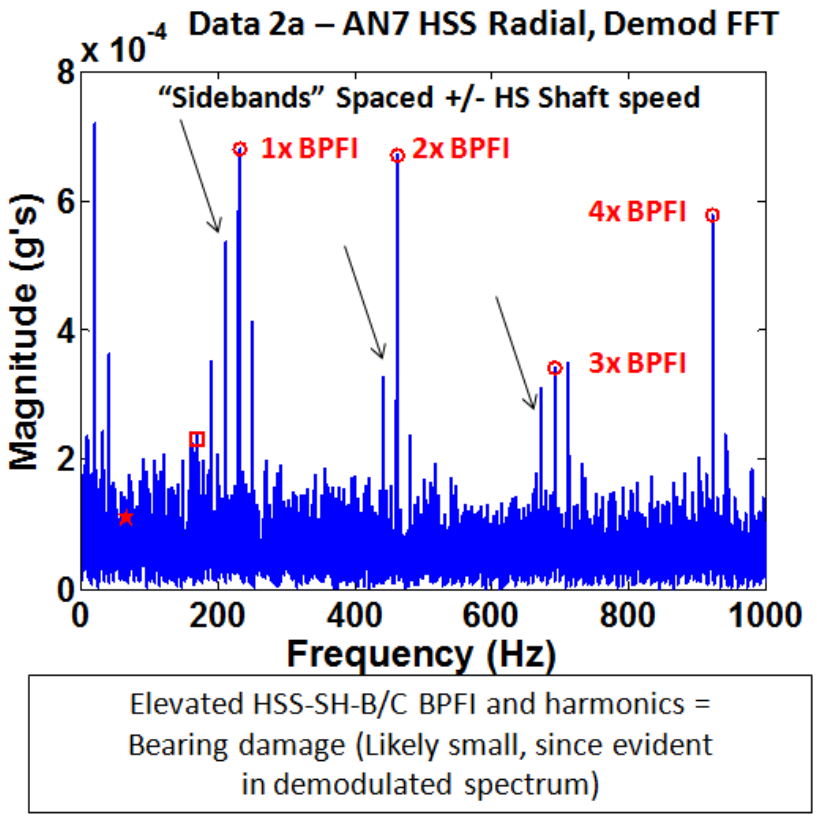

Figure 4.13. High speed downwind bearing fault evidence, revisited (Data 2a)

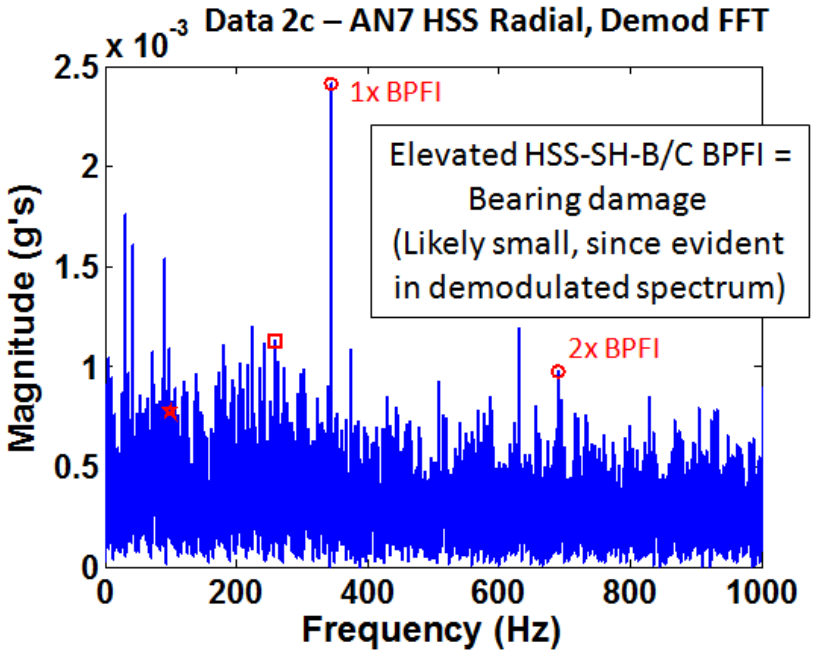

Figure 4.14. High speed downwind bearing fault evidence, revisited (Data 2c)

4.4 Lessons Learned and Conclusions

Impact's blind analysis successfully detected three of the seven damaged components that were present in the gearbox, with a fourth component detected but not called out due to the relative immaturity of the approach that detected the damage. Of the remaining three, two were detected during the secondary analysis that was performed after the inspection report was provided. These two were originally missed due to: 1) the use of incorrect bearing design information that was provided in the original analysis, and 2) the presence of the damage during assembly, which caused the baseline results that were used for comparison to be higher. It is Impact's opinion that the seventh damaged component is not detectable with vibration analysis since the damage appears on the outside bore of the outer raceway, not in the contact zone of the bearing.

In general, this analysis was confounded by the number and severity of the defects, especially the obfuscation of bearing and other faults by the widespread gear damage. Impact believes that in actual practice the expected diagnostic performance will be better since a smaller and less severe set of faults will be present during the early stages of fault evolution. To clarify, this data set contains multiple progressed faults that would be better detected as they individually occur over time versus diagnosing each one once they have all occurred. Additionally, assessing the fault severity was more difficult due to the lack of time-domain baseline data. Although this was overcome by using our experience of previous analysis of different machinery, higher fidelity results may be produced by comparing like data to like data and allowing the algorithms to be baselined against typical, healthy vibration levels and trended over time. Regardless of these minor issues, this analysis and effort should enable a good assessment on the state of wind turbine diagnostics, as well as an indication of what work remains.

5 Analysis Algorithms and Diagnostics Results from NRG Systems

Eric Bechhoefer
NRG Systems
Email: erb@nrgsystems.com

5.1 Introduction

NRG Systems, as a participant of this Round Robin study, wished to validate the effectiveness of analysis algorithms used in the aerospace community, for the wind industry. The aerospace industry, specifically vertical flight, developed an extensive toolset for gearbox fault detection as a result of helicopter gearbox failures. These algorithms were specifically developed for shaft, gear, and bearing fault detection. This is counter to most installed condition monitoring systems, which have matured out of industrial monitoring of large turbo-machinery (turbo-machinery have no gearbox, focusing extensively on shaft misalignment, out of balance, or rub conditions). NRG implemented two analysis methodologies: synchronous analysis of shaft/gear components and non-synchronous analysis of bearings. Synchronous methods were based on the work of McFadden [23], while the bearing analysis was based on the work of Randall [24].

The data set consisted of 10 samples each under three operating conditions, for a total of 30 files. The samples were separated by a short time interval. Because these industrial gearboxes are designed to run for years versus minutes, we assumed that the analysis would consist of taking a snap shot of the current gearbox condition. No attempt was made to trend component condition indicators or look at statistical differences between early and late files. It was assumed that over the period of the test, there was no appreciable degradation of the gearbox. The analysis consisted of viewing the output of various analysis algorithms for each component, and based on some nominal experience with aerospace gearboxes, defining the wind turbine gearbox as good, bad, or indifferent.

5.2 Analysis Algorithms

5.2.1 Condition Analysis Algorithms - Feature Extraction to Improve Signal to Noise

Vibration signatures for machinery faults tend to be small relative to other vibration signatures. For example, in the typical gearbox, the energy associated with gear mesh and shaft vibrations will be orders of magnitude larger than a fault feature. Spectral analysis or root mean squares (RMS) of vibration are not powerful enough analyses to find early faults or defects. Techniques to improve the signal to noise are needed to remove frequencies associated with nominal components, while preserving the fault signatures.

Gear analysis was based on operations of the time synchronous average [23]. Time synchronous averaging (TSA) is a signal processing technique that extracts periodic waveforms from noisy data. The TSA is well suited for gearbox analysis, where it allows the vibration signature of the gear under analysis to be separated from other gears and noise sources in the gearbox that are not synchronous with that gear. Additionally, variations in shaft speed can be corrected, which would otherwise result in spreading of spectral energy into adjacent gear mesh bins. To do this, a signal is phased-locked with the angular position of a shaft under analysis.

This phase information can be provided through an *n* per revolution tachometer signal (such as a Hall sensor or an optical encoder, where the time at which the tachometer signal crosses from low to high is called the zero crossing) or though demodulation of gear mesh signatures [25]. In the case of the GRC data set, the phase information was extracted from the generator signal itself (e.g., voltage signal capacitively coupled onto the RPM signal).

The model for vibration in a shaft in a gear box was given in [23] as:

$$x(t) = \Sigma_{i=1:K} X_i(1 + a_i(t))\cos(2\pi i f_m(t) + \Phi_i) + b(t)$$

where:

X_i is the amplitude of the *k*th mesh harmonic
$f_m(t)$ is the average mesh frequency
$a_i(t)$ is the amplitude modulation function of the *k*th mesh harmonic.
$\phi_i(t)$ is the phase modulation function of the *k*th mesh harmonic.
Φ_i is the initial phase of harmonic *k*, and
$b(t)$ is additive background noise.

The mesh frequency is a function of the shaft rotational speed: $f_m = Nf$, where N is the number of teeth on the gear and f is the shaft speed, with no reduction in the analysis performance. This vibration model assumes that f is constant. In most systems, there is some wander in the shaft speed due to changes in load or feedback delay in the control system. This change in speed will result in smearing of amplitude energy in the frequency domain. The smearing effect, and non-synchronous noise, is reduced by re-sampling the time domain signal into the angular domain: $m_x(\theta) = E[x(\theta)] = m_x(\theta + \Theta)$. The variable Θ is the period of the cycle that the gearbox operation is periodic, and E[] is the expectation (e.g., ensemble mean). This results in the assumption that $m_x(\theta)$ is stationary and ergodic. If this assumption is true, then non-synchronous noise is reduced by 1/sqrt(*rev*), where *rev* is the number of cycles measured for the TSA.

5.2.2 TSA Techniques for Condition Indicators

The TSA is an example of angular resampling [23], [25], where the number of data points in one shaft revolution (r_n) is interpolated into m number of data points, such that:

- For all shaft revolutions n, m is larger than r,
- And $m = 2^{\text{ceiling }(\log 2\ (r))}$ (typical for radix 2 Fast Fourier Transform).

The TSA itself can be used for Condition Indicators (CIs). Typically, a CI is a statistic of a waveform (in the case the TSA). Common statistics are RMS, peak to peak, Crest Factor, kurtosis and skewness. For the shaft, a shaft order (SO) of 1, 2, and 3 (first, second and third shaft rate harmonic) can be used to determine shaft out of balance, bent shaft, and/or shaft coupling damage, respectively. Figure 5.1 outlines the process of generating the TSA, and shaft CIs.

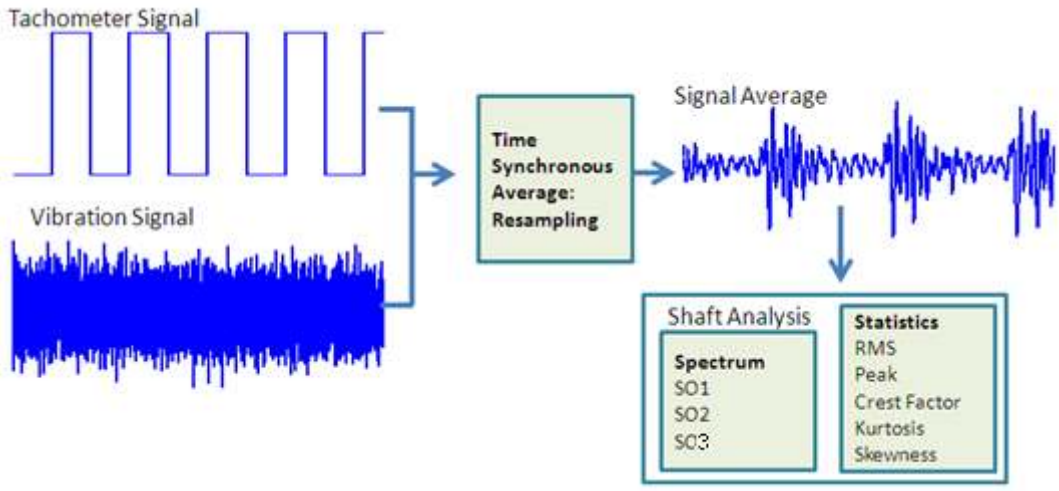

Figure 5.1. Generation of the TSA and selected CIs

5.2.3 Gear Fault Indicators

There are at least six failure modes for gears: surface disturbances, scuffing, deformations, surface fatigue, fissures/cracks, and tooth breakage. Each type of failure mode, potentially, can generate a different fault signature. Additionally, relative to the energy associated with gear mesh tone and other noise sources, the fault signatures are typically small. A number of researchers have proposed analysis techniques to identify these different faults [25,26]. Typically, these analyses are based on the operation of the TSA. Examples of analysis are:

- Residual Analysis. Shaft order 1, 2, and 3 frequencies, and the gear mesh harmonics, of the TSA are removed. Faults such as a soft/broken tooth generate a 1 per rev impact in the TSA. In the frequency domain of the TSA, impacts are expressed as multiple harmonics of the 1 per rev. The residual analysis removes the shaft order 1, 2, and 3 frequencies and gear mesh harmonics in the frequency domain, and then the inverse FFT is performed. This allows the impact signature to become prominent in the time domain. CIs are statistics of this waveform (RMS, peak to peak, Crest Factor, and kurtosis).
- Energy Operator (EO), which is a type of residual of the autocorrelation function. For a nominal gear, the predominant vibration is gear mesh. Surface disturbances and scuffing generate small higher frequency values, which are not removed by autocorrelation. Formally, the EO is: $TSA_{2:n-1} \times TSA_{2:n-1} - TSA_{1:n-2} \times TSA_{3:n}$. The bold indicates a vector of TSA values. The CIs of the EO are the standard statistics of the EO vector.
- Narrowband Analysis operates the TSA by filtering out all tones except that of the gear mesh and with a given bandwidth. It is calculated by zeroing bins in the Fourier transform of the TSA, except the gear mesh. The bandwidth is typically 10% of the number of teeth on the gear under analysis. For example, a 23-tooth gear analysis would retain bins 21, 22, 23, 24, and 25, and their conjugates in the Fourier domain. Then, the inverse FFT is taken, and statistics of the waveform are taken. Narrowband analysis can capture sideband modulation of the gear mesh tone due to misalignment, or detect a cracked/broken tooth.

- Amplitude Modulation (AM) analysis is the absolute value of the Hilbert transform of the Narrowband signal. For a gear with minimum transmission error, the AM analysis feature should be a constant value. Faults will greatly increase the kurtosis of the signal.
- Frequency Modulation (FM) analysis is the derivative of the angle of the Hilbert transform of the narrowband signal. It is a powerful tool capable of detecting changes of phase due to uneven tooth loading, a characteristic of a number of fault types.

For a more complete description of these analyses, see [25] or [26]. Figure 5.2 is an example of the processing to generate the gear CIs for a spiral bevel gear with surface pitting and scuffing.

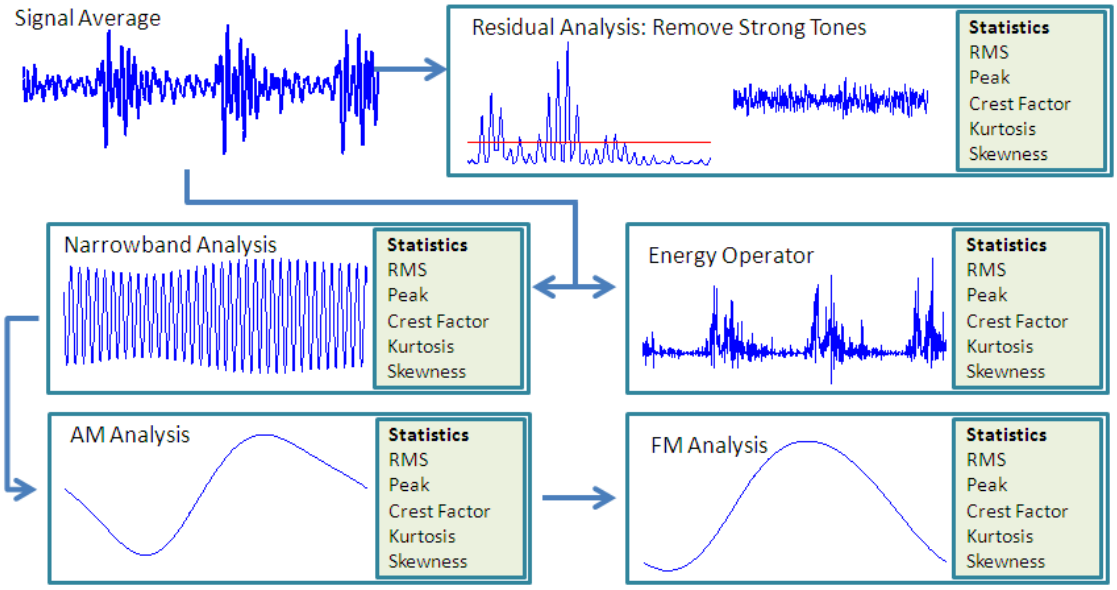

Figure 5.2. Process for generating gear CIs

The cepstrum was also evaluated, although it is difficult to implement in an automated system. For bearing analysis, the envelope analysis was used.

5.3 Analysis Results

5.3.1 Synthetic Tachometer Signal

All shaft and gear analysis is based on the TSA, which requires a tachometer signal for a key-phasor. The data set contained an RPM signal, but not a raw tachometer signal. It was noticed that the RPM signal carried modulated noise. It was conjectured that this was the convolution of 60 Hz power, with the 20/30 Hz output of the generator onto the RPM signal (indicating a poor ground). By removing the DC value of the RPM signal, then low pass filtering, the generator 20 Hz signal was isolated and used as a tachometer zero crossing index. This is possible because the 20 Hz generator signal is synchronous with the high speed shaft, see Figure 5.3.

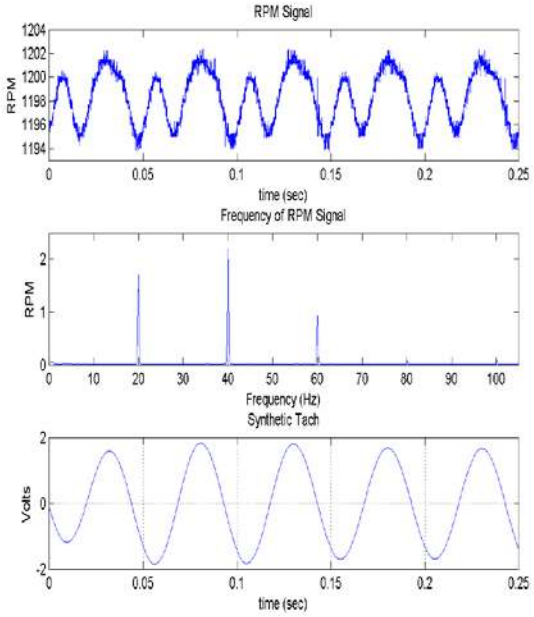

Figure 5.3. Synthetic tachometer

5.3.2 High Speed Shaft/High Speed Pinion

The HSS/HSP showed a large shaft order 1 in the TSA Figure 5.4a (spectrum in G's) and a large vibration in the AM signal (units of G's) of Figure 5.4b coupled with a large phase change in the FM signal (units of radian). This indicates a large eccentricity (the gear was not centered on the shaft). Additionally, the energy operator was large and periodic, indicating severe scuffing/pitting. There was limited evidence of a soft/broken tooth (a broken or soft tooth result in a 1/rev impact, which is visible in the residual analysis, the EO signal (units of G's), and the AM and FM analysis).

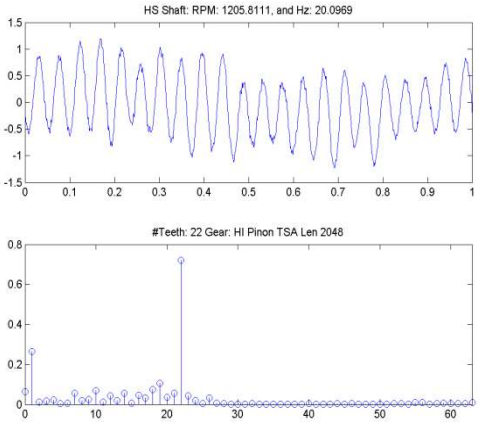

Figure 5.4a. HSS TSA/spectrum

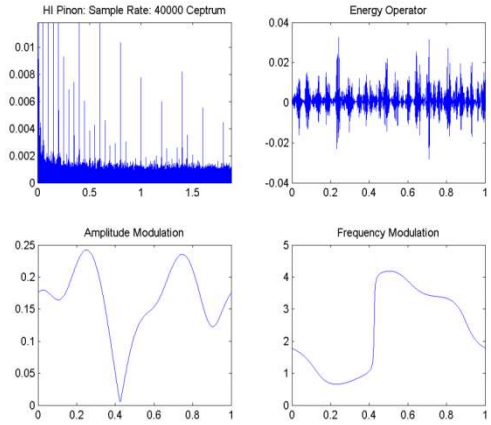

Figure 5.4b. HSS gear analysis

5.3.3 Intermediate Speed Shaft/High Speed Gear and Intermediate Speed Pinion

The ISS/HSG/ISP showed a large shaft order 4 in the TSA (Figures 5.5a and 5.5b). Since there is a 4:1 relationship with the HSS, this further confirms the eccentricity of the HSP. Both the HSG and ISP showed large (e.g., .05 G's) energy operator, indicative of sever pitting/scuffing. The AM and FM signals did not indicate any missing teeth/soft teeth, but did reflect a high variation in loading due to the HSP (Figure 5.5b).

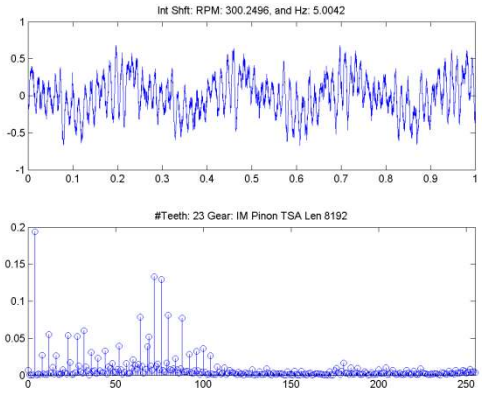

Figure 5.5a. TSA intermediate shaft

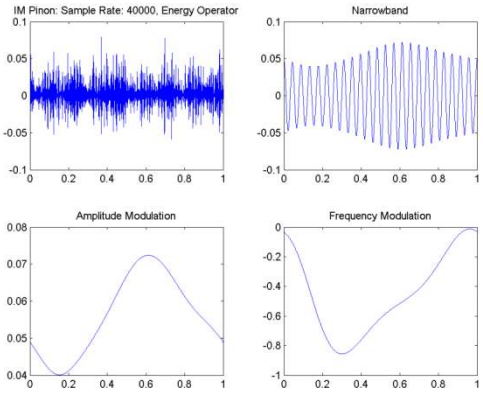

Figure 5.5b. Intermediate speed pinion, where the units for the Energy Operator, Narrowband and Amplitude Modulation analysis are in G's, and the Frequency Modulation analysis is in radians.

5.3.4 Sun/Planet Gear Analysis

The Sun Gear showed no soft/broken teeth. However the EO values are large. Similarly, the planet gears showed large EO values. This suggests that there is pitting/scuffing on these gears (Figures 5.6a and 5.6b). Because the accelerometer is in a fixed frame relative to the planet, the planet AM analysis should show a sinusoid of three cycles (corresponding to the number of plants passing the sensor. Because this is not present, it could indicate that one of the planet bearings is worn and the planet is not sharing the load evenly with its two neighboring planets (Figure 5.6b AM and FM plots). The bearing analysis could not confirm the presence of a planet bearing fault, although this may be due to poor window selection. The units for the Energy Operator, Narrowband and Amplitude Modulation analysis is in G's, and the Frequency Modulation analysis is in radians.

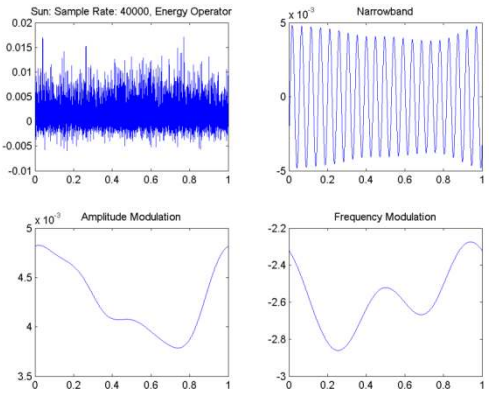

Figure 5.6a. Sun gear

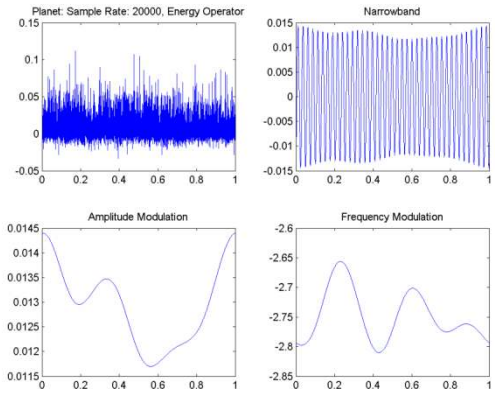

Figure 5.6b. Planet gears

5.3.5 Annulus/Ring Gear

The ring gear shows no cracked tooth/soft tooth. The carrier is not cracked. The large EO indicates scuffing/pitting. There is some suggestion that the pitting is larger on the ring gear than the planet (Figure 5.7). Note that in the AM analysis, the variation in load is a function of the planets passing the fixed sensor. As suggested earlier, because the load is not even across all three planets, this may indicate planet bearing error. The units for the Energy Operator, Narrowband and Amplitude Modulation analysis is in G's, and the Frequency Modulation analysis is in radians.

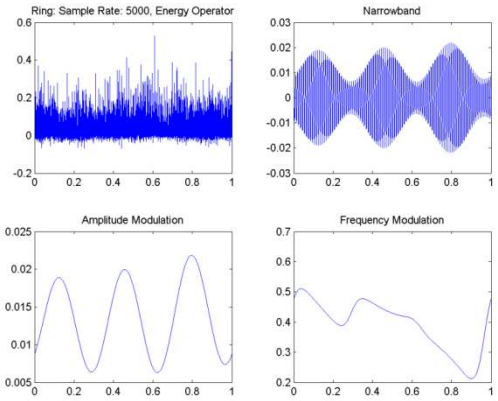

Figure 5.7. Ring gear

5.3.6 Bearing Analysis

Bearing analysis was based on the envelop algorithm. The raw data was heterodyned to the base band; the carrier frequency is based on the resonance of the bearing structure. The energy spectrum (units of G's) is taken on the base band signal, where the modulation rate is taken as the bearing fault frequency [28].

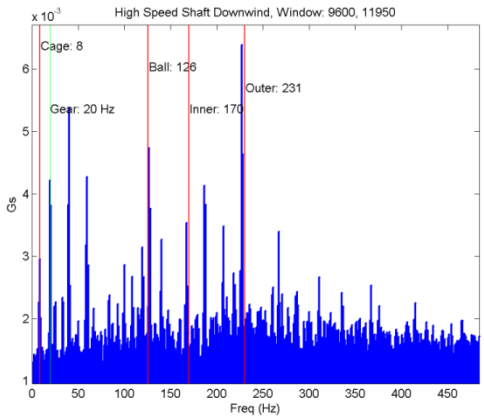

Figure 5.8a. High speed shaft, downwind side

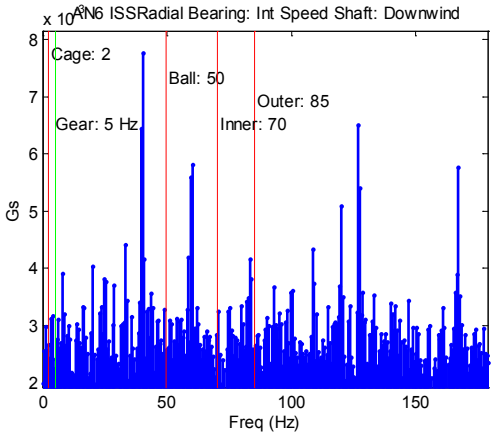

Figure 5.8b. Intermediate speed shaft downwind side

It was found (Figures 5.8a, 5.8b, and 5.9) that most bearings had some level of damage. The analysis could not find direct evidence of a fault on the planet bearing. While some attempt was made in optimizing the window frequency using spectral kurtosis, it's likely that the lack of performance was due to poor window selection in the envelope analysis.

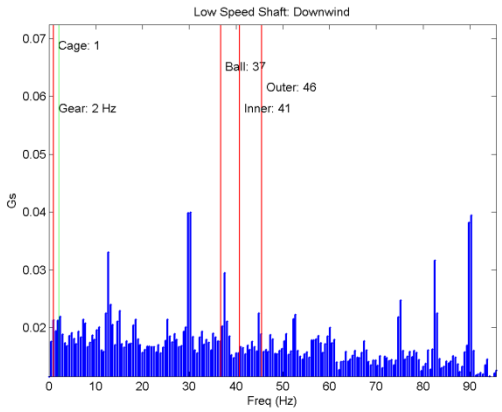

Figure 5.9. Low speed shaft downwind side

5.4 Discussion

The lack of fleet data forces one into an analysis of individual algorithm waveforms. It is desirable to have vibration analysis off of a fleet of gearboxes to compare the test gearbox against. Additionally, it is desirable to have at least six months of condition indicator data on a gearbox to observe (or capture) degradation. Because of the lack of fleet data or any appreciable history, analysis was based on a "by eye" analysis. It is likely that better performance could be gained with more experience on this gearbox, or in comparison of waveforms with a known, good gearbox. The algorithms, based on the TSA, appear to find faults that were consistent with [26]. In fact, most analysis did show a response indicative of a wear/fault. Because there seemed to be no broken/soft tooth, the residual analysis was nominal on all gears. It was noted that

cepstrum analysis showed numerous harmonics (indicative of fault), but because the cepstrum is not a synchronous analysis, it was difficult to assign a particular frequency with a component.

In general, the analysis methodology seemed appropriate for wind turbines, and has the advantage of being relatively simple to implement in an autonomous manner, e.g., the generation of statistics from the analysis waveforms, which could be trended or a threshold set to indicate when a maintenance action needs to be performed. This lends credence that aerospace gearbox analysis techniques are appropriate for wind turbine gearbox analysis.

6 Review and Application of Methods and Algorithms in Wind Turbine Gearbox Fault Detection

David Siegel*, Wenyu Zhao, Edzel Lapira, Mohammed AbuAli, and Jay Lee
Center for Intelligent Maintenance Systems, University of Cincinnati
*Corresponding Author Email: siegeldn@mail.uc.edu

6.1 Introduction

This chapter contains a description of the method and algorithms used by the research team at the University of Cincinnati – Center for Intelligent Maintenance Systems (IMS) for the Round Robin study. The outline of this chapter is as follows: Section 6.2 provides an overview of the signal processing and feature extraction methods evaluated in the study by the IMS research team, followed by more specific details for each method. Section 6.3 provides a summary of the results for each evaluated method along with some additional discussion. The final summary table in Section 6.3 also provides an indication of which analysis methods were considered prior to and after the failure report was released. Lastly, conclusions and suggestions for future work are provided in Section 6.4.

6.2 Signal Processing and Feature Extraction Methods

An overview of the signal processing methods evaluated during this study is provided in Table 6.1, along with the advantages and disadvantages of each method. Despite its simplicity, the use of analyzing the vibration data in the frequency domain does have its merits for detecting gear related problems. Gear mesh frequencies and associated sidebands can be identified in the vibration spectrum and various vibration indicators or features can be calculated in the frequency domain [27]. The real cepstrum is particularly useful for analyzing a family of harmonics, which has application for gear related faults [24]. A series of sidebands can be analyzed by calculating the cepstrum and comparing them to the baseline condition; the magnitude of the peaks compared to that baseline can be used to diagnose the health condition for each gear. The calculation of the real cepstrum can also be performed from the frequency spectrum; this was a useful asset for this analysis since only a baseline frequency spectrum was provided.

For bearing condition monitoring, the most established method in the literature is bearing envelope analysis, also called the high frequency resonance technique [24]. The general concept is that a spall or damage on the bearing race or rolling element causes a series of impacts that excite the structural resonances of the mechanical system; this causes an amplitude modulation effect in which the carrier frequency is the resonance frequency and the bearing fault frequency is the modulation frequency. By filtering around the excited resonance and performing the demodulation, the envelope spectrum, along with the calculated fault frequencies, can be used to diagnose the bearing condition. A more detailed description of bearing faults, the bearing envelope analysis method, and methods for selecting the band-pass filter frequency range are provided in [24]. Despite bearing envelope analysis being a very effective technique; the method usually requires a high sampling rate since the excited resonance can occur at frequencies above 10 KHz for many applications. The selection of the band-pass filter is also a crucial aspect in the method and a current area of research [24]. The use of spectral kurtosis filtering can be used to select the filter band for the bearing envelope analysis method, as well as for calculating indicators for the overall health condition of the monitored gearbox [28].

Time synchronous averaging represents one of the most established signal processing techniques for gear condition monitoring. The method is ideally suited for the processing of gear vibration, since the synchronous averaging method enhances and separates the periodic gear vibration from the cyclostationary vibration of rolling element bearings. Additional processing methods can be performed on the time synchronous average signal, including the gear residual signal and the amplitude and phase modulation functions [18]. For planetary gearboxes, due to the relative motion of the planet gears and the multiple contact points between each planet gear meshing with the sun and ring gear, the traditional synchronous averaging algorithm is not able to isolate the individual vibration for each planet gear or the sun gear. Specific algorithms for performing synchronous averaging for planetary gears are also evaluated in this work; the method suggested by McFadden [29] is used in this study. This specific algorithm for planetary gearboxes does have some potential drawbacks; in particular, the long data acquisition period needed to perform the calculation procedure is a major challenge for implementing this method.

Table 6.1. Summary of evaluated methods – advantages and disadvantages

#	Technique	Advantages	Disadvantages
1	Frequency Domain	Sidebands around gear mesh frequencies can be identified and provide a relatively simple method for extracting gear condition indicators without a tachometer signal [27].	Signal to noise ratio is not enhanced by using a tachometer signal, which can help reduce the vibration from other sources not synchronous with the shaft and gear components.
2	Cepstrum	Convenient method for extracting information from a family of harmonics; ideally suited for extracting gear condition indicators due to sidebands and amplitude modulation [24].	Family of harmonics could be related to shaft problems such as imbalance or misalignment and may not be due to a gear related fault; requires a baseline for comparing the cepstrum and determining whether there is a significant change.
3	Bearing Envelope Analysis	Most established method for bearing diagnosis in the literature [28]; is more suited for detecting incipient bearing spalls.	Selection of the demodulation band is not trivial and still an area of active research [28], also could require a higher sampling rate depending on the excited system resonance.
4	Spectral Kurtosis Filtering	Filters signal based on the frequency band that is most impulsive [30]; can be used to calculate features on the filtered signal and to select an appropriate filter in envelope analysis.	Extended spalls or faults might not be impulsive, and hence, this affects the ability of this method to detect these types of faults.
5	Time Synchronous Averaging	Enhances vibration synchronous with the shaft, residual signal can look for abnormalities in the regular meshing pattern, demodulation around gear mesh frequency can detect a soft tooth by analyzing amplitude and phase modulation signals [18].	Requires accurate tachometer signal for performing the synchronous averaging, might require a long acquisition time for low speed shafts due to the low rotational speed and collecting an ensemble of readings for averaging.
6	Planet Separation Method	Specific algorithm designed for performing synchronous averaging for planetary gearboxes [29], provides a way to individually analyze the health condition of the multiple planet gears and the sun gear.	Requires very long acquisition time, collecting enough rotations to perform the averaging; also requires a tachometer for aligning the data with respect to the carrier rotation.

6.2.1 Frequency Domain Methods

For rotating machinery, gaining an understanding of the time domain and frequency domain signature is a typical first approach prior to applying more advanced processing methods. For meshing gears in particular, there are signature frequencies related to the gear mesh frequencies and sidebands; the use of the Fast Fourier Transform (FFT) and an analysis of the gear mesh frequency peaks and sidebands can provide an initial evaluation of the gear wheel health condition. Gears in a nominal healthy or degraded condition typically have a similar gear mesh frequency peak; however, the magnitude of the sidebands is more useful for assessing the gear health condition. In addition, the spacing of the sidebands can indicate which particular shaft and associated gear wheel is degraded [27]. An example vibration spectrum from this study is provided in Figure 6.1, in this example one can clearly identify the gear mesh frequency peak (for the high speed shaft gear and pinion) at 662 Hz in the vibration spectrum for the gearbox in the nominal baseline condition. The gear mesh frequency peak is also present in the vibration spectrum of the degraded gearbox; however, there are very large sidebands at 631 Hz and 691 Hz for the degraded gearbox. The sidebands are spaced at 30 Hz, which is the high speed shaft

rotational speed; this initial example provides some evidence that the high speed pinion is degraded due to the sidebands observed in the vibration spectrum.

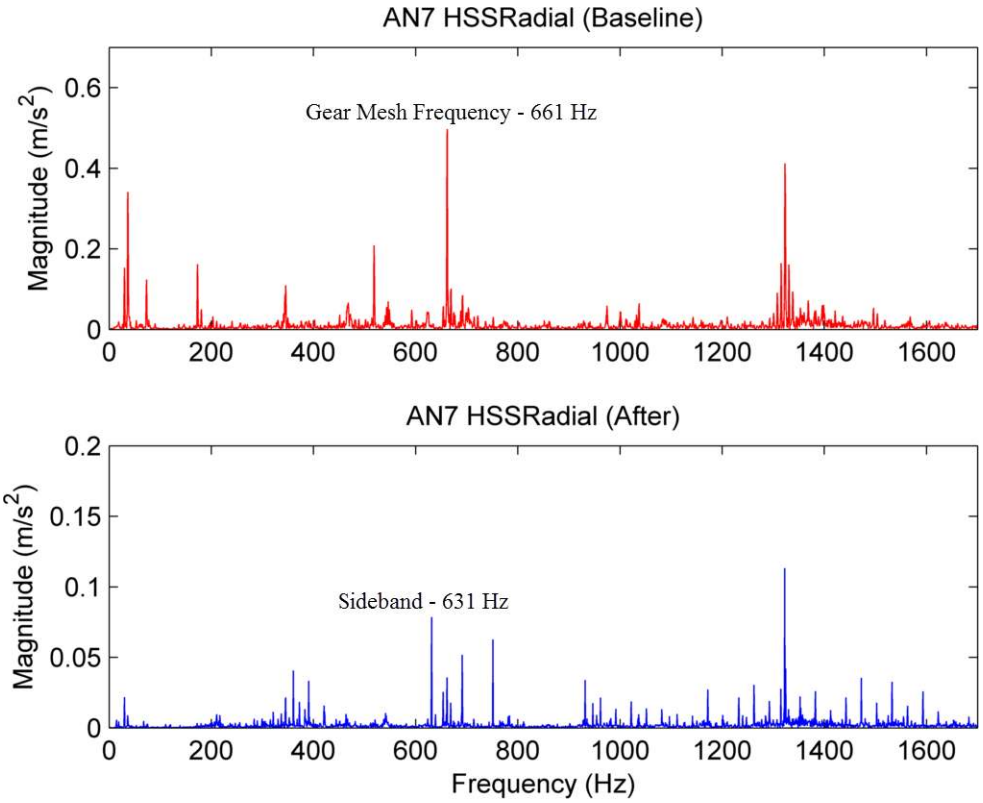

Figure 6.1. Vibration spectrum - Case C: top plot - AN7 baseline; bottom plot - AN7 degraded gearbox

To further quantify these observations from the vibration spectrum; a set of gear wheel vibration features was extracted using the baseline spectrum and the spectrum from the degraded gearbox. To quantify the magnitude of the sidebands, the sideband level was calculated using Equation (6). In this calculation, SBL_a stands for the sideband level, Sb_{a1} is the magnitude of the lower sideband and SB_{a2} is the magnitude of the upper sideband. In addition, a sideband ratio was also calculated using Equation (7); this normalizes the sideband ratio by the gear mesh frequency peak. Prior work by Combet et al. [31] has shown this sideband ratio feature to be an effective metric to quantify gear health since it is less susceptible to load fluctuations due to the sideband magnitude being divided by the gear mesh frequency peak [31]. Table 6.2 provides a listing of the frequency domain gear features; a total of 16 were calculated. For each respective gear, four features were calculated. The sideband ratio and sideband level were calculated for the gear mesh frequency and the first harmonic of the gear mesh frequency. Also, the frequency domain gear features were only calculated for the four gears on the parallel gearbox stage; the analysis of the sideband patterns for the planetary gearbox is quite complicated and more advanced techniques were evaluated for the planetary gearbox.

Table 6.2. Frequency domain gear features

Signal	Feature Name	# of Features
AN5	Side Band Ratio and Sideband level for Intermediate Speed Shaft Gear	4
AN6	Side Band Ratio and Sideband level for Intermediate Speed Shaft Pinion and High Speed Shaft Gear	8
AN7	Side Band Ratio and Sideband level for High Speed Shaft Pinion	4

$$\mathrm{SBL}_a = \mathrm{SB}_{a1} + \mathrm{SB}_{a2} \tag{6}$$

$$SBR_a = \frac{SB_{a1} + SB_{a2}}{GMF_{peak}} \tag{7}$$

Example results using the frequency domain gear features are provided in Figure 6.2. In this example, the sideband ratio for the intermediate speed shaft pinion and the high speed shaft pinion are much larger in magnitude for the degraded gearbox when compared to the gearbox at the baseline condition. The sideband ratio for the high speed shaft gear is very similar to the baseline level and would imply that this particular gear is normal using this frequency domain feature. It should be noted in the failure report that the high speed shaft gear set was observed to have severe scuffing on both gears. In addition, the failure study reported that the intermediate speed shaft gear set had severe fretting corrosion and scuffing for both gears as well. From the frequency domain method, there is a strong indication that there is damage on the high speed shaft pinion. There also is an indication, but with lower confidence, of damage on the intermediate speed shaft pinion. However, there is little evidence from the frequency domain gear features of damage on the high speed shaft gear or the intermediate speed shaft gear despite the reported damage in the failure report. Other processing algorithms were used to further investigate the health condition of the parallel stage gear wheels, as well as the other bearing and gear components. If several processing methods provide evidence of a degraded component, this can provide an increased level of confidence that the component is damaged.

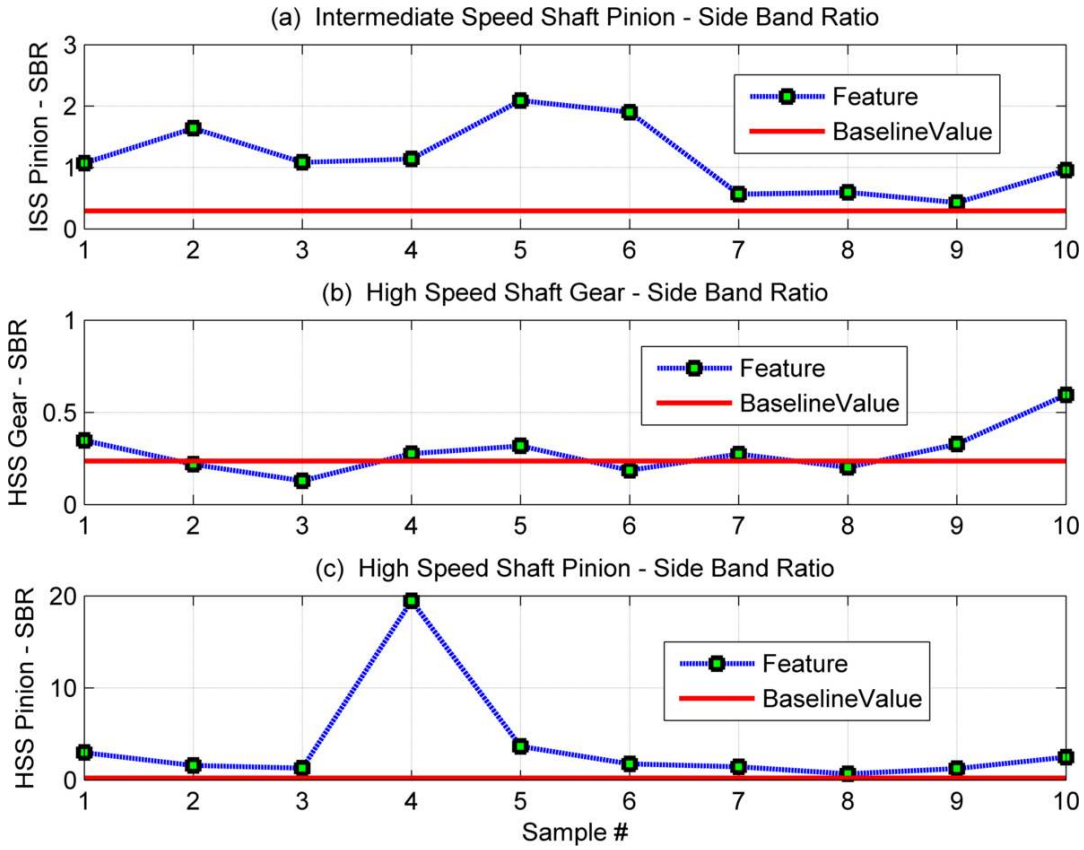

Figure 6.2. Sideband ratio gear features – Case C: (a) Low speed shaft pinion; (b) High speed shaft gear; (c) High speed shaft pinion

6.2.2 Cepstrum Processing Method

The real cepstrum provides a processing method that is ideally suited for analyzing a family of harmonics, in a much more consolidated way than the frequency domain representation. For calculating the real cepstrum, the inverse Fourier Transform is applied to the logarithm of the power spectrum, as shown in Equation (8), where $C_{xx}(t)$ is the real cepstrum and A(f) is the frequency spectrum [24]. For mechanical systems and gears in particular, the cepstrum provides a convenient way of analyzing a series of sidebands that are spaced at a given shaft speed; comparing the cepstrum from a baseline and current state can be used to infer the health condition of each gear. The example cepstrum result in Figure 6.3 further illustrates this aspect, in which the cepstrum from the baseline gearbox is compared to the degraded gearbox. In both instances, one can observe a peak in the cepstrum at 0.133s, which corresponds to 7.5 Hz and the intermediate speed shaft. This implies that a family of harmonics spaced at 7.5 Hz was always present in this gearbox. However, an additional peak at 0.0325s, which corresponds to 30 Hz and the high speed shaft, can be seen in the cepstrum of the degraded gearbox. This additional set of harmonics spaced at 30 Hz for the degraded gearbox provides evidence that the gear wheel on the high speed shaft (high speed shaft pinion) is degraded and is responsible for this noticeable change in the cepstrum.

$$C_{xx}(\tau) = \Im^{-1}\left[2\ln(A(f))\right] \tag{8}$$

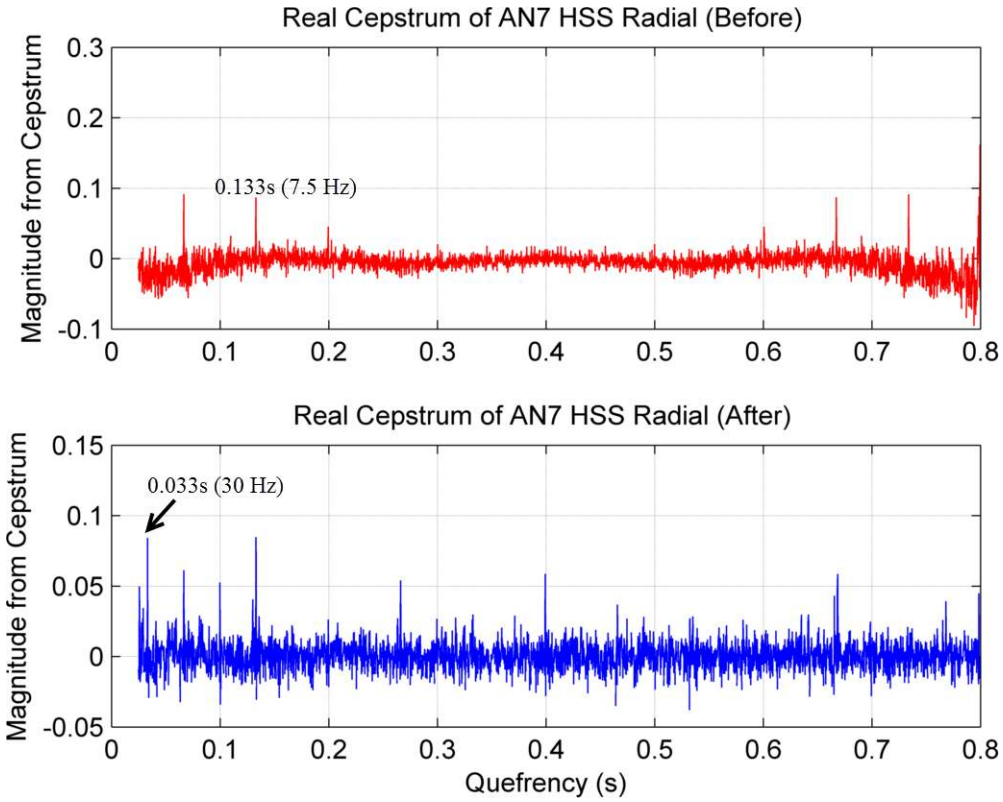

Figure 6.3. Real cepstrum - Case C: top plot - AN7 baseline; bottom plot - AN7 degraded gearbox

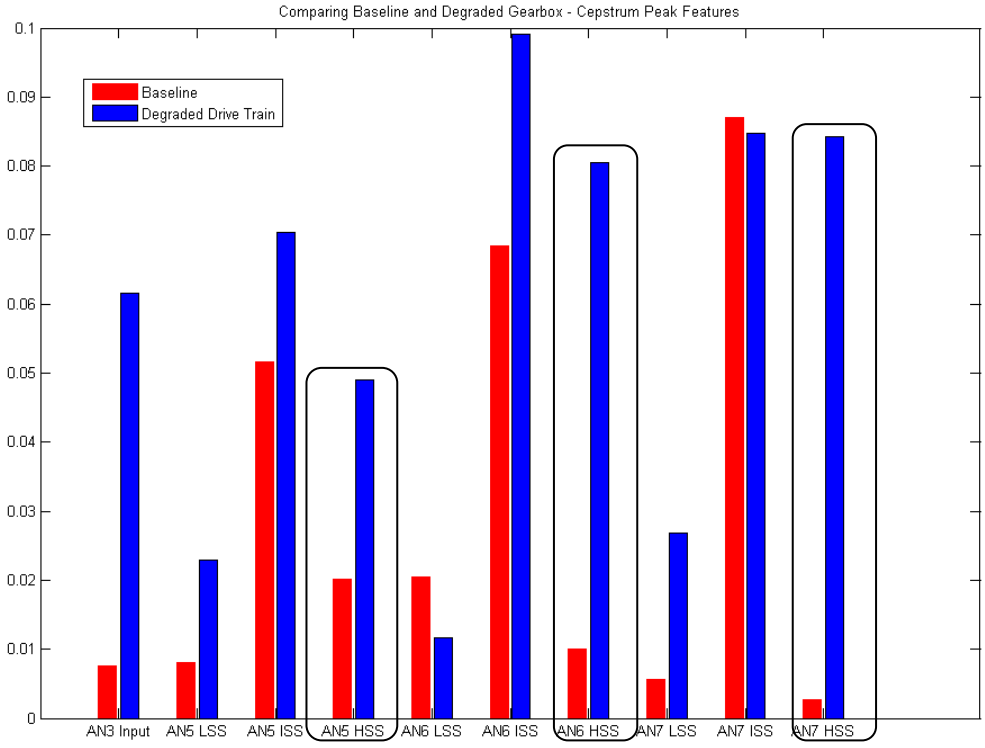

Figure 6.4. Cepstrum peak features from Case C: blue – baseline; red - degraded gearbox

Additional vibration features were extracted from the cepstrum at the corresponding shafts, using data from both the baseline gearbox and the degraded gearbox. Example results from the cepstrum features are provided in Figure 6.4, in which several peaks in the cepstrum are noticeably larger in magnitude when comparing the degraded gearbox to the baseline gearbox. The cepstrum peak related to the high speed shaft pinion is highlighted, since this feature was dramatically larger in magnitude for the degraded gearbox. This provides an additional set of evidence that the high speed shaft pinion is damaged. To further quantify the difference in the cepstrum features from the baseline state, and diagnose which gear in a meshing pair had the most severe condition, a cepstrum based health indicator using Equation (9) was calculated [32]. In this calculation, d(t) is the cepstrum health indicator, $A_p(t)$ is the cepstrum peak for the input gear at time t, $A_r(t)$ is the cepstrum peak for the output gear at time t, $A_p(0)$ is the cepstrum baseline peak for the input gear, and $A_r(0)$ is the cepstrum baseline peak for the output gear. For a monitored system, this health indicator would be zero in the baseline condition, close to -1, if the output gear is degraded, and close to 1 if the input gear is degraded. Figure 6.5 provides a result from this health indicator calculation, for the high speed shaft gear and pinion meshing pair. The health indicator is near -1 for all 10 data samples, which indicates that the high speed pinion is the gear with the more severe level of damage, according to this metric. This agrees with the previous result from the sideband features in the vibration spectrum, in which there was evidence of damage on the high speed shaft pinion, but little evidence of damage on the high speed shaft gear.

$$d(t) = \frac{A_p(t)/A_p(0) - A_r(t)/A_r(0)}{A_p(t)/A_p(0) + A_r(t)/A_r(0)} \tag{9}$$

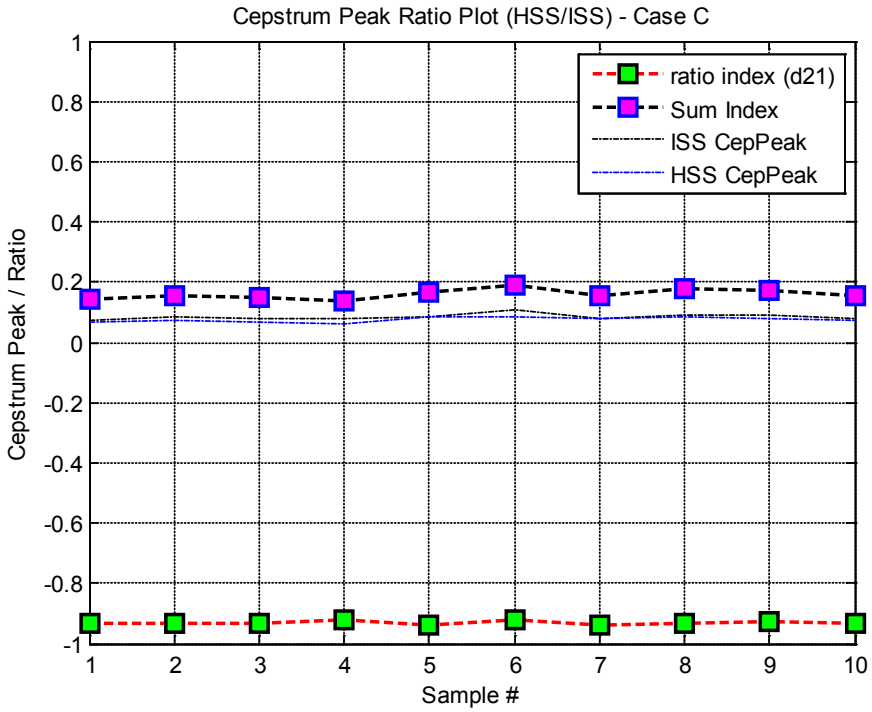

Figure 6.5. Cepstrum health Indicator for Case C calculated for high speed shaft gear and pinion

6.2.3 Bearing Envelope Analysis

Although the area of bearing condition monitoring has been an area of research for quite some time, with new algorithms and methods proposed each year; the bearing envelope analysis method remains one of the more effective techniques for bearing condition monitoring [28]. A more detailed description of bearing envelope analysis can be found in prior work [28, 33], therefore, this study simply provides a brief review of the method and highlights the results for this study. A flow chart that shows the steps in this algorithm is provided in Figure 6.6, in which the initial step is to band pass filter around an excited natural frequency. The selection of the band-pass filter center frequency and bandwidth is an important step and also a current area of research [28]. In this study, the filter parameters were selected by inspection of the frequency domain spectrum for the respective accelerometers, but alternative methods could also be considered. After filtering the signal, the Hilbert Transform is used to extract the envelope signal, which is further analyzed in the frequency domain. For a bearing with damage on the rolling element or bearing races, the bearing fault frequency peaks are usually much easier to distinguish in the envelope spectrum when compared to the frequency spectrum.

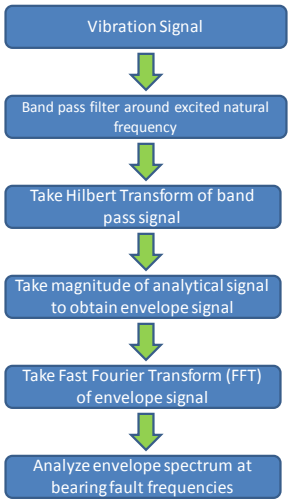

Figure 6.6. Bearing envelope analysis flow chart

For performing envelope analysis in this Round Robin study, a band pass filter centered at 10,000 Hz, with a bandwidth of 1000 Hz was used, with the exception of accelerometer AN10 in which two different frequency bands were evaluated. Sample results from this method are provided in Figure 6.7, in which the envelope spectrum is shown for accelerometer AN6 and AN7. The envelope spectrum for AN6 shows noticeable peaks at 73 Hz and 345 Hz. The peak at 73 Hz corresponds to the ball pass frequency inner race (BPFI) for the intermediate shaft upwind bearing. The failure report confirms the inner race damage for this particular intermediate shaft bearing. The peak at 345 Hz is very close to the calculated BPFI frequency (336 Hz) for the high speed shaft downwind bearing; the failure report confirms that this bearing had inner race damage, with overheating as the mode. The envelope spectrum for AN7 also clearly shows a peak at the BPFI frequency (345 Hz) for the high speed shaft downwind bearing. The envelope spectrum for accelerometer AN10 in Figure 6.8 is provided using two different band pass filter ranges; the first one is at a high frequency from 9,500 Hz - 10,500 Hz and the later is from a frequency range of 4,000 Hz – 6,000 Hz. The results shown in Figure 6.8 (a) clearly show a peak at the BPFO and its first harmonic for the intermediate speed shaft downwind bearing; the failure report confirms that there was an outer race damage on this

bearing. The envelope spectrum in Figure 6.8 (b) shows a peak at the BPFO for the planet carrier upwind bearing; this bearing also had outer race damage according to the failure report. Using a filter from 9,500 Hz-10,500 Hz would have resulted in a missed detection for the planet carrier upwind bearing. Using the frequency band from 4000 Hz - 6000 Hz resulted in a detection of an outer race fault on the planet carrier bearing; however, it provided a less clear detection for the ISS downwind bearing, in which only the first harmonic of the BPFO could be identified.

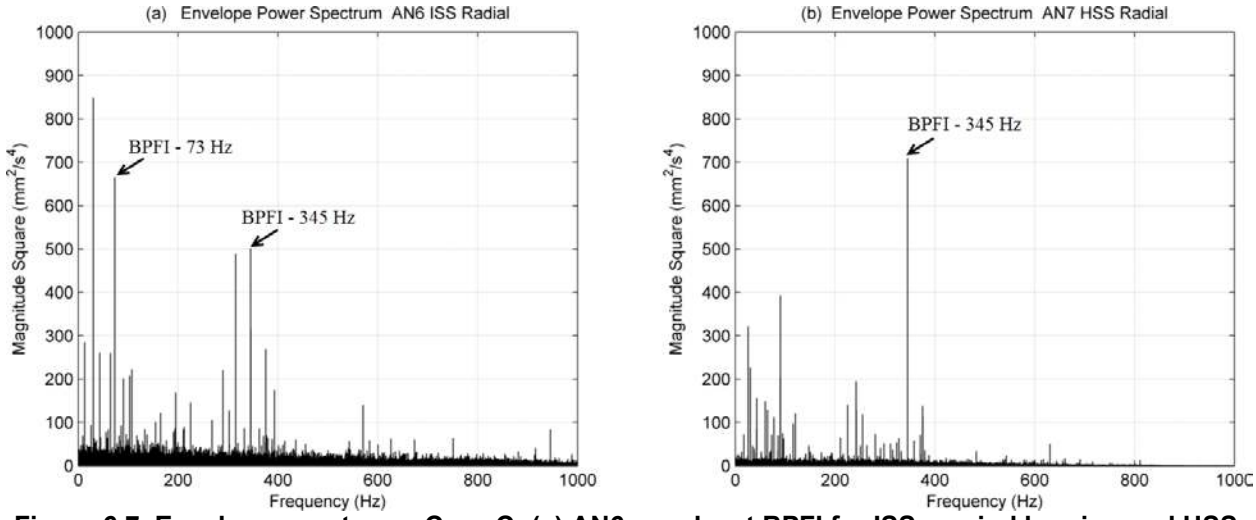

Figure 6.7. Envelope spectrum - Case C: (a) AN6 - peaks at BPFI for ISS upwind bearing and HSS downwind bearing; (b) AN7 - BPFI peak for HSS downwind bearing

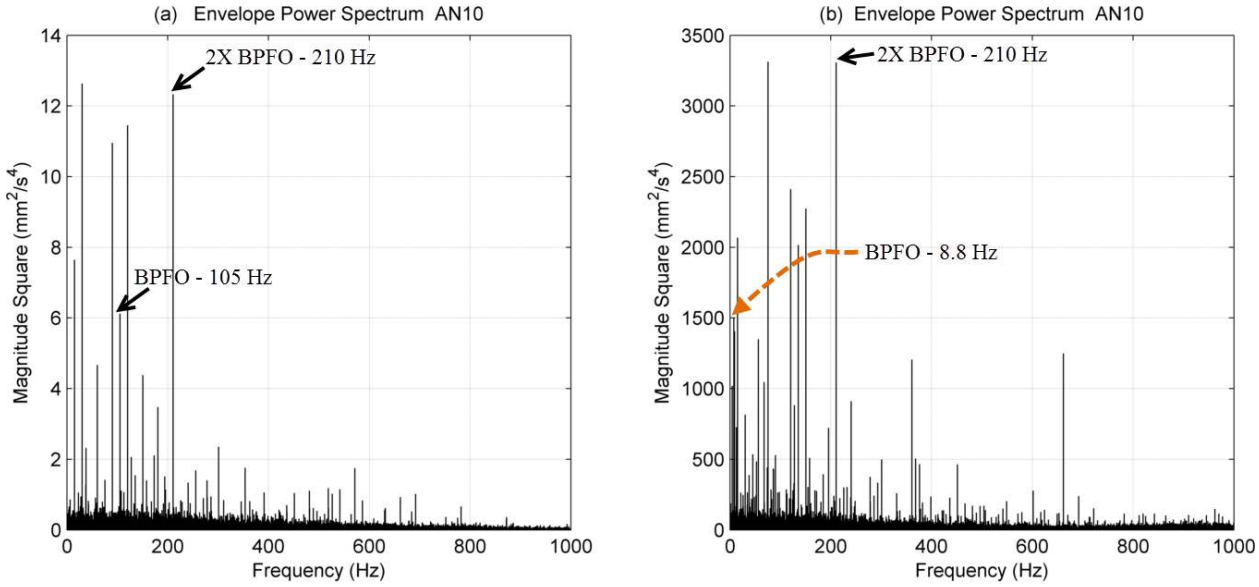

Figure 6.8. Envelope spectrum accelerometer AN10 - Case C: (a) band-pass filter from 9500 Hz - 10,500 Hz, peaks at BPFO and 2X BPFO for ISS downwind bearing; (b) band pass filter from 4000 Hz - 6000 Hz, peak at BPFO for planet carrier upwind bearing and also peak at 2X BPFO for ISS downwind bearing

6.2.4 Spectral Kurtosis Filtering

For condition monitoring of mechanical systems, the vibration signals for damaged gear and bearing components typically display an impulsive signature. Detecting that impulsive signature is not a trivial task since the signature could be masked by other sources of vibration. Techniques and filtering methods based on spectral kurtosis are aimed at finding the optimal frequency band for recovering the impulsive fault signature that could be hidden in the raw vibration waveform. A brief review of the calculation procedure and the results of this study are provided, and the interested reader is referred to the work by Antoni et al [30] and Combet et al [34] for a more detailed discussion on the use of spectral kurtosis for filtering vibration signals. The initial step in this algorithm is to calculate the short time Fourier Transform of the vibration signal, denoted by H(t,f). Equation (10) indicates that the average value of the fourth power of H(t,f) is divided by the mean square value of H(t,f), which provides a kurtosis value as a function of frequency. The Wiener filter is constructed using the kurtosis values for each frequency bin, as shown in Equation (11); the frequency bin is only included if the kurtosis value is above a statistical threshold at a given confidence level [30]. The Wiener filter is then multiplied by the frequency domain representation of the original signal, X(f), and the result is transformed back to the time domain as indicated in Equation (12). The advantage of this method is that the signal is filtered without any a priori knowledge of which frequency band to filter in, and instead is based on which frequency band is most impulsive.

$$K_r(f) = \frac{\left\langle H^4(t,f) \right\rangle}{\left\langle H^2(t,f) \right\rangle^2} - 2 \tag{10}$$

$$\hat{W}(f) = \begin{cases} \sqrt{K_r(f)} & \text{for } \mathrm{K_r}(f) > s_\alpha \\ 0 & \text{Otherwise} \end{cases} \tag{11}$$

$$y(t) = \Im^{-1}\left\{\hat{W}(f)X(f)\right\} \tag{12}$$

In this study, the filtering algorithm was used to process data for all 12 accelerometers using a block size of 256 data samples and an overlap of 80% when performing the short time Fourier Transform calculation. When applying this processing method, only high kurtosis values were observed for accelerometers AN3 and AN4; thus, the example results do not include the other accelerometers. An example result from the filtering method is provided in Figure 6.9 from accelerometer AN4, in which one can observe that the Wiener filter is focused on the high frequency content of the signal from approximately 8 KHz - 18 KHz. This implies that although the rotational frequencies of the carrier are quite low; structural resonances at a high frequency appear to be excited by defects and damage from the internal components within the planetary gearbox. Figure 6.9 illustrates how the impulsive signature is masked in the raw time signal, but is quite clear in the filtered signal; the raw signal has a kurtosis value of only 3.39 compared to a kurtosis value of 169 for the filtered signal. Further examination of the filtered signal shows a pattern that repeats for every 2 revolutions of the carrier. This periodic pattern in the filtered signal from accelerometer AN4 is shown in Figure 6.10. The high kurtosis value of the filtered signal, along with the periodic pattern that is related to the carrier rotation, and the location of the accelerometer each point to a problem with the internal components in the planetary gearbox. However, it was difficult to determine which gear or bearing component was the cause of this problem from the filtered signal and the envelope spectrum; a potential reason is that multiple

faults occurred in the planetary gearbox. The results from the failure report indicate that the ring gear and sun pinion both had scuffing and corrosion damage and the planet carrier's upwind bearing had damage on the outer race.

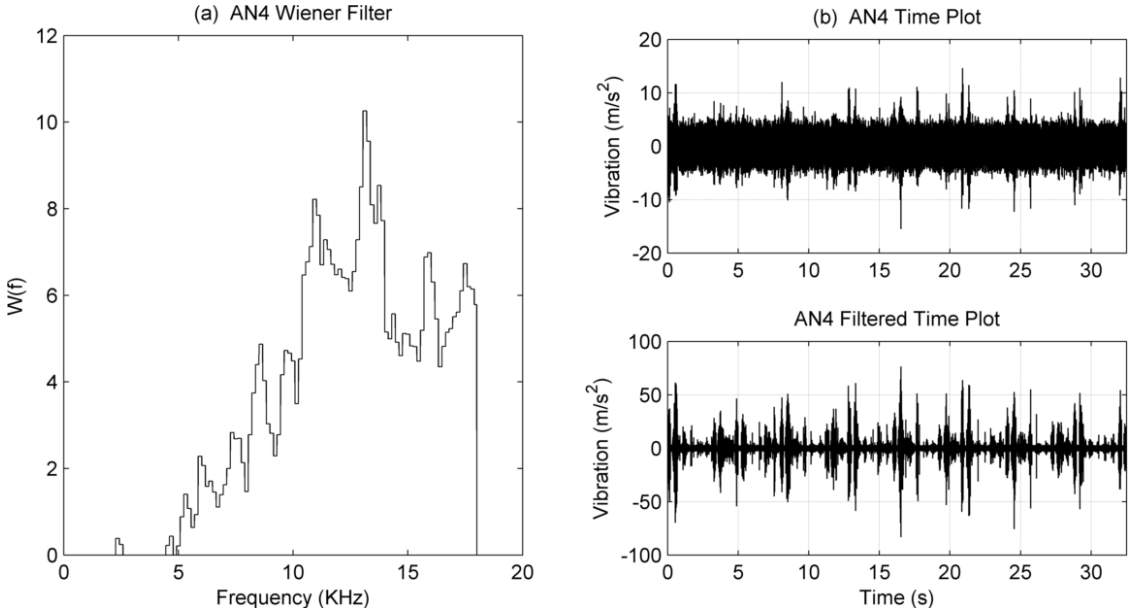

Figure 6.9. (a) Wiener filter based on spectral kurtosis; (b) raw and filtered AN4 accelerometer signal – Case A

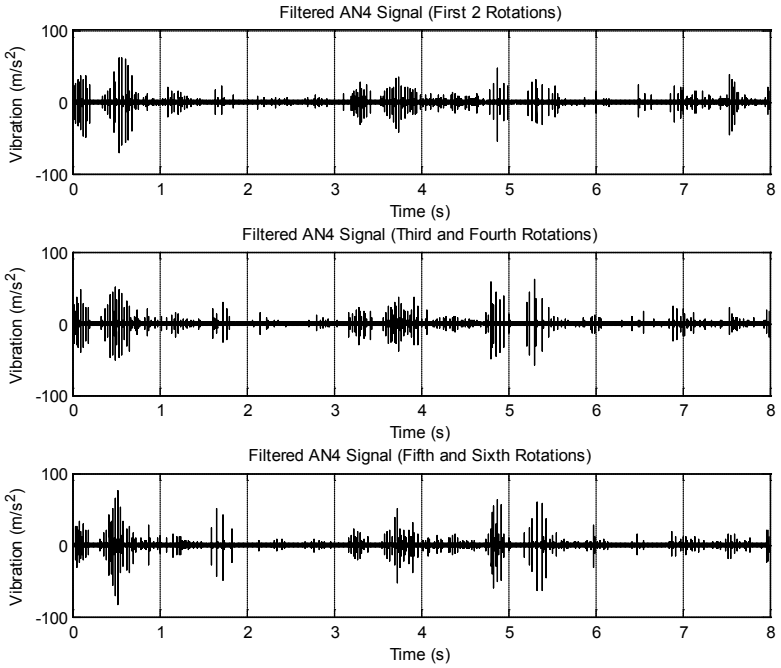

Figure 6.10. Filtered AN4 signal showing the periodic repetition based on 2 revolutions of the carrier – Case A

The results in Figures 6.9 and 6.10 and were from an example data file from Case A. The same filtering method was also applied to the remaining data files and the kurtosis feature from the filtered signal was stored. The results of the filtered kurtosis value are provided in Figure 6.11 and provide an interesting point for discussion. The kurtosis values were very large for files from Case A, with values above 50. It is also worth noting that the kurtosis values show a decreasing trend for the data files in Case A, in which each file was collected in sequential order. For Case B and Case C, the kurtosis values are quite low and in a normal range between 2 and 4. This implies that the fault signature was not present for accelerometer AN3 and AN4 for the operating conditions in Case B and Case C. This could imply that the operating conditions for Case A are more conducive for detecting this type of problem in the planetary gearbox. However, it is also worth noting that the data was collected in sequential order from Case A to Case C; this could imply that the vibration signature became less impulsive with the running time of the gearbox. Despite these discussion points for potential reasons as to why the signature was not present in all three operating conditions, the spectral kurtosis filtering method provided a very clear detection of a problem in the planetary gearbox for Case A, based on the very high kurtosis values. This provided enough confidence and evidence to believe that the internal components in the planetary gearbox stage were degraded.

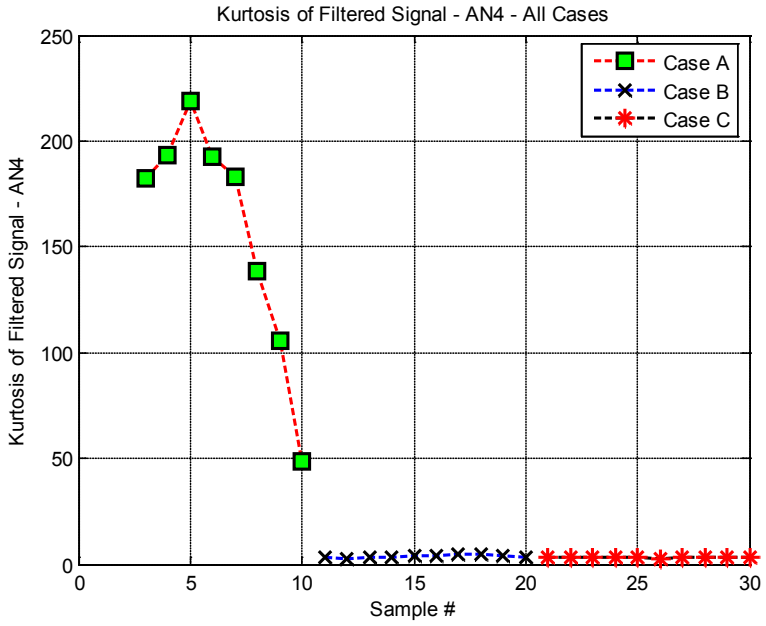

Figure 6.11. Kurtosis of filtered signal - shown for all 3 cases

6.2.5 Time Synchronous Averaging

This section discusses the results using time synchronous averaging for the parallel stage gears and the ring gear. The rationale for excluding the results for the planet and sun gears in this section is that a specific algorithm is needed for extracting the synchronous average signals for the individual planet and sun gears. The synchronous averaging algorithm and results for the plant and sun gears are provided in section 6.2.6. For all gears, the results from the residual signal, amplitude modulation signal, and the phase modulation signal are extracted and analyzed for determining the health condition of each gear.

The additional processing methods for the residual signal (section 6.2.5.1) and the amplitude and phase modulation signals (section 6.2.5.2), first require the extraction of the time synchronous average signal for each shaft. The time synchronous averaging algorithm requires a reference pulse train for aligning the data with respect to a given shaft, and ensemble averaging the signal over several rotations. In this study, a tachometer signal was not provided, but an alternative method was used for extracting a reference signal. The provided speed signal had a clear tone at the generator shaft speed (20 Hz or 30 Hz); band pass filtering in a range between 15 Hz – 35 Hz provided a way of extracting a pulse train from the speed signal. The filtered speed signal was used as a surrogate for the tachometer signal; alternative methods that use the gear mesh frequency peak for estimating a synthetic tachometer signal could also have been used [35]. With the necessary reference signal, the vibration signals could be aligned and ensemble averaged with respect to the carrier, low speed shaft, intermediate speed shaft, and the high speed shaft, using the established synchronous averaging methods. More specific details on the synchronous averaging method including the different interpolation methods; the frequency domain implementation can be found in [36]. In this study, a time domain interpolation method was used. From the provided vibration signals, accelerometer AN3 was used for calculating the time synchronous average signal for the carrier shaft, AN5 was used for the low speed shaft, AN6 was used for the intermediate speed shaft, and AN7 was used for the high speed shaft.

6.2.5.1 Gear Residual Signal

The extraction of the periodic vibration waveform using time synchronous averaging allows one to further analyze the vibration signature and meshing pattern for each gear. Departures of the regular meshing pattern could be indicative of a fault in the gear; the residual signal aims to remove the regular meshing pattern from the synchronous signal to further examine this aspect. The residual signal for a gear can be calculated by removing the shaft harmonics and the gear mesh frequency and harmonics from the time synchronous average signal [18]. Considering that the time synchronous average signal of the gear is aligned with the shaft, the signal is periodic and the filtering can be conveniently performed in the frequency domain and transformed back to the time domain. It is common to remove the first five shaft harmonics, the gear mesh frequency, and all of the gear mesh frequency harmonics when calculating the residual signal. Prior works from seeded fault studies have also shown the residual signal to be effective for detecting gear tooth pitting faults [37].

The time synchronous average signal and the residual signal are shown in Figure 6.12 for the high speed shaft pinion. The kurtosis value of the residual signal for this gear is quite low (2.34), and there appear to be no abnormalities that can be seen in the time averaged signal or the residual signal. However, previous results from the cepstrum and frequency domain methods indicated large sidebands and a significant problem with this high speed shaft pinion; these were also confirmed in the failure report study. Large sidebands are noticed in the frequency domain representation of the time synchronous average signal for the high speed shaft, which is provided in Figure 6.13. The gear mesh frequency peak (order 22) is lower in magnitude then a peak at one of the sidebands (order 23). The inability for the residual signal to detect this fault on the high speed shaft pinion highlights the importance of extracting multiple gear vibration features to have better coverage for the different failure modes.

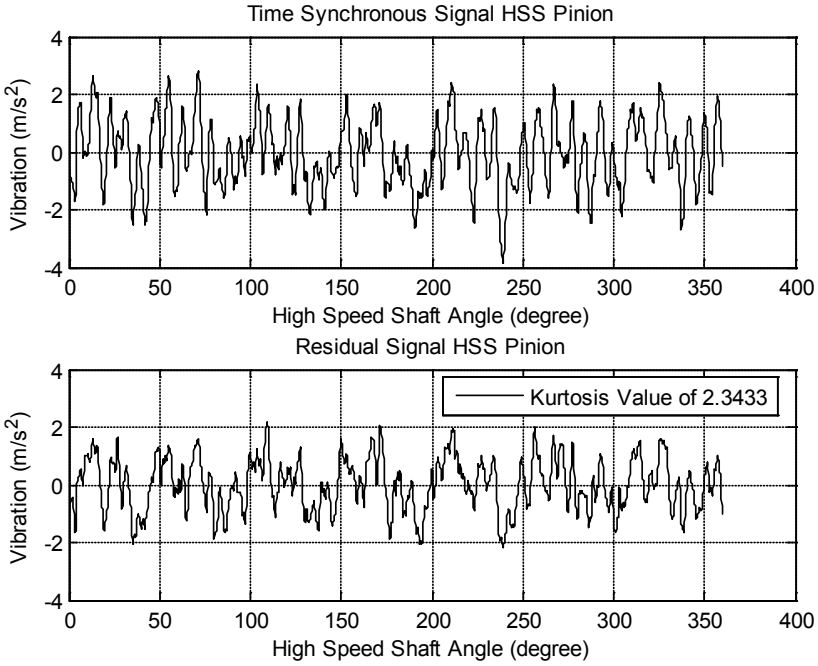

Figure 6.12. TSA signal and residual signal from accelerometer AN7 - Case C: top plot - TSA signal for high speed shaft pinion; bottom plot - residual signal for high speed shaft pinion

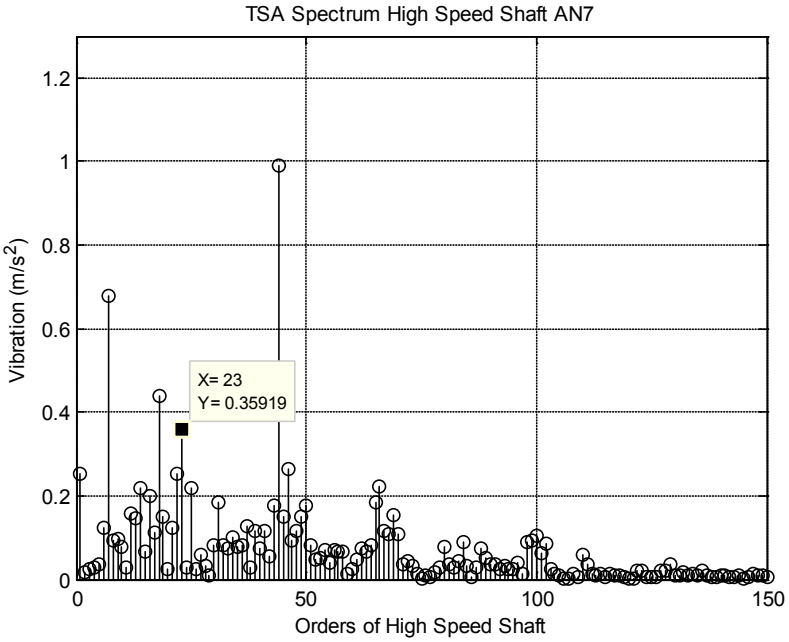

Figure 6.13. TSA vibration spectrum for accelerometer AN7 and high speed shaft – Case C

Another example residual signal is shown for the ring gear in Figure 6.14. The kurtosis value of the ring gear is also in a normal range (3.36), and there appears to be no abnormal patterns or an

indication of a fault in the time synchronous average signal or the residual signal for the ring gear. This is in sharp contrast to the results from the phase modulation function provided in the subsequent section, in which there is a clear indication of damage on the ring gear. The residual signal for the other parallel shaft gears also offers no indication of damage. This highlights that the residual signal was not the most appropriate algorithm for detecting the failure modes that were occurring on the parallel shaft gears and the ring gear.

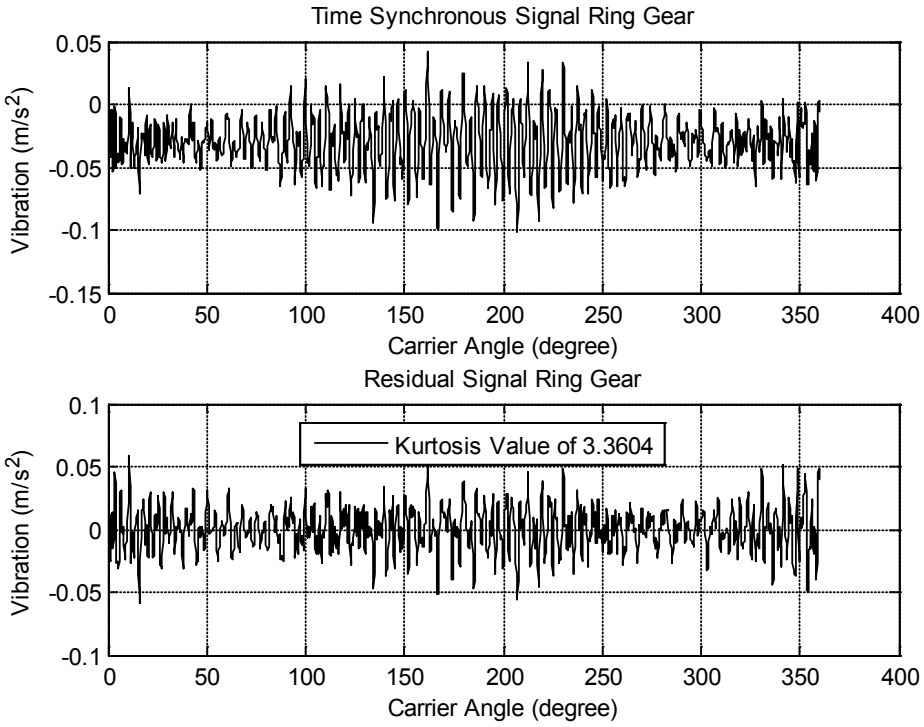

Figure 6.14. TSA signal and residual signal from accelerometer AN3 - Case C: top plot - TSA signal for ring gear; bottom plot - residual signal for ring gear

6.2.5.2 Amplitude and Phase Modulation

For detecting local defects, such as a fatigue crack in a gear wheel, the prior work done by McFadden [38] suggested an analysis of the amplitude and phase modulation function of the gear vibration. For performing this analysis, the synchronous average signal for a given shaft is performed. A band pass filter around a dominant gear mesh frequency is used and typically includes a number of sidebands around the gear mesh frequency peak. The Hilbert Transform is then performed on the filtered signal. The modulus and phase of the analytical signal provide the envelope and phase modulation functions, respectively. The amplitude and phase modulation functions were calculated for each gear wheel in this study. In addition, the kurtosis of the amplitude modulation function and the kurtosis of the derivative of the phase modulation function were also calculated to quantify the health condition of each gear. For the parallel shaft gears, the band pass filter included four sidebands, while the band pass filter for the ring gear included six sidebands. The accelerometer AN3 was also effectively down sampled to 200 Hz prior to extracting the synchronous average for the ring gear. Sample results for this method are provided in Figure 6.15, in which the amplitude and phase modulation functions are plotted for

the high speed shaft pinion. As one can observe, there are significant jumps in the phase modulation function for this gear and a high kurtosis value at 12.8. This would be an indication of a damage on the high speed shaft pinion. In addition, the amplitude modulation function is close to zero when these significant changes in phase occur. The phase modulation function for the high speed shaft gear had a moderate indication of a gear problem, with a kurtosis value of 5.2. However, there was no indication of a problem for the intermediate speed shaft gear or pinion. Another example is provided in Figure 6.16, in which the amplitude and phase modulation for the ring gear is provided. There appears to be a clear indication of a problem with the ring gear through visual observation of the amplitude and phase modulation signals. The phase modulation function, in particular, has a high kurtosis value and two noticeable shifts in phase, which indicate a damaged gear. In summary, the amplitude and phase modulation functions provide a strong indication of a problem with the ring gear and high speed shaft pinion, and a moderate indication for the high speed shaft gear; however, there was no indication of a problem for the other gear wheels.

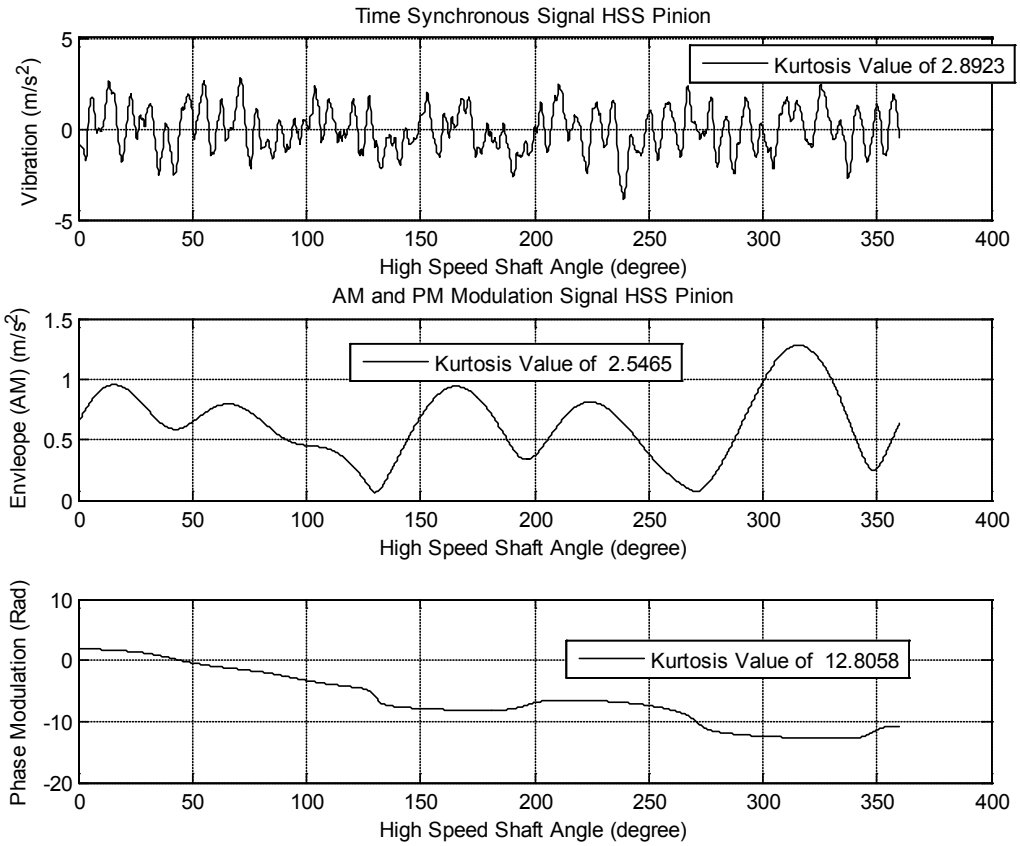

Figure 6.15. High speed pinion amplitude and phase modulation signal from accelerometer AN7 - Case C: top plot - Time Synchronous Average; middle plot - amplitude modulation signal; bottom plot - phase modulation signal

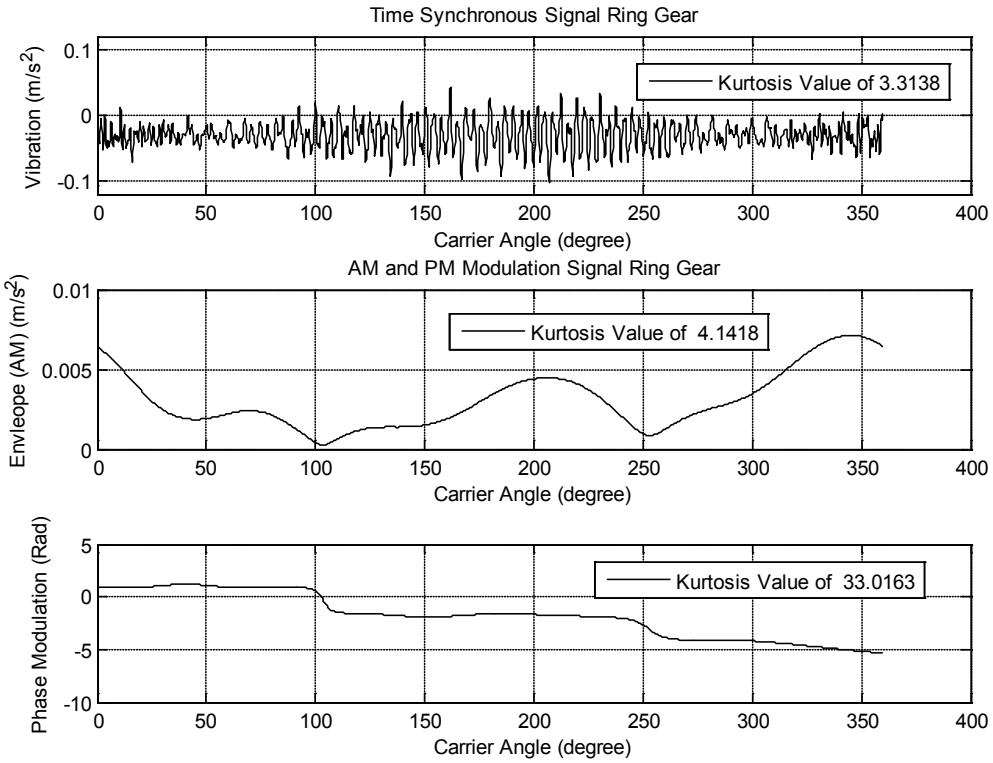

Figure 6.16. Ring gear amplitude and phase modulation signal from accelerometer AN3 - Case C: top plot – TSA; middle plot - amplitude modulation signal; bottom plot - phase modulation signal

6.2.6 Planet Separation Algorithm – Time Synchronous Averaging

Considering the relative motion of the planet gears and the multiple mesh points that occur because the planet gears mesh with the ring gear and sun gear simultaneously, it is necessary to use a specific algorithm for extracting the time synchronous average signal for the individual planet and sun gears. The algorithm considered in this study follows the algorithm proposed by McFadden et al [29]. There are variations of this algorithm, including the method proposed by researchers at the Defence Science and Technology Organisation (Australia) (DSTO) [39], as well as a version that uses multiple accelerometers on the planetary gearbox housing [40]. A flow chart of the algorithm is provided in Figure 6.17 and highlights the algorithm processing steps. The initial step is to calculate the time synchronous average signal with respect to the carrier rotation. The central idea in this method is to capture a meshing period of each tooth when the planet gear is in very close proximity to the fixed accelerometer on the gearbox housing. To accomplish this, it is necessary to know when the planet gear is passing by the fixed accelerometer. Considering the amplitude modulation effect from the increased vibration level, as each planet passes the fixed accelerometer; the narrow band envelope signal can be used to determine the number of planet passing instances. A window function is applied to the synchronous average signal when each planet gear passes for a short period of time; the short period of time is typically one to three gear mesh periods. Based on the number of teeth for each respective gear, a lookup table can be used to determine which tooth was meshing during that captured time signal. Then, it is stored in the proper location in the array. This capture of the windowed data is repeated for each tooth and requires several rotations of the carrier; the number

of rotations is equal to the reset time for the planet or sun gear. The result is an assembled vibration signal for each gear tooth. This process is repeated until several assembled signals can be constructed. Lastly, the constructed waveforms are ensemble averaged and this completes the process for extracting the time synchronous average

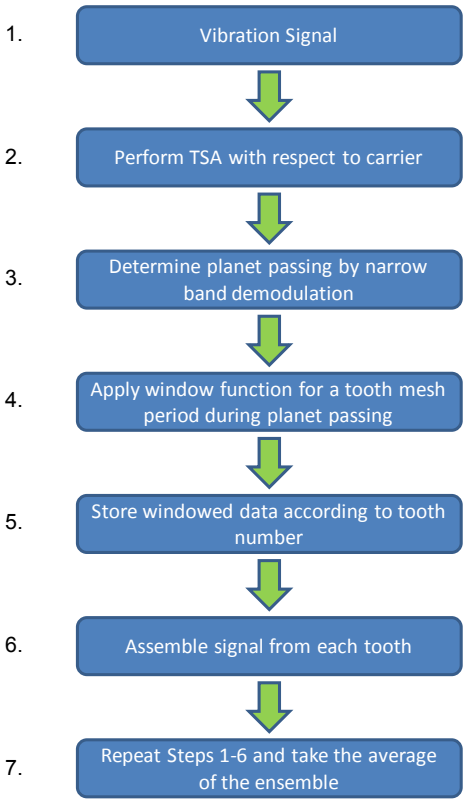

Figure 6.17. Flow chart for planet separation algorithm

For implementing this method, accelerometer AN3 was initially down sampled to a 200 Hz sampling rate. Considering the number of carrier rotations and time period needed by this algorithm, five files from Case C were concatenated and combined prior to applying the algorithm. A narrow band filter that included four sidebands around the gear mesh frequency was applied to the time synchronous average signal for the carrier. The envelope signal of the filtered signal is provided in Figure 6.18 and one can clearly observe noticeable peaks that are related to the planet passing the fixed accelerometer. The angular spacing of the peaks is approximately 120 degrees, which again confirms that these peaks correspond to the passing of the three planet gears. For capturing the meshing vibration during the planet passing, a Tukey window is used. An example Tukey window is shown in Figure 6.19, in which N_v was set to three to capture the vibration for three mesh periods. Using these parameters for the planet separation algorithm, the synchronous average signal was extracted for each planet gear and the sun gear; the number of averages was eight for the planet gears and 15 for the sun gear. The residual signals and amplitude and phase modulation signals were also calculated to further analyze the health condition of the gear wheels. For the amplitude and phase modulation signals, a band pass filter that included three sidebands was used.

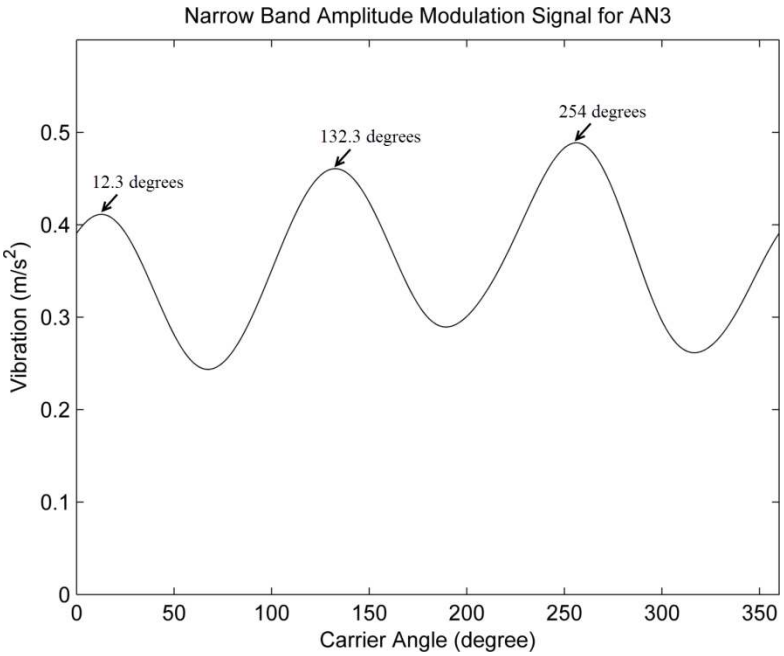

Figure 6.18. Narrow band amplitude modulation signal for determining planet passing - Case C

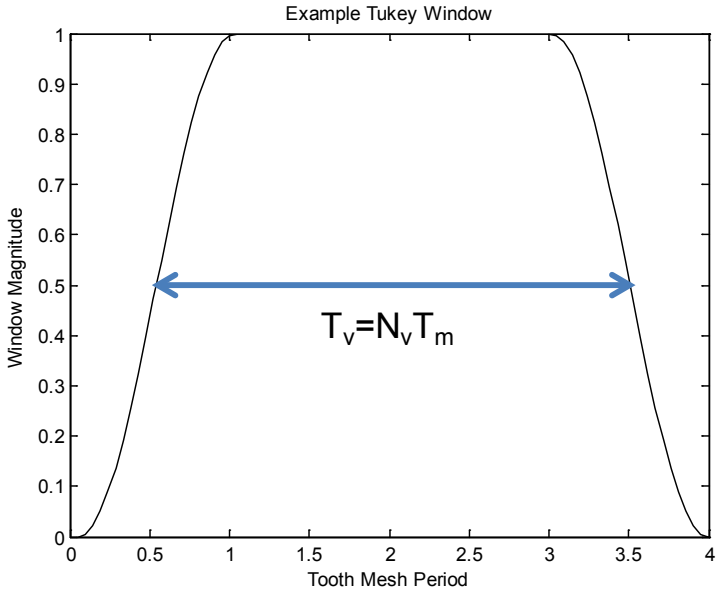

Figure 6.19. Example Tukey window used for planet separation algorithm - in this study, N_v was set to 3 to include 3 mesh periods

Sample results from the synchronous averaging signal and the residual signal are provided in Figure 6.20, in which the result is shown for one of the planet gears. In this example, the time synchronous average signal and the residual signal show no abnormal behavior for the planet gear; the failure report found no defects on any of the planet gears. The spectrum for the time

synchronous average signal for this planet gear is shown in Figure 6.21, and one can observe a clear gear mesh frequency peak at the 39th order. The sidebands are not large in magnitude in the spectrum and the planet gear appears to be in a health state from these data processing results. The other two planet gears were also considered to be in a normal condition based on similar results that were observed in their time synchronous average signal and residual signal.

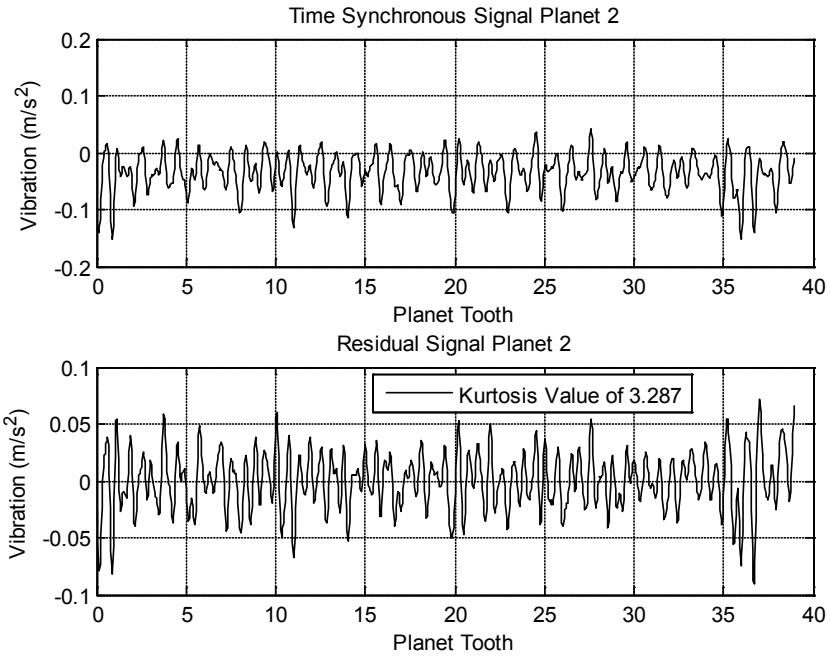

Figure 6.20. Top - TSA signal for Planet 2; bottom - residual signal for Planet 2 – Case C

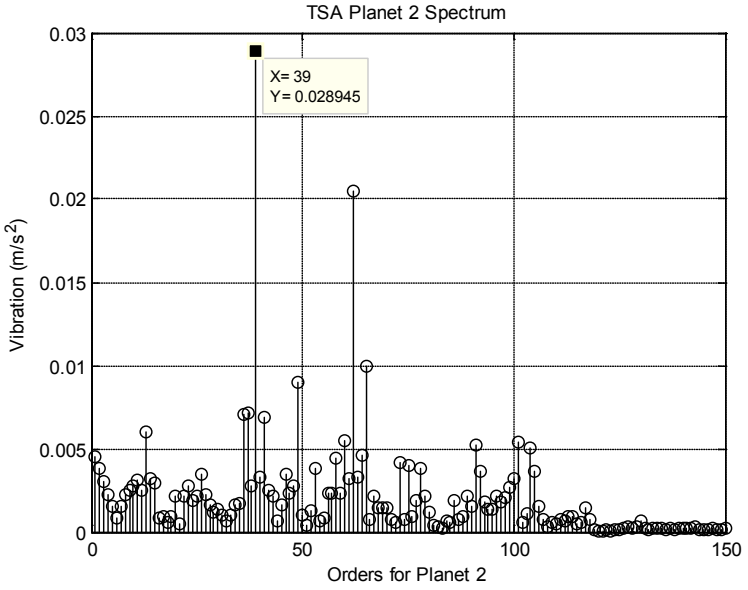

Figure 6.21. TSA vibration spectrum for Planet 2 – Case C

The time synchronous average signal and the residual signal analysis were also performed for the sun gear, with the results provided in Figure 6.22. In this example, the residual signal is providing a moderate indication of damage on the sun gear, with a kurtosis value of 5.36. The failure report confirms scuffing and fretting corrosion on the sun pinion. Additional narrowband amplitude modulation and phase modulation analysis was also performed on the time synchronous average signals for the planet gears and the sun gear. Although the residual signal provided an indication of damage on the sun gear, the amplitude and phase modulation signals did not provide any indication of damage on the sun gear. A sample result from one of the planet gears is provided in Figure 6.23. Both the amplitude and phase modulation signals do not indicate damage on this particular planet gear. The other two planet gears also did not have any indication of damage from the narrowband amplitude and phase modulation analysis; this is encouraging since the failure report did not find any damage on any of the three planet gears. For the sun gear, the residual signal provided a moderate indication of damage, but no damage was indicated from the amplitude and phase modulation signals.

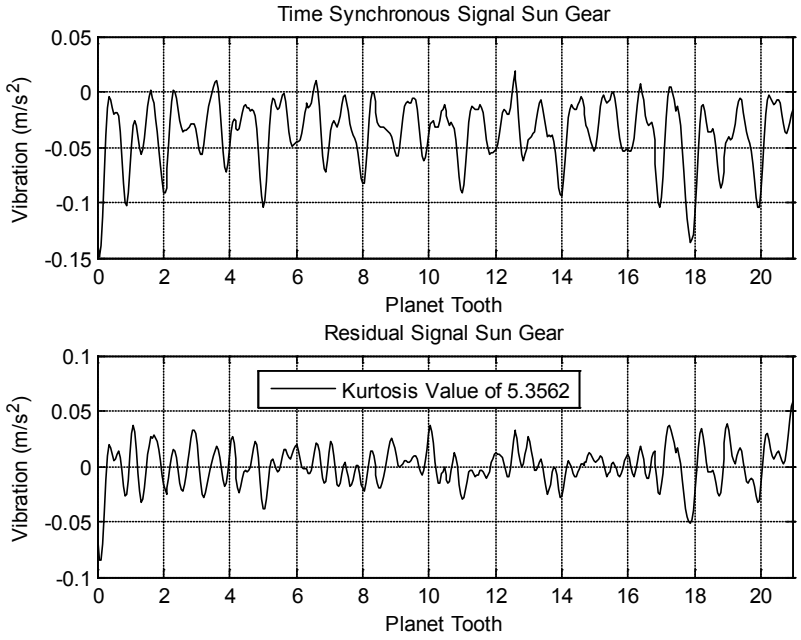

Figure 6.22. Top - TSA signal for sun gear; bottom - residual signal for sun gear – Case C

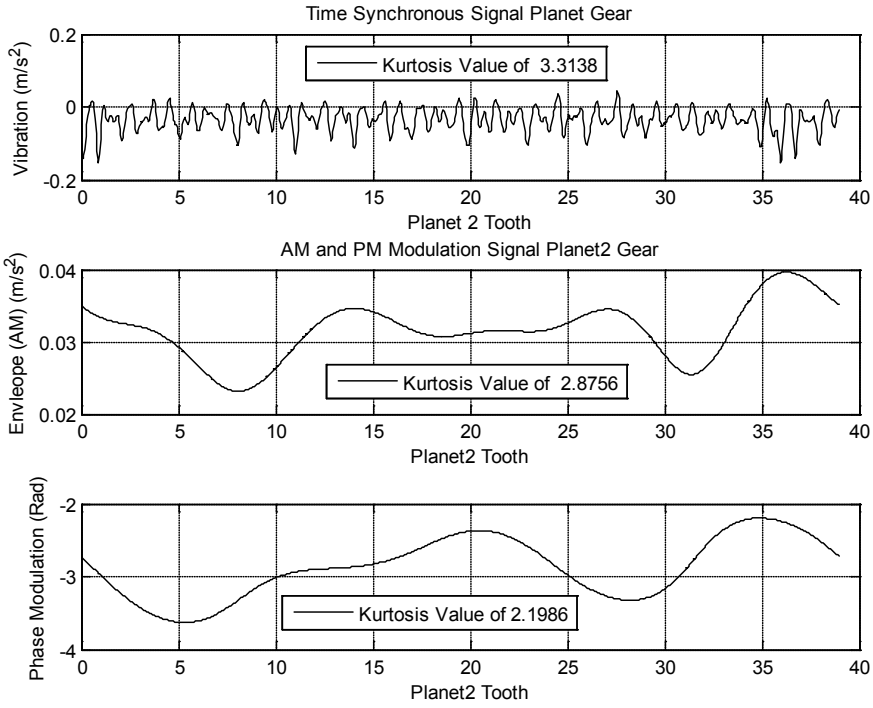

Figure 6.23. Planet Gear 2 amplitude and phase modulation signal from accelerometer AN3 – Case C: top plot – TSA; middle plot - amplitude modulation signal; bottom plot - phase modulation signal

6.3 Summary of Results

For each data processing method, a qualitative metric was assigned based on its ability to detect each failed component in the gearbox used in this study; the results are provided in Table 6.3. For each failed component and algorithm, a ranking of three levels is assigned for low, medium, and high confidence; the rankings are based on examining the output plots and the calculated features. An example of a high confidence rating is the amplitude and phase modulation results for the high speed pinion, in which the output plots and large kurtosis values are clear indications of damage. In certain instances, an algorithm was not evaluated for detecting a failed component or the algorithm is not designed or suited for that task. In this case, the label of NA (not applicable) was assigned. An example of the NA ranking is a bearing envelope analysis for detecting damage on any of the gear wheels. The spectral kurtosis method was only applied to the planetary gearbox (signals AN3 and AN4) and could only provide an indication of degradation to the planetary stage, but not which specific gear was degraded. This is reflected in the table with the additional notation of "stage" for the spectral kurtosis technique. Lastly, the rankings are given a black color if the method was applied prior to the release of the failure report and a blue color if the method was applied after the failure report was provided. Bearing envelope analysis, time synchronous averaging, and the planet separation algorithm were all performed after the failure report was released.

From the tabular results in Table 6.3, one can observe that the high speed pinion had high indications of damage from several techniques, including the vibration spectrum, cepstrum processing, and narrowband analysis from the phase modulation signal. Only the residual signal

did not provide an indication of a fault for the high speed pinion. The residual signal in general did not detect damage on the gear wheels for this study, with only a moderate indication of damage on the sun gear. The intermediate speed shaft pinion had a moderate indication of damage from both frequency domain analysis and the cepstrum features; however, there was no indication of damage by the narrow band analysis. Bearing envelope analysis provided high confident indications for three of the bearing failures that were on the intermediate and high speed shafts. The bearing damage on the planet carrier upwind bearing had only a moderate detection; the peak was less noticeable and a different band pass filter range had to be used to detect this fault. For the planetary gearbox, the ring gear appeared to be the easiest to detect, with a high confidence indication of damage from the narrowband phase modulation signal. It should be noted that none of the planet gears had damage according to the failure report; this agrees with the results from the data processing, in which none of the algorithms detected any abnormality or damage with the planet gears. In summary, many of the failed components could be detected using the evaluated algorithms. However, for gear components, in particular, multiple algorithms appear necessary since many of the algorithms are only tuned to one failure mode.

Table 6.3. Summary of results for each algorithm with the following notation: L-low confidence, M-medium confidence, H-high confidence, NA –not applicable or evaluated; black - indicates a method that was evaluated before the failure report, blue - indicates a method that was evaluated after the failure report

Failed Component	Frequency Domain	Cepstrum	Spectral Kurtosis	Bearing Envelope Analysis	TSA – Residual Signal	TSA – Amplitude / Phase Modulation
HSS Pinion	H	H	NA	NA	L	H
HSS Gear	L	L	NA	NA	L	M
ISS Pinion	M	M	NA	NA	L	L
ISS Gear	L	M	NA	NA	L	L
Ring Gear	NA	NA	H - stage	NA	L	H
Sun Pinion	NA	NA	H - stage	NA	M	L
ISS Upwind Bearing	NA	NA	NA	H	NA	NA
ISS Downwind Bearings	NA	NA	NA	H	NA	NA
HSS Downwind Bearings	NA	NA	NA	H	NA	NA
Planet Carrier Upwind Bearing	NA	NA	NA	M	NA	NA

6.4 Conclusions and Future Work

This chapter provides an evaluation of vibration signal processing and feature extraction algorithms used by the research team at the Center for Intelligent Maintenance Systems (IMS) for the Condition Monitoring Round Robin study. As one can observe from the summary results table, most of the failed components could be detected by one or more of the processing methods. This is encouraging and highlights that vibration-based condition monitoring can be used to assess and diagnose which components are in a failed condition. For gear wheels in particular, the use of multiple algorithms appears necessary, considering the different number of gear failure modes that are possible. The residual signal, in particular, did not seem suited for the failure modes exhibited by the damaged gear wheels on the parallel stage shaft, while the other algorithms provided more confident detections. The detection results for each algorithm do not account for the additional hardware or on-board processing requirements. The planet separation algorithm, in particular, is difficult to implement given the time period required to accumulate enough rotations of the carrier shaft.

Although the results from this study were encouraging, there are some aspects that could have aided the study or should be considered for future work. This study could have been aided by time domain waveforms instead of frequency spectrums provided for the baseline data. Many of the more advanced algorithms require the raw time waveform and they could not be evaluated based on the baseline data set. In addition, alternative methods were used for acquiring a reference signal for performing synchronous averaging. Further experimental studies should acquire and save a tachometer pulse train to avoid this issue. Considering that the gearbox was already in a severely damaged condition, the algorithms were evaluated on the basis of their ability to detect the health state of the various bearing and gear components. Unfortunately, this does not allow one to evaluate the algorithms ability to provide an early detection of a problem or whether the extracted vibration features are monotonic with the damage level. Both early detection and severity estimation are additional aspects worth evaluating for vibration-based condition monitoring techniques for wind turbine drivetrains. Continuous monitoring of a wind turbine drivetrain from a baseline condition until failure could provide a way to further evaluate the merits of the vibration-based condition monitoring algorithms.

7 Defect Diagnosis in Wind Turbine Gearbox based on Sideband Energy and Enveloping Spectral Analysis

Robert X. Gao[*1], Jinjiang Wang[1], and Ruqiang Yan[2]
[1]Department of Mechanical Engineering, University of Connecticut, Storrs, CT, USA
[2]School of Instrument Science and Engineering, Southeast University, Nanjing, China
[*]Corresponding Author Email: rgao@engr.uconn.edu

7.1 Introduction

To improve cost-effectiveness of wind energy, wind turbines must operate in a highly reliable fashion, given the significant cost associated with system repair, maintenance, and unexpected failure. Accordingly, techniques for the condition monitoring and fault diagnosis of wind turbine structures and components have been gaining increasing attention [41].

Of the various components in a wind turbine, the gearbox is a major component that is costly and vulnerable to failure. Accordingly, signal processing for gearbox defect identification and diagnosis has been an active research area. There are two major components in a gearbox: gears and bearings. For gear diagnosis, sideband analysis, amplitude, and phase modulation [42], wavelet transform [43], and spectral kurtosis [44] have been investigated. Typically, diagnosis is achieved through comparisons between a defective gear and a healthy gear. As for the bearing diagnosis, a band pass resonant signal processing technique has been reported. Choosing an appropriate bandwidth remains an important issue, given its effect on the diagnosis result.

As part of the CM Round Robin study, three sets of vibration data measured by NREL on a wind turbine gearbox (of unknown damaged condition) were analyzed at three different operating speeds. For gear fault diagnosis, sideband pattern analysis was performed on all gears. Data from torque measurements were also analyzed to facilitate annulus gear diagnosis; whereas for bearing diagnosis, the multi-scale enveloping spectra technique [45] has been investigated. The result of the analysis was compared with that of a spectral analysis of a healthy gearbox that was provided by NREL as a reference base.

7.2 Algorithms

Vibration of a gearbox can be caused by various sources, such as gear meshing, interaction between the rolling elements and raceways in bearings, and shaft rotation. Structural defects on gear's surface also constitute a source of vibrations that are carried by gear meshing frequencies. Research reported in the literature has shown that the energy associated with frequency components at the sidebands around the gear meshing frequency will increase as the health condition of the gear deteriorates, in comparison to a healthy gear. Accordingly, sideband analysis has been performed for gear analysis in this study.

For bearing defect diagnosis, the multi-scale enveloping spectra technique has been investigated [45], which makes use of the time, scale, and frequency information contained in the bearing vibration signal. The algorithm first decomposes the bearing vibration signal into a series of wavelet basis functions, through variations of the scales and time shifts of the wavelet function. The envelope of each decomposed wavelet function is then extracted from the modulus of the wavelet coefficients. Next, spectral analysis is performed repeatedly on the envelope signal, resulting in an envelope spectrum of the original signal at the various scales. The integration of

the wavelet transform, using post-spectral analysis, reveals the defect characteristic more clearly, enhancing its effectiveness in bearing defect diagnosis.

7.3 Results

Vibration data measured by NREL on a wind turbine gearbox was analyzed for gear and bearing defect diagnosis, respectively. Figure 7.1 illustrates the physical system analyzed for this study, with the locations of the specific bearings, shaft, and gears identified.

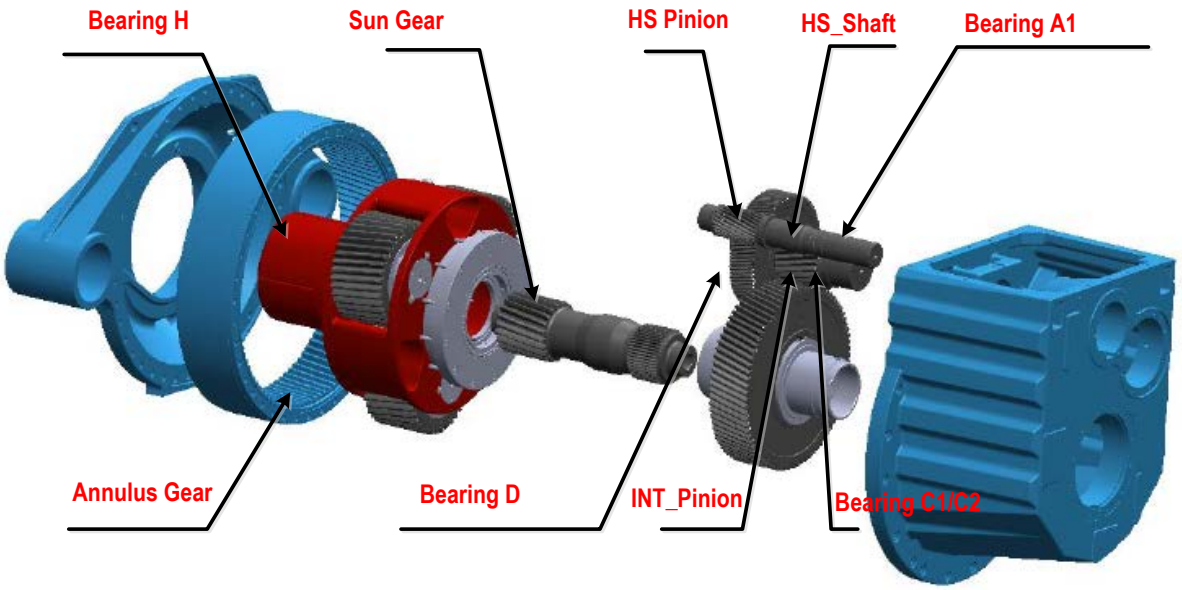

Figure 7.1. Locations of defective components in the gearbox assembly

7.3.1 Gear Diagnosis Results

Gear test data at 1,800 rpm measured by vibration sensor AN7, was analyzed by means of sideband analysis, and the result is presented in this chapter. Figure 7.2 (a) and Figure 7.2 (b) show the spectra of gear vibrations under healthy and deteriorated (at the end of service life) conditions, at the locations of HS_Pinion and INT_Pinion, respectively. From the figures, the gear meshing frequencies of the HS_Pinion and INT_Pinion can be clearly seen. A zoom-in view around the INT_Pinion and HS_Pinion gear meshing frequencies are shown in Figure 7.2 (c) to Figure 7.2 (f). Comparing the result of the gearbox under healthy and deteriorated conditions, the increase in energy content of the sideband frequencies can be identified, for both the HS_Pinion and INT_Pinion. This indicates that the tested gear is defective. The same trend is observed from the sideband analysis of Annulus_Gear and Sun_Gear, in Figure 7.3, which indicates that the Annulus_Gear and Sun_Gear are also defective. In Table 7.1, the sideband energy ratios (defined as the first order sideband energy over the energy at the gear meshing frequency) of these four gears are summarized. It is seen that for all the four gears, there is a consistent increase in the sideband energy ratio (e.g., from 29.4% to 107.7% for the INT_Pinion).

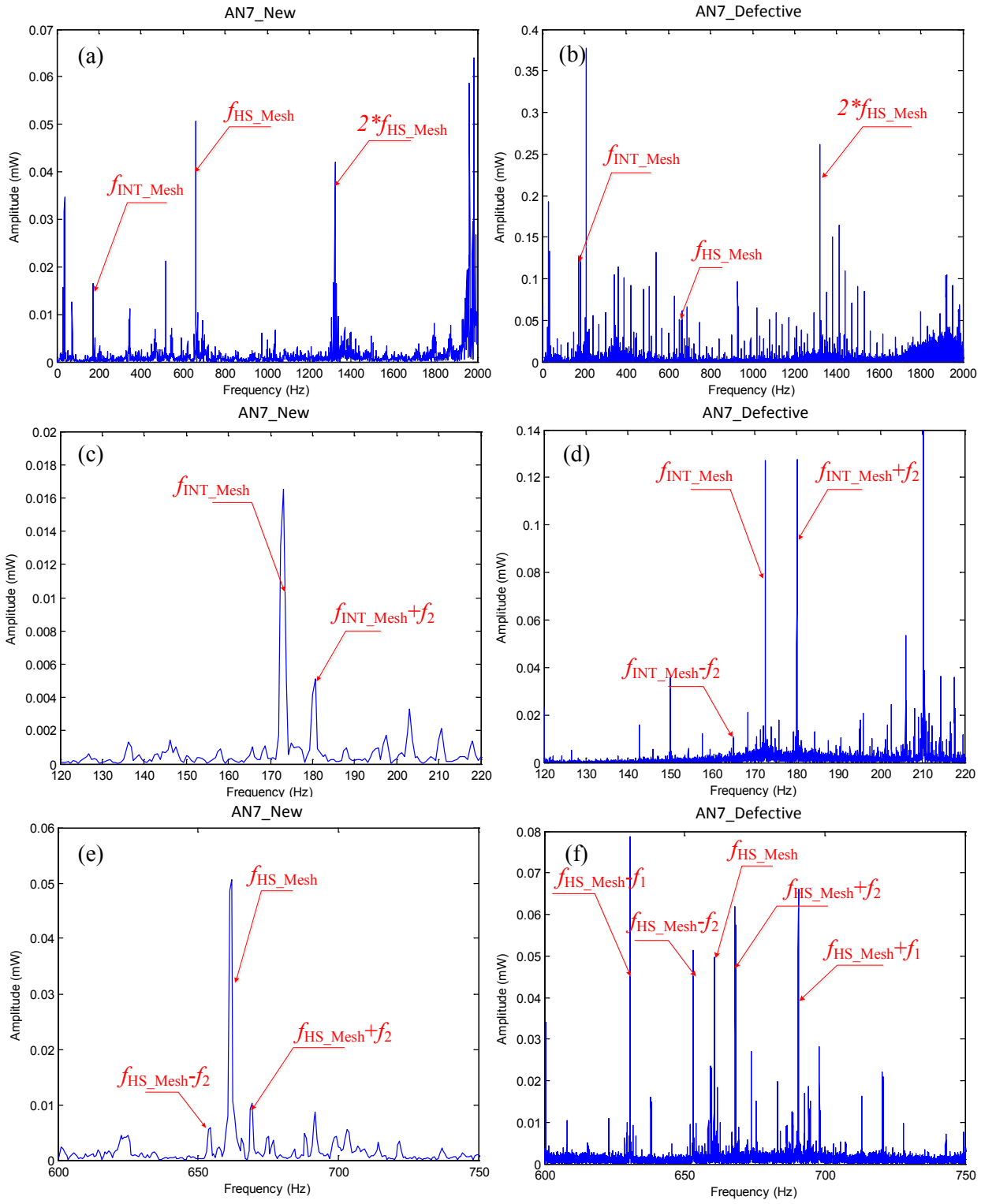

Figure 7.2. Comparison analysis between test data and reference data for HS_Pinion and INT_Pinion

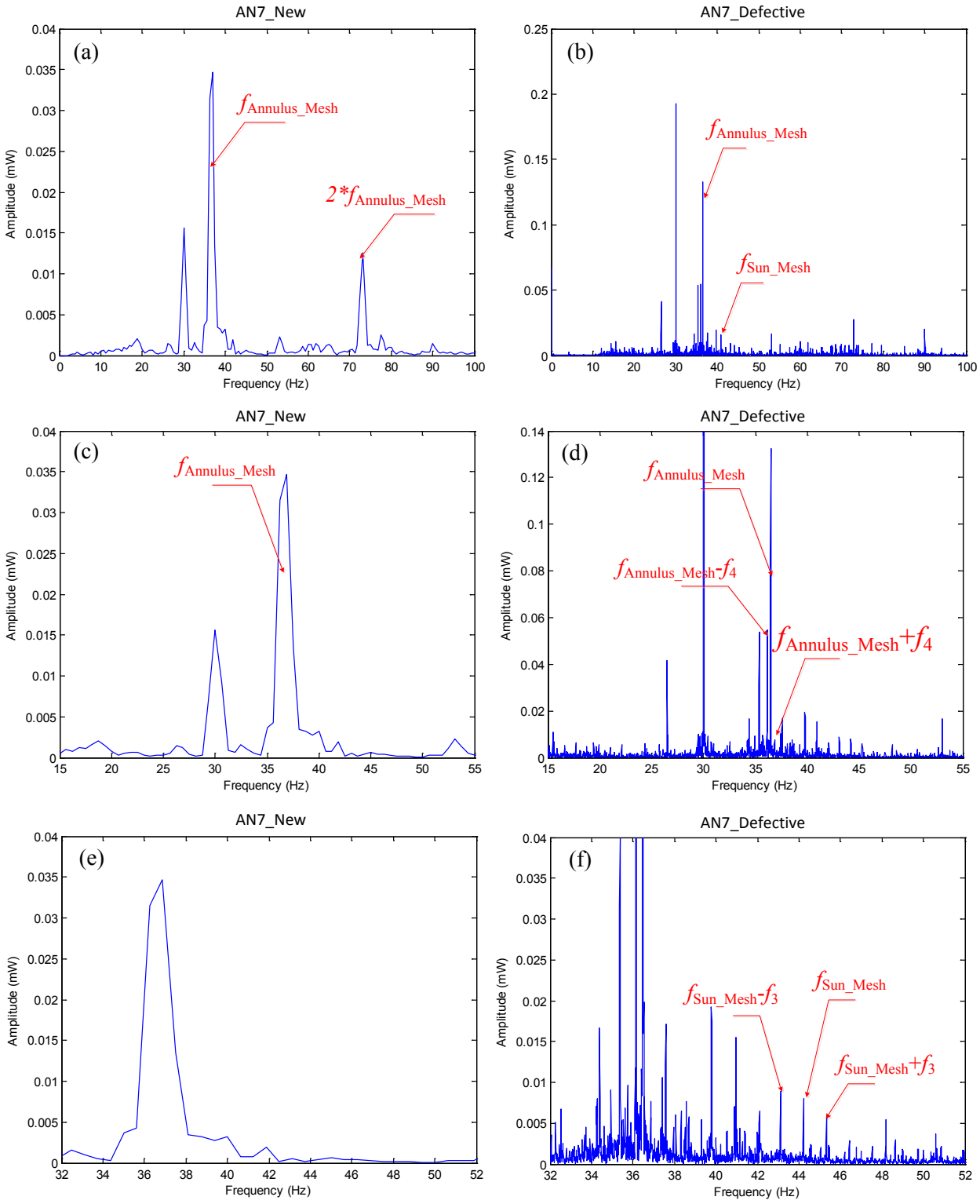

Figure 7.3. Comparison analysis between test data and reference data for Annulus_Gear and Sun_Gear

Table 7.1. Sideband energy comparison between new gearbox and gearbox at the end of service life

Components	Healthy Gearbox			Gearbox at End of Service Life		
	Meshing energy (mw)	1st sideband energy (mw)	Sideband Energy ratio	Meshing energy (mw)	1st sideband energy (mw)	Sideband Energy ratio
HS_Pinion	0.051	0.016	31.4%	0.051	0.114	223.5%
INT_Pinion	0.017	0.005	29.4%	0.13	0.14	107.7%
Sun_Gear	0.0002	0.0004	200%	0.008	0.019	237.5%
Annulus_Gear	0.035	0.014	40%	0.135	0.059	43.7%

The increase in the sideband energy ratio related to the annulus gear is not as significant as that of the other three gears (relative increase is 9.3%). Considering that the annulus gear runs at low speed under high torque conditions resulting from the gearbox transmission mechanism, the torque measurement may be more effective for low speed gear diagnosis, due to its sensitivity to angular vibrations of the gear. Based on this consideration, data obtained from torque measurements of the gearbox have been analyzed. Figure 7.4 shows the waveform of the torque data under 1,200 RPM. The interval between the peaks is approximately 4.03s, corresponding to the rolling-over period of the annulus gear. Figure 7.5 shows the result of envelope spectrum analysis of torque data. A peak at frequency of 0.248 Hz, which corresponds to the roll-over period of the annulus gear, is identified. This indicates a structural defect on the annulus gear.

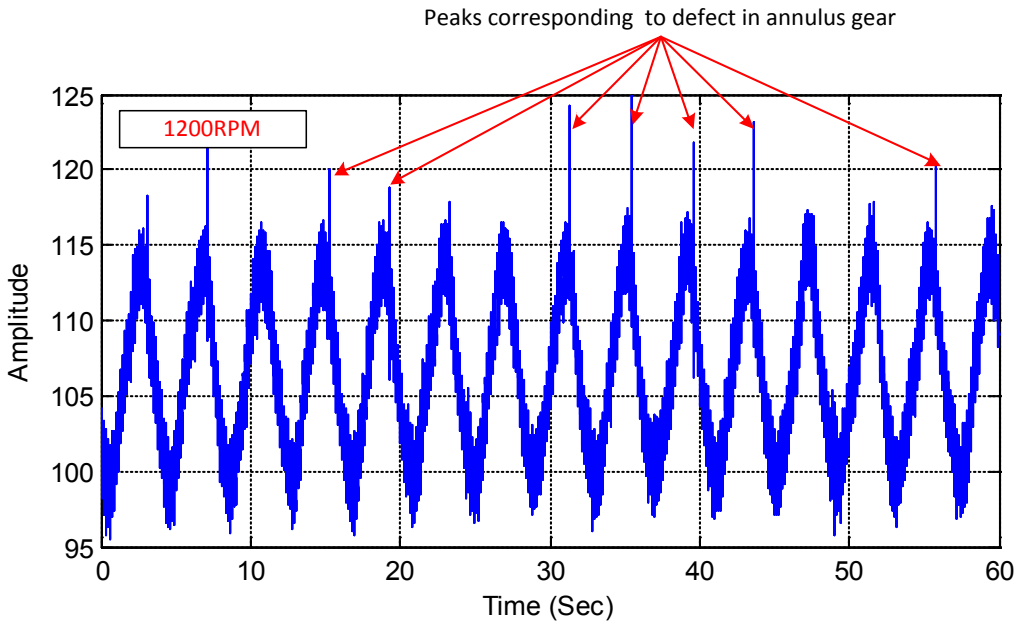

Figure 7.4. Time series of torque data under 1200 rpm

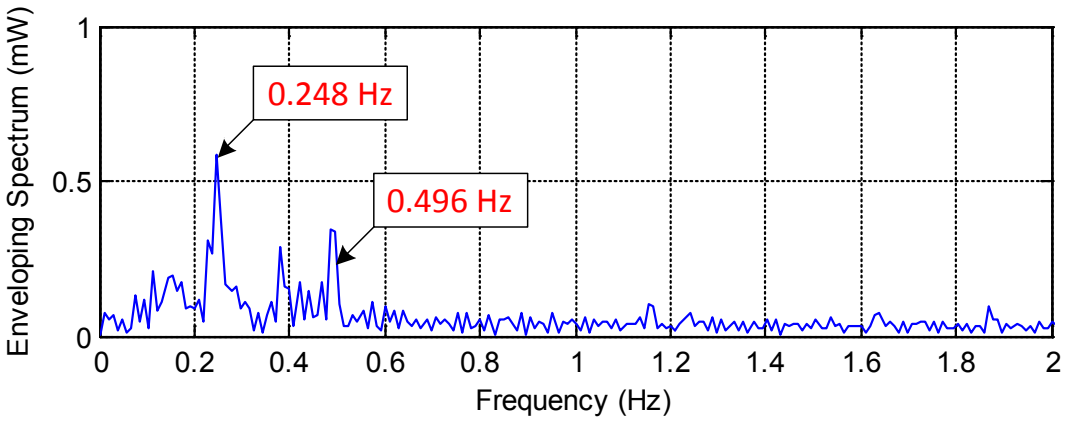

Figure 7.5. The envelope spectrum of torque data under 1200 rpm

7.3.2 Bearing Diagnosis Results

Using the wavelet enveloping technique [45], vibration data of the tested gearbox was analyzed. In Figure 7.6, wavelet enveloping spectrum of data measured by sensor AN3 (close to bearing H) under rotational speed 1,800 rpm is presented. Given the high peak related to the frequency component f_{BPFO}, bearing H is considered defective. Furthermore, from the energy concentration at the HSS_Shaft rotating frequency (1,000 mw) and its harmonics, it can be concluded that the HSS_Shaft has imbalance or misalignment.

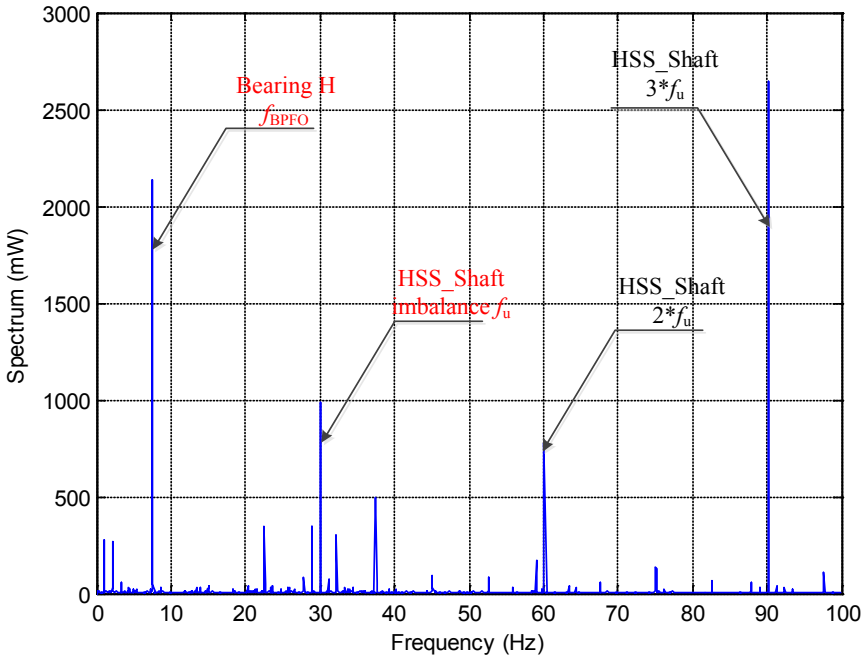

Figure 7.6. Wavelet enveloping spectrum of sensor AN3 at 1,800 rpm

Figure 7.7 shows the wavelet enveloping spectrum of data measured by sensor AN6 (adjacent to bearing D) at the running speed of 1,800 rpm. Defect frequency, f_{BPFI}, of bearing D can be identified, although its amplitude is not as significant due to masking from the high energy component, f_u, which is related to imbalance of the HSS_Shaft.

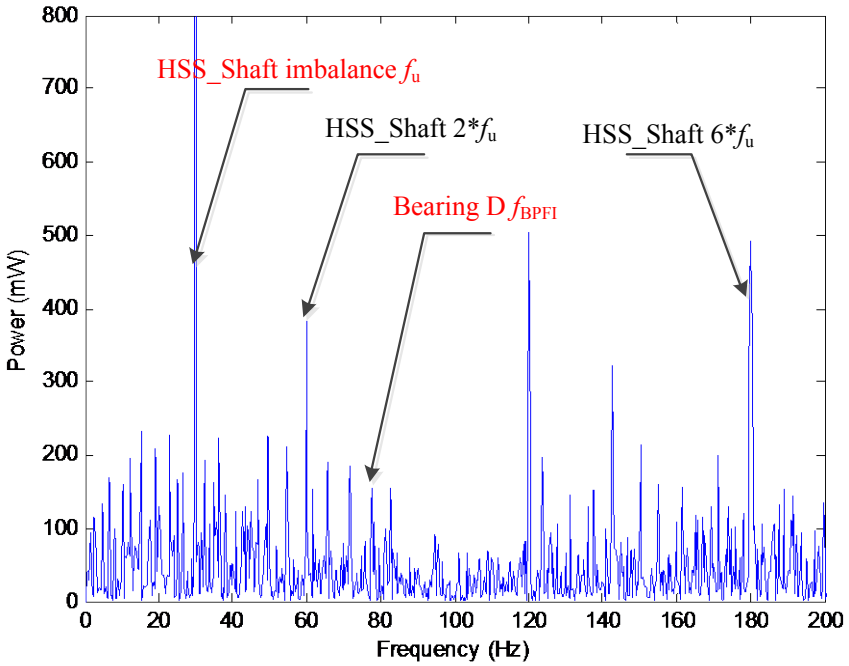

Figure 7.7. Wavelet enveloping spectrum of sensor AN6 at 1,800 rpm

7.3.3 Comparison with Inspection Result

The analyses results have been compared with physical damages identified in the gearbox when it was disassembled for visual inspection. As shown in Table 7.2, all gear defects were successfully identified. Also, two of the four bearings were identified as defective.

Table 7.2. Comparison between the analysis result and the actual damage of a tested gearbox

Damage	Component	Damage mode	Severity	Rationale
1	HS gear set	Scuffing	Severe	Sideband
2	Intermediate gear set	Fretting corrosion and scuffing	Severe	Sideband
3	Annulus gear	Scuffing/polishing	Moderate	Sideband
4	Sun pinion	Fretting corrosion	Severe	Sideband
5	Bearing H	Fretting corrosion	Severe	Wavelet envelope
6	Bearing D	Assembly damage	Moderate	Wavelet envelope
7	Bearing C1/C2	Assembly damage on spacer	Severe	Not identified
8	Bearing A1	Overheating	Severe	Not identified

7.4 Lessons Learned

The diagnosis results have demonstrated that sideband analysis provides an effective and computationally efficient approach to gear defect diagnosis. Considering that the energy content associated with a structural defect may not be significant at the defect incipient stage, complementing sideband analysis with other advanced techniques should be considered.

As for the bearing diagnosis, defects in bearing H and D have been identified by means of wavelet enveloping. Because of the low signal-to-noise ratio and interference caused by gear meshing frequencies, diagnosis of bearing D was more challenging than that of bearing H. This indicates the need for separating the signal related to gear meshing from that of the bearing vibration before performing the bearing diagnosis. Because the nature of the damage to Bearing A1 is related to overheating, instead of a surface defect, and damage on bearing C1/C2 is not on the roller raceway, but on the spacer, defects from bearings C1/C2 and A1 could not be identified by the vibration data analysis conducted herein. This leads to the consideration that, besides vibration sensing, other sensing techniques (e.g., temperature sensing) should be considered as well to enable fusion of diverse sensing modalities for improved gearbox diagnosis. Research is needed to address this issue.

8 Fault Analysis of a Wind Turbine Gearbox: A Data Driven Approach

Zijun Zhang*, Anoop Verma, Andrew Kusiak
Department of Mechanical and Industrial Engineering, The University of Iowa
*Corresponding Author Email: zijun-zhang@uiowa.edu

8.1 Introduction

The wind industry has been affected by failures of wind turbine components, such as main bearings, gearboxes, and generators. The high cost of replacing failed components impacts the energy cost. Therefore, research in fault identification and condition monitoring is warranted. Fault identification is concerned with a fault that has occurred and its labeling. In condition monitoring, parameters reflecting the component conditions are identified and their changes are analyzed to detect an emerging failure. In this chapter, the fault identification analysis is studied in the time domain based on the vibration data of an impaired gearbox tested by NREL, which is different from the traditional fault analysis from the frequency domain [46-51].

8.2 Methodologies

This section describes the data processing and analysis methods applied to the detection of the gearbox faults.

8.2.1 Change Rate of Vibration Acceleration

To analyze the gearbox vibration in the time domain, jerk is utilized. Jerk describes the rate of acceleration change, and it is often used to indicate the excitement of vibration. For the high-frequency vibration acceleration data in Section 2.4, the jerk is approximated in Equation (13).

$$\vec{J} \approx \frac{\vec{a}_t - \vec{a}_{t-T}}{T} \tag{13}$$

The expression in Equation (13) is derived in Equation (14).

$$\vec{J} = \frac{d\vec{a}}{dt} = \lim_{\Delta t \to 0} \frac{\Delta \vec{a}}{\Delta t} \approx \frac{\vec{a}_t - \vec{a}_{t-T}}{t-(t-T)} = \frac{\vec{a}_t - \vec{a}_{t-T}}{T},\ \Delta\vec{a} = \vec{a}_t - \vec{a}_{t-T} \text{ and } \Delta t = t-(t-T) \tag{14}$$

where $\vec{J}$ is jerk, $\vec{a}$ is acceleration, t is the time index, and T represents the sampling interval, 1/40000 s.

8.2.2 Root Mean Square, Crest Factor and Kurtosis

Besides jerk, the root mean square (RMS), crest factor (CF), and kurtosis are estimated based on the acceleration data and utilized in time domain analysis.

RMS is the simplest method for measuring abnormalities in the time domain. The RMS value can be used to detect unbalanced rotating elements. It is a statistical measure of the magnitude with varying quantity, and it is expressed in Equation (15).

$$RMS = \sqrt{\frac{1}{N}\sum_{i=1}^{N}(s_i)^2} \tag{15}$$

The crest factor (CF) is a measure used to detecting changes in the signal pattern due to impulsive vibration sources, such as tooth breakage. It can be useful in detecting high peaks in the signal at higher magnitudes of the peak and for smaller numbers of peaks. A small value of

RMS and high peak value implies a higher crest factor. A CF with values in the range 2-6 represents normal operations; whereas, a value higher than six represents a defective component. The crest factor is computed by dividing the peak level of the signal average by the standard deviation (RMS) of the signal average, as shown in Equation (16).

$$CF = \frac{Peak\ level}{RMS} \tag{16}$$

Kurtosis is defined as the fourth statistical moment of an array of values about the mean. It indicates the existence of major peaks. A kurtosis value of less than three represents a component in a normal health condition; whereas, a value greater than three represents abnormality. The greater the number of peaks in the signal, the larger is the kurtosis. The kurtosis is expressed in Equation (17).

$$K = \frac{N.\sum_{i=1}^{N}\left(s_i - \overline{s}\right)^4}{\left(\sum_{i=1}^{N}\left(s_i - \overline{s}\right)^2\right)^2} \tag{17}$$

8.2.3 Correlation Coefficient

The correlation coefficient is a quantity that measures the linear relationship between two parameters ranges from -1 to 1. The value of the correlation coefficient equal to 1 (-1) indicates a strong positive (negative) relationship between two parameters. A value of the correlation coefficient close to zero means there is a weak linear relationship. The formulation of correlation coefficient can be written as Equation (18).

$$r = \frac{n\sum xy - (\sum x)(\sum y)}{\sqrt{n(\sum x^2) - (\sum x)^2}\sqrt{n(\sum y^2) - (\sum y)^2}} \tag{18}$$

where r is the correlation coefficient, and x and y are two different parameters.

8.2.4 Clustering

Clustering analysis is an unsupervised method of data analysis. Clustering algorithms group observations into clusters by evaluating similarities among the observed data. A *k*-means algorithm [52] is modified in this study to establish clusters. In the original version of the *k*-means algorithm, the number of clusters, *k*, should be arbitrarily set by the analyst. In this study, a clustering cost function is introduced to evaluate the cluster quality with *k*. The clustering cost function is formulated as Equation (19) and used in a 10-fold, cross-validation scheme [53,54].

$$d(k, \mathbf{x}, \mathbf{c}) = \frac{1}{\sum_{i=1}^{k} m_i}\sum_{i=1}^{k}\left(\sum_{\mathbf{x}_j \in C_i}\left\|\mathbf{x}_j - \mathbf{c}_i\right\|^2\right) \tag{19}$$

where d is the clustering cost, k is the number of clusters, m is the number of observations (sensors) contained in each cluster, $\mathbf{x}$ is a vector of parameters used in this research, $\mathbf{c}$ presents the centroid of each cluster, j is the index of each data point, and C_i represents cluster i.

The modified k-means algorithm involves the following steps:

Step 1. Set the initial value of k to 2

Step 2. Divide the data set into 10 subsets of equal size.

Step 3. Repeat 10 times.

Step 3.1. Randomly select nine subsets for training and use the 10^{th} subset for testing.

Step 3.2. Initialize k centroids.

Step 3.3. Repeat the following two steps until the centroids do not change.

Step 3.3.1. Assign data point to the closest cluster by $C_i^t = \{\mathbf{x}_j : \left\|\mathbf{x}_j - \mathbf{c}_i^t\right\| \le \left\|\mathbf{x}_j - \mathbf{c}_{i^*}^t\right\|, i^* = 1,2,\cdots,k\}$.

Step 3.3.2. Update the values of the centroids by $\mathbf{c}_i = \sum_{\mathbf{x}_j \in C_i} \mathbf{x}_j / n$, where n is the total number of observations.

Step 3.4. Compute the clustering cost, d.

Step 4. Estimate the average of clustering cost d in 10-fold cross-validation.

Step 5. Stop the algorithm if $d(k,\mathbf{x},\mathbf{c}) - d(k-1,\mathbf{x},\mathbf{c}) \le \xi$ or $k = 12$; otherwise, go back to Step 1.

To implement the modified k-means algorithm, the parameter, ξ, is set to 0.05.

8.3 Results

8.3.1 Data Process and Description

Acceleration data are sampled at 40,000 Hz and recorded for 10 minute intervals. The data set is large. As the sensors are used to recording acceleration, the data is transformed based on (1) to obtain the jerk values. Acceleration data for all three test cases (2a, 2b, and 2c) at 10 minute intervals are transformed. Each data set is divided into 40 data subsets of equal size (or equal length, 15 seconds) for the further investigation.

Since the sampling frequency of the acceleration data is high, 40,000 Hz, viewing and data analysis of the high frequency data directly in the run-chart form is not feasible. Therefore, four statistical metrics, the mean, standard deviation, maximum, and minimum, are utilized to compute the Jerk value for each data subset discussed in Section 8.2.1. The values of the mean, standard deviation, maximum, and the jerk for all 40 data subsets are used to develop three new data sets for analysis discussed in Section 8.3.2, 8.3.3, and 8.3.4. The minimum Jerk value is always zero and, therefore, it is excluded from this research.

8.3.2 Detection of Ring Gear Fault

Figure 8.1 displays the time series speed data for 10 minutes. As shown, it is obvious that the speed experiences significant change at the third minute. The maximum rate of change is about 500 rpm/15s and at the same time the change of LSS Torque suddenly increases to 15 kNm/15 s. These two phenomena point to a fault. To analyze the faulty component and its location, the maximum jerk data from 12 accelerometers, at each 15 second interval, is utilized. The

maximum and minimum of the maximum jerk data of each accelerometer are estimated. Then, the ratio, R, is estimated based on the maximum and minimum values of the maximal jerk based on Equation (20).

$$R = (\text{Max}\{\text{maximum jerk}\} - \text{Min}\{\text{maximum jerk}\}) / \text{Max}\{\text{maximum jerk}\} \quad (20)$$

Figure 8.2 shows the R for each accelerometer. As shown, the Ratio 1 of sensors AN3 and AN4 is much higher than the R of other sensors. Therefore, the location and component that AN3 and AN4 monitored are considered as the possible location where the fault occurred. From the specification provided by NREL, the component monitored by AN3 and AN4 is a ring gear and the location is in the low speed stage (LSS-T) of the gearbox.

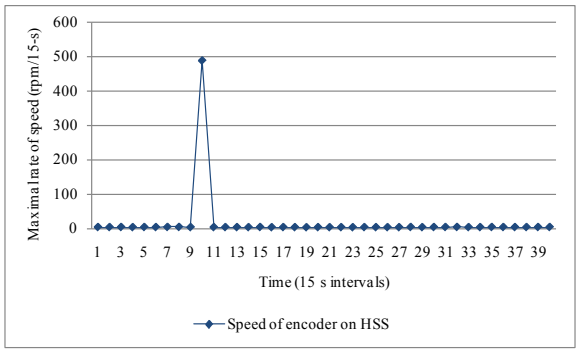

Figure 8.1. Run chart of maximum rate of speed

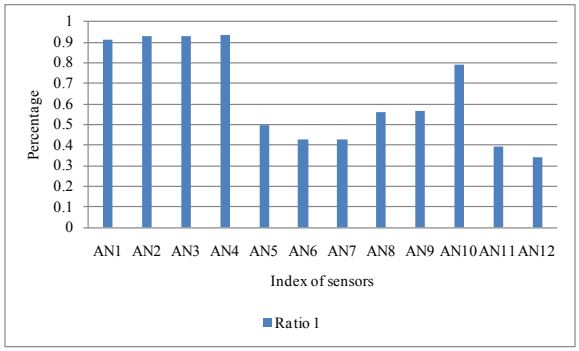

Figure 8.2. Bar char of R

8.3.3 Detection of Faults in Intermediate and High Speed Stages

The suspected faults in intermediate and high speed stages manifest themselves by significant vibration observed at the high speed stage (HS-ST) and intermediate speed stage (IS-ST) of gearbox in testing case 2b and 2c. As HS-ST is connected with IS-ST, there are three possible causes: HS-ST damaged, IS-ST damaged, or both are damaged. One possible root cause of high vibration in HS-ST and IS-ST is the oil leakage and gear wear at the two stages.

In this section, a correlation coefficient analysis is performed based on a data set containing the mean jerk described in Section 8.3.1. Table 8.1 and Table 8.2 present the results of correlation coefficient analysis based on cases 2b and 2c. As shown in Table 8.1 and Table 8.2, sensors,

AN5, AN6, AN7, AN8, AN9, AN11, and AN12, are highly correlated. Since the component monitored by AN1 and AN2 is considered healthy, results in Table 8.1 and Table 8.2 indicate that significant vibration originates at one of the areas AN5, AN6, AN7, AN8, and AN9 monitored (HS-ST and IS-ST), and it impacts the generator monitored by AN11 and AN12.

Table 8.1. Correlation coefficient analysis of the mean of jerk data: Case 2b

Sensor	AN1	AN2	AN3	AN4	AN5	AN6	AN7	AN8	AN9	AN10	AN11	AN12
AN1	1.00	0.98	0.53	0.20	0.02	0.14	0.00	-0.11	0.16	0.16	0.16	0.03
AN2	0.98	1.00	0.59	0.06	0.18	0.30	0.17	0.05	0.32	0.25	0.33	0.19
AN3	0.53	0.59	1.00	0.09	0.31	0.53	0.41	0.19	0.62	0.77	0.48	0.32
AN4	0.20	0.06	0.09	1.00	-0.88	-0.78	-0.85	-0.94	-0.70	-0.11	-0.76	-0.89
AN5	0.02	0.18	0.31	-0.88	1.00	0.94	0.97	0.97	0.90	0.50	0.92	0.97
AN6	0.14	0.30	0.53	-0.78	0.94	1.00	0.98	0.93	0.99	0.60	0.95	0.96
AN7	0.00	0.17	0.41	-0.85	0.97	0.98	1.00	0.97	0.96	0.56	0.94	0.97
AN8	-0.11	0.05	0.19	-0.94	0.97	0.93	0.97	1.00	0.88	0.39	0.90	0.98
AN9	0.16	0.32	0.62	-0.70	0.90	0.99	0.96	0.88	1.00	0.67	0.92	0.93
AN10	0.16	0.25	0.77	-0.11	0.50	0.60	0.56	0.39	0.67	1.00	0.59	0.42
AN11	0.16	0.33	0.48	-0.76	0.92	0.95	0.94	0.90	0.92	0.59	1.00	0.92
AN12	0.03	0.19	0.32	-0.89	0.97	0.96	0.97	0.98	0.93	0.42	0.92	1.00

Table 8.2. Correlation coefficient analysis of the mean of jerk data: Case 2c

Sensor	AN1	AN2	AN3	AN4	AN5	AN6	AN7	AN8	AN9	AN10	AN11	AN12
AN1	1.00	0.83	0.32	-0.73	0.50	0.56	0.49	0.67	0.49	0.48	0.64	0.56
AN2	0.83	1.00	0.76	-0.91	0.88	0.90	0.87	0.92	0.87	0.86	0.91	0.91
AN3	0.32	0.76	1.00	-0.67	0.94	0.92	0.95	0.78	0.96	0.95	0.80	0.90
AN4	-0.73	-0.91	-0.67	1.00	-0.85	-0.90	-0.84	-0.97	-0.83	-0.80	-0.94	-0.91
AN5	0.50	0.88	0.94	-0.85	1.00	0.99	0.99	0.92	0.99	0.98	0.92	0.98
AN6	0.56	0.90	0.92	-0.90	0.99	1.00	0.99	0.95	0.98	0.97	0.95	0.99
AN7	0.49	0.87	0.95	-0.84	0.99	0.99	1.00	0.91	0.99	0.98	0.92	0.98
AN8	0.67	0.92	0.78	-0.97	0.92	0.95	0.91	1.00	0.91	0.88	0.96	0.96
AN9	0.49	0.87	0.96	-0.83	0.99	0.98	0.99	0.91	1.00	0.98	0.90	0.98
AN10	0.48	0.86	0.95	-0.80	0.98	0.97	0.98	0.88	0.98	1.00	0.88	0.96
AN11	0.64	0.91	0.80	-0.94	0.92	0.95	0.92	0.96	0.90	0.88	1.00	0.96
AN12	0.56	0.91	0.90	-0.91	0.98	0.99	0.98	0.96	0.98	0.96	0.96	1.00

Besides correlation coefficient analysis, the *k*-means clustering algorithm is utilized to examine the relationship among sensors. Since the *k*-means algorithm groups parameters into clusters by examining their similarity, it is capable of evaluating the relationship among sensors. Table 8.3 shows the clustering result of both case 2b and 2c. In Table 8.3, AN6, AN7, AN8, AN9 and AN12 are grouped into one cluster while other sensors are grouped into another cluster. This

result points to the same pattern as the correlation coefficient analysis, which indicates the faulty location of HS-ST and IS-ST.

Table 8.3. Clustering based classification

Case 2b		Case 2c	
Index of AN	Final classification	Index of AN	Final classification
1	2	1	2
2	2	2	2
3	2	3	2
4	2	4	2
5	2	5	2
6	1	6	1
7	1	7	1
8	1	8	1
9	1	9	1
10	2	10	2
11	2	11	2
12	1	12	1

The results of RMS, CF, and kurtosis also show an agreement with the correlation and clustering analysis. Figure 8.3 presents the RMS values of 2b, averaged over a 1 minute interval. The case 2b reveals a pattern; whereas, the low RMS values of sensors AN1 and AN2 cause a high crest factor. The increase in RMS of AN8 may indicate that a fault is in progress in the gearbox. It could be due to the oil leakage.

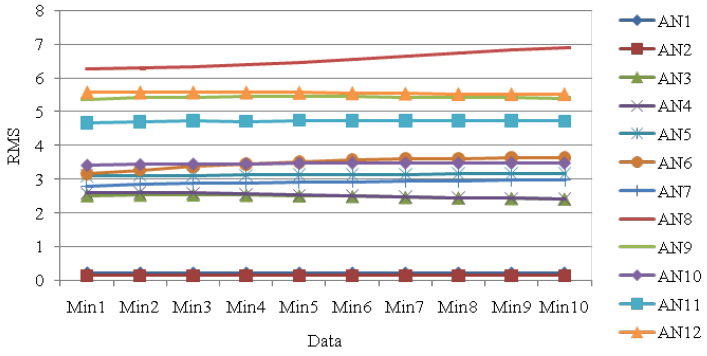

Figure 8.3. RMS across 12 sensors - Case 2b

Figure 8.4 displays the crest factor of 2b across 12 sensors. In Figure 8.4, it can be observed that the main bearing is affected in test case 2b. It can be assumed that the significant amount of crest factor near AN1 is contributed by the vibrations of other components.

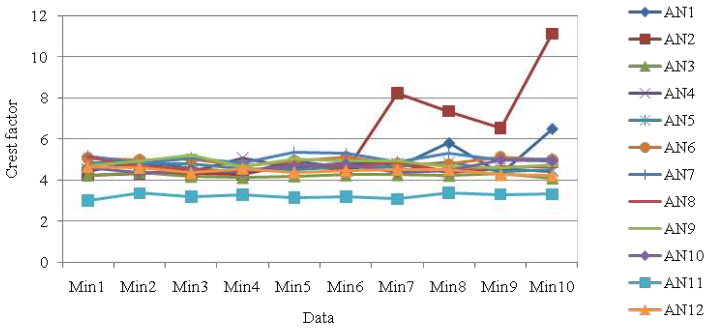

Figure 8.4. Crest factor across 12 sensors - Case 2b

Figure 8.5 represents the kurtosis of three test cases across 12 sensors. In case of CM_2b, kurtosis across all 12 sensors shows increasing patterns. This could indicate a gradual wear.

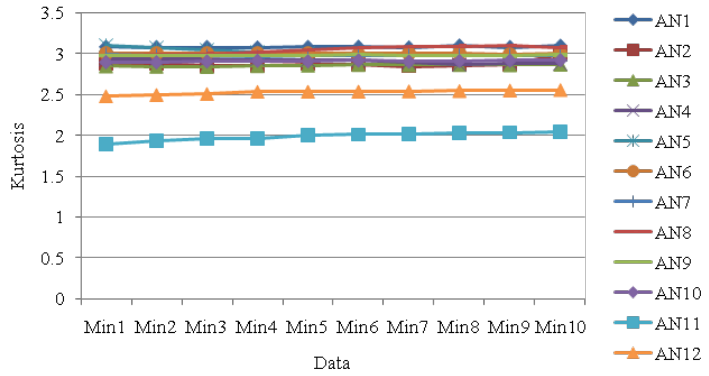

Figure 8.5. Kurtosis across 12 sensors - Case 2b

8.4 Conclusion and Discussion

Analysis of jerk data derived from vibration acceleration data of the test wind turbine gearbox was discussed in this chapter. In the analysis of the component failure identification, the correlation coefficient analysis and clustering analysis were applied to identify the failure stage of the gearbox in the time domain. Some faults of the intermediate and high-speed stages of the gearbox were correctly identified by the approaches discussed in this chapter. Some root causes could be inferred based on the data patterns of some specific sensors. Since the drivetrain was fixed to the floor, other factors (e.g., force from the wind and tower) that could impact the vibration excitement were not presented. In the future research, gearbox vibration acceleration data collected from field operated wind turbines, as well as data such as wind speed, generator torque and tower vibration, is needed to validate applicability of the proposed approach in fault identification.

9 Techniques for Separation and Enhancement of Various Components in the Analysis of Wind Turbine Vibration Signals

Nader Sawalhi[1], Robert B. Randall[2*], and David Forrester[3]
[1]College of Engineering, Prince Mohammad Bin Fahd University, The Kingdom of Saudi Arabia.
[2]School of Mechanical and Manufacturing Engineering, The University of New South Wales, Australia
[3]Defence Science and Technology Organisation, Australia
[*]Corresponding Author Email: b.randall@unsw.edu.au

9.1 Introduction

This chapter provides a summary of the handling and processing of wind turbine data provided by NREL for the CM Round Robin study. The University of New South Wales took an active role in this study through Dr. Nader Sawalhi and Professor Bob Randall.

NREL provided three sets of data (taken from a number of accelerometers on the planetary gearbox) at different speeds and load conditions. The data was for a faulty condition only. The data was first analyzed blindly, in the sense that there was originally no information given as to the type and location of faults in the gearbox. Our group concentrated on the search for bearing faults, because it is our opinion that to be sure of detecting gear faults, it is necessary to make comparisons with signals from the gears in healthy condition. We did, however, look for indications of local faults on the gears, as these might show up clearly as local impulsive responses in the gear signatures.

Later, after receiving the inspection report, and spectra from the gearbox in good condition, we made a further analysis, in particular of the gear signals, and were able to detect other indicators of the actual faults. Most of these could have been detected in the original blind analysis, if we had had the signals for good condition.

Our group had already had a certain amount of experience in analyzing signals from wind turbine transmissions, and was aware that the main differences, with respect to other similar gearboxes, were because the load can vary considerably over relatively short periods, at least with respect to the low speed input sections of the transmission. The vibration signal from gears is affected greatly by the load, and so some means has to be found to distinguish such variations from changes in condition. We have considerable experience with the diagnoses of helicopter gearboxes, which are somewhat similar. However, these operate at perhaps ten times higher speeds, and it is possible to obtain reasonably long signals with an approximately constant load. In contrast to gear fault signals, bearing signals are not so sensitive to torque load (although in gearboxes, radial load depends on torque load), and there is usually a dramatic difference in the signals in the presence of faults, which often allows them to be diagnosed without necessarily having access to historical data. This is because of the development of spectral kurtosis (SK) techniques in recent years by our group and colleagues, in particular Professor Jerome Antoni, now of INSA Lyon, in France [55]. The techniques we have used for analyzing the signals for gear and bearing faults are described in more detail below. Those bearing diagnosis are primarily based on a semi-automated procedure, with several different stages to separate and enhance the

bearing signals. Then envelope analysis is applied (spectrum analysis of squared envelope signals) to diagnose the fault repetition frequencies and their modulations by lower frequencies [56]. We also applied a recently developed cepstral pre-whitening technique, which can circumvent some of the stages in the earlier procedure [57]. For gear diagnosis we applied classic techniques based on obtaining a synchronously averaged signature for each gear, and then looking for localized impulses characteristic of local faults. This requires the signals to be "order tracked," or re-sampled in the angular domain, with equal numbers of samples in each revolution. This normally requires a tachometer or shaft encoder signal for synchronization. The supplied speed signal was not suitable for this so we extracted a "pseudo-encoder" signal from the vibration signal to use for order tracking. For obtaining signatures of the individual planet gears and sun gear in the planetary part of the gearbox, the premium current method is one patented by DSTO (Defence Science and Technology Organisation), of the Australian Defence Department. We engaged Dr. David Forrester of DSTO, the inventor of the technique, to obtain these signatures for us for the latest results presented at the Wind Turbine Condition Monitoring Workshop in Broomfield, CO, in September 2011. Those results are included here. It should be mentioned that Dr. Forrester was surprised by the design of the planetary section of the gearbox, as the choice of tooth numbers was far from a hunting tooth design, normally considered good practice, and as a result of this, groups of teeth always mesh in the same way and repeat frequently. The effects of this are discussed below. It is also somewhat unusual that the ratio of the high speed section was exactly 4:1 (88:22) meaning that the 22 teeth on the pinion always mesh in exactly the same way with four groups of 22 teeth on the intermediate shaft wheel. Therefore, a fault on one tooth transfers to individual teeth on the mating gear, and is not smeared out as it is in a hunting tooth design.

After receiving spectra for the gearbox in good condition, we were also able to make spectrum comparisons to detect changes in modulation sideband patterns, often indicative of faults, and also cepstrum analysis to concentrate the information in the sideband patterns.

9.2 Algorithms

Our general approach is to separate the signals, into the components coming from the gears and bearings, and analyze them separately. The separation is based on the assumption that the gear signals are deterministic (with respect to rotation angle), and the bearing signals are stochastic, because of the minor random slip between the components and the random positioning of the rolling elements in the clearance of the cage. These two effects give an approximately 1-2% deviation of the mean value of the actual bearing fault frequencies, with the same order of random variation around the mean from those frequencies and calculated on the basis of no slip and perfectly uniform spacing. The signals can then be classified as approximately second order cyclostationary, which allows their separation from the deterministic gear components [58]. There are a number of methods for achieving this separation [28], but the one initially used in this research was to first isolate and then remove the deterministic components corresponding to each gear in the system, by synchronous averaging, leaving a residual stochastic signal, which should be dominated by bearing faults in some frequency bands. The optimum frequency bands are found using some sort of kurtogram to find the frequency band with maximum SK. In this case, a wavelet kurtogram [59] was used. An alternative preprocessing technique used in this case was cepstrum pre-whitening [57]. By this means, the signal spectrum amplitude is set to a constant value (whitened) and the original phase used to generate a time signal. This simultaneously nullifies the effect of both discrete frequencies and resonances, so that a

frequency band containing an impulsive signal will tend to dominate the time signal. SK can be used to further isolate the impulsive band.

9.2.1 Summary of Processing Algorithm

The five basic steps in the processing algorithm used during the first stage of analysis are listed in Figure 9.1.

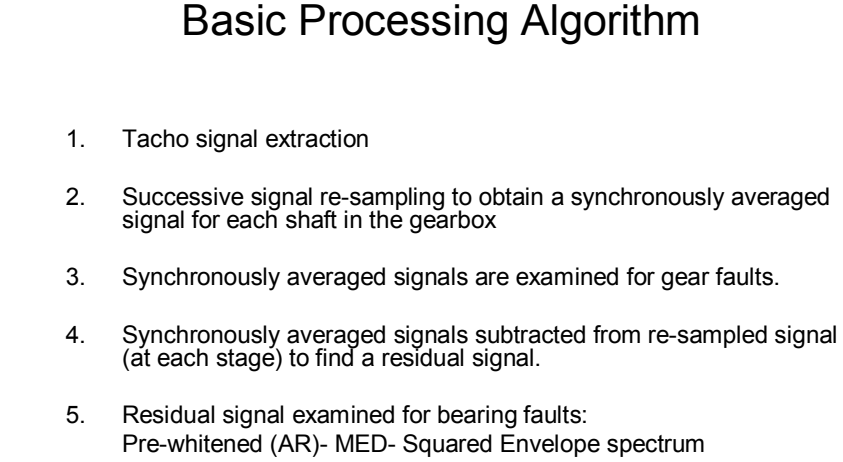

Figure 9.1. Signal processing approach pre release of inspection report

The first stage involves extracting a pseudo tachometer/encoder (tacho) signal from the measured vibration signal; it was found that the speed signal provided by NREL was only useful for giving an arithmetic mean estimate of the speed of the high speed shaft (generator rotor) and could not be used for re-sampling purposes. The extracted tacho signal was used to resample the signal of interest and extract the synchronous average for the intermediate shaft. The residual signal was pre-whitened as a first step. The squared envelope spectrum was then obtained using the Hilbert transform and scanned for bearing defect frequencies, which had been calculated for each bearing in the gearbox. Pre-whitening was achieved using the newly proposed approach based on the cepstrum (Cepstrum-pre-whitening). This squared enveloped signal was extracted and inspected for bearing faults.

9.2.2 Pseudo Encoder Extraction and Speed Estimate

The process of extracting a reference speed signal is described schematically in Figure 9.2 [60]. In the first step, Figure 9.2 (a), the spectrum of the signal is visually examined to identify a proper HSS (high speed shaft) gear mesh harmonic (and a suitable band around it). Highest separable harmonics are preferable due to the more evident effect of smearing and will give more accurate results. In the second step, Figure 9.2 (b), a buffer (filled with zeros) of a size equal to the FFT size is created. The complex spectrum of interest (band) is transferred to this buffer (placed in the same lines as in the original spectrum). Note that the presentation in Figure 9.2 (b) only shows the amplitude of the spectrum; however, it is the complex spectrum that has been transferred to this buffer and the phase information is thus preserved. Finally the buffer is inverse transformed to the time domain to obtain the reference signal, Figure 9.2 (c). As the buffer is

filled with zeros up to the sampling frequency - negative frequencies were set to zero - the inverse transform signal is analytic (complex), and it is the real part that will then represent the reference signal. Note that zero crossings represent 180° increments in rotation phase, and this is unaffected by amplitude modulation by any positive modulating function.

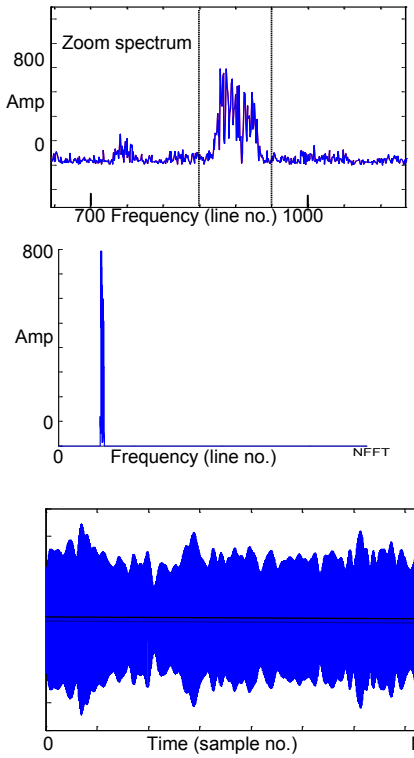

(a) Step 1: Identifying the band of interest. The plot shows the amplitude of the spectrum. Frequency axis scaled in lines rather than Hz

(b) Step 2: Band of interest moved into a buffer filled with zeros

(c) Step 3: real part of the IFFT (Inverse Fast Fourier Transform) of the buffer obtained in step 2.

Figure 9.2. Reference (speed) signal extraction stages: (a) identifying a separable band; (b) extracting the band into a new buffer; (c) inversing the transform signal b into the time domain [60]

The signal obtained in 2.c is a sinusoidal-type signal whose periods represent the speed for each shaft rotation. The speed variation in this signal (a reflection of the speed variation of the shaft under investigation) can be traced using the zero crossings of the consecutive periods, which can be achieved by detecting the zero crossings (an interpolation between the samples on either side). This signal can also be used to order track the signal. Note, however, that this process may have to be repeated progressively to order track the signal to higher harmonics and achieve better results. This means that after each stage, a higher harmonic will be made available due to the reduction of speed fluctuations and the analyst can select bands around the gear mesh harmonics to improve the quality of order tracking and gain more accuracy.

The approach illustrated in Figure 9.2 was used to extract a tachometer and speed signal for the High Speed shaft (HSS) of the gearbox. The speed extraction was based on the gear mesh frequency of the high speed stage (22 × HSS). For this purpose, sensor 7 was selected for extracting the gear mesh signal for the HSS, although this can also be achieved using other

sensors in close proximity to the high speed shaft. The zero crossings for the signal in Figure 9.2 (c) were used to estimate the speed of the HSS. Examples of estimates at two speeds based on this procedure (scaled in rpm) from data *set a* and data *set c* are presented in Figure 9.3. It is noted that the speed is relatively constant.

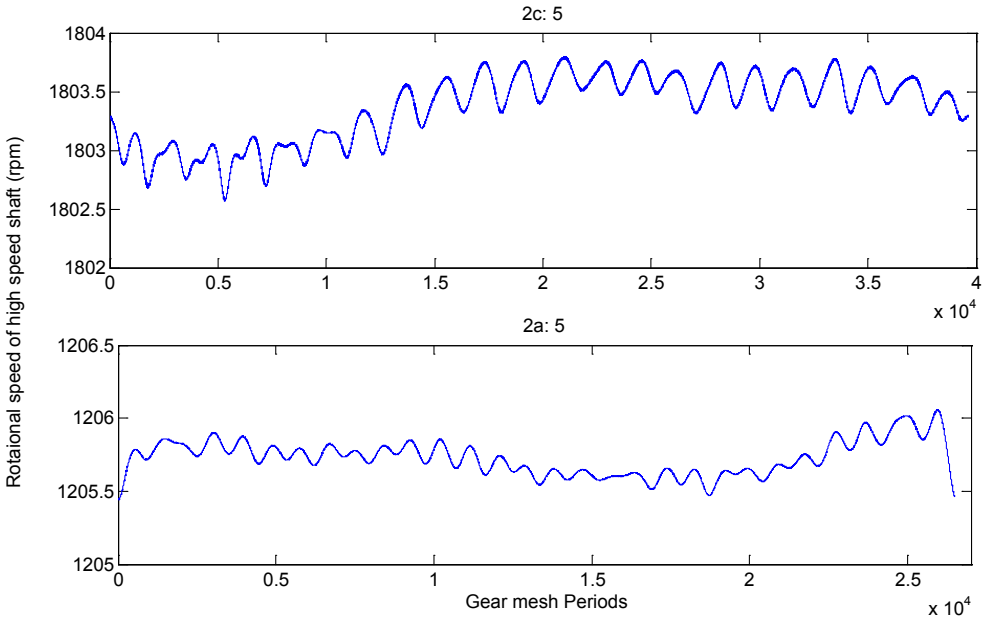

Figure 9.3. HSS estimates: Top - data 2a:5; Bottom - data 2c:5

9.2.3 Successive Re-sampling and Synchronous Average Extraction

A separation algorithm (gear/bearing signal separation) [61,62], which is based on successive re-sampling of the signal under analysis has been adopted to obtain synchronously averaged signals for each shaft and to completely remove the shaft harmonics, without much disruption of the vibration signal.

The algorithm works by re-sampling the order-tracked signal to obtain an integer number of samples per revolution for a specific shaft. The removal of the harmonics of that specific shaft can be achieved by one of two methods. The first is by finding the synchronous average and subtracting it (repeated periodically) from the signal. The second is by truncating the signal to an integer number of revolutions (preferably a power of 2) and setting the lines corresponding to the harmonics of that shaft (after FFT analysis) to $\sqrt{2}$ times the mean (complex) value of the adjacent frequencies (the multiplication by $\sqrt{2}$ is to make the amplitude statistically the mean of the two amplitudes). To avoid treating the negative frequency components, it is recommended that they be set to zero after the FFT step, and double the positive frequency components, then take the real part of the resulting analytic signal in the time domain. Both methods arrive at the same result, as was presented in [62].

The extracted tacho signal was used to resample the signal of interest and extract the synchronous average for the intermediate shaft. As the HSS and the intermediate speed shaft (ISS) have a ratio of four, the removal of the harmonics of HSS was included at this stage. The end result of this stage was four synchronously averaged signals for the ISS, Low Speed shaft

(LSS), the planet carrier shaft, and the planetary gears (a composite of all the planetary gears; this was later updated to extract an average for each planetary gear). Typical results for the four synchronously averaged signals are presented in Figure 9.4 and Figure 9.5 for sensor three (planetary stage and low speed shaft) for both *data set a* and *data set c*.

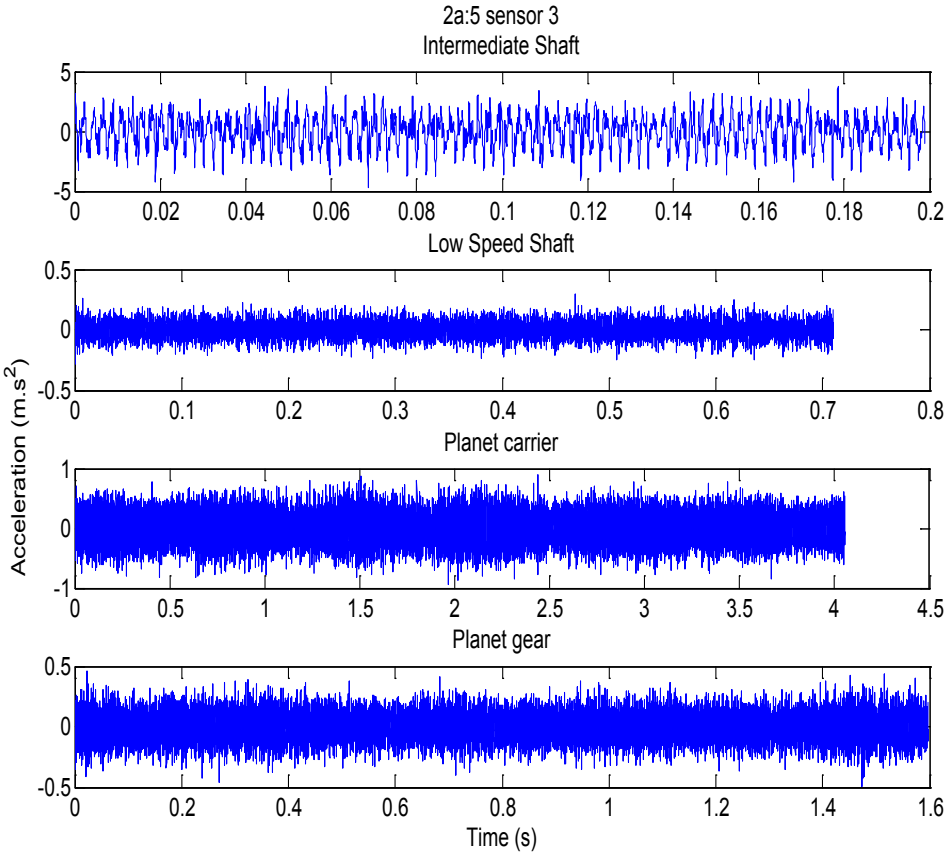

Figure 9.4. Synchronously averaged signals from sensor 3, data 2a:5

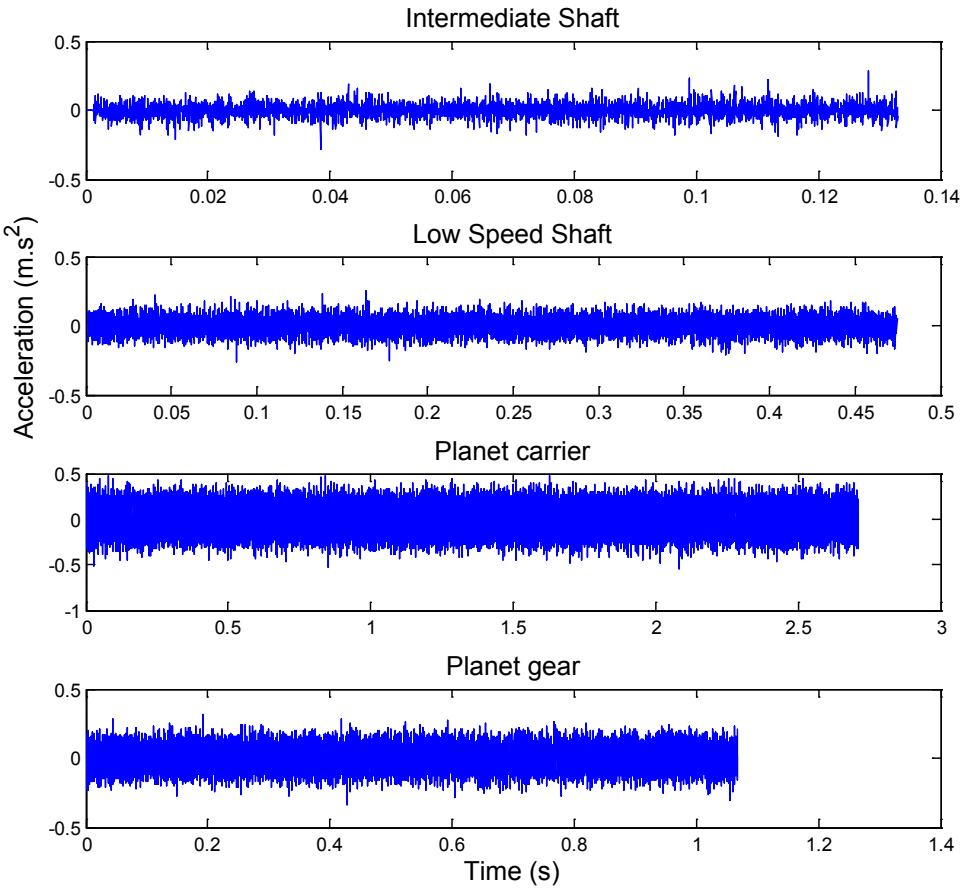

Figure 9.5. Synchronously averaged signals from sensor 3, Data 2c:5

9.2.4 Residual Signal Processing for Bearing Fault Detection

After the removal of the synchronously averaged signals, a residual signal is obtained. This should contain non-stationary and second order cyclostationary components. As a first step to enhance the residual signal and maximize the impulsiveness, the residual signal was pre-whitened. Pre-whitening was attempted using a newly proposed approach based on the cepstrum (cepstrum-editing). The approach is described in Figure 9.6. The extreme case of this approach is where the real cepstrum is set to zero (spectrum amplitude set to one, i.e. whitened). Both discrete frequencies and resonances are thus removed. Uniform spectrum weighting means that impulsive frequency bands dominate the time signals.

The whitening stage can, in fact, be used on the raw signals giving an enhancement of the bearing related signature. The advantage of pre-whitening is that all frequency components in this signal are equally weighted and, thus, the potential to detect faults is enhanced.

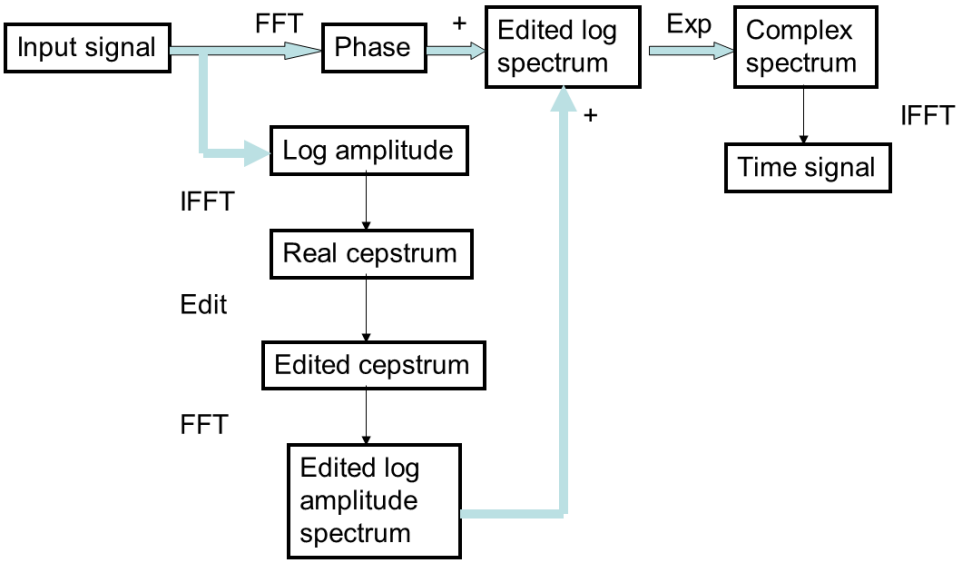

Figure 9.6. Schematic diagram of the cepstral method for removing selected families of harmonics and/or sidebands from time signals [57]

The squared envelope spectra for the pre-whitened residual signals were obtained using Hilbert Transform techniques (simply by inverse transforming one-sided spectra, shifted to zero frequency, and taking the modulus of the resulting complex numbers).

9.3 Results

9.3.1 Bearings

9.3.1.1 Initial Bearing Diagnosis Results

Through the inspection of the squared envelope spectra of the residual signals obtained from section 9.2.4, two defective bearings were identified. These are FAG 3222 and NU 2220 ECM. The diagnosis indicated an inner race fault on bearing FAG 3222 and an inner race fault and roller/cage defect on the NU 2220 bearing.

The inner race fault (localized spalling) of the FAG thrust bearing (3222) was mainly detected through signals from sensors seven and nine. The envelope spectra from these sensors contained the ball pass frequency of the inner race (BPFI), and its harmonics were clearly modulated by the high speed shaft speed. An example from the low speed data (*set a*) and the high speed data (*set c*) is shown in Figure 9.7 and Figure 9.8 respectively. In Figure 9.7, the high speed shaft frequency (20.1 Hz) and its second harmonic are clearly visible. The 230.7 Hz component (suspected BPFI) and its second harmonic are modulated by the frequency of the high speed shaft. The calculated BPFI for the FAG bearing (3222) at an inner race shaft speed of 20.1 Hz is around 218.5 Hz. The difference between the observed BPFI in the figure and the calculated one is around 5.5%, which can be due to slippage and an incorrect estimation of load angle. This rate of slippage is also observed for the high speed data (*set c*) in Figure 9.8, where the BPFI of 345.3 Hz and its second harmonic are observed. The 345.3 Hz component has around a 5% difference from the calculated BPFI, which is in agreement with the low speed data observation of Figure 9.7.

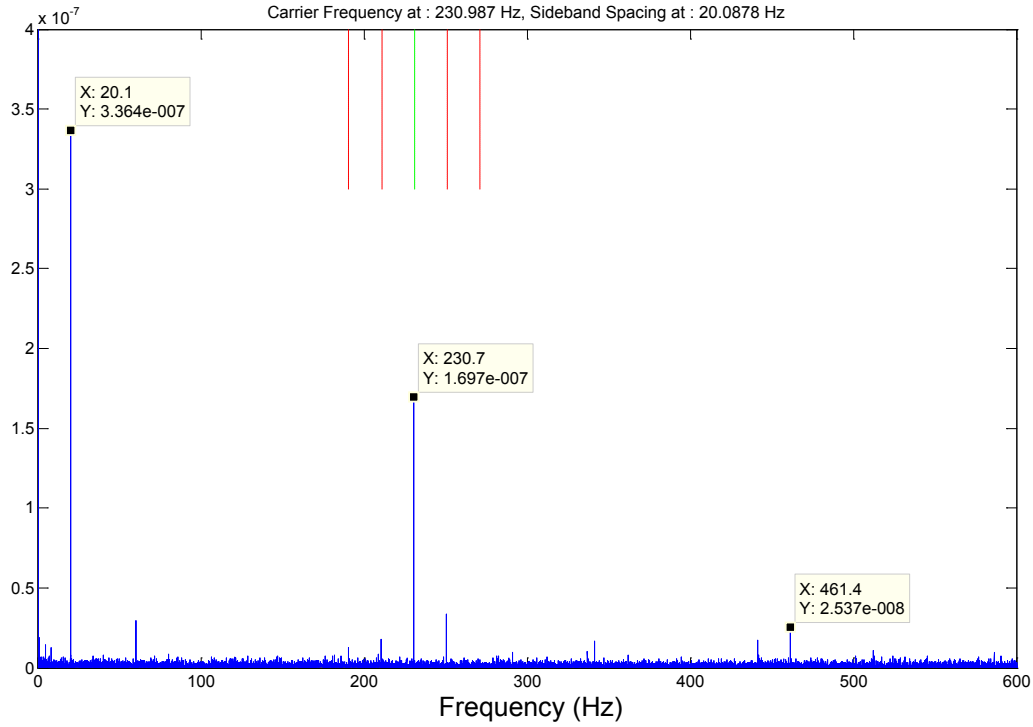

Figure 9.7. Squared envelope spectrum for data 2_a_10 sensor 7

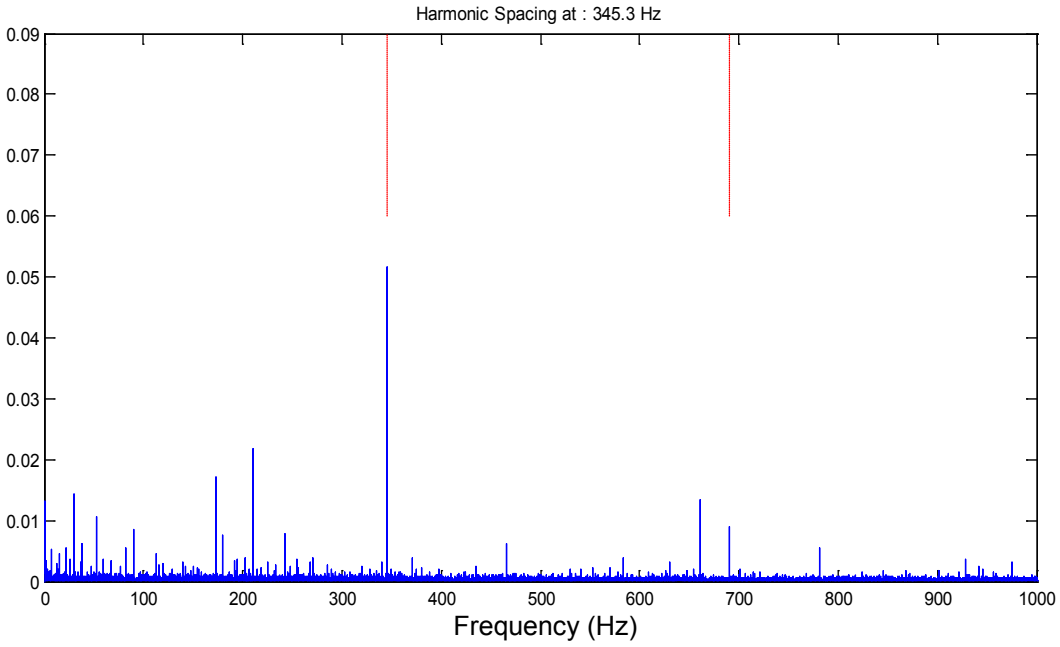

Figure 9.8. Squared envelope spectrum for data 2_c_10 sensor 7

Figure 9.9 shows that the suspected BPFI of 345.3 Hz is close to one of the harmonics of the intermediate shaft (46th harmonic), but is not in fact a harmonic of the intermediate shaft.

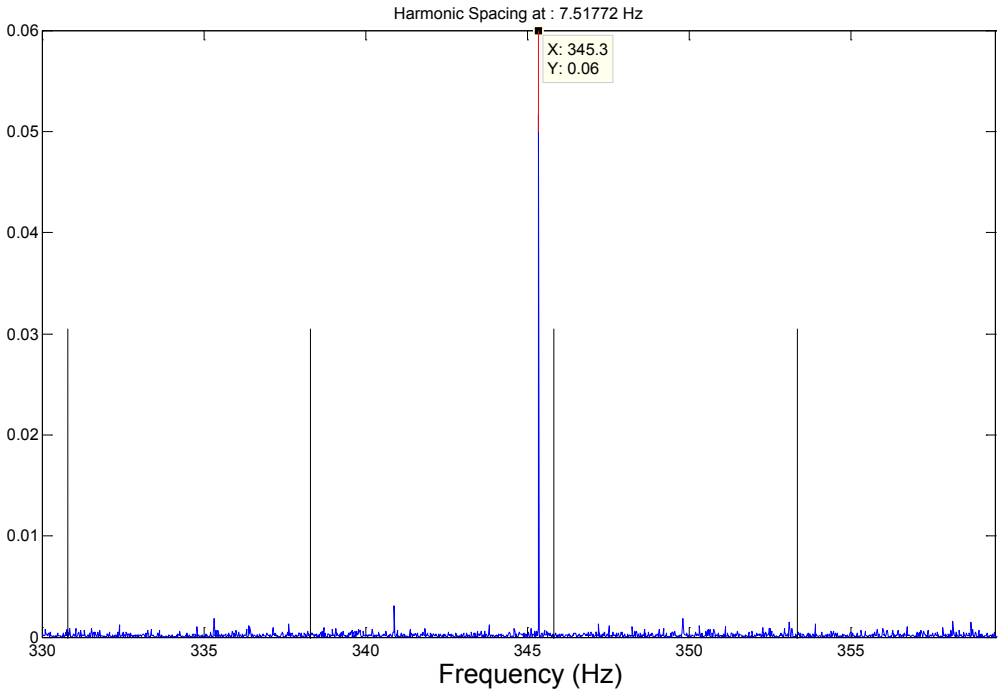

Figure 9.9. Zoom-in around the BPFI. Harmonic cursors for the ISS

The second bearing fault diagnosis indicated the presence of an inner race fault and possible roller/cage pitting in the SKF HSS upwind bearing (NU 2220 ECM). This was detected mainly through sensor eight and was confirmed by testing data from *set a* through the presence of the BPFI, its harmonics, and the modulation of these harmonics by the high speed shaft speed. There are also indications of modulations by the fundamental train frequency (FTF), which can come from variations between rollers.

In Figure 9.10, the BPFI at 198.08 Hz modulated by a shaft speed of 20.091 Hz is observed. This matches very closely the calculated BPFI of bearing NU 2220 ECM at a shaft speed of about 20.1 Hz. The FTF harmonics (12.8 Hz) are at the same speed for the NU 2220 bearing, as shown in Figure 9.11.

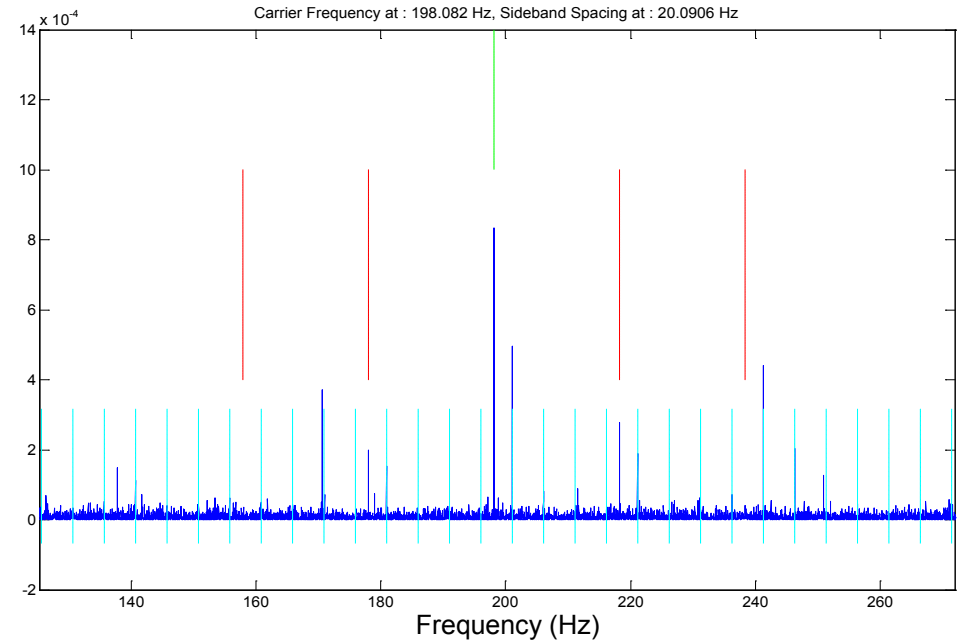

Figure 9.10. Squared envelope spectrum for data 2_a_5 sensor 8 showing the BPFI of bearing NU2220

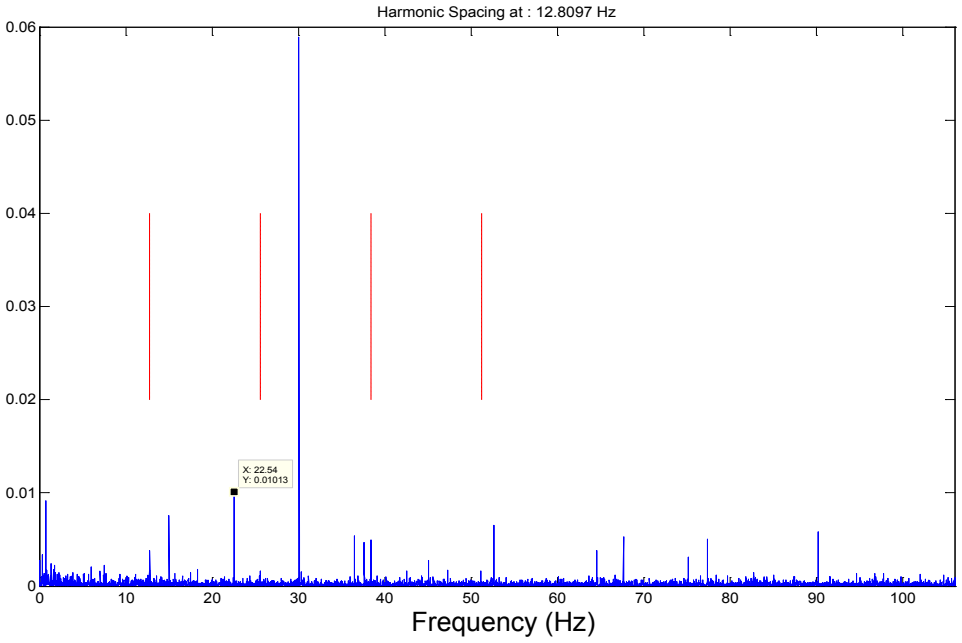

Figure 9.11. Squared envelope spectrum for data 2_a_5 sensor 8 showing the FTF harmonics of bearing NU2220

9.3.1.2 Actual Findings and Missed Detection

In the test gearbox failure analysis report [4], it was shown that the IR raceway and rollers of bearing 3222 had straw-yellow temper colors. The color implies that the temperature reached about 400°F. The root cause of the overheating was probably lubricant starvation. Even though no spalls were detected, it is likely there was geometric distortion from the overheating. The IR of bearing NU 2220 ECM had assembly damage at the roller spacing caused by cocking of the rollers during blind assembly. Debris dents and lines of false brinelling were also observed. The IR of bearing NU 2220 ECM had corrosion at roller spacing.

The spacer for bearing 32032X outer race had assembly damage at the roller spacing caused by interference with the bearing rollers during assembly. This damage was missed in our initial (and later) diagnosis. The ball-pass frequency of the outer race (BPFO), when the HSS speed is 30 Hz is estimated at 105. 9 Hz. Figure 9.12 shows the squared envelope analysis for data c_5, sensor 6, where the HSS is 30.06 Hz and is present. A frequency at 210.4 Hz appears clearly in this figure. This is close to 7×HSS, but it is also close to 2×BPFO. This main evidence seems to indicate the presence of the fault in the 32032X, but it was not considered strong enough for us to call the fault. Note also the presence of the 345.1 Hz, which is the BPFI of the NU 2220 bearing. Also, upon inspection of the spectrum comparison of sensor five (Figure 9.13), there is a strong presence of 210 Hz and a change around this frequency, in particular.

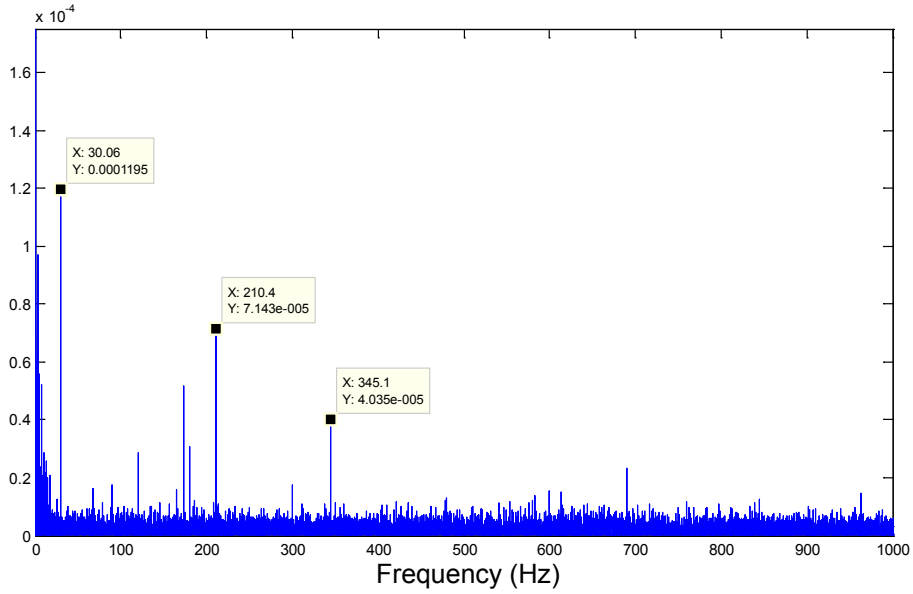

Figure 9.12. Squared envelope spectrum of data 2c_5 sensor 6 showing the shaft speed (30.06 Hz), what appears as 2×BPFO for bearing 32032X and the BPFI for bearing NU 2220

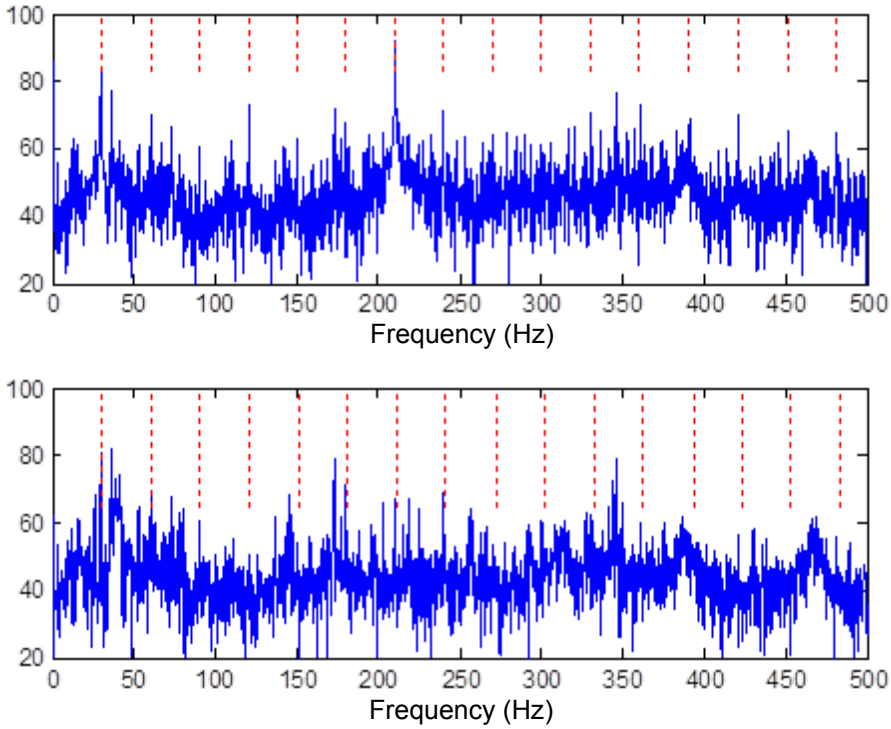

Figure 9.13. Power spectrum density comparison of the high speed data through sensor 5

9.3.2 Gears

9.3.2.1 Initial Diagnosis

Initial diagnosis indicated the possibility of severe damage in the planetary stage of the gearbox. The main indications came through sensors three and four and were observed more in the low speed data (set a). It was noticed that the impact pattern came in pairs (roughly separated by 10-12 teeth on the planetary gear). This was clearly observed in data 2_a, but not very clearly in 2_c. The residual signal from sensor five for data 2a_5 is shown in Figure 9.14, where the impacts are seen clearly. The analysis of the squared envelope spectrum of the signal, Figure 9.14, is shown in Figure 9.15. The carrier speed (around 0.25 Hz), the spin frequency of the planetary gear (PGSF) at around 0.625 Hz, and 3×PGSF are very clear in Figure 9.15. It was indicated at the time of this diagnosis that to confirm this, further analysis would be required to obtain the synchronous average with respect to each planet.

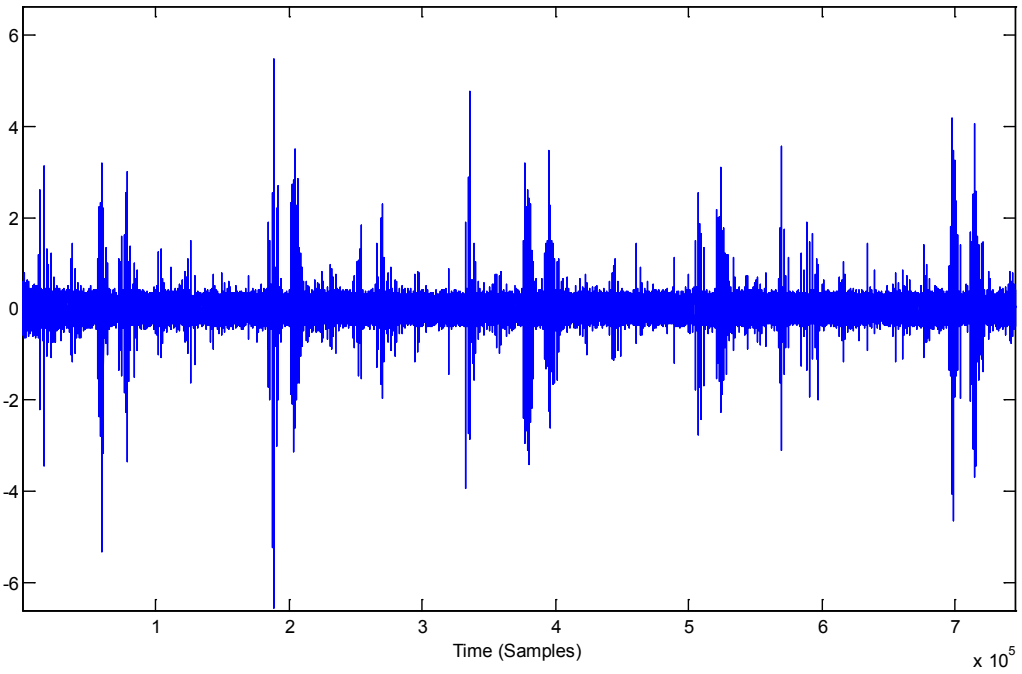

Figure 9.14. Residual of signal 2a_5 sensor 5

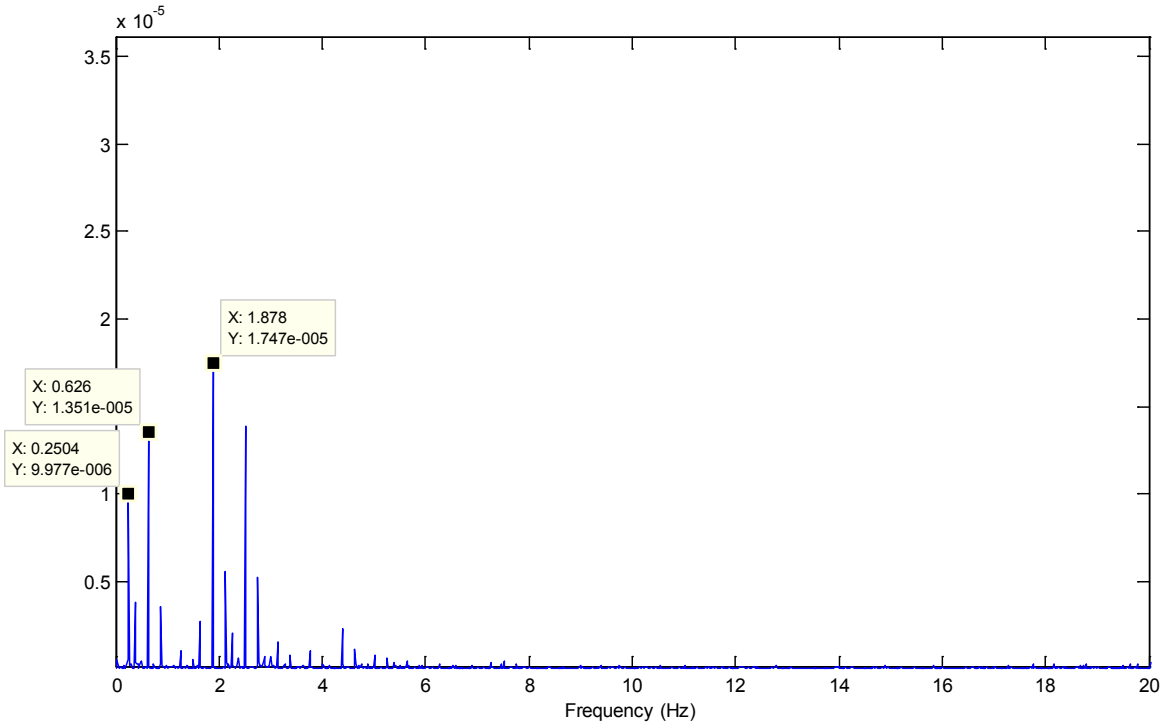

Figure 9.15. Squared envelope spectrum of the residual signal shown in Figure 9.14

9.3.2.2 Revised Diagnosis

The revised diagnoses included using the healthy set of data and comparing it with the faulty one, in both the frequency domain (using power spectrum density) and the cepstrum domain. The revised analysis also included the removal of shaft related components from the synchronously averaged signals through pre-whitening. Finally synchronous averages were extracted for the sun gear and each planet using an algorithm earlier developed by DSTO.

9.3.2.2.1 Power spectrum and cepstrum comparisons (healthy and faulty signals)

The scaling for the healthy spectra was given in g's, while the time domain was reported in ms^{-2}. The resolution of the healthy spectra was determined and used to find the equivalent FFT transform size to use with the faulty data. When scaling both in dB, reference level $1e^{-6}$ was used for the faulty data and $1e^{-7}$ for the healthy data to compensate for the units. Comparisons show increases at the gear mesh frequencies and sideband families. This is shown clearly for all sensors (AN3, AN5, AN6 and AN7). Harmonic and sideband cursors show dominant components and modulations.

Cepstra were generated from the corresponding spectra to give more information on sideband patterns. The cepstra represent the amplitude of the analytic cepstrum (from the one-sided log spectrum). This version can also be used on zoom spectra [24].

Figure 9.16 shows the spectrum comparison using the data from sensor three, in the low speed section of the gearbox. There is a noticeable increase (more than 20 dB) in the HSS, the epicyclic mesh frequency, and its sidebands. Most noticeable are the sidebands at the planet pass frequency around the epicyclic mesh frequency in the fault case. This is evident in the cepstrum comparison presented in Figure 9.17. Note the second rahmonic in the healthy case, corresponding to 1½ times the carrier speed, which is unexplained. It is possible that it has something to do with the "far from hunting tooth" design of the planetary section and means that the particular tooth combinations occur much more frequently than usual.

In Figure 9.18 and Figure 9.19, the spectrum and cepstrum comparisons based on the data from sensor five, with generator speed 30 Hz, are presented. The fact that the cepstrum does not change appreciably shows that modulation at ISS (which would come from local faults) did not occur, and the corresponding lack of sidebands in the faulty spectrum confirms that the faults are distributed.

The distributed wear of the intermediate shaft pinion, ascribed in the inspection report to the hunting tooth ratio, is shown in Figure 9.20 in the growth of the harmonics of the IS gear mesh.

Figure 9.21 shows the same spectra, but concentrates on the growth of sidebands around the HS gear mesh harmonics, and they are spaced at the HS shaft speed. The corresponding cepstra of Figure 9.22 shows that the local faults causing the sideband generation have grown from nothing in the healthy condition; whereas, the increased peak corresponding to the ISS probably indicates some growth of harmonics at this shaft speed since the sidebands were not in evidence. Both the high speed pinion and gear had localized scuffing, which would explain the strong modulation at HSS speed.

Data from sensor seven in Figure 9.23 shows the same story as Figure 9.21.

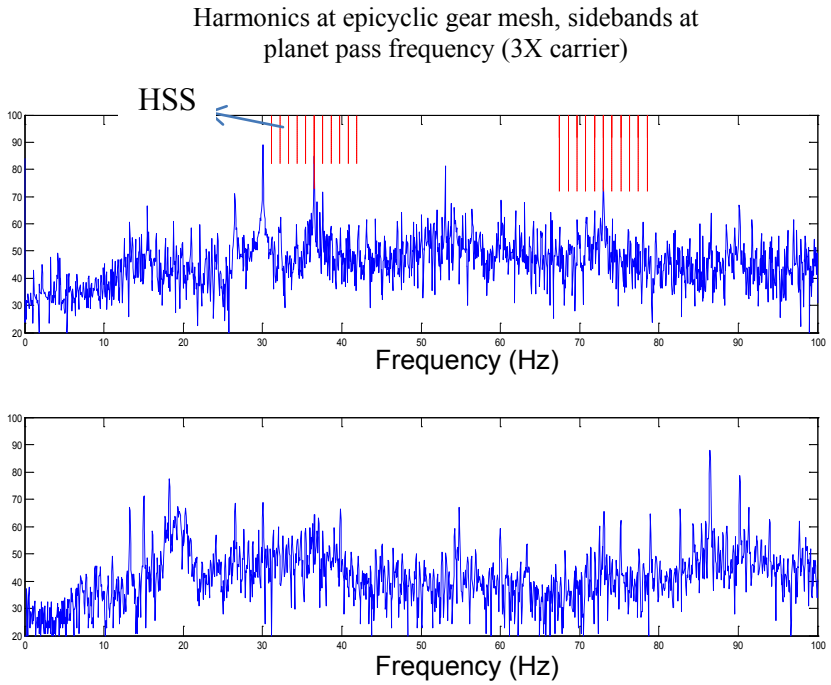

Figure 9.16. Spectrum comparison using the data from sensor 3

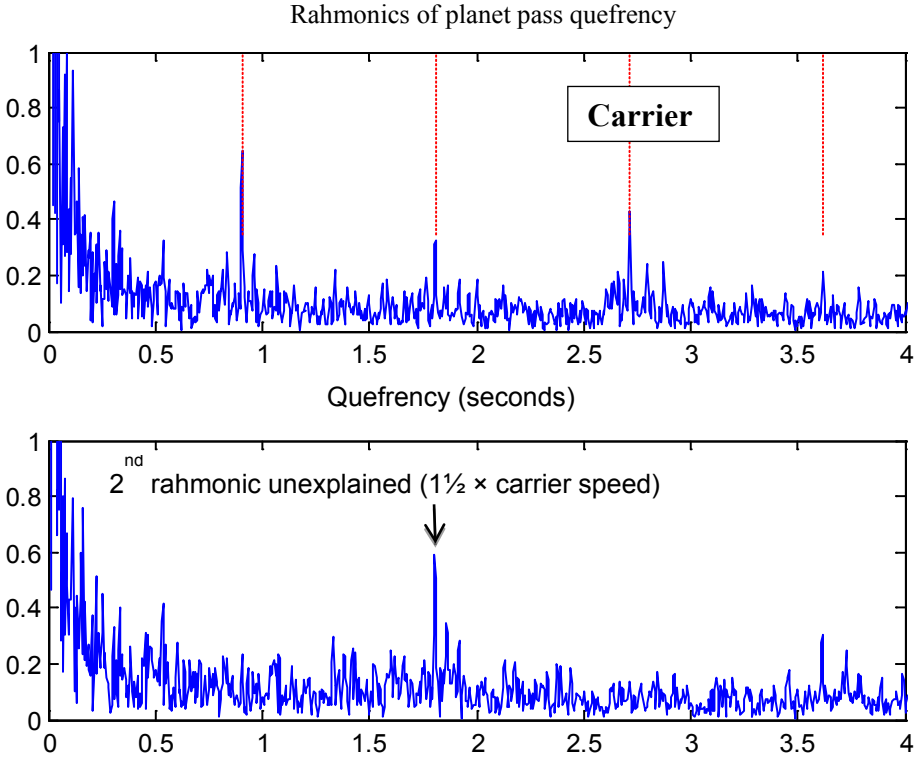

Figure 9.17. Cepstrum comparison using the data from sensor 3

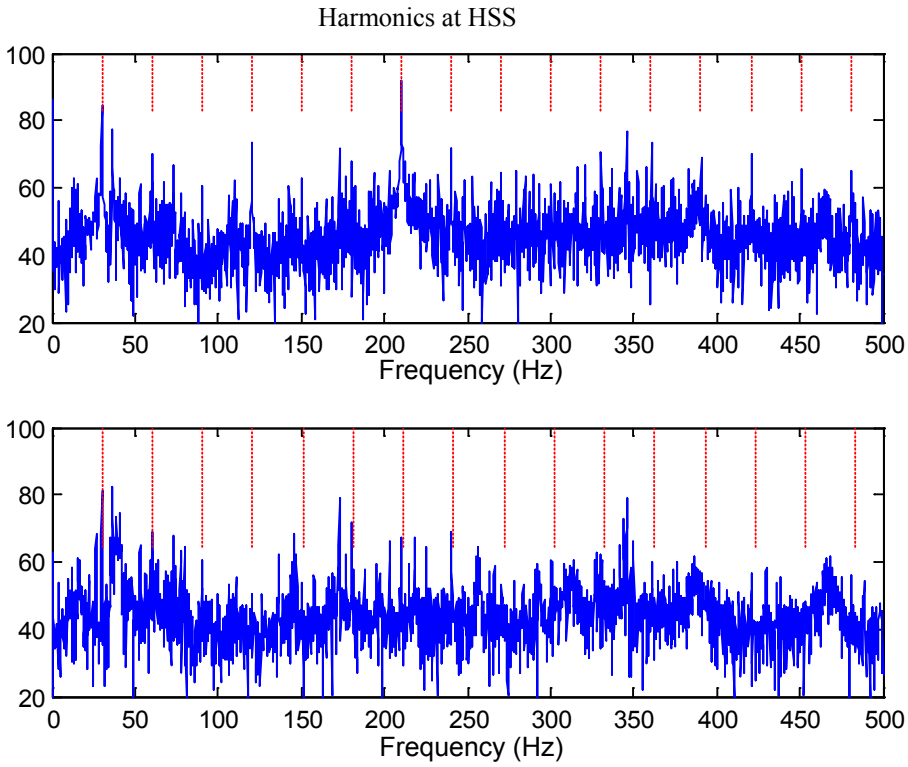

Figure 9.18. Spectrum comparison using the data from sensor 5

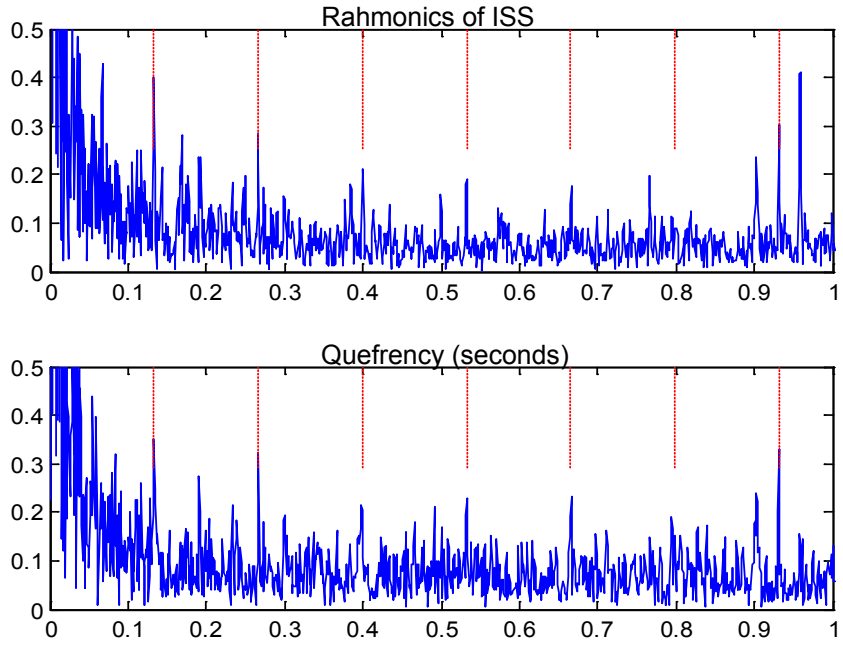

Figure 9.19. Cepstrum comparison using the data from sensor 5

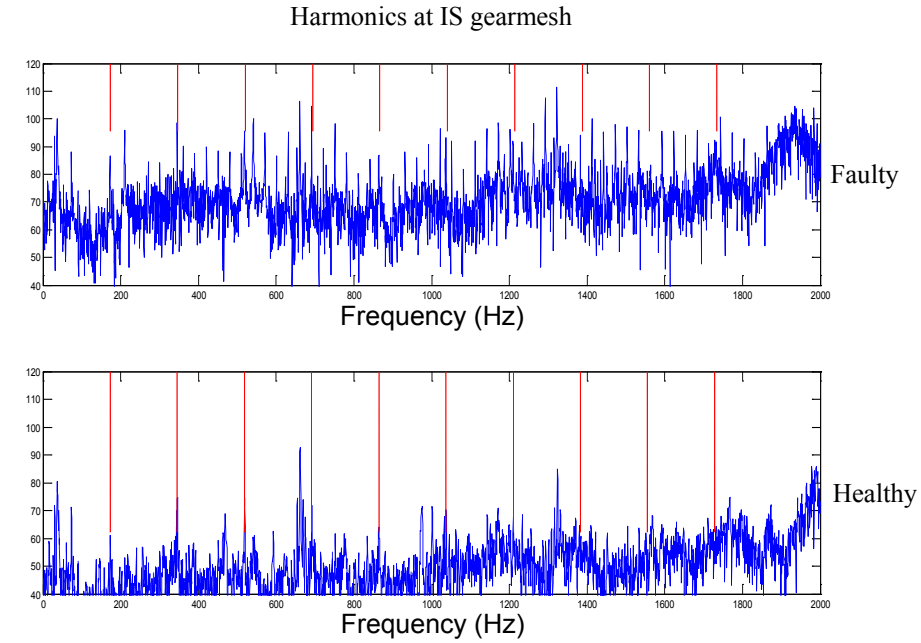

Figure 9.20. Spectrum comparison using the data from sensor 6

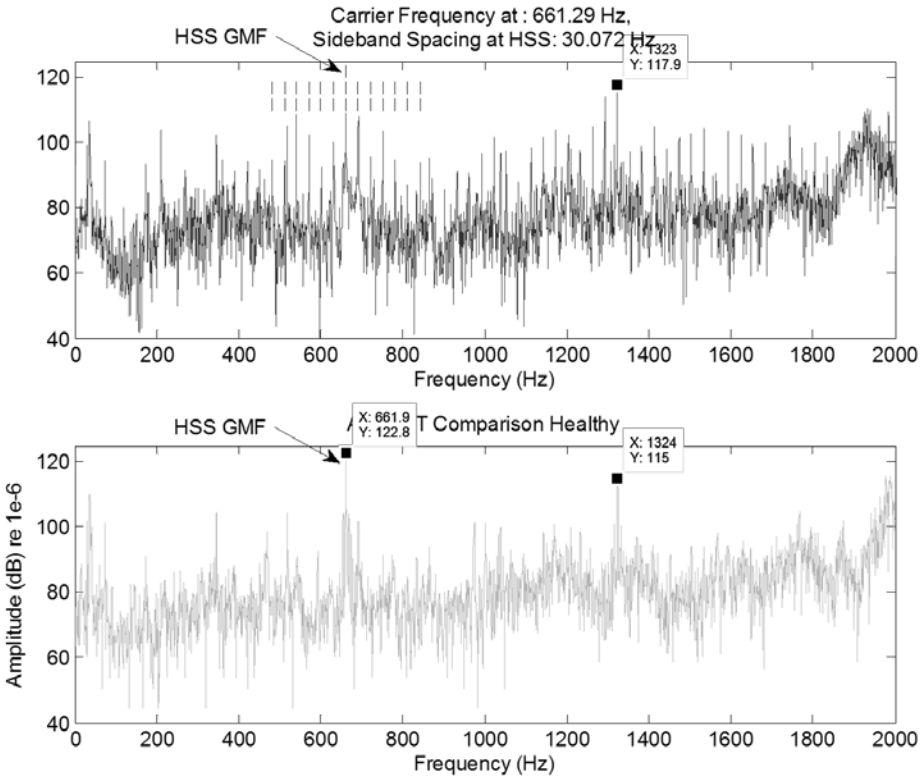

Figure 9.21. Spectrum comparison using the data from sensor 6

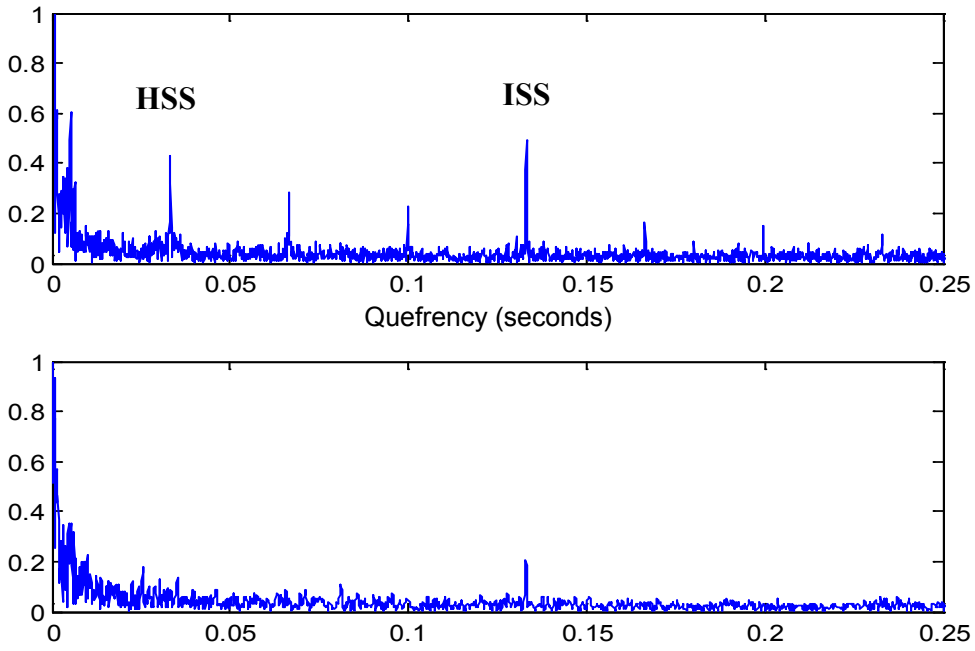

Figure 9.22. Cepstrum comparison using the data from sensor 6

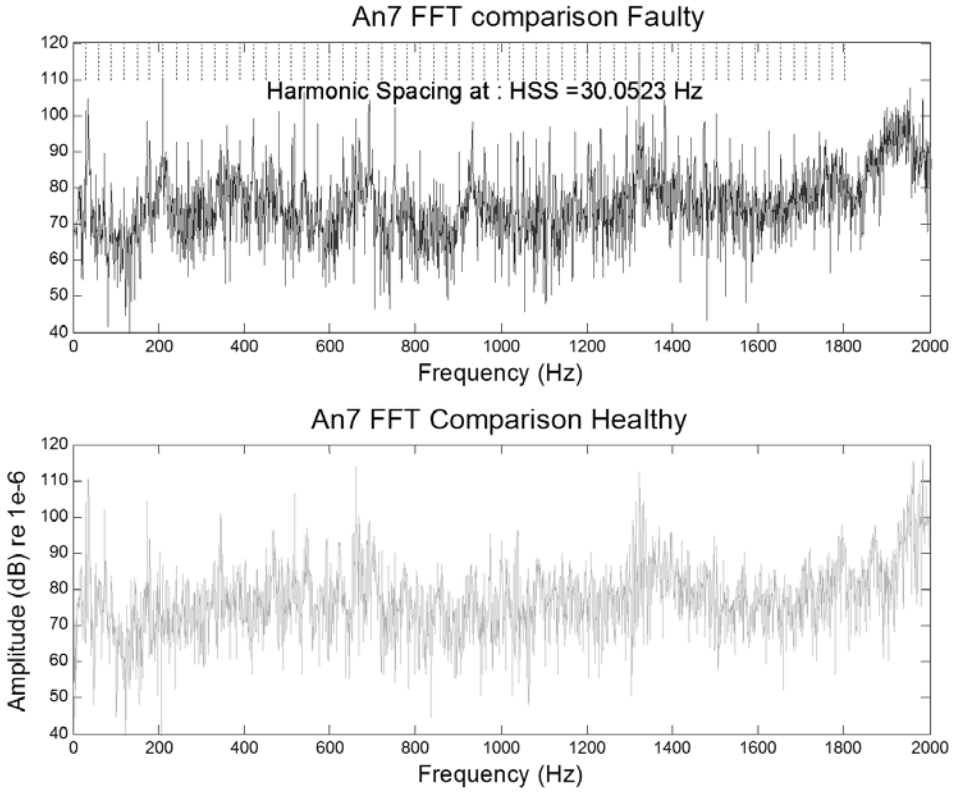

Figure 9.23. Spectrum comparison using the data from sensor 7

9.3.2.2.2 AN6 ISS signal processed to remove effects of HSS

Because the ratio is exactly 4:1, the ISS record was divided into four sections, which were averaged, recombined, and subtracted. The residual record should contain only information from the ISS, for example, the shaft harmonics that are not divisible by four and the IS gear mesh frequency (23X). Time signals and spectra are shown in Figures 9.24 and 9.25.

The HS gear mesh is strongly modulated by the HSS, because damage is more localized. The IS gear mesh is much distorted, with many harmonics, but it is not modulated. This is compatible with the distributed damage attributed to the hunting tooth design.

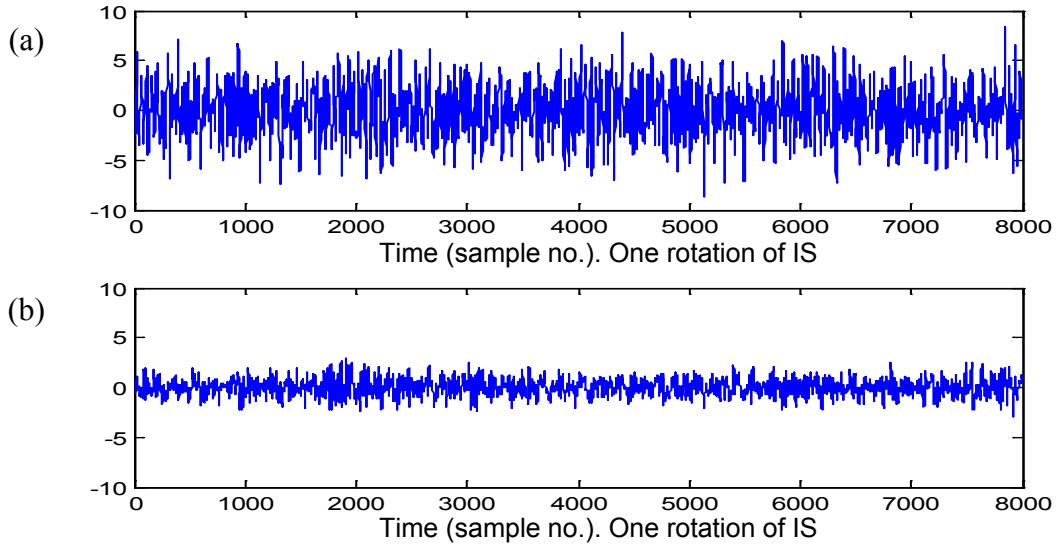

Figure 9.24. Time records from the averaged ISS signals: (a) original, including four rotations of the HSS; (b) Residual after removal of the HSS average.

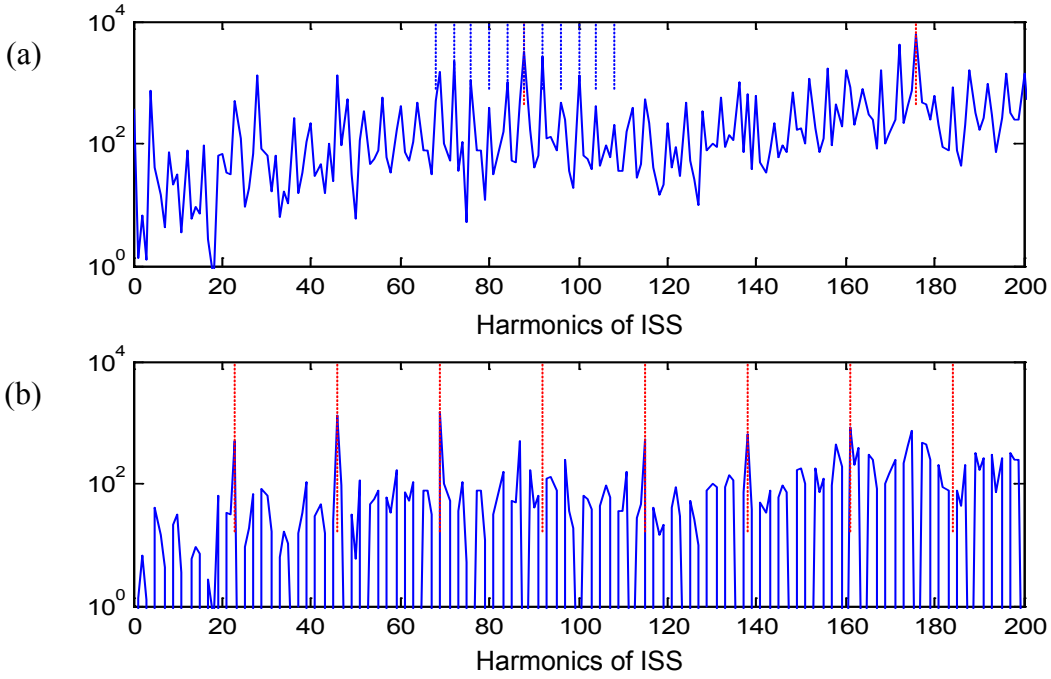

Figure 9.25. Spectra of signals of Figure 9.24: (a) original including four rotations of the HSS; (b) residual after removal of the HSS average.

9.3.2.2.3 Synchronously averaged signals pre-whitened

The pre-whitened synchronous averages presented in Figure 9.26 show impact events of the damaged gears (not just a single impact). Such impacts appear clearly in all stages (AN3). Note that the denomination "Planet Carrier" really refers to an average over the annulus gear, since one revolution of the planet carrier corresponds to meshing with all teeth on the annulus. Local faults were found on the HS gear of the intermediate shaft, on the sun gear (and spline) of the

low speed shaft, and on the annulus gear. No faults were reported on the planet gears, but this is discussed in the next section.

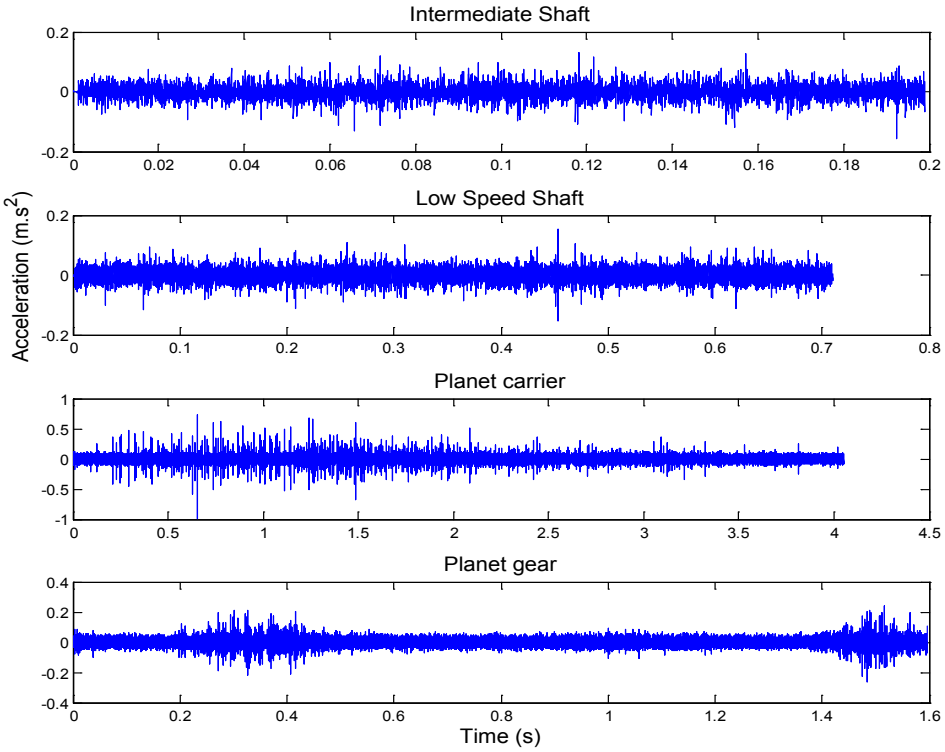

Figure 9.26. Whitened synchronously averaged signals corresponding to the periods of all major gear components in the gearbox, which enhance local faults

Note that the "Planet gear" result is a composite of all planets, and shows a similar result to the individual planets in the next section.

9.3.2.2.4 Planet, sun, and annulus gear signatures extracted by Dr. David Forrester using patented DSTO software[#]

Signatures for each planet and the sun gear were extracted by shifted and weighted averages of signals taken as the various planets pass the measurement point [63]. Note that the signature for each planet tooth is actually a composite of the two teeth meshing simultaneously with the annulus and sun gears (opposite flanks). This is an important observation since no faults were reported on the planet gears, even though virtually all Round Robin partners detected apparent faults corresponding to the planet gear rotation period. This is discussed further below.

The DSTO patented method described in [63] and illustrated below produces average time signals for each individual planet gear and the sun gear using shifted weighted signals from passage of each planet past the transducer, with correction for the phase offset of individual teeth

for each passage. Note that the average for the sun gear can include the contact of individual teeth with all planet gears.

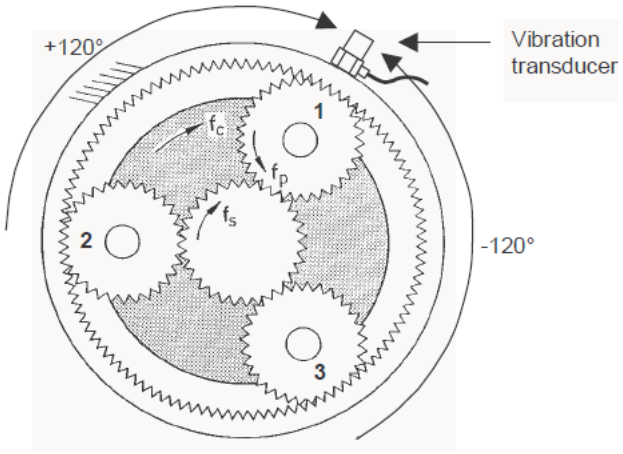

Figure 9.27. Phase shifts for separated sun gear averages

The residual mentioned in some figures is the result of removing the regular tooth mesh signal so as to highlight local faults on a gear.

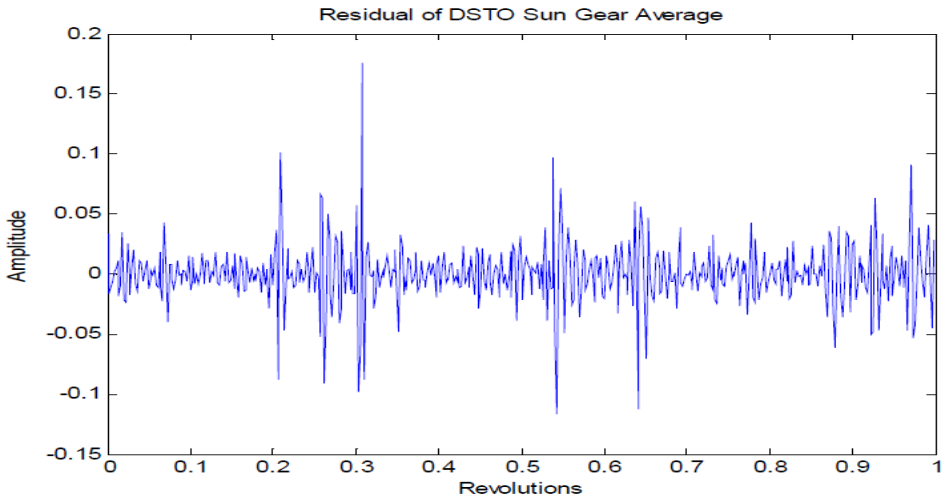

Figure 9.28. Sun Gear – residual of DSTO average data set 2c (high speed, high load)

Figure 9.28 shows the residual signal for the sun gear at high speed and load. This result is compatible with the observation of the inspection report that the sun gear had localized fretting corrosion**.**

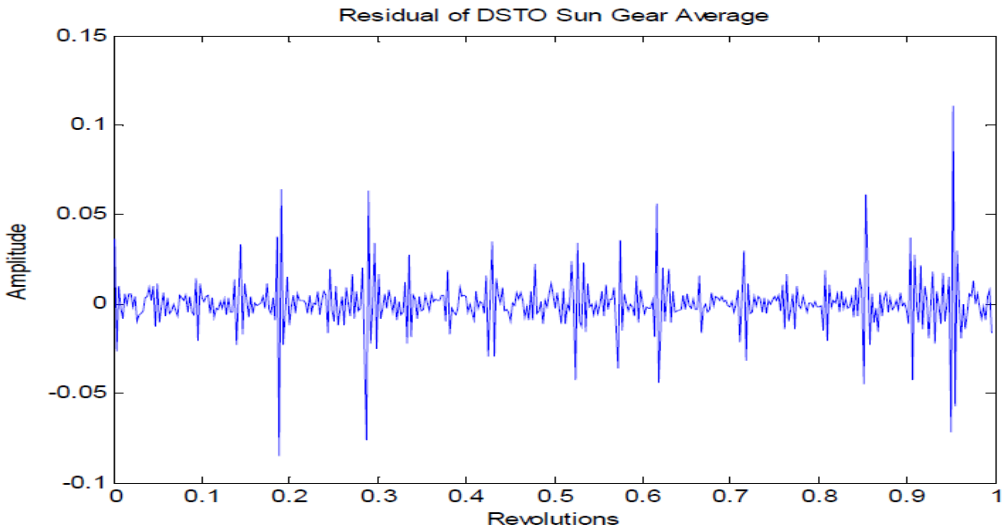

Figure 9.29. Sun Gear – residual of DSTO average data set 2a (low speed, low load)

Even at a very different speed and load, in Figure 9.29, the sun gear signature is almost identical (though displaced because there is no common phase reference). The same was found for the individual planet gear signatures discussed below, in Figure 9.30.

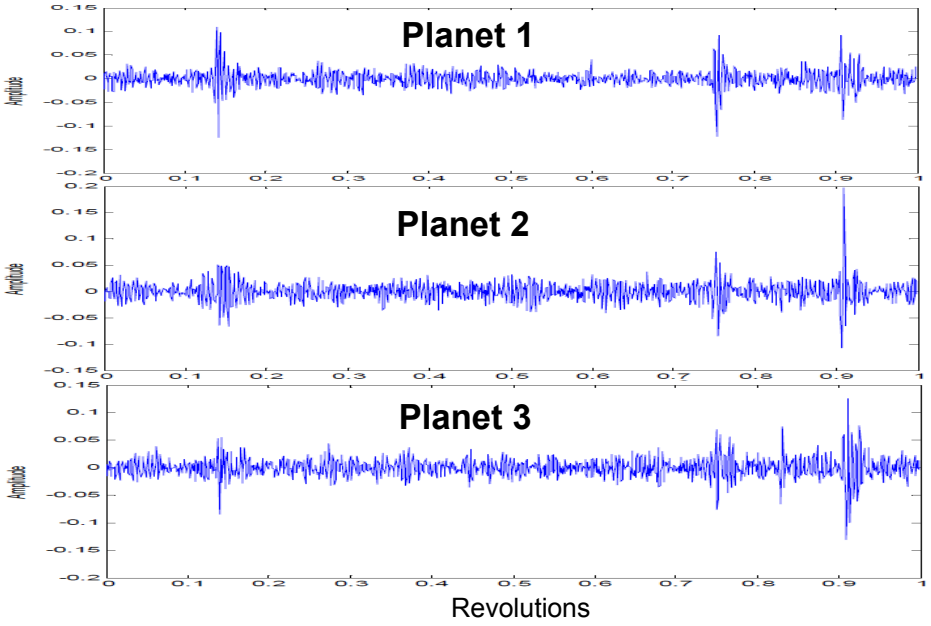

Figure 9.30. Residual signals for the three planet gears

Several Round Robin partners found evidence of faults on the planet gears, even though none were reported in the inspection report, but the above figure implies that the fault patterns are the same on all three planets. This could be caused by the "far from hunting tooth" design of the planetary section. Individual pairs of teeth on the annulus and sun gears, both of which had

faults, could mesh simultaneously on opposite sides of a given planet gear relatively frequently. It would be natural for this to occur identically for all three planets, since all tooth numbers are divisible by three. This potential explanation should be confirmed by more detailed analysis of the kinematics of this particular configuration.

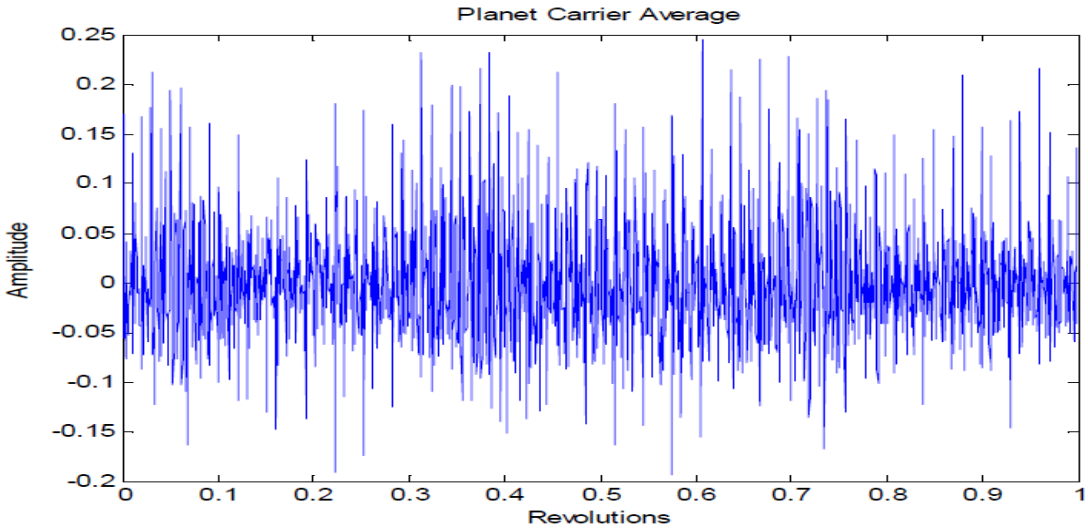

Figure 9.31. Average for the annulus gear

Figure 9.31 shows a typical average signal for the annulus gear. The residual in this case did not clarify the local faults to any great extent. However, the visible variations are compatible with the results of the inspection report, which found a distributed fault pattern from a local area of scuffing. Because of the numbers of teeth of all planetary components being divisible by three, the damage tended to imprint on every third tooth, and many examples this pattern over groups of three teeth can be seen in the above figure.

9.4 Discussion, Conclusions, Lessons Learned

This research showed that our methods for analyzing gear and bearing faults in wind turbine transmissions are basically sound, and picked up most faults that could be expected to change the vibration patterns. In the initial blind analysis, we correctly detected faults in two of the three bearings with faults, usually in data from both low and high speed operation. We did, however, miss a fault in the ISS bearing, which should have been detectable, and are at a loss to explain why. There is a possibility that there was not good transmission to any of the measurement points. We did find indications of local faults on a gear on the IS shaft (initially not separated from the HS shaft because of the exact 4:1 ratio), the sun gear, and the annulus gear. There was also an indication of local faults on one or more of the planet gears.

When spectra were received for the gearbox in healthy condition, at about the same time as receiving the inspection report, considerably more detailed analysis could be done as to the details of the faults on each gear. An exception was the indication of faults on the planet gears, which were not found on inspection. Much of this analysis could have been done blind, with the availability of a healthy data for comparison from the outset.

Much more detailed analysis was later performed by Dr David Forrester, of DSTO in Australia, using patented algorithms that allowed for the production of separate averages for the individual planet gears and sun gear. These corresponded well with the detected faults on most gears, but once again indicated faults on the planet gears. Other Round Robin partners found the same. It now seems likely that the misdiagnosis was due to the "far from hunting tooth" design of the planetary section, which could mean that faulty teeth on the sun and annulus gears could mesh simultaneously with a healthy planet gear relatively frequently, and thus give an indication of a fault on the planet gear. The fact that the three planets had the same fault pattern lends credence to this interpretation, as the meshing patterns would likely be the same for all three planets (with all tooth numbers divisible by three). This hypothesis needs to be further investigated before it can be confirmed.

This highlighted the fact that gear diagnostics is made easier by the adoption of designs as close as possible to "hunting tooth" designs, considered good design practice in any case. The exact 4:1 ratio between the IS and HS shafts also made it difficult to separate the faults on gears on these two shafts, although luckily the second mesh on the ISS was a hunting tooth design.

For the relatively modest speed variations in the test data, it was possible to extract information on instantaneous speed from the signals themselves in the form of a "pseudo-encoder" signal. The signal, typically based on a high speed gear mesh component, can be used for order tracking and, thus, synchronous averaging of gear signals throughout the gear train. For larger speed variations, which are not uncommon with pitch controlled wind turbines, it would be necessary to start with a lower order harmonic of the shaft speed; however, in principle, the process can be done iteratively to improve the speed correction. This should be tested in the future.

10 A Two Stage Fault Detection Framework for Wind Turbine Gearbox Condition Monitoring

Pingfeng Wang* and Prasanna Tamilselvan
Department of Industrial and Manufacturing Engineering, Wichita State University
*Corresponding Author Email: pingfeng.wang@wichita.edu

10.1 Introduction

Maintaining wind turbines in top operating condition ensures not only a continuous revenue generation but a reduction in electric power drawn from non-renewable and more polluting sources. Despite the large capital for establishing a wind farm, the maintenance activities of wind turbines are the primary contributors for the wind energy costs [64-66]. The need for reduction in O&M costs are likely to increase due to the rising competition in today's global economy. Effective health diagnosis of wind turbines provides various benefits, such as improved reliability and reduced costs for operation and maintenance (O&M). Research on real-time diagnostics and prognostics, which interpret data acquired by smart sensors and distributed sensor networks, and utilization of these data streams to make critical O&M decisions offers significant advancements in creating early awareness of wind turbine health condition before unexpected failures. The unexpected breakdowns can be prohibitively expensive since they immediately result in lost production [67-70]. To reduce, and possibly eliminate such problems, real time condition monitoring is required to avoid sudden catastrophic system failures. Vibration analysis is the most vastly used mechanism of condition monitoring in wind turbines. It is mainly applied to identify the current condition of rotating components, such as gearbox, generator, and main bearing, by installing mechanical sensors on the components. The defects of the components are estimated based on the vibrations produced by these components during operation. This chapter presents the vibration based condition monitoring framework with analytical defect detection method and graphical analysis developed for the CM Round Robin study.

10.2 Vibration Based Condition Monitoring Framework

The framework for the proposed vibration-based condition monitoring is shown in Figure 10.1. The two major stages included in the vibration based condition monitoring framework are analytical diagnostics and graphical analysis of frequency domain signals. The raw time domain vibration data is pre-processed and converted into frequency domain data. The sideband and kurtosis-based online defect detection method is employed to process the frequency data analytically. The results from the analytical diagnosis are used as inputs to the graphical verification process. The failure modes and their severity levels are determined by graphical verification from the multi-dimensional vibration-based sensory signals.

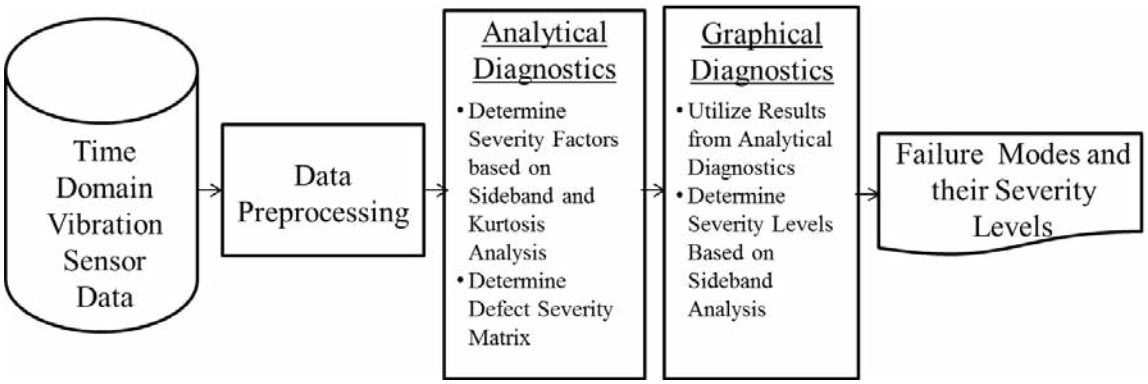

Figure 10.1. Vibration based condition monitoring approach

The pre-processing of vibration data involves three steps, as shown in Table 10.1. The primary step of the vibration analysis is the calculation of gear and bearing frequencies. The gear meshing frequencies of all the gears, bearing frequencies such as Ball Passing Frequency Outer (BPFO), Ball Passing Frequency Inner (BPFI), and Ball Spinning Frequency (BSF) of all the bearings were determined for both speeds 1200 rpm and 1800 rpm. The next step involves the identification of the relationship between the sensor and the components. The final step in the pre-processing is to develop the frequency spectrum from the raw time domain vibration signal using the fast Fourier transformation (FFT) process for the desired sensors.

Table 10.1. Procedure for vibration data preprocessing

Step 1	Calculate Gear Meshing Frequency (GMF) for gears and bearing frequencies
Step 2	Determine relationship between sensors and components
Step 3	Develop FFT plot for desired sensors in each case

The Round Robin study involves three speed stages: low speed (LS), intermediate speed (IS) and high speed (HS). In this research, the high frequency rotating components such as intermediate and high speed stages of the gearbox are only considered for damage detection. Among the total of 10 sensor values from the Round Robin gearbox, the desired sensors for the IS and HS are AN 5 to AN 9. The relationships between these sensors and the components are determined based on the location and proximity to the rotating components, as listed in Table 10.2.

Table 10.2. Sensor and component relationship

Sensor	Sensor Name	GMF	SRF	Bearing	Damage
AN5	LSS radial	IS gear	LSS	LSS upwind and downwind bearing	LSS bearings defect and ISS gear defect
AN6	ISS radial	IS pinion and HS gear	ISS	ISS	ISS bearings defect, IS pinion defect, HS gear defect
AN7	HSS radial	HS pinion	HSS	HSS	HSS bearings defect, HS pinion defect
AN8	HSS front radial	HS pinion	HSS	HSS upwind bearing	HS pinion defect, HSS upwind bearing defect
AN9	HSS rear radial	HS pinion	HSS	HSS downwind bearing	HS pinion defect, HSS downwind bearing defect

The raw vibration signals from the sensors are time domain signals. The defects from the bearings and gears can be identified from their corresponding desired frequency amplitudes in the frequency spectrum. The FFT converts the time domain signal into a frequency domain signal and helps in analyzing each desired frequency based on its amplitude and its harmonics.

10.3 Analytical Diagnostics

The sideband and kurtosis based online defect detection method is employed to process the frequency data analytically and the stepwise procedure is shown in Table 10.3. The maximum amplitude of the desired frequency, the sidebands, and the kurtosis values for the sidebands are determined to calculate the severity factors to formulate the defect severity matrix. The failure modes and their severity levels are determined by the defect severity matrix from the vibration-based sensory signals.

Table 10.3. Procedure for analytical diagnostics

Step 1	Determine maximum amplitude values for sidebands and desired frequency
Step 2	Determine kurtosis values for sidebands
Step 3	Calculate severity factor 1, 2 and 3
Step 4	Formulate defect severity matrix

10.3.1 Sideband and Kurtosis Analysis

The sidebands are indicators of the failure modes in the frequency spectrum of the rotating components based on their spread on both the sides of the desired frequency. The rising and inequality of the sidebands correspond to component defects, and moreover, the severity of the defect can be identified based on the frequency sideband features, as listed in Table 10.4 [71]. The height and sharpness of the peak amplitudes in the frequency spectrum are measured by kurtosis. The spread of the sidebands on either side of the desired frequency can be analyzed

using the kurtosis values. The differences in the kurtosis values of both sidebands denote the inequality in the sidebands. The kurtosis ratio *KR*, is the ratio of the left side of j^{th}, the desired frequency is K_{Lj}, to the right side of j^{th}, the desired frequency K_{Rj} is as shown in Equation (21). Similarly, the ratio of maximum amplitude of the sideband on left and right sides of the j^{th} frequency is determined as *AR* shown in Equation (21).

$$KR = \frac{K_{Lj}}{K_{Rj}}; \quad AR = \frac{A_{Lj}}{A_{Rj}} \tag{21}$$

Table 10.4. Sideband-based severity definition

Frequency Sideband Feature	Severity Level
Rising of sidebands around desired frequency	Low
Unequal sidebands on both sides	Medium
High sideband amplitude than frequency amplitude	High

10.3.2 Severity Factors

The different failure modes and their severity levels are determined from the converted frequency domain signal through analytical sideband and kurtosis analysis.

Table 10.4 shows the different severity levels based on the frequency sideband features. The severity factor analysis resulted in three severity factor metrics for online defect detection. The severity factor 1 (SF1) ensures equal spread of the sidebands using the kurtosis ratio metric, as shown in Equation (22). The threshold kurtosis ratio, KR_T, is considered to be 0.6. The value of SF1<1 denotes the unequal spread of sidebands and vice versa. The severity factor 2 (SF2) ensures equal maximum amplitude of sidebands on both sides of the desired frequency, as shown in Equation (23). The threshold amplitude ratio, A_T, is considered to be 0.9. The value of SF2< 1 denotes the unequal frequency amplitudes on both sides of the sidebands and vice versa.

$$SF_1 = \frac{\text{Min}\ (KR_j, KR_j^{-1})}{KR_T} \tag{22}$$

$$SF_2 = \frac{\text{Min}\ (AR_j, AR_j^{-1})}{A_T} \tag{23}$$

The severity factor 3 (SF3) ensures that the maximum desired frequency amplitude is higher than the maximum amplitude of the sideband A_{max}, as shown in Equation (24), where A_F is the maximum amplitude at the desired frequency. The value of SF3< 1 denotes the frequency amplitude of the sideband, A_{max}, which is higher compared to the desired frequency, A_{max}.

$$SF_3 = \frac{A_F}{\text{Max}\ (A_{Lj}, A_{Rj})} \tag{24}$$

Table 10.5. Severity factor analysis of sensor AN 6 for Case 2a

Component	Desired Frequency	SF1	SF2	SF3	Low	Medium	High
ISS gear and ISS pinion	GMF	0.49	0.97	0.46	0	0	1
ISS upwind bearing	BPFI	0.98	0.73	2.85	0	1	0
ISS downwind bearing	BPFO	0.86	0.42	2.94	0	1	0
HSS upwind bearing	BPFO	0.58	1.06	0.23	0	0	1
HSS downwind bearing	BPFI	0.72	0.58	1.67	0	1	0

The conditions SF1 ≤ 1, SF2> 1, and SF3> 1 show that the component has a low severity defect. The severity factor characteristics of the medium severity defect are SF1 ≤ 1, SF2 ≤ 1, and SF3> 1 and SF1> 1, SF2 ≤ 1, and SF3> 1. Similarly, the high severity defect conditions are SF1 ≤ 1, SF2 ≤ 1, and SF3 ≤ 1; SF1> 1, SF2 ≤ 1, and SF3 ≤ 1; SF1 ≤ 1, SF2> 1, SF3 ≤ 1, and SF1> 1, SF2> 1, SF3≤ 1. Based on these rules, the severity levels and the failure modes of the components are identified based on the each sensor. The severity factor analysis of sensor AN 6 for 2a case is listed in Table 10.5.

10.3.3 Severity Defect Matrix

The failure modes and their severity levels of the rotating components based on the each sensor are identified with different severity metrics. However, the same defect of the rotating components can be identified by different sensors in and around the component location. Therefore, there is a need for developing a unified metric to make decisions on the failure mode and its severity level. This, in turn, will lead to the development of a defect severity matrix, combining the results of all the components from the different sensors. The desired component matrix U is shown in the Equation (25).

$$U = \begin{pmatrix} \text{ISS Gear and ISS Pinion} \\ \text{HSS Gear and HSS Pinion} \\ \text{LSS upwind bearing} \\ \text{LSS downwind bearing} \\ \text{ISS upwind bearing} \\ \text{ISS downwind bearing} \\ \text{HSS upwind bearing} \\ \text{HSS downwind bearing} \end{pmatrix} \tag{25}$$

The desired component matrix and the severity factor levels of all the components are utilized for developing a defect severity matrix. The severity ratio of component u at severity level g, S_{ug} is represented as Equation (26), where g represents the different severity levels, such as low, medium, and high, and S_{ugm} represents the severity level of component u at level g through sensor m.

$$S_{ug} = \sum_{m=1}^{M} S_{ugm} \Big/ \sum_{g=1}^{3} \sum_{m=1}^{M} S_{ugm} \tag{26}$$

The defect severity matrix, DS, represents the defect component and its severity level in the matrix format as shown in Equation (27), where rows of the matrix represent each desired component and columns represent the severity level of the components, such as low, medium and high.

$$DS = \begin{pmatrix} S_{11} & S_{12} & S_{13} \\ \vdots & \ddots & \vdots \\ S_{U1} & S_{U2} & S_{U3} \end{pmatrix} \tag{27}$$

The unified DS matrix of the Round Robin study is determined and shown in the Equation (28). The analytical diagnostics results indicated that there is no defect in the LSS upwind and downwind bearings. The IS gear and pinion each have a high severity defect and the HS gear and pinion each have a medium severity defect. The analytical results are further fine-tuned using the graphical verification process.

$$DS = \begin{pmatrix} 0.33 & 0.50 & 0 & 0 & 0.67 & 0.50 & 0.50 & 0.60 \\ 0.34 & 0.50 & 0 & 0 & 0.33 & 0.50 & 0.33 & 0.40 \\ 0.33 & 0.00 & 0 & 0 & 0.00 & 0.00 & 0.17 & 0.00 \end{pmatrix}^{T} \tag{28}$$

10.4 Graphical Diagnostics

The unified defect severity matrix results provide the initial insights about the component defects and their severity levels. There is the possibility of false identifications in the analytical methodology due to the overlap of different frequencies and their harmonic levels. Therefore, there is a need for verification of identified component defects graphically. The frequency spectrum of the predetermined component defects are verified graphically based on the sideband amplitudes and their spread. The second harmonic of the BPFO (172 Hz) of HSS downwind bearing at (344 Hz) in AN 6 ISS is the radial sensor value shown in Figure 10.2. The A_{max} of right sideband is almost two times the A_{max} of left sideband and moreover, the high amplitude of the right sideband is almost eight times the high amplitude of the desired frequency. These inferences from the figure prove that there is a high severity failure in the outer raceway. Since the sideband amplitudes are found in the second harmonic, there is a chance of misalignment of the bearing. Similarly, component defects are identified graphically and the results are discussed in the next section.

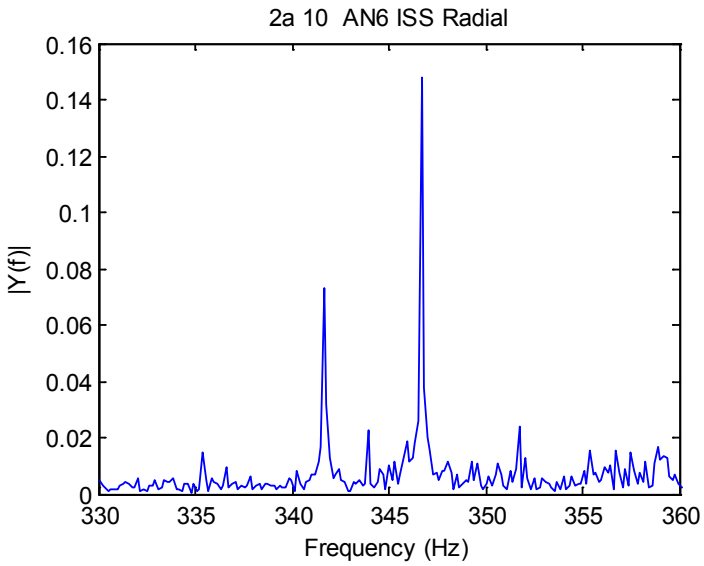

Figure 10.2. HSS downwind bearing BPFO – graphical analysis

10.5 Results

The results from the online analytical defect detection method are used as inputs to the graphical verification. The failure modes and their severity levels from the multi-dimensional vibration-based sensory signals are verified graphically, and the results are unified to the component level, with their corresponding severity levels, as shown in Table 10.6.

Table 10.6. Vibration-based condition monitoring results

Damage	Component	Mode	Severity
1	HSS pinion	Gear tooth failure of HSS pinion	High
2	HSS downwind bearing	OR failure and bearing misalignment	High
3	ISS gear	Early stages of gear failure	Low
4	ISS upwind bearing	IR failure and bearing misalignment	Medium
5	ISS downwind bearing	OR failure	High

The tabulated results were identified before the receiving knowledge of the actual failure modes. The possible number of failures that can be identified from the vibration analysis for this Round Robin study is about seven. The proposed condition monitoring approach identified five failures and their severity levels. Moreover, the failures identified by the proposed vibration analysis approach do not have any false identification. The accuracy of the condition monitoring approach is due to its two fold analysis process, i.e. the analytical identification and the graphical verification. The preliminary results from the analytical identification are further fine-tuned using the graphical verification to avoid false identifications.

As a summary, this research showed that the developed vibration based two stage fault detection framework that integrates both analytical diagnostics and graphical diagnostics is quite effective for analyzing gear and bearing faults in wind turbine transmissions, as proved by the CM Round Robin study results. With successful studies and lessons learned on the drivetrain CM, the research can be extended to a probabilistic complex system design framework that potentially can quantify the functionality, reliability, uncertainty, and cost/benefits of condition monitoring techniques. It can integrate them into a system-level wind turbine design practice, as a fundamental solution of enhancing reliability and reducing life cycle cost.

11 Recommended Practices

Based on the comparison of diagnostics results provided by sixteen partners during the blind study stage, as presented in Chapter 1, and the detailed results from eight of the sixteen partners, as presented in Chapters 3-10, it is clear that there is still room for the industry to improve vibration analysis algorithms. Some algorithms presented in this report have not been widely adopted in commercialized vibration-based condition monitoring (CM) systems. If adopted, they can lead to increased accuracy of vibration-based wind turbine drivetrain condition monitoring. They may potentially help increase the cost effectiveness of wind turbine condition monitoring techniques. In addition, based on the lessons learned in this study, some recommended practices were provided by several partners, especially Impact Technologies, National Instruments, and STC Consultants. They will be discussed in this chapter. It is hoped that these recommended practices can be considered in future research and development efforts within the wind turbine condition monitoring community.

11.1 Data Acquisition

To meet the dynamometer retest schedule of the damaged GRC gearbox, the vibration CM data acquisition system used in this study was put together within an extremely tight time window. However, efforts were made, as much as possible, to represent a typical commercialized vibration CM system and meet the guidelines recommended by Germanischer Lloyd (GL) [72]. For example, anti-aliasing filters and 24 bit ADC were adopted for all sensor channels.

This study, however, was challenged by poor speed measurements. As pointed out by almost all of the project partners, there was no once per revolution signal, which is valuable for time synchronous averaging for gear health condition diagnostics. The measured high speed shaft rpm also showed oscillations, which could be worked around but was a challenge. A once per revolution signal could have been generated based on the raw encoder readings throughout the test and provided to all Round Robin project partners. It was not attempted so the project partners could have enough time to conduct the blind stage data analysis. However, it is recommended that a once per revolution signal be provided in gear health monitoring since tachometer signal acquisition requires converting pulse trains into a series of timestamps and speeds. In general, to isolate mechanical vibration frequencies from one another, accurate speeds and angular positions of the shaft's rotation are critical. The GL guidelines [72] call for high resolution speed measurements as part of an instrumentation system in the field. Further, to track vibration frequencies with respect to speed, both vibration and speed measurements should be made simultaneously or clocked from the same base clock. In the Round Robin project, speed information came from the high speed shaft. Adding a tachometer to monitor the input rotor shaft might provide a more accurate result for the lower speed components.

This Round Robin study focuses on the gearbox, as it is the only component with disassembled information. If the main bearing is considered for study, accelerometers, with a measurement frequency range down to 0.1 Hz, are recommended. Alternatively, new sensing techniques, such as acoustic emission [73], can be investigated. This recommendation may also be applicable to the ring gear. In addition, for some bearing locations and types inside the gearbox, it may be worth evaluating axial-mounted accelerometers.

In this study, only the frequency domain baseline data was provided. Also, the test data was collected from one test gearbox for a short period of time. Diagnostics results could have been further improved by providing the baseline data in the time domain from a bigger population of gearboxes of the same model, and a longer data acquisition window of months or years.

The data acquisition system developed for this study was put together to facilitate the Round Robin research. Its main emphasis was to collect high resolution raw time series data, which can be provided to vibration analysts for diagnosis of the monitored gearbox condition. When deploying a condition monitoring system in the field, it is important to balance the amount of data, communications, and timing of the data acquisition. Communications may be expensive when using a cellular modem, or slow using a 900 MHz radio. The amount of data storage on-board an embedded data acquisition system may be limited. For this balancing task, a machine with a check trigger state containing continuous acquisition and analysis of incoming sensory data can be investigated. When the monitored wind turbine is operating, and measured values have changed by a specific percentage or delta, then both pre-trigger and post-trigger sensory data is stored to a binary file with a complete descriptive set including enterprise, wind farm, and wind turbine. By combining both periodic data recordings with data change driver recordings, a complete picture of the wind turbine is possible, using just the right amount of data.

11.2 Data Analysis

Once data is collected, the challenge lies in how to interpret the data and derive useful information. The diagnostic tasks in the Round Robin project are more challenging because the drivetrain damage was more complex than in a typical operational wind turbine. Therefore, the diagnostics techniques presented in this report could potentially perform better when deployed in the field. For this project, NREL is fortunate to have the support from vibration analysts across the world. Main recommended practices mentioned by the project partners for vibration data analysis are discussed below.

Though no sensor faults were present in the test data sets shared by NREL for this study, it is generally recommended to perform sensor validation before using vibration data for condition monitoring of rotating components. GL uses a similar guideline. [72] This will help reduce ambiguity between sensor and mechanical faults and reduce false alarms.

The GRC test turbine operates at two relatively constant speeds. For variable speed wind turbines, the GL guidelines call for order tracking using measured speed [72].

Due to the complexity in gearbox design and the dynamic operating conditions, an integrated approach must be taken that uses diagnostic information from all components (gears, bearings, and shafts) as a whole. In other words, the analysis needs to integrate all available diagnostic information to confidently detect and isolate problems via a high level reasoning / classifier method. In addition, vast differences in speed/torque could cause dramatic differences in results of vibration analysis. The accuracy can be increased by comparing results from similar steady state operating conditions, e.g., the operational-category concept [74], by applying techniques that are less sensitive to the effects, or by normalizing results. Conventional gear diagnostic features are limited for planetary gear component fault detection because of the changing transmission path, moving fault location, and modulation. As such, special consideration should be given to fault detection of these components. For example, multiple cycles of the hunting

tooth ratio should be recorded for each planetary component. In addition, diagnostic approaches that are specifically designed for planetary gear fault detection should be used.

Enveloping or demodulation has proven to be an effective approach for bearing diagnostics. However, proper selection of various filters used by this approach is critical to diagnostic performance, in particular for the incipient fault detection capabilities. These filters should also be optimized for each sensor location [75]. Note, too, that these resonant frequencies may likely change with operating conditions as well. Enveloping or demodulation at higher frequencies is desirable to avoid higher order gear mesh harmonics that obfuscate bearing fault frequencies. Ideally, both the sensor and data acquisition system would provide data above 20 kHz. However, an increase in only the sampling rate has been shown to increase diagnostic performance. Another factor to consider is how much additional cost is needed for collecting data above 20 kHz.

Fusing vibration results with those from other sensors would help complete the diagnostic coverage. In particular, oil debris, oil temperature, and casing temperature [72,76] would provide additional evidence of impending failures. Modeling/simulation of expected vibration at different operating and fault conditions is useful and a good compliment to seeded fault and accelerated life testing.

Appendix A – Project Partners

Brüel & Kjær Vibro A/S

Colorado School of Mines

GE Bently Nevada

Impact Technologies

IVC Technologies

National Instruments

NRG Systems Inc.

Purdue University

Schenck Corporation

Sentient Corporation

STC Consultants (SKF)

University of Cincinnati

University of Connecticut

University of Iowa

University of New South Wales in Australia

Wichita State University

References

1. Motavalli, J. (2004). “Catching the Wind.” *The Environmental Magazine*; Dec 31, 2004. http://www.emagazine.com/archive/2176

2. Link, L.; LaCava, W.; van Dam, Jeroen.; McNiff, B.; Sheng, S.; Wallen, R.; McDade, M.; Lambert, S.; Butterfield, S.; Oyague, Francisco. *Gearbox Reliability Collaborative Project Report: Findings from Phase 1 and Phase 2 Testing*. NREL/TP-5000-51885. Golden, CO: National Renewable Energy Laboratory, June 2011. http://www.nrel.gov/docs/fy11osti/51885.pdf.

3. Sheng, S.; Link, L.; LaCava, W.; van Dam, J.; McNiff, B.; Veers, P.; Keller, J.; Butterfield, S.; Oyague, Francisco. *Wind Turbine Drivetrain Condition Monitoring During GRC Phase 1 and Phase 2 Testing*. NREL/TP-5000-52748. Golden, CO: National Renewable Energy Laboratory, October, 2011. http://www.nrel.gov/docs/fy12osti/52748.pdf

4. Errichello, R.; Muller, J. (2012) *Gearbox Reliability Collaborative Gearbox 1 Failure Analysis Report*. NREL/SR-5000-530262. Work performed by Geartech, Townsend, Montana. Golden, CO: National Renewable Energy Laboratory, February 2012. http://www.nrel.gov/docs/fy12osti/53062.pdf

5. Musial,W.; McNiff, B. “Wind Turbine Testing in the NREL Dynamometer Test Bed.” *American Wind Energy Association’s WindPower 2000 Conference; April 30-May 4, 2000, Palm Springs, CA*. NREL/CP-500-28411. Golden, CO: National Renewable Energy Laboratory, June 2000 . http://www.nrel.gov/docs/fy00osti/28411.pdf

6. National Renewable Energy Laboratory. *Dynamometer Testing (Fact Sheet)*. NREL/FS-5000-45649. Golden, CO. http://www.nrel.gov/docs/fy11osti/45649.pdf.

7. Frarey, J.L. “The History and Application of the Envelope Detector.” Technology Showcase: Integrated Monitoring, Diagnostics and Failure Prevention, Proceeding of a Joint Conference, Mobile, Alabama, and April 22-26, 1996. Haymarket, VA: Society for Machinery Failure Prevention Technology. http://www.dtic.mil/cgi-bin/GetTRDoc?AD=ADP010154

8. Broderick, J.J.; Burchill, R.F.; Clark, H.L. *Design and Fabrication of Prototype System for Early Warning of Impending Bearing Failure*. NASA-CR-123717, MTI-71TR1. Hunstville, AL: National Aeronautics and Space Administration (NASA), January 1972. http://ntrs.nasa.gov/archive/nasa/casi.ntrs.nasa.gov/19720020851_1972020851.pdf

9. Luo, H.; Qiu, H.; Ghanime, G.; Hirz, M.; van der Merwe, G. “Synthesized Synchronous Sampling Technique for Differential Bearing Damage Detection.” *Journal of Engineering for Gas Turbines and Power*; Vol.132, Issue 7, 2010. http://dx.doi.org/10.1115/1.4000092

10. Hochmann, D.; Sadok, M. “Theory of Synchronous Averaging.” *Proceedings of the 2004 IEEE Aerospace Conference; March 6-13, 2004, Big Sky, Montana*. Washington, DC: IEEE, 2004; pp. 3636-3653. http://dx.doi.org/10.1109/AERO.2004.1368181

11. Hanna, J.; Hatch, C.; Kalb, M.; Weiss, A.; Luo, H. "Detection of Wind Turbine Gear Tooth Defects Using Sideband Energy Ratio™." *China Wind Power 2011;October, 19-21, 2011, Beijing, China.* http://www.ge-mcs.com/download/monitoring/SER-Technical-Paper.pdf

12. Marple, L. Jr., "Computing the Discrete-Time Analytic Signal via FFT." *IEEE Transactions on Signal Processing*, Vol. 47, No. 9, 1999; pp.2600-2603. http://dx.doi.org/10.1109/78.782222

13. Luo, H.; Fang, X.; Ertas, B. "Hilbert transform and its engineering applications." *AIAA Journal*, Vol. 47, No. 4, 2009' pp. 923-932. http://dx.doi.org/10.2514/1.37649

14. Bagnoli, S.; Capitani, R.; Citti, P. "Comparison of Accelerometer and Acoustic Emission signals as Diagnostic Tools in Assessing Bearing Damage," *Proceedings of the 2nd International Conference: Condition Monitoring; 24-25 May 1988, London, UK*. Cranfield, England: BHRA, 1988.

15. Braun, S.; Datner, B. "Analysis of Roller/Ball Bearing Vibrations." *Transactions of the ASME*, Vol. 101, 1979; pp. 118-125.

16. Harris, T.A. *Rolling Bearing Analysis*. 4th edition. New York, NY: John Wiley & Sons, York, 2001; pp. 993-1000.

17. Braun, S.G.; Seth. B.B. "On the Extraction and Filtering of Signals Acquired from Rotating Machines." *Journal of Sound and Vibration*, Vol. 65, No. 1, 1979; pp. 37-50.

18. Lebold, M.; McClintic, K.; Campbell, R.; Byington, C.; Maynard, K. "Review of Vibration Analysis Methods for Gearbox Diagnostics and Prognostics." *Proceedings of the 54th Meeting of the Society for Machinery Failure Prevention Technology; May 1-4, 2000,Virginia Beach, VA.* Haymarket, VA: Society for Machinery Failure Prevention Technology, 1985. http://php.scripts.psu.edu/users/k/p/kpm128/pubs/FeatureTutorialBody18.PDF

19. Szczepanik, A. "Time Synchronous Averaging of Ball Mill Vibrations." *Mechanical Systems and Signal Processing*; Vol. 3, No. 1, 1989, pp. 99-107. http://dx.doi.org/10.1016/0888-3270(89)90025-3

20. Ma, J. "Energy Operator and Other Demodulation Approaches to Gear Defect Detection." *Proceedings of the 49th Meeting of the Society of Mechanical Failures Prevention Technology; April 18-20, Virginia Beach, VA*. Haymarket, VA: Society for Machinery Failure Prevention Technology, 1995; pp. 127-140.

21. Favaloro, S.C. *A Preliminary Evaluation of Some Gear Diagnostics Using Vibration Analysis*. ARL-AERO-RPOP-TM-427. Melbourne, Australia: Aeronautical Research Laboratory, 1985.

22. Watson, M. J.; Sheldon, J.S.; Lee, H. "Novel Joint Time Frequency Vibration Diagnostics of Turbine Engine Accessories." *ASME Turbo Expo 2010: Power for Land, sea, and Air; June 14-18, 2010, Glasgow, UK*. New York, NY: ASME, 2010; pp. 353-363. http://dx.doi.org/10.1115/GT2010-23539

23. McFadden, P. “A Revised Model for the Extraction of Periodic Waveforms by Time Domain Averaging.” *Mechanical Systems and Signal Processing*; Vol. 1, No. 1, 1999; pp. 83-95. http://dx.doi.org/10.1016/0888-3270(87)90085-9

24. Randall, R.B. *Vibration-based Condition Monitoring*. Hoboken, NJ: Wiley, 2011.

25. McFadden, P.; Smith, J. “A Signal Processing Technique for Detecting Local Defects in a Gear from a Signal Average of the Vibration.” *Proceedings of the Institution of Mechanical Engineers, Part C: Journal of Mechanical Engineering Science*; Vol. 199, No. 4, 1985; pp. 287-292.

26. Zakrajsek, J.J.; Townsend, D.P.; Decker, H.J. “An Analysis of Gear Fault Detection Method as Applied to Pitting Fatigue Failure Damage.” *47th Mechanical Failure Prevention Group; April 13-15, 1993, Virginia Beach, VA*. *NASA Technical Memorandum* 105950. Cleveland, OH: National Aeronautics and Space Administration (NASA), Lewis Research Center, 1993. http://www.dtic.mil/cgi-bin/GetTRDoc?AD=ADA263115.

27. Mark, W.D.; Lee, H.; Patrick, R.; Coker, J.D. “A Simple Frequency-Domain Algorithm for Early Detection of Damage Gear Teeth.” *Mechanical Systems and Signal Processing*; Vol. 24, No. 8, 2010; pp. 2807-2823. http://dx.doi.org/10.1016/j.ymssp.2010.04.004

28. Randall, R.B.; Antoni, J. “Rolling Element Bearing Diagnostics-A Tutorial.” *Mechanical Systems and Signal Processing*; Vol. 25, No. 2, 2011; pp. 485-520. http://dx.doi.org/10.1016/j.ymssp.2010.07.017.

29. McFadden, P.D. “Window Functions for the Calculation of the Time Domain Averages of the Vibration of the Individual Planet Gears and Sun Gear in an Epicyclic Gearbox.” *Journal of Vibration and Acoustics*; Vol. 116, No. 2, 1994. http://dx.doi.org/10.1115/1.2930410

30. Antoni, J.; Randall, R.B. “The Spectral Kurtosis: Application to the Vibratory Surveillance and Diagnostics of Rotating Machines.” *Mechanical Systems and Signal Processing*; Vol. 20, No. 2, 2006; pp. 308-331. http://dx.doi.org/10.1016/j.ymssp.2004.09.002.

31. Combet, F.; Gelman, L. “Novel Adaptation of the Demodulation Technology for Gear Damage Detection to Variable Amplitudes for Mesh Harmonics.” *Mechanical Systems and Signal Processing*; Vol. 25, No. 3, 2011; pp. 839-845. http://dx.doi.org/10.1016/j.ymssp.2010.07.008

32. El Badaoui, M.; Guillet, F.; Daniere, J. “New Applications of the Real Cepstrum to Gear Signals, Including Definition of a Robust Fault Indicator.” *Mechanical Systems and Signal Processing*; Vol. 18, No. 5, 2004; pp. 1031-1046. http://dx.doi.org/10.1016/j.ymssp.2004.01.005

33. McFadden, P.D.; Smith, J.D. “Vibration Monitoring of Rolling Element Bearings by the High-Frequency Resonance Technique-A Review.” *Tribology International*; Vol. 17, No. 1, 1984; pp. 3-10. http://dx.doi.org/10.1016/0301-679X(84)90076-8

34. Combet, F.; Gelman, L. “Optimal Filtering of Gear Signals for Early Damage Detection Based on the Spectral Kurtosis.” *Mechanical Systems and Signal Processing*; Vol. 23, No. 3, 2009; pp. 652-668. http://dx.doi.org/10.1016/j.ymssp.2008.08.002

35. Bonnardot, F.; El Badaoui, M.; Randall, R.B.; Daniere, J.; Guillet, F. “Use of the Acceleration Signal of a Paradox in Order to Perform Angular Resampling (with Limited Speed Fluctuation).” *Mechanical Systems and Signal Processing*; Vol. 19, No. 4, 2005; pp. 766-785. http://dx.doi.org/10.1016/j.ymssp.2004.05.001

36. Bechhoefer, E.; Kingsley, M. “A Review of Time Synchronous Average Algorithms.” *Annual Conference of the Prognostics and Health Management Society; September 27-October 1, 2009, San Diego, CA*. New York, NY: PHM Society, 2009. http://www.phmsociety.org/sites/phmsociety.org/files/phm_submission/2009/phmc_09_5.pdf

37. Dempsey, P.J. “A Comparison of Vibration and Oil Debris Gear Damage Detection Methods Applied to Pitting Damage.” *13th International Congress on Condition Monitoring and Diagnostic Engineering Management; December 3-8, 2000, Houston, Texas*. NASA/TM-2000-210371. Cleveland, OH: National Aeronautics and Space Administration (NASA), Glenn Research Center, 2000; 18 pp. http://ntrs.nasa.gov/archive/nasa/casi.ntrs.nasa.gov/20000120403_2000175883.pdf

38. McFadden, P.D. “Detecting Fatigue Cracks in Gears by Amplitude and Phase Demodulation of the Meshing Vibration.” *Journal of Vibration, Acoustics, Stress, and Reliability in Design*; Vol. 108, No. 2, 1986; pp. 165-170. http://dx.doi.org/10.1115/1.3269317

39. Forrester, D. “A Method for the Separation of Epicyclic Planet Gear Vibration Signatures.” *Proceedings of the Acoustical and Vibratory Surveillance Methods and Diagnostic Techniques; Senlis, France*. 1998; pp. 539-548.

40. Samuel, P.D.; Conroy, J.K.; Pines, D.J. *Planetary Transmission Diagnostics*. NASA/CR-2004-213068. Cleveland, OH: National Aeronautics and Space Administration (NASA), Glenn Research Center, May 2004. http://ntrs.nasa.gov/archive/nasa/casi.ntrs.nasa.gov/20040073522_2004069093.pdf

41. Ciang, C.C.; Lee, J.-R.; Bang, H.-J. “Structural Health Monitoring for a Wind Turbine System: A Review of Damage Detection Methods.” *Measurement Science and Technology*; Vol. 19, No. 12, 2008. http://dx.doi.org/10.1088/0957-0233/19/12/122001

42. McFadden, P.D. “Detecting Fatigue Cracks in Gears by Amplitude and Phase Demodulation of the Meshing Vibration.” *Journal of Vibration, Acoustics, Stress, and Reliability in Design*; Vol. 108, No. 2, 1986; pp. 165-170. http://dx.doi.org/10.1115/1.3269317

43. Lin, J.; Zuo, M.J. “Gearbox Fault Diagnosis Using Adaptive Wavelet Filter.” *Mechanical Systems and Signal Processing*; Vol. 17, No. 6, 2003; pp. 1259-1269. http://dx.doi.org/10.1006/mssp.2002.1507

44. Barszcz, T.; Randall, R.B. “Application of Spectral Kurtosis for Detection of a Tooth Crack in the Planetary Gear of a Wind Turbine.” *Mechanical Systems and Signal Processing*; Vol. 23, No. 4, 2009; pp. 1352-1365. http://dx.doi.org/10.1016/j.ymssp.2008.07.019

45. Yan, R.; Gao, R.X. “Multi-Scale Enveloping Spectrogram for Vibration Analysis in Bearing Defect Diagnosis.” *Tribology International*; Vol. 42, No. 2, 2009; pp. 293-302. http://dx.doi.org/10.1016/j.triboint.2008.06.013.

46. Tsai, C.-S.; Hsieh, C.-T.; Huang, S.-J. “Enhancement of Damage-Detection of Wind Turbine Blades via CWT-Based Approaches.” *IEEE Transactions on Energy Conversion*; Vol. 21, No. 3, 2006; pp. 776-781. http://dx.doi.org/10.1109/TEC.2006.875436

47. Watson, S.J.; Xiang, B.J.; Yang, W.; Tavner, P.J.; Crabtree, C.J. “Condition Monitoring of the Power Output of Wind Turbine Generators Using Wavelets.” *IEEE Transactions on Energy Conversion*; Vol. 25, No. 3, 2010; pp. 715-721. http://dx.doi.org/10.1109/TEC.2010.2040083

48. Mohanty, A.R.; Kar, C. “Fault Detection in a Multistage Gearbox by Demodulation of Motor Current Waveform.” *IEEE Transactions on Industrial Electronics*; Vol. 53, No. 4, 2006; pp. 1285-1297. http://dx.doi.org/10.1109/TIE.2006.878303.

49. Wang, W.J.; McFadden, P.D. “Application of Wavelets to Gearbox Vibration Signals for Fault Detection.” *Journal of Sound and Vibration*; Vol. 192, No, 5, 1996; pp. 927-939. http://dx.doi.org/10.1006/jsvi.1996.0226

50. Yuan, X.; Cai, L. “Variable Amplitude Fourier Series with its Applicationh in Gearbox Diagnosis-Part I: Principle and Simulation.” *Mechanical Systems and Signal Processing*; Vol. 19, No. 5, 2005; pp. 1055-1066. http://dx.doi.org/10.1016/j.ymssp.2004.10.011

51. Yuan, X.; Cai, L. “Variable Amplitude Fourier Series with its Applicationh in Gearbox Diagnosis-Part I: Principle and Simulation.” *Mechanical Systems and Signal Processing*; Vol. 19, No. 5, 2005; pp. 1067-1081. http://dx.doi.org/10.1016/j.ymssp.2004.10.012

52. Tan, P.-N.; Steinbach, M.; Kumar, V. *Introduction to Data Mining*. Boston, MA: Pearson Addison Wesley, 2006.

53. Devijver, P.A.; Kittler, J. *Pattern Recognition: A Statistical Approach*. Englewood Cliffs, NJ: Prentice-Hall, 1982.

54. Mosteller, F. “A *k*-Sample Slippage Test for an Extreme Population.” *The Annals of Mathematical Statistics*; Vol. 19, No. 1, 1948; pp. 58-65. http://www.jstor.org/stable/2236056

55. Antoni, J. “The Spectral Kurtosis: A Useful Tool for Characterising Non-Stationary Signals.” *Mechanical Systems and Signal Processing*; Vol. 20, No. 2, 2006; pp. 282-307. http://dx.doi.org/10.1016/j.ymssp.2004.09.001

56. Sawalhi, N.; Randall, R.B. “Semi-Automated Bearing Diagnostics-Three Case Studies.” *Comadem Conference;June 13-15, 2007, Faro, Portugal*. Coimbra : Inst. de Telecomunicações, 2007.

57. Sawalhi, N.; Randall, R. B. “Signal Pre-Whitening for Fault Detection Enhancement and Surveillance in Rolling Element Bearings.” *Eighth International Conference on Condition Monitoring and Machinery Failure Prevention Technologies; June 20-22,2011, St David's Hotel, Cardiff, UK, 20-22 June.*

58. Antoni, J. “Differential Diagnosis of Gear and Bearing Faults.” *Journal of Vibration and Acoustics*; Vol. 124, No. 2, 2002; pp. 165-171. http://dx.doi.org/10.1115/1.1456906

59. Sawalhi, N.; Randall, R.B. “Spectral Kurtosis Optimization for Rolling Element Bearings.” *ISSPA 2005: The 8th International Symposium on Signal Processing and its Applications; August 28-31, 2005, Sydney, Australia*. Piscataway, NJ: IEEE, 2005; pp. 839-842. http://dx.doi.org/10.1109/ISSPA.2005.1581069

60. Urbanek, J.; Barszcz, T.; Sawalhi, N.; Randall, R.B. “Comparison of Amplitude Based and Phase Based Methods for Speed Tracking in Application to Wind Turbines.” *IMEKO TC 10, 11th Workshop on Smart Diagnostics of Structures; October 18-20, Krakow, Poland*.

61. Sawalhi, N.; Randall, R.B. “Localised Fault Diagnosis in Rolling Element Bearings in Gearboxes.” The Fifth International Conference on Condition Monitoring and Machinery Failure Prevention Technologies; July 15-18, Edinburgh, UK, 2008. Oxford, UK: Coxmoor Publishing Company, 2008.

62. Randall, R.B.; Sawalhi, N.; Coats, M. “A Comparison of Methods for Separation of Deterministic and Random Signals.” *International Journal of Condition Monitoring*; Vol. 1, No. 1; 2011; pp. 11-19. http://dx.doi.org/10.1784/204764211798089048

63. Forrester, D.; Blunt, D. “Analysis of Epicyclic Gearbox Vibration.” *DSTO HUMS; Conference, Melbourne*. 2003.

64. Tamilselvan, P.; Wang, P.; and Twomey, J. “Quantification of Economic and Environmental Benefits for Prognosis Informed Wind Farm Operation and Maintenance.” *ISERC 2012, 62nd Annual IIE Industrial Systems and Engineering Research Conference; May 19-23, 2012, Orlando, FL, USA.*

65. Tamilselvan, P.; Wang, Y.; and Wang, P. “Optimization of Wind Turbines Operation and Maintenance Using Failure Prognosis.” *PHM 2012, IEEE 2012 Prognostics and Health Management; June 18-21, 2012, Denver, CO, USA.*

66. Tamilselvan, P.; Wang, P.; and Twomey, J. “Prognosis Informed Stochastic Decision Making Framework for Operation and Maintenance of Wind Turbines.” *ISFA 2012, ASME 2012 International Symposium on Flexible Automation; June 18-20, 2012, St. Louis, MO, USA.*

67. Tamilselvan, P.; Wang , P.; and Jayaraman, R. “Diagnostics with Unexampled Faulty States Using a Two-Fold Classification Method.” *PHM 2012, 2012 IEEE International Conference on Prognostics and Health Management; June 18-21, 2012, Denver, CO, USA.*

68. Tamilselvan, P.; and Wang P. “A Hybrid Inference Approach for Health Diagnostics with Unexampled Faulty States.” *AIAA 2012-1784, 53th AIAA/ASME/ASCE /AHS/ASC Structures, Structural Dynamics, and Materials Conference; April 23-26, 2012, Honolulu, Hawaii, USA.*

69. Tamilselvan, P.; and Wang, P. “Structural Health Diagnosis Using Deep Belief Network Based State Classification.” *AIAA 2012-1783, 53th AIAA/ASME/ASCE /AHS/ASC Structures, Structural Dynamics, and Materials Conference; April 23-26, 2012, Honolulu, Hawaii, USA.*

70. Tamilselvan, P.; Wang, P.; and Youn, B. “Multi-Sensor Health Diagnosis Using Deep Belief Network Based State Classification.” *ASME 2011 International Design Engineering Technical Conference; August 29-31, 2011, Washington DC, USA.*

71. Spectra Quest Tech Note. “Analyzing Gearbox Degradation Using Time-Frequency Signature Analysis.” March, 2006.

72. Germanischer Lloyd. “Guidelines for the Certification of Condition Monitoring Systems for Wind Turbines.” Hamburg, Germany, 2007.

73. Smulders, A. “Challenges of Condition Monitoring for Wind Turbines and Successful Techniques.” *Wind Turbine Condition Monitoring; October 8-9, 2009, Omni Interlocken Resort, Broomfield, CO*. Golden, CO: National Renewable Energy Laboratory, 2009. http://wind.nrel.gov/public/Wind_Turbine_Condition_Monitoring_Workshop_2009/3.2.Smulders.Challenges_of_CM_for_WT_and_Successful_Techniques.pdf

74. Gellermann, T.; Walter, G. *Requirements for Condition Monitoring Systems for Wind Turbine*. AZT Report No. 03.01.068, 2003.

75. Wade, D. and Larsen Christopher. "Measurement of Gearbox Surface Frequency Repsonse Functions for HUMS Algorithm Improvement. *Presented at the American Helicopter Society 68th Annual Forum, Fort Worth, TX.* May 1-3, 2012.

76. Sheng, S. “Investigation of Various Condition Monitoring Techniques Based on a Damaged Wind Turbine Gearbox.” *8th International Workshop on Structural Health Monitoring; 13-15 September 2011, Stanford, CA*. NREL/CP-5000-51753. Golden, CO: National Renewable Energy Laboratory, 2011; 10 pp.